Formation and evolution of compact binaries

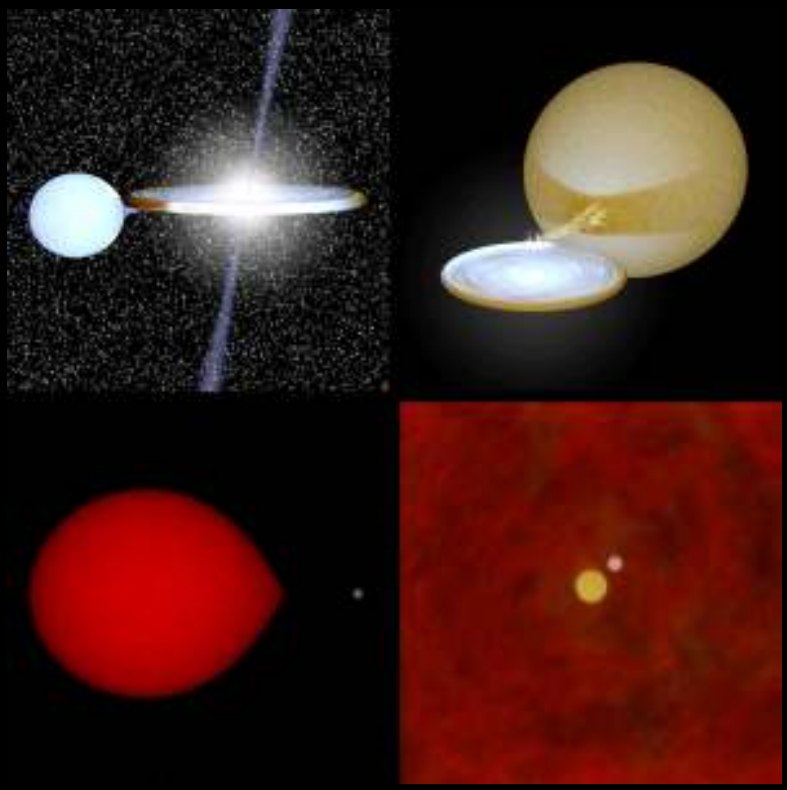

Marc van der Sluys

Formation and evolution of compact binaries

Cover:

a	b
c	d

a): The donor in the 11.4-minute X-ray binary in the globular cluster NGC 6624 is probably the inner 0.1 $M_{\odot}$ or less of a helium white dwarf.

b): A low-mass X-ray binary in which a star as massive as the sun transfers mass to a neutron star.

c): A red giant on the verge of filling its Roche lobe and engulfing the white dwarf, that is six times less massive, in a common envelope.

d): At the end of a spiral-in phase a common envelope becomes too dilute to cause any more drag forces and a double white dwarf emerges.

The figures a) through c) were created with the programme Binsim 0.8.1, written by Robert Hynes (http://www.phys.lsu.edu/∼rih/binsim/).

This book was typeset in LaTeX by the author and printed by MultiCopy in Utrecht.

ISBN-10: 90–393–4234–2
ISBN-13: 978–90–393–4234–3

Formation and evolution of compact binaries

Vorming en evolutie van compacte dubbelsterren

(met een samenvatting in het Nederlands)

Proefschrift

ter verkrijging van de graad van doctor
aan de Universiteit Utrecht
op gezag van de rector magnificus, prof. dr. W.H. Gispen,
ingevolge het besluit van het college voor promoties
in het openbaar te verdedigen op

dinsdag 2 mei 2006 des middags te 2.30 uur

door

Marcel Vincent van der Sluijs

geboren op 15 januari 1976 te De Bilt

Promotor: Prof. Dr. Frank Verbunt

Copromotor: Dr. Onno Pols

This research has been supported by the Netherlands Research School for Astronomy (NOVA).

to Daphny,
who will live on in my heart
for the rest of my life

and to Birgit,
who makes my life
worthwhile again

Contents

Contents i

Curriculum vitae iv

1 Introduction and summary 1
- 1.1 The evolution of single stars . . . 1
- 1.2 Binary-star evolution . . . 2
- 1.3 Summary of this thesis . . . 4
  - 1.3.1 The formation of luminous X-ray binaries in globular clusters . . . 5
  - 1.3.2 The presumed ultra-compact X-ray binary 2S 0918–549 . . . 9
  - 1.3.3 The formation of double white dwarfs . . . 10

2 Creating ultra-compact binaries in globular clusters through stable mass transfer 15
- 2.1 Introduction . . . 16
- 2.2 Binary evolution code . . . 18
  - 2.2.1 The stellar evolution code . . . 18
  - 2.2.2 Angular momentum losses . . . 19
- 2.3 Binary models . . . 19
  - 2.3.1 Calculated grid . . . 19
  - 2.3.2 Interpretation of the models . . . 20
  - 2.3.3 Bifurcation models . . . 26
- 2.4 Statistics . . . 27
  - 2.4.1 Interpolation between models . . . 27
  - 2.4.2 Results for Z=0.01 . . . 28
  - 2.4.3 Results for other metallicities . . . 29
- 2.5 Discussion . . . 34
  - 2.5.1 The importance of converging evolution for the formation of ultra-compact binaries . . . 34
  - 2.5.2 Comparison to Pylyser & Savonije . . . 38
  - 2.5.3 Comparison to Podsiadlowski et al. . . . 39
  - 2.5.4 Comparison with observations and other models . . . 40

3 Reduced magnetic braking and the magnetic capture model for the formation of ultra-compact binaries **43**
3.1 Introduction . . . 44
3.2 Binary evolution code . . . 44
3.2.1 The stellar evolution code . . . 44
3.2.2 Angular momentum losses . . . 44
3.3 Creating theoretical period distributions . . . 46
3.3.1 Binary models . . . 46
3.3.2 Statistics . . . 47
3.4 Results . . . 47
3.4.1 Reduced magnetic braking . . . 47
3.4.2 Saturated magnetic braking . . . 49
3.4.3 The influence of mass loss . . . 50
3.5 Discussion . . . 52
3.6 Conclusions . . . 55

4 On the possibility of a helium white dwarf donor in the presumed ultracompact binary 2S 0918–549 **57**
4.1 Introduction . . . 58
4.2 Synopsis of X-ray bursts from 2S 0918–549 . . . 59
4.3 Analysis of the long burst . . . 62
4.4 Flux history of persistent emission . . . 66
4.5 Discussion . . . 68
4.5.1 Short and long helium bursts . . . 68
4.5.2 Evolutionary considerations . . . 72
4.6 Conclusion . . . 77

5 Modelling the formation of double white dwarfs **79**
5.1 Introduction . . . 80
5.2 Observed double white dwarfs . . . 81
5.3 The stellar evolution code . . . 82
5.4 Giant branch models . . . 84
5.4.1 Basic models . . . 85
5.4.2 Chemical enrichment by accretion . . . 88
5.4.3 Wind mass loss . . . 90
5.5 Second mass-transfer phase . . . 93
5.5.1 The treatment of a spiral-in . . . 95
5.5.2 Results of the spiral-in calculations . . . 97
5.6 First mass-transfer phase . . . 100
5.6.1 Conservative mass transfer . . . 101
5.6.2 Unstable mass transfer . . . 107
5.6.3 Formation by multiple mechanisms . . . 112
5.6.4 Constraining the age difference . . . 113

5.6.5 Description of the individual solutions . . . 115
5.7 Discussion . . . 119
5.7.1 Comparison to other work . . . 119
5.7.2 Alternative formation scenario for massive white dwarfs . . . 120
5.8 Conclusions . . . 122
5.9 Appendix: Table of model solutions . . . 123

6 Vorming en evolutie van compacte dubbelsterren 127
6.1 Ontstaan en evolutie van enkele sterren . . . 127
6.2 Evolutie van dubbelsterren . . . 131
6.3 Dit proefschrift . . . 135
6.3.1 Ontstaan en evolutie van compacte röntgendubbelsterren . . . 136
6.3.2 De vorming van dubbele witte dwergen . . . 138

7 Formation und Evolution von kompakten Doppelsternen 139
7.1 Entstehung und Evolution von einzelnen Sternen . . . 139
7.2 Evolution von Doppelsternen . . . 142
7.3 Diese Dissertation . . . 145
7.3.1 Formation und Evolution von kompakten Röntgendoppelsternen . . . 146
7.3.2 Die Formation von doppelten Weissen Zwergen . . . 148

Acknowledgements 149

References 151

Curriculum vitae

I was born in De Bilt, the Netherlands on Thursday, January 15, 1976, around 15:50. I studied astrophysics at the University of Utrecht, the Netherlands, and obtained the degree 'Master of Science' in 2001. From 2001 to 2006 I did my PhD research at the Astronomical Institute in Utrecht, of which this thesis is the result. I will defend my thesis on May 2nd, 2006. From March to August 2006 I have a short postdoc position at the Astronomical Institute in Utrecht. On September 1st 2006 I will start working as a postdoc at Northwestern University in Illinois, U.S.A.

Current address

My current address is a variable of time and therefore it would be silly to write it in a book. Instead, I intend to keep the following web page up-to-date:
`http://www.vandersluys.nl/Marc/Contact/`

Chapter 1
Introduction and summary

1.1 The evolution of single stars

Stars are formed in clouds that are predominantly found in the spiral arms of galaxies. If such a cloud contracts, its temperature rises and it fragments into several hot cores. Such a condensation contracts in its turn, until the circumstances in its centre allow hydrogen fusion to take place. The condensation has become a zero-age main-sequence star and the mass and composition of the young star determine how it will spend the rest of its life.

The main sequence is the longest phase in the active evolution of a star (about 80%), so that most stars we observe are main-sequence stars. During this phase the luminosity and surface temperature of the star change only little, but when the star runs out of hydrogen in its core, it will change drastically. Because the core consists of helium only, nuclear fusion stops and the helium core will contract and heat up. The hydrogen-rich layers just outside the core become sufficiently compressed and heated that hydrogen fusion can take place in a shell around the core. The hydrogen-burning shell converts hydrogen into helium, and the core becomes more massive, more compact and hotter. Calculations show that a more compact core causes the density in the burning shell to drop so that the density in the envelope must drop as well to maintain hydrostatic equilibrium. The envelope of the star expands and cools, so that the opacity in the envelope rises and the envelope becomes convective. The star becomes a red giant and keeps expanding as long as the helium-core mass grows and becomes more compact. Because red giants are luminous and the surface gravity is low, they are thought to have strong stellar winds that blow appreciable amounts of gas into the interstellar medium, although the exact mass-loss rates due to stellar wind are unknown.

For all stars that evolve within a Hubble time ($M \gtrsim 0.8\,M_\odot$) the core pressure and temperature become sufficiently high to start helium fusion. In the case of stars with masses $\lesssim 2.4\,M_\odot$ the helium core is degenerate, therefore isothermal and the core grows up to $0.47\,M_\odot$ before helium is ignited. Because the core is degenerate, the rise in temperature due to the helium fusion does not lead to a rise in pressure and density, so that a thermonuclear runaway ensues, in what is called the 'helium flash', until the rising temperature eventually lifts the degeneracy. The helium cores in stars more massive than $2.4\,M_\odot$ are non-degenerate, so that helium fusion begins at a lower helium-core mass, hence a smaller

radius, and without a helium flash. These stars ascend the red-giant branch only little and as a consequence lose relatively little mass in a stellar wind at this stage.

While helium is ignited in the core, the core expands and as a consequence the star shrinks again. The star is now on the horizontal branch until all helium has been converted to carbon and oxygen and the star expands again. Stars more massive than about $10\,M_\odot$ can have many burning phases in which they produce increasingly more massive elements, until their core consists of iron and further nuclear fusion no longer releases energy. The core of such a massive star collapses to a neutron star or perhaps a black hole, while the outer layers are blown off the star in an explosive event that is known as a supernova.

In this thesis we discuss the evolution of stars that are less massive than about $10\,M_\odot$. When helium is exhausted in the core of such a low- or intermediate-mass star, it develops a degenerate carbon-oxygen core surrounded by a helium-burning shell which is in turn surrounded by the hydrogen-burning shell. These two burning shells come closer to one another while they move out and when they come very close, so-called thermal pulses occur. Meanwhile, the star has expanded again, onto the asymptotic giant branch (AGB). These large stars experience Mira pulsations, which typically have periods on the order of a year. At the moment of maximum radius during such a pulsation, the surface temperature of the star drops sufficiently to allow the formation of dust. If the dust couples to the gas, the high radiation pressure will cause the star to rapidly lose its envelope. The star loses enough mass that a supernova is prevented and ends its life as a white dwarf consisting of carbon and oxygen or, for the more massive stars, oxygen and neon. The former envelope of the star is visible for some time as a planetary nebula surrounding the proto-white dwarf, irradiated by the intense radiation of the hot central star. The white dwarf no longer produces energy, save for a possible thermonuclear shell flash when the white dwarf is still young, but cools and becomes less luminous. The cooling rate is determined by the mass of the white dwarf, the thickness of the hydrogen layer on its surface and the occurrence of shell flashes. A computer model for a star of $1\,M_\odot$ is shown in Fig. 1.1.

1.2 Binary-star evolution

Of the about 5000 stars that we can see with the naked eye, about 2000 are actually binary or multiple-star systems and it is thought that this fraction is representative for the stars in our Galaxy. The star closest to our Sun, Proxima Centauri, is a member of a triple system and it seems reasonable to assume that more than half of all stars are in a binary or multiple system.

Stars in a binary evolve in a potential that is determined by the gravity of the stars and the orbital motion in the binary. The surface that defines the sphere of influence within which a particle is bound to one of the two stars in the frame corotating with the binary is called the Roche equipotential surface and the two droplet-shaped spaces it confines are called the Roche lobes of the two stars. The point where the two Roche lobes touch is called the first Lagrangian point.

Stars in a binary with an orbital period in excess of 10 yr are likely to spend their lives

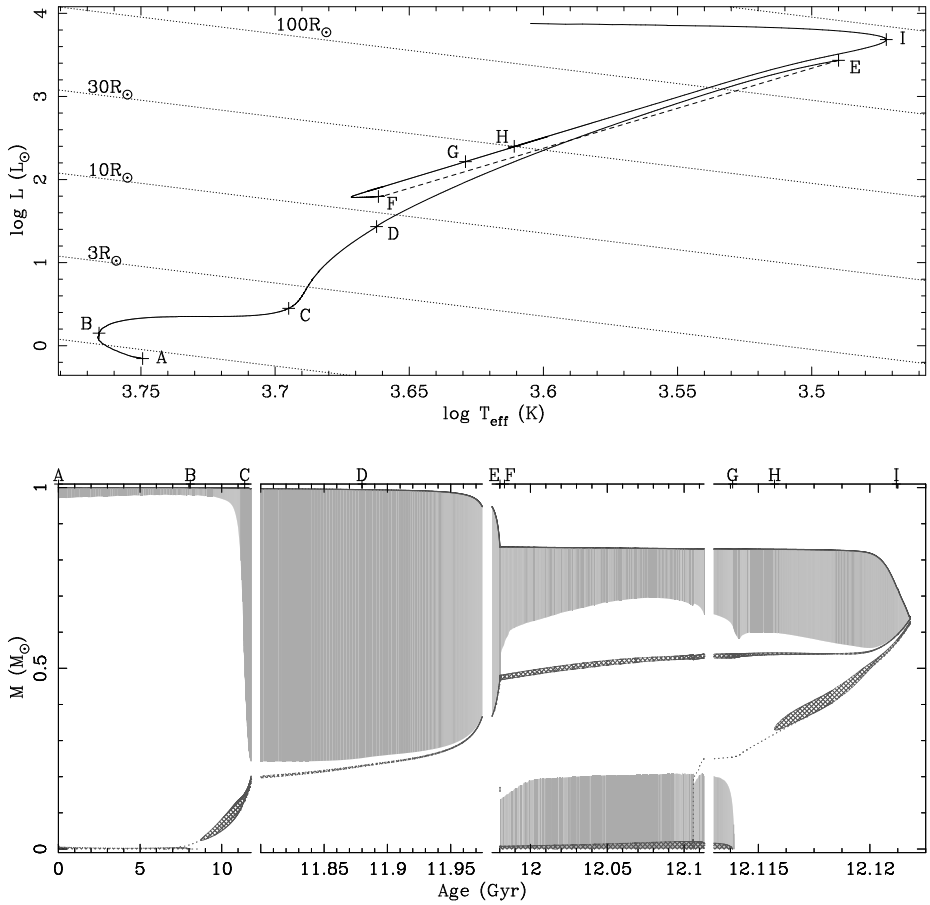

Figure 1.1: A computer model for the evolution of a star of 1 $M_\odot$ with wind mass loss, calculated with the evolution code of P. Eggleton. *Upper panel* (**a**): A Hertzsprung-Russell diagram for the model. The dashed line is where the helium flash occurs; the code replaces the pre-helium-flash model (E) with a post-helium-flash model (F). The dotted lines are lines of constant radius. *Lower panel* (**b**): A Kippenhahn diagram that shows the internal structure of the star as a function of time. Grey areas are convective regions, in hatched areas intense nuclear burning takes place. The thick line is the total mass of the star, the dotted lines are the masses of the helium and carbon-oxygen cores and often coincide with the burning shells. Notice the changes in scale of the time axis. The labelled points are A: zero-age main sequence, B: terminal-age main sequence, C: base of the giant branch, D: first dredge-up, E: helium flash, F–G: core helium burning phase, H: early asymptotic giant branch, and I: point where the hydrogen envelope has been blown away and the star starts contracting.

effectively as single stars, well inside their Roche lobes. In closer binaries, at least one of the stars may expand up to the size of its Roche lobe, for instance if the star becomes a giant. If this happens, gas from the giant can funnel through the first Lagrangian point into the Roche lobe of its companion, which may or may not accrete it. Thus, in a close-enough binary, mass can be transferred from one star to the other and in a later stage of evolution the reverse process may take place. Since the mass of a star is the dominant factor that determines the evolution of the star, mass transfer between stars can change the evolution of the two stars in a binary appreciably. A star of 1 $M_\odot$ on the red-giant branch could lose its envelope prematurely due to mass transfer, so that an undermassive helium white dwarf is formed, rather than the more massive carbon-oxygen white dwarf that would be the end product of such a star if it were single. In addition, the orbital period of the binary usually changes during mass transfer, because the transferred matter carries angular momentum from the donor to the accretor.

If the companion of the donor star is large enough and the mass-transfer rate not too high, the transferred matter will be accreted by the companion. If the companion is very small compared to the orbit, like in the case of a neutron star, the matter carries too much angular momentum to be accreted directly. In this case the matter will form an accretion disc around the neutron star and if the mass-transfer rate is higher than the Eddington accretion limit, some or most of the matter could be driven out of the system rather than accreted by the compact object. The gas in the accretion disc is heated and emits copious X-rays. Such systems, with a neutron star or black hole as accretor, are observed as X-ray binaries.

In the solar neighbourhood, the average distance between stars is rather high (~ 1 pc) so that it is unlikely that a binary interacts with other stars. It is therefore reasonable to assume that binaries in the galactic disc are primordial binaries. However, this is not true for dense stellar environments, like the galactic centre and globular clusters. The stellar density in the core of a globular cluster can be on the order of one million times higher than in the solar neighbourhood and hence the probability that an interaction between stars or between a star and a binary occurs is about 10^{12} times larger in the core of a dense globular cluster than in the solar neighbourhood. The fact that many luminous X-ray binaries are observed in globular clusters can probably be explained by this high density, for instance if these binaries are formed by the collision of a neutron star and a (sub)giant star (see Sect. 1.3.1).

1.3 Summary of this thesis

In this thesis we study the formation and evolution of compact binaries. Chapter 2 and 3 deal with the formation of luminous, ultra-compact X-ray binaries in globular clusters and rule out one of the proposed formation scenarios for these systems. In Chapter 4 we look in detail at observations of one particular X-ray binary in the galactic disc that is believed to be ultra-compact. Based on the observation of a long X-ray burst and a high neon-to-oxygen ratio in the X-ray spectrum, we show that the donor of this binary is probably the remnant of a helium white dwarf that was produced by a star no more massive than about 2.25 $M_\odot$. In Chapter 5 we discuss the formation of double white dwarfs. We present models that

Cluster	Position	P_{orb}	Indirect indication		
			low f_{opt}/f_x	burst max.	spectrum
NGC 1851	0512–40	?	U	U	U
Terzan 2	1724–31	?	—	U	N
Liller 1	1730–33	?	—	—	—
Terzan 1	1732–30	?	—	—	—
NGC 6440	1745–20	?	—	—	N
Terzan 5	1745–25	?	—	—	U
NGC 6441	1746–37	5.7 hr	—	N	N
Terzan 6	1751–31	12.4 hr	—	—	N
NGC 6624	1820–30	11.4 min	U	U	U
NGC 6652	1836–33	?	U	U	U
NGC 6712	1850–09	20.6 min	U	U	U
NGC 7078	2127+12a	22.6 min	—	U	—
NGC 7078	2127+12b	17.1 hr	—	—	—

Table 1.1: Luminous X-ray binaries in the galactic globular clusters. The columns list the name of the cluster, the position of the source, the orbital period and three indications for an ultra-short (U) or normal (N) period, based on the optical to X-ray luminosity ratio, the maximum luminosity in bursts and the X-ray spectrum. See the main text for more explanation. Adapted from Verbunt & Lewin (2004).

describe the evolution of a binary through two mass-transfer phases in which the two white dwarfs are formed. We conclude that we can explain the observed masses and periods well, but that it is more difficult to find a model that also explains the observed age difference of the two components.

1.3.1 The formation of luminous X-ray binaries in globular clusters

(Chapter 2 and 3)

Thirteen luminous X-ray sources are detected in the globular clusters of our Galaxy (Verbunt & Lewin 2004; Verbunt 2005). All of these sources are low-mass X-ray binaries in which a low-mass star transfers mass to a compact object. Twelve of these systems are X-ray bursters and hence the compact object must be a neutron star, for the 13th source this is not certain. For 6 of these 13 systems the orbital period is measured and 3 out of these 6 have an ultra-short ($\lesssim 40$ min) period. These systems are 4U 1820–30 in NGC 6624 which has an 11.4 min period (Stella et al. 1987), 4U 1850–087 in NGC 6712 with a 20.6 min period (Homer et al. 1996) and recently a 22.6 min orbital period was found for M15 X-2 (in M 15/NGC 7078) (Dieball et al. 2005) (see Table 1.1).

The other 7 X-ray sources have no detected orbital periods. However, indirect methods are available that give an indication as to whether an X-ray binary is ultra-compact or not.

The first method uses the fact that most optical light from luminous low-mass X-ray binaries comes from re-processing of X-rays in the accretion disc. A short orbital period means a small disc and hence a relatively low optical luminosity with respect to the X-ray luminosity (Van Paradijs & McClintock 1994). The second method was found by Kuulkers et al. (2003) and is based on the peak luminosity reached during X-ray bursts. This maximum luminosity is compatible with the Eddington luminosity for hydrogen-poor material for two systems with measured ultra-short periods, whereas it is compatible with the Eddington luminosity for hydrogen-rich material for a source with a normal period. The third method comes from a simple two-component model to explain the X-ray spectra of these systems by Sidoli et al. (2001). This model gives realistic and self-consistent solutions for three systems believed to be ultra-compact, and non-consistent solutions with unrealistic parameters for sources with normal periods. For more details on these methods, see Verbunt & Lewin (2004); Verbunt (2005). The last three columns of Table 1.1 show for each of the luminous X-ray sources in the globular clusters whether they are ultra-compact (U) or normal (N) according to these indirect methods. From the Table one can infer that of the thirteen luminous X-ray sources in globular clusters, certainly 3, probably 5 and possibly 6–8 are ultra-compact binaries. This is in sharp contrast to the much-lower fraction of ultra-compact binaries in the field (Deutsch et al. 1996).

There are three explanations for the formation of ultra-compact X-ray binaries in globular clusters. The first formation scenario starts with a binary of a neutron star and a massive companion. If the companion becomes a giant its envelope can engulf the neutron star and cause a spiral-in. The core of the companion thus forms a close binary with the neutron star and the orbital period will become shorter due to gravitational radiation until mass transfer starts. If the companion had a helium core and the orbit after the spiral-in is very close, there may be no time to burn the helium so that helium is the main constituent of the transferred matter. If the star had a helium core and the orbit is wider, the core would become a helium star and convert most of its helium to carbon and oxygen. This would be similar to the case where the companion had a carbon-oxygen core at the time of the spiral-in. Although stars of sufficient mass for a spiral-in with a neutron star do no longer exist in the galactic globular clusters, it can take some time before gravitational radiation causes Roche-lobe overflow to occur so that this could explain the observed systems in the galactic disc and in globular clusters today. A second formation scenario is likely to happen only in dense stellar environments, such as (the cores of) globular clusters. In this scenario the neutron star collides with a (sub)giant star, the envelope is expelled and the neutron star forms a binary with the core of the giant (Verbunt 1987). Since the probability of such a collision is largest if the star is on the sub-giant branch, the companion to the neutron star is likely to be a helium white dwarf. It has recently been found that this scenario could provide for a sufficiently large formation rate to explain the observed numbers of luminous sources (Ivanova et al. 2005).

A third mechanism to explain the ultra-compact X-ray binaries starts with a neutron star and a main-sequence star that loses angular momentum due to strong magnetic braking. The angular-momentum is lost from the orbit due to spin-orbit coupling and causes the

orbit to shrink. We call such a system converging. When the initial orbital period is short, the minimum period lies around 70 min (Paczynski & Sienkiewicz 1981). At this point the donor becomes degenerate and the orbit starts expanding again. If the initial period is long, a helium core develops and mass transfer becomes fast enough to overcome the effect of angular-momentum loss, so that the orbit expands until the donor has transferred all of its mantle and a low-mass helium white dwarf is formed (Webbink et al. 1983). Such a system diverges. For a narrow range of initial periods around the bifurcation period between converging and diverging systems the donor star fills its Roche lobe around the terminal-age main sequence. Such a star becomes degenerate at smaller radius due to the high helium abundance while a pure helium core is not yet formed. In this case, the period minimum can be much smaller than $\sim$ 70 min (Tutukov et al. 1985) and ultra-short orbital periods of 11 min can be reached (Podsiadlowski et al. 2002). We will refer to this mechanism as *magnetic capture*. Pylyser & Savonije (1988) investigated the magnetic-capture scenario and found no periods lower than about 38 minutes. They stopped their calculations at the Hubble time, while Podsiadlowski et al. (2002) only show the time that elapsed since mass transfer started.

The interesting feature about the magnetic-capture scenario is that for an X-ray binary with an orbital period of 11 min the period derivative can be either positive or negative, depending on whether the system has already passed the period minimum or not. A negative period derivative has been observed several times for the 11.4 min binary in NGC 6624 (Van der Klis et al. 1993b; Chou & Grindlay 2001) and this suggests that the binary evolved along the lines of the magnetic-capture scenario. However, the negative period derivative could be apparent due to acceleration of the binary in the cluster potential (Van der Klis et al. 1993a). Figure 1.2 shows that the acceleration at the projected distance of the binary from the centre of the cluster seems insufficient to explain the observed period derivative, especially if the gravitational acceleration should be twice as strong in case the intrinsic $\dot{P}$ is positive. However, observations with HST of the optical counterpart of the X-ray binary place it six times closer to the cluster centre (King et al. 1993), which makes it again more probable that the negative period derivative is due to acceleration.

We investigate the magnetic-capture scenario in Chapter 2 and 3. In Chapter 2 we investigate the magnetic-capture scenario along the lines of Podsiadlowski et al. (2002), using the magnetic-braking law by Verbunt & Zwaan (1981) and assuming that half of the transferred mass is lost from the system. In addition we do not allow evolution beyond the Hubble time. We calculate models starting with a binary that consists of a neutron star and a low-mass ($0.7\,M_\odot \leq M_\mathrm{i} \leq 1.5\,M_\odot$) zero-age main-sequence star. We vary the initial mass of the donor, the initial period and the metallicity of the stars and produce several grids of models. We use these grids and interpolate between two adjacent models to derive an evolutionary scenario for a binary with an arbitrary initial period. This way we calculate the distribution of a simulated population of one million stars with an age between 10 and 13 Gyr for each initial donor mass in our grid. Next we add these distributions to produce a period distribution for a population of 10 million of these stars at the age of the globular clusters. The distribution for $Z = 0.01$ thus obtained shows us that one in 10^7 binaries

that evolved this way should have an orbital period of 11 min and that for each such system there should be about 100 binaries with an orbital period $\lesssim 20$ min. We conclude that the initial period of a binary must be very close to the bifurcation period in order for it to evolve to an ultra-compact system. Furthermore, such a system evolves very rapidly through the period minimum, so that there is only a small probability to observe it in the ultra-compact regime. We also find that there is no contribution from the most massive donors in our grid ($\geq 1.2\,M_{\odot}$) to the ultra-compact binaries.

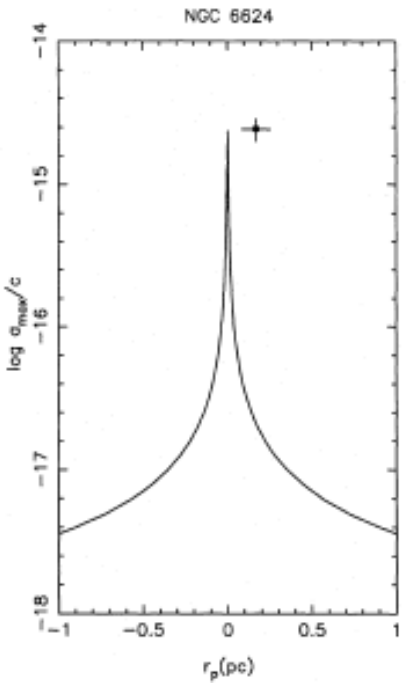

Figure 1.2: The maximum acceleration along the line of sight $a_{\max}$ as a function of the projected distance from the cluster centre, according to a cluster model for NGC 6624 (curve) compared to the measured position and acceleration of the 11.4 min binary (dot with error bars). In more recent observations the binary is closer to the centre (King et al. 1993). Taken from Van der Klis et al. (1993a).

In Chapter 3 we expand these grids of models by varying more parameters. We reduce the strength of the magnetic-braking law that we used in Chapter 2 and in addition we use a more modern law, based on the measured ranges in rotational velocities of stars in the Hyades and Pleiades and including saturation of the angular-momentum loss at a certain critical rotation velocity (Sills et al. 2000). We show that our results from Chapter 2 depend strongly on the magnetic-braking law we used. If we reduce the strength of magnetic braking by simply scaling down this law with a factor of 4, the shortest orbital period found in our models increases from about 10 min to 23 min. This is due to the fact that since magnetic braking is weaker, the systems need more time to reach the ultra-compact regime. Thus many systems may only reach this regime after the Hubble time, so that they do not contribute to the simulated population at 10 to 13 Gyr. Secondly, because the evolution needs more time, a small offset in initial period has larger consequences for the evolution than before. This basically means that the range of initial periods that lead to ultra-compact binaries is even narrower than before. If there is no magnetic braking at all, or if we use the saturated magnetic-braking law by Sills et al. (2000), the shortest periods found lie around 70 min. Reducing the strength of the magnetic braking used in our models to perhaps more realistic values

thus changes the probability of forming an ultra-compact X-ray binary with the magnetic-capture scenario from very improbable to impossible.

The conclusions of these two chapters have important consequences for our understanding of the formation of the observed low-mass X-ray binaries; they cannot have been formed by the magnetic-capture scenario. Interestingly, this could be confirmed observationally, as we mention in Chapter 3. Our models for magnetic capture predict that donors in an ultra-compact binary with a negative period derivative still have hydrogen on their surface and this surface hydrogen vanishes around the period minimum. Thus, if hydrogen were observed in the 11.4 min binary this would prove that the orbit is shrinking, whereas conclusive evidence of the lack of hydrogen at the surface would suggest that the intrinsic period derivative is positive. Furthermore, if in such a study carbon and oxygen would be found abundantly, this would suggest that the binary was formed long ago in a spiral-in caused by a massive star and the white dwarf was brought to Roche-lobe overflow by gravitational radiation only recently. Most probably, helium will be the most abundant element which would allow both the the spiral-in scenario and the collision-scenario to explain the formation of this binary.

1.3.2 The presumed ultra-compact X-ray binary 2S 0918–549

(Chapter 4)

The object 2S 0918–549 is an X-ray binary with a low optical to X-ray flux ratio (Chevalier & Ilovaisky 1987). As shown by Van Paradijs & McClintock (1994), this is an indication that the system might be an ultra-compact binary with an orbital period less than 1 hr. The object also has an unusually high neon-to-oxygen abundance ratio. Juett et al. (2001) show that of a set of 56 low-mass X-ray binaries, there are four sources that display this phenomenon. Two of these four systems have measured ultra-short periods of 18 min (in 4U 1543–624, see Wang & Chakrabarty 2004) and 21 min (in 4U 1850–087, see Homer et al. 1996). This observation therefore provides an extra indication that 2S 0918–549 is an ultra-compact binary. Because such a binary cannot be formed by stable mass transfer (Chapter 2 and 3) and a collision between a neutron star and a (sub)giant is rather improbable in the galactic disc, 2S 0918–549 probably formed from a spiral-in following dynamically unstable mass transfer by the companion to the neutron star and leaving the core of that companion exposed.

Optical spectroscopy of 2S 0918–549 shows a lack of spectral lines from hydrogen and helium (Nelemans et al. 2004). This suggests that the donor is a carbon-oxygen or neon-magnesium-oxygen white dwarf. However, like two other LMXBs identified by Juett et al. (2001), this system shows type-I X-ray bursts caused by thermonuclear shell flashes on neutron stars (see Sect. 4.1). Such bursts, of duration 10 s to several minutes, can only be explained by the presence of helium, possibly in combination with hydrogen (Juett & Chakrabarty 2003; Nelemans et al. 2004) and the duration of the burst is proportional with the hydrogen content. 2S 0918–549 experienced a burst that lasted almost 40 min (see Sect. 4.3) which would suggest a high hydrogen content, in blatant contradiction to the op-

tical spectrum and the presumed ultra-compact nature of the binary.

Because 2S 0918–549 is a persistent source with a low accretion rate ($\sim$ 1% of the Eddington accretion limit, see Jonker et al. 2001) we argue that pure helium has been accreted slowly but for a long time by the neutron star. Thus, a thick layer of helium has accumulated on the surface of the neutron star, which explains the long duration of the burst. The donor could therefore be a helium white dwarf, although it is not clear why lines of helium should be missing from the spectrum. My contribution to this chapter is mainly in Sect. 4.5.2, where we present a number of progenitor models for the donor of 2S 0918–549. We assumed that the star that is now the donor in 2S 0918–549 was the core of its progenitor and exposed after a spiral-in. First we argue that the donor cannot be a massive carbon-oxygen white dwarf or a neon-magnesium-oxygen white dwarf. Such stars have masses that are higher than about 0.4–0.5$M_{\odot}$, which is thought to be the upper limit to the mass of a white dwarf that can have stable mass transfer. Thus, any white-dwarf donor with stable mass transfer should be either a helium white dwarf or a low-mass carbon-oxygen white dwarf, once the core of a giant star. We therefore consider the cores of our model stars that evolve from the zero-age main sequence (ZAMS), via the red giant branch (RGB) to the asymptotic giant branch (AGB).

Stars of 1 $M_{\odot}$ or more on the RGB have a helium core that was formed by hydrogen fusion at least in part via the CNO cycle. In this process the neon abundance does not change, but the oxygen abundance drops because oxygen is converted to nitrogen in the CNO cycle. Thus the neon-to-oxygen abundance ratio in a helium core is higher than it was at the ZAMS. The precise number depends on the temperature at which the burning takes place and thus, among others, on the mass of the star. In our stellar models this ratio increases to about twice the ZAMS ratio for a star of 1 $M_{\odot}$ and to almost 20 times the ZAMS ratio for a 5 $M_{\odot}$ star.

A star on the AGB has a carbon-oxygen core, the 'ashes' of helium burning. In a side reaction to the helium-burning process some nitrogen is converted into neon-22, but this happens on a much smaller scale than the production of oxygen. The oxygen abundance therefore rises much more than the neon abundance and the models show a neon-to-oxygen ratio that is much lower than it was initially: 13–16% of the ZAMS value. We conclude that the donor of 2S 0918–549 that we observe today is probably the central part of a helium-white dwarf, the former core of a progenitor no more massive than about 2.25 $M_{\odot}$. This is compatible with the observations of long X-ray bursts and the high neon-to-oxygen abundance ratio, although it is unclear why helium lines are lacking in the optical spectrum.

1.3.3 The formation of double white dwarfs

(Chapter 5)

Double white dwarfs, binaries in which both components are white dwarfs, are sought for systematically by the SPY (ESO SN Ia Progenitor surveY) project (*e.g.* Napiwotzki et al. 2001). If these systems have short enough orbital periods and a mass that exceeds the

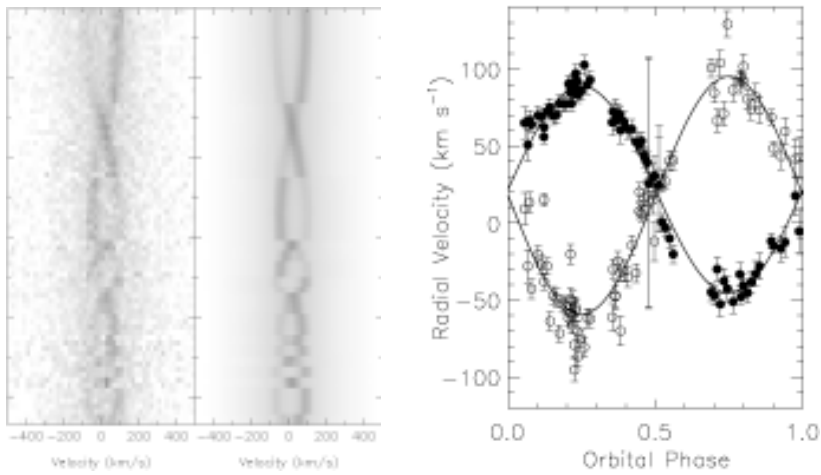

Figure 1.3: Observations of WD 0316+768. *Left panel:* Spectrograms (left-most) and the fit to these data. *Right panel:* Radial velocities measured for both components (symbols) and least-squares fits of sine functions to these points (solid curve). Adapted from Maxted et al. (2002b).

Chandrasekhar limit, they might produce supernovae of type Ia (Iben & Tutukov 1984). Furthermore, they may be the dominant source of low-frequency gravitational radiation (Evans et al. 1987; Hils et al. 1990). Ten double white dwarfs have been observed as double-lined spectroscopic binaries to date. These systems typically have orbital separations of a few solar radii or less and component masses between about 0.3 and 0.8 $M_{\odot}$ (see Table 6.1). Since these white dwarfs were once the cores of stars on the giant branch with radii of several tens to several hundreds of solar radii, a drastic orbital shrinkage must have taken place around the formation of the youngest white dwarf. It is usually assumed that the progenitor of this white dwarf filled its Roche lobe while it had a deep convective envelope, so that the ensuing mass transfer was dynamically unstable and the envelope of the donor engulfed the white dwarf that was already formed. The two compact objects would then spiral inwards due to drag forces inside this common envelope, while the orbital energy that is liberated is used to expell the envelope from the system (Webbink 1984).

In Chapter 5 we try to find an evolutionary scenario for these 10 observed systems. We follow the lines of Nelemans et al. (2000) who did very similar work, but based on 3 observed systems rather than 10 and with use of many analytical approximations where we use a stellar evolution code for more detailed calculations. Among the advantages of the use of an evolution code is that we can calculate for a set of progenitor models the radius of the star and the binding energy of its envelope at every moment of its evolution. This enables us to calculate the efficiency parameter for a common envelope with spiral-in $\alpha_{\rm ce}$. Another difference is that we consider more-massive progenitors and stars on the asymptotic giant

branch as possible progenitors.

We confirm the conclusion of Nelemans et al. (2000) that the formation of the observed systems cannot be explained by the scenario where the first white dwarf is formed after conservative mass transfer and the second white dwarf in a common envelope with spiral-in, or by the scenario in which two occurrences of such a spiral-in take place. A different mechanism in which a donor star can lose its envelope is therefore required and we again follow Nelemans et al. (2000) in their prescription of envelope ejection with angular-momentum balance, rather than energy balance. This prescription uses an efficiency factor γ to relate the angular momentum that is carried by the ejected envelope to the average angular momentum of the progenitor system. This prescription was also used for this purpose by Nelemans & Tout (2005), but again with approximations for the stellar parameters. We share their conclusion that all observed masses and orbital periods can be explained with this mechanism, if $1.5 \leq \gamma \leq 1.75$. However, this would imply that the envelope matter somehow gains extra angular momentum from the binary before it is lost and at this moment there is no physical explanation for this.

We therefore introduce two slightly different prescriptions for the scenario of envelope ejection with angular-momentum balance. In the first prescription it is assumed that the matter is transferred from the donor to the companion and then re-emitted isotropically. The second prescription is for an isotropic wind from the donor star. These two prescriptions can explain the masses and periods of all observed systems, but now with an efficiency parameter $0.9 \leq \gamma \leq 1.1$. These prescriptions therefore need no additional physical explanation for the high angular-momentum losses. The observed masses and periods can be explained with either an envelope ejection with a γ-prescription followed by a spiral-in with the α-prescription, or with two subsequent γ-envelope ejections. However, if we want our models to explain in addition the difference in cooling age between the two components of a binary, found by the observers by comparing their observations to white-dwarf cooling models, we find that this is more problematic. Some systems can still be explained with the same values for γ, while for others we must allow values that are much farther form the desired values than before. We list the best solutions in Table 6.5 and one of them is schematically displayed in Fig. 1.4.

Among the solutions that can explain the observed double white dwarfs there is one that could explain the observation that the oldest white dwarf in the system PG 1115+116 is a DB white dwarf, *i.e.* has no hydrogen in the spectrum (Maxted et al. 2002a). The scenarios for stable mass transfer or envelope ejection predict that there is a thin layer of hydrogen at the surface of a white dwarf produced this way so that it should be a DA white dwarf, *i.e.* with hydrogen in its spectrum. Maxted et al. (2002a) suggest that the star may have experienced a giant phase after the first mass-transfer phase. This scenario corresponds to solution 54 in Table 6.5, in which the $0.89\,M_{\odot}$ helium core of a $5.42\,M_{\odot}$ progenitor is exposed due to envelope ejection with the γ-prescription. Such an exposed core becomes a helium star and massive helium stars can become giants. Most of the mass in such a giant is in the carbon-oxygen core and it is possible that this star loses its outer layers, either by Roche-lobe overflow or by a stellar wind, without much change to the total mass and the

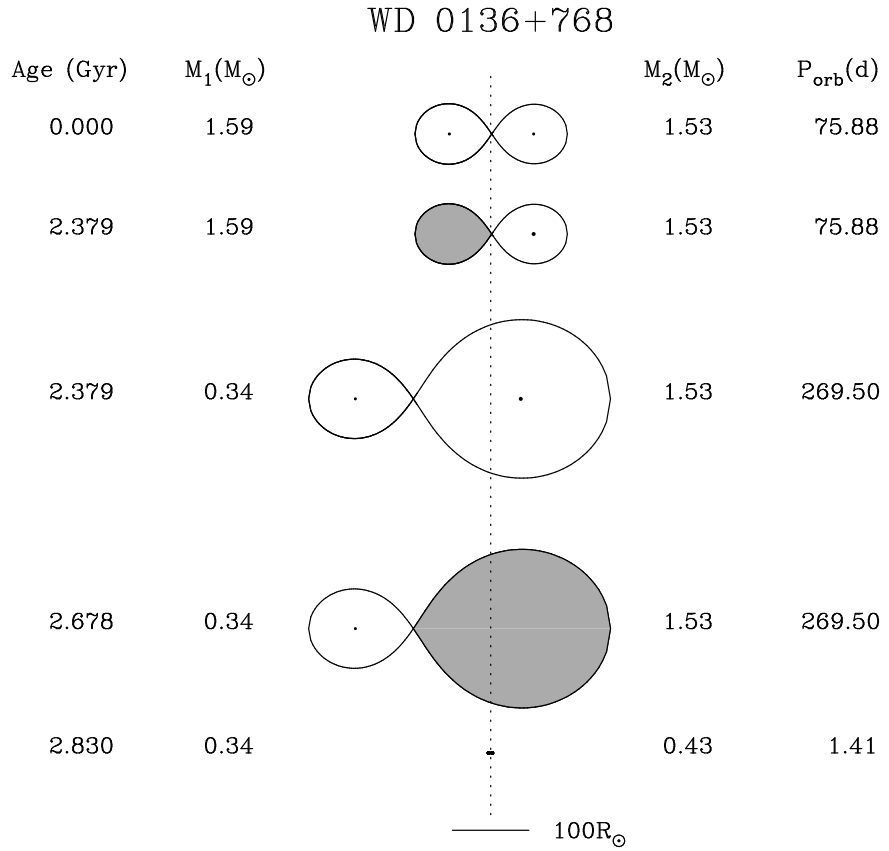

Figure 1.4: Schematic representation of the evolution of an initial binary that leads to the double white dwarf WD 0136+768 with the observed masses, orbital period and age difference. This scenario corresponds to solution 22 in Table 6.5, in which the primary ejects its envelope with $\gamma \approx 0.95$ (from panel 2 to 3 in the Figure) and the secondary causes a spiral-in with $\alpha_{\rm ce} \approx 1.00$ (panel 4 to 5). The Figure shows the stars and their Roche lobes with respect to the centre of mass of the binary (dotted vertical line). The numbers are the age since the zero-age main sequence, the two masses and the orbital period. The components of the double white dwarf that is formed in this scenario have an age difference of 299 Myr; compare the observed age difference of 450 Myr according to the cooling models. The final panel shows the binary at its current age, according to the cooling age for the youngest white dwarf. The final orbital separation is less than 5 $R_\odot$ and hardly visible.

orbital period. It is interesting that such an evolutionary scenario is indeed amongst our solutions.

Chapter 2

Creating ultra-compact binaries in globular clusters through stable mass transfer

M.V. van der Sluys, F. Verbunt and O.R. Pols

Astronomy and Astrophysics, v.431, p.647–658 (2005)

Abstract A binary in which a slightly evolved star starts mass transfer to a neutron star can evolve towards ultra-short orbital periods under the influence of magnetic braking. This is called magnetic capture. We investigate in detail for which initial orbital periods and initial donor masses binaries evolve to periods less than 30–40 minutes within the Hubble time. We show that only small ranges of initial periods and masses lead to ultra-short periods, and that for those only a small time interval is spent at ultra-short periods. Consequently, only a very small fraction of any population of X-ray binaries is expected to be observed at ultra-short period at any time. If 2 to 6 of the 13 bright X-ray sources in globular clusters have an ultra-short period, as suggested by recent observations, their formation cannot be explained by the magnetic capture model.

2.1 Introduction

The globular clusters belonging to our Galaxy house thirteen bright ($L_{\rm X} \gtrsim 10^{35}\,{\rm erg\,s^{-1}}$ in the 0.5–2.5 keV range) X-ray sources, neutron stars accreting from a low-mass companion. A surprisingly large fraction of these has ultra-short orbital periods of less than about 40 minutes, as first noticed by Deutsch et al. (1996). Two of the five orbital periods known are 11.4 min and 20.6 min (or its alias 13.2 min) for the sources in NGC 6624 and NGC 6712, respectively (Stella et al. 1987; Homer et al. 1996). The orbital periods of eight systems are not known, but for four of them indirect evidence points to an ultra-short period. This evidence consists of the absolute magnitude of the optical counterpart (Van Paradijs & McClintock 1994), of the energy distribution of the X-ray spectrum (Sidoli et al. 2001), and of the maximum flux reached during X-ray bursts (Kuulkers et al. 2003). Collating this evidence, Verbunt & Lewin (2004, their Table 1) suggest that two more sources probably, and two others possibly have ultra-short orbital periods (in NGC 1851 and NGC 6652, and in NGC 7078 and Terzan 5, respectively). The 43.6 min period found by Deutsch et al. (1996) is not the period of the bright X-ray source in NGC 6652, but of a fainter source (Heinke et al. 2001).

Thus both among the known periods and among the suggested periods, about half of the bright X-ray sources have ultra-short orbital periods. This is in marked contrast to the period distribution of bright X-ray sources in the galactic disk, where only one period much shorter than 40 minutes has been suggested so far (Wang & Chakrabarty 2004).

Ultra-short-period binaries with a neutron star can be formed in a number of ways. An expanding giant star can engulf the neutron star, which then spirals in to form a binary with the helium-burning core. If mass transfer starts immediately after spiral-in, the donor is a helium-burning star (Savonije et al. 1986), if mass transfer starts only after a long time, the donor has evolved into a CO white dwarf or a CO white dwarf with helium mantle (Yungelson et al. 2002). The process requires a giant of higher mass than exists in globular clusters today; but the waiting time between end of the spiral-in and onset of the mass transfer allows us to observe the mass transfer stage today of systems formed long ago. Indeed, it has been argued that this in fact is the dominant formation process for ultra-short-period binaries in globular clusters (Davies & Hansen 1998; Rasio et al. 2000). Alternatively, it has been suggested that in a cluster, a neutron star can also in a collision with a giant expell its envelope and form a binary with its core (Verbunt 1987). It is not obvious that this leads to a binary sufficiently close to start mass transfer within the Hubble time (Rasio & Shapiro 1991). A white dwarf donor implies an expanding orbit, and thus predicts an increasing orbital period.

Yet another scenario starts from a binary of a neutron star and a main-sequence star. The evolution of this binary depends critically on the initial orbital period. When the period is short, mass transfer is driven by loss of angular momentum, and the orbital period decreases with the donor mass until a minimum period is reached near 70 min (Paczynski & Sienkiewicz 1981). We will call this a converging system. At the minimum period, the donor becomes degenerate, and further mass transfer expands the orbit. When the orbital

period is long, mass transfer is driven by expansion of the donor star, and the orbit expands with the donor radius until the donor has transferred its full envelope (Webbink et al. 1983). These are diverging systems. However, for a narrow range of periods loss of angular momentum can still shrink the orbit for a slightly evolved donor. Due to its higher helium content, the donor becomes degenerate at smaller radius, and correspondingly shorter orbital period (Tutukov et al. 1985). Orbital periods shorter than 11 min can be reached (Podsiadlowski et al. 2002). These systems therefore converge, but the process may take more than a Hubble time. At 11.4 min, the period derivative may be negative or positive, depending on whether the system is still on its way to the period minimum, or has already rebounded. We will refer to this scenario as magnetic capture.

The repeated observation that the 11.4 min period of the bright X-ray source in the globular cluster NGC 6624 is decreasing (Van der Klis et al. 1993b; Chou & Grindlay 2001) would appear to indicate that the system evolved according to the magnetic capture scenario. However, it is not impossible that the negative period derivative is only apparent, the consequence of an acceleration of the binary in our direction, in the gravitational potential of the innermost part of the globular cluster. A more accurate position of the (optical counterpart to the) X-ray binary and a re-determination of the centre of the cluster shows that the X-ray source is much closer to the cluster centre than was thought before, and thus increases the probability that the measured period is affected by acceleration. Nonetheless, the measurement of a period decrease is a strong incentive to investigate the magnetic capture scenario in more detail.

A possible problem with the magnetic capture scenario is suggested by computations for binaries in the galactic disk, by Pylyser & Savonije (1988). None of their calculated evolutions lead to periods of about 11 minutes within the Hubble time. Podsiadlowski et al. (2002) do not address this problem explicitly, but only show the time elapsed since the onset of mass transfer.

In this chapter, we address the question under which circumstances the very short orbital periods observed in NGC 6624 and NGC 6712 are reached within the Hubble time, in the magnetic capture scenario described above. The parameters that we vary are the initial mass of the donor star, the initial orbital period (or more or less equivalently, the orbital period at which mass transfer starts), and the metallicity of the donor. In Sect. 2.2 we briefly describe the code that we use, and the algorithms specific to the evolutionary scenario that we study. In Sect. 2.3 we give the results for two specific cases, to compare with earlier work and to illustrate the possible evolution paths. We then describe the expected outcomes for an initial distribution of donor masses and initial orbital periods in Sect. 2.4. We find that orbital periods of 11.4 and 20.6 min are possible, but very unlikely in this scenario. The consequences of this conclusion are discussed in Sect. 2.5.

2.2 Binary evolution code

2.2.1 The stellar evolution code

We calculate our models using the STARS binary stellar evolution code, originally developed by Eggleton (1971, 1972) and with updated input physics as described in Pols et al. (1995). Opacity tables are taken from OPAL (Iglesias et al. 1992), complemented with low-temperature opacities from Alexander & Ferguson (1994).

The equations for stellar structure and composition are solved implicitly and simultaneously, along with an adaptive mesh-spacing equation. Convective mixing is modelled by a diffusion equation for each of the composition variables, and we assume a mixing length ratio $l/H_p = 2.0$. Convective overshooting is taken into account as in Schröder et al. (1997), with a free parameter $\delta_{\rm ov} = 0.12$ calibrated against accurate stellar data from non-interacting binaries (Schröder et al. 1997; Pols et al. 1997). The helium core mass is defined as the mass coordinate where the hydrogen abundance becomes less than 10%.

We use a version of the code (see Eggleton & Kiseleva-Eggleton (2002), hereafter EK02) that allows for non-conservative binary evolution, even though the evolution of only one component star is calculated in detail. The companion, in our case a neutron star, is treated as a point mass. With the adaptive mesh, mass loss by stellar winds or by Roche-lobe overflow (RLOF) in a binary is simply accounted for in the boundary condition for the mass. Spin-orbit interaction by tides is treated according to the equilibrium tide theory (Hut 1981) with a tidal friction timescale as given by EK02. This is taken into account by solving additional equations for the moment of inertia $I(r)$, the uniform stellar rotation frequency $\Omega_{\rm rot}$, the orbital angular momentum $J_{\rm orb}$ and the orbital eccentricity e. These equations (of which the latter three are independent of the interior structure and only depend on time) are also solved implicitly and simultaneously with the usual set of equations, at little extra computational cost. The rotation induces a centrifugal potential that influences the stellar structure through a reduction of the effective gravity. The centrifugal potential for each mesh point is averaged over a spherical shell. Rotationally induced mixing is not taken into account in this code.

Unlike EK02, we do not include their model for dynamo-driven mass loss and magnetic braking. Rather we apply a magnetic braking law without accompanying mass loss, as discussed in Sect. 2.2.2. This facilitates direct comparison to previous binary evolution calculations in which similar assumptions have been made. Although we follow tidal interaction in detail, the effect on the current calculation is limited because the short orbital periods we consider ensure that the orbit is always circularised and synchronised with the stellar spin. However, exchange of angular momentum between spin and orbit is taken into account.

The initial hydrogen and helium abundances of our model stars are a function of the metallicity Z: $X = 0.76 - 3.0Z$ and $Y = 0.24 + 2.0Z$. In this research we use the metallicities $Z = 0.0001$ (with $X = 0.7597, Y = 0.2402$), $Z = 0.002$ (with $X = 0.754, Y = 0.244$), $Z = 0.01$ (with $X = 0.73, Y = 0.26$) and $Z = 0.02$ (with $X = 0.70, Y = 0.28$).

2.2.2 Angular momentum losses

If the lower mass star in a binary fills its Roche lobe and starts to transfer mass to a more massive companion, the orbit will widen, unless there are enough angular momentum losses to compensate for this effect. We assume three sources of angular momentum loss from the system.

The most important source is magnetic braking. Due to magnetic braking, spin angular momentum is lost from the secondary and eventually, due to the tidal spin-orbit coupling, from the orbit. We use the formula given by Rappaport et al. (1983):

$$\frac{dJ_{\rm MB}}{dt} \;=\; -3.8\times10^{-30}\,M_2\,R^4\,\omega^3\,{\rm dyn\,cm}. \tag{2.1}$$

Like Podsiadlowski et al. (2002), we apply full magnetic braking when the mass of the convective envelope of the donor exceeds 2% of the total mass of the star, and if $q_{\rm conv} < 0.02$ reduce the strength of the magnetic braking in Eq. 2.1 by a factor of $\exp(1-0.02/q_{\rm conv})$, where $q_{\rm conv}$ is the mass fraction of the convective envelope of the star. The fact that the magnetic braking removes angular momentum from the spin of the star rather than directly from the orbit is different from Podsiadlowski et al. (2002). The main difference is that our study takes into account stellar spin at all, which influences the radius of the star and thus the moment at which Roche-lobe overflow commences.

For short orbital periods, gravitational radiation is a strong source of angular momentum loss. We use the standard description

$$\frac{dJ_{\rm GR}}{dt} \;=\; -\frac{32}{5}\,\frac{G^{7/2}}{c^5}\,\frac{M_1^2\,M_2^2\,(M_1+M_2)^{1/2}}{a^{7/2}} \tag{2.2}$$

(Peters 1984).

The third way of angular momentum loss from the system is by non-conservative mass transfer. We assume that only a fraction β of the transferred mass is accreted by the neutron star. The remainder is lost from the system, carrying away a fraction α of the specific angular momentum of the neutron star

$$\frac{dJ_{\rm ML}}{dt} \;=\; -\alpha\,(1-\beta)\,a_1^2\,\omega\,\dot{M}_2, \tag{2.3}$$

where a_1 is the orbital radius of the neutron star and ω is the orbital frequency.

To keep the models simple, we applied no regular stellar wind to our models, so that all mass loss from the system and angular momentum loss due to this result from the non-conservative mass transfer described above.

2.3 Binary models

2.3.1 Calculated grid

Using the binary evolution code described in Sect. 2.2, we calculated an initial grid of models for $Z = 0.01$, the metallicity of NGC 6624, and Y=0.26. We choose initial masses

between 0.7 and 1.5 $M_\odot$ with steps of 0.1 $M_\odot$, and initial periods between 0.50 and 2.75 days, with steps of 0.25 days. Around the bifurcation period between converging and diverging systems, where the shortest orbital periods occur, we narrow the steps in P to 0.05 days.

We specify the bifurcation period more precisely as the longest initial period that leads to an ultra-short period, *within a Hubble time*. With this definition, the bifurcation period corresponds to the initial period of the binary that reaches its minimum period exactly after a Hubble time. This extra constraint is needed because there is no sharp transition between converging and diverging systems, especially since every diverging system will eventually converge due to gravitational radiation, if given the time. For instance, the system with an initial secondary mass of 1.1 $M_\odot$ and an initial period of 0.90 days — that is shown to run out of the right of Fig. 2.2 at $\log P \approx -0.4$ — does converge to a period of slightly more than 5 minutes, but only after almost 32 Gyr. This system is therefore considered to be diverging. Since the last part of the converging tracks in Figs. 2.1 and 2.2 is very steep, a system that reaches an ultra-short minimum period shortly after a Hubble time will usually have an orbital period at the Hubble time that is on the order of hours.

The total number of calculations for $Z = 0.01$ is 150; 90 for the initial grid, and 60 for the finer grid. We follow Podsiadlowski et al. (2002) in choosing $\alpha = 1$ and $\beta = 0.5$ in Eq. 2.3. The orbital evolution of the systems with initial masses of 1.0 and 1.1 $M_\odot$ is displayed in Figs. 2.1 and 2.2.

2.3.2 Interpretation of the models

Fig. 2.1 shows that the models with the shortest initial periods converge to minimum periods of about 70 minutes. After this, the stars become degenerate, and the orbits expand. Before the minimum period is reached, the stars become fully convective, thus mixing all of the star to a homogeneous composition. These stars have not yet formed a helium core, but are still a mixture of hydrogen and helium when they become degenerate. The stars with larger initial periods have a lower hydrogen abundance when they reach their minimum period.

For the longest initial periods, the Roche lobe is filled in a later evolution stage and the evolutionary time scale is shorter, so that the star expands faster and the mass transfer rate is higher. Because of this, and the fact that the mass ratio is less than 1, the angular momentum loss is not strong enough to shrink the orbit, so that it starts to expand shortly after mass transfer starts. These stars are sub-giants, and have a compact helium core inside their hydrogen envelopes. After they have transferred all of this envelope, they shrink and become helium white dwarfs. The systems with larger initial periods are more evolved when they fill their Roche lobes and produce more massive white dwarfs.

In between the smallest and largest initial periods, there are a number of models that reach orbital periods that are much shorter than 70 min. This happens due to magnetic capture: the orbital period is reduced strongly under the influence of strong magnetic braking. When magnetic braking disappears, the orbit is close enough to shrink to ultra-short periods by angular momentum loss due to gravitational radiation. The magnetic captures come

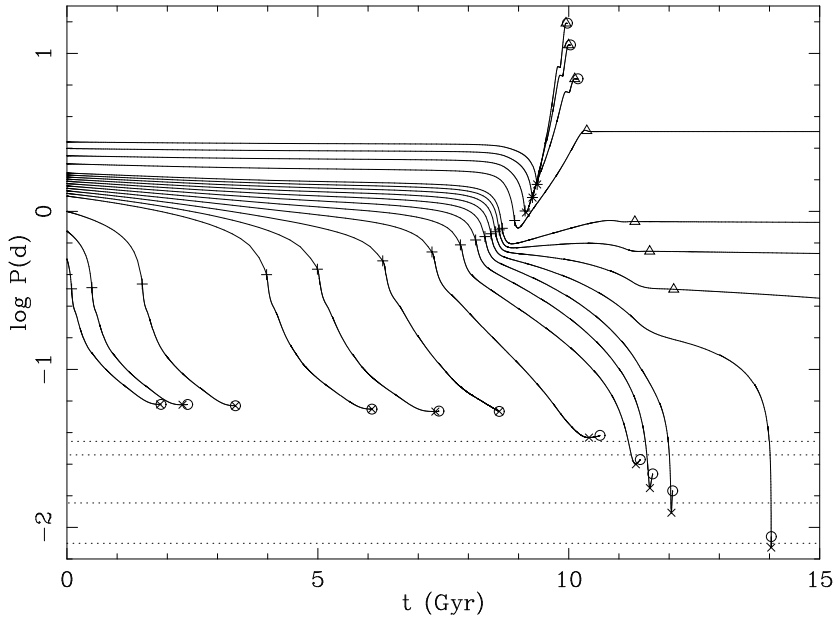

Figure 2.1: Evolution of the orbital periods of selected systems with $Z = 0.01$, an initial secondary mass of 1.0 $M_\odot$ and initial periods of 0.50, 0.75, 1.00, 1.25, 1.30, 1.35, 1.40, 1.45, 1.50, 1.55, 1.60, 1.65, 1.70, 1.75, 2.0, 2.25, 2.5 and 2.75 days. The symbols mark special points in the evolution: $+$ marks the start of Roche-lobe overflow (RLOF), $\times$ the minimum period, $\triangle$ the end of RLOF and $\bigcirc$ marks the end of the calculation. The four dotted horizontal lines show the orbital periods of the closest observed LMXBs in globular clusters: 11.4 and 20.6, and in the galactic disk: 41 and 50 minutes.

from models with a very narrow initial period range. The four models with $M_{\rm i} = 1.0 M_\odot$ that reach a period less than 40 minutes, for instance, have initial periods of 1.45 1.50, 1.55 and 1.60 days, where the last model reaches the ultra-short period regime only after 14 Gyr. By interpolation, as described later in Sect. 2.4.1, we find that the models that reach a minimum period below 40 min and within 13.6 Gyr, have initial periods in the range 34.5 – 38.1 hours. These stars fill their Roche lobes when their orbital periods are in the range of 14.3 – 17.2 hours. The lowest orbital period reached, by the system with the initial period of 38.1 hours, is 12.0 min, after 13.6 Gyr.

If one draws a vertical line in Fig. 2.1 at 11.5 Gyr (about the age of the globular clusters), one can imagine that there is a distribution of observable X-ray binaries at that moment in time. The lowest orbital period found at that time is about $10^{-1.75}$ days, or 25 minutes. All models with orbital periods higher than about 1 day have stopped mass transfer and will not be visible as X-ray binaries. Because the lines in Fig. 2.1 are steeper at lower periods, it is clear that the higher periods, around one day, will dominate.

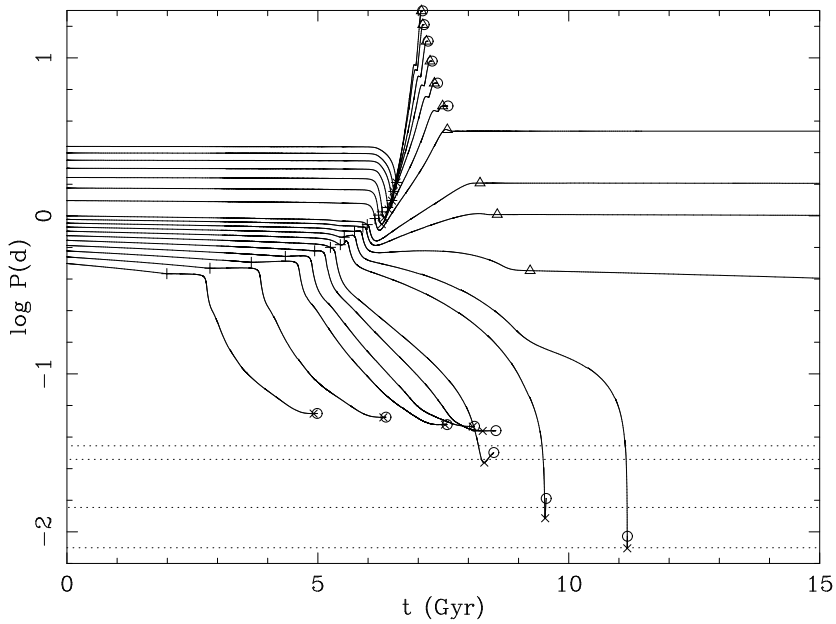

Figure 2.2: Evolution of the orbital periods of selected systems with $Z = 0.01$, an initial secondary mass of 1.1 $M_\odot$ and initial periods of 0.50, 0.55, 0.60, 0.65, 0.70, 0.75, 0.80, 0.85, 0.90, 0.95, 1.00, 1.25, 1.50, 1.55, 1.60, 1.65, 1.70, 1.75, 2.0, 2.25, 2.5 and 2.75 days. See Fig. 2.1 for more details.

Figure 2.2 shows the same data as Fig. 2.1, but for models with an initial secondary mass of 1.1 $M_\odot$. The results are qualitatively similar, but the ultra-short period regime is reached from lower initial periods, and after a shorter period of time. We find that the models that reach periods lower than 40 min before 13.6 Gyr have initial periods of 18.0 – 20.9 hr and fill their Roche lobes in the period range 15.1 – 18.2 hr. The system with the initial period of 18.0 hr reaches 40 min after 8.3 Gyr, the system with a 20.9 hr initial period has the smallest minimum period: 8.0 min.

If we again imagine the period distribution at 11.5 Gyr, but now for Fig. 2.2, we see that the period range that we expect for mass transferring binaries is shifted downwards in period. Orbital periods as short as 10.6 min can now occur, and systems with periods over 9.5 hr do not transfer mass anymore at that moment. With respect to the tracks in Fig. 2.1, we see that their density is much lower here. This is partially due to the fact that we use linear equally spaced periods at a lower initial period, so that they are more widely spaced in $\log P$.

Figure 2.3 illustrates the evolution of the convective envelope of a 1.1 $M_\odot$ star for the grid models with initial periods between 0.5 and 0.9 d. Looking at the models in the order of increasing initial period we find that in the first five the stars become fully convective

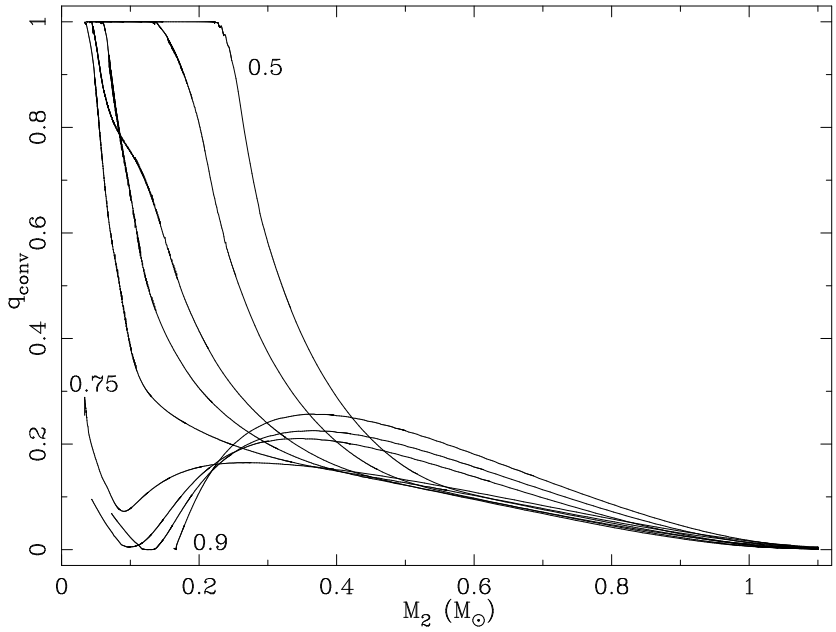

Figure 2.3: Mass fraction of the convective envelope ($q_{\rm conv}$) as a function of the total mass of the donor, for the models with the shortest 9 initial orbital periods in Fig. 2.2. The numbers in the plot give the initial periods in days for that line. As evolution proceeds towards lower donor masses, the mass faction of the convective envelope increases. For the 5 models with initial periods between 0.5 and 0.7 d, the total mass at which the star becomes fully convective is anti-correlated with the initial period. At initial periods of 0.75 d and longer, the initial increase of the mass fraction of the convective envelope is followed by a decrease.

at decreasing total masses. The first model that evolves towards ultra-short periods, with an initial period of 0.75 d is also the first model in which the donor never becomes fully convective: an initial increase of the mass fraction of the convective envelope is followed by a decrease. For initial periods of 0.85 d and 0.9 d the convective envelope disappears completely. The general trend with increasing initial period that is visible in Fig. 2.3, is the consequence of an increasing helium abundance in the core. The cores with a higher helium abundance tend to be hotter and thus more stable against convection. The absence of convection in the core in turn keeps the helium abundance high. The third model, with an initial period of 0.6 d shows a track that is slightly different from those of the neighbouring models. This model becomes almost fully convective, but the central $10^{-4}\,M_\odot$ does not, and as a consequence the mixing from the core to the surface is suppressed. We have repeated this calculation with a slightly different convective mixing efficiency and find the same results.

$P_{\rm i}$ (d)	$P_{\rm rlof}$ (h)	$P_{\rm min}$ (m)	t (Gyr)	$\dot{M}_{\rm tr}$	M_2 ($M_\odot$)	$\log L/L_\odot$	$\log T_{\rm eff}$	$\log T_{\rm c}$	$\log \rho_{\rm c}$	$\log X_{\rm c}$	$\log Y_{\rm c}$	$\log X_{\rm s}$	$\log Y_{\rm s}$
0.50	10.3	80.7	4.92	-10.31	0.060	-3.64	3.33	6.44	2.53	-0.23	-0.40	-0.23	-0.40
0.55	11.2	76.3	6.31	-10.39	0.052	-3.75	3.32	6.45	2.57	-0.31	-0.30	-0.31	-0.30
0.60	12.2	68.7	7.53	-10.49	0.042	-3.85	3.32	6.54	2.81	-1.46	-0.02	-0.53	-0.16
0.65	13.3	66.8	8.09	-10.31	0.038	-3.96	3.31	6.54	2.68	-0.64	-0.12	-0.64	-0.12
0.70	14.4	62.7	8.28	-10.36	0.043	-3.67	3.38	6.72	2.82	-1.32	-0.03	-0.89	-0.07
0.75	15.2	39.5	8.32	-9.67	0.056	-3.46	3.48	6.93	3.43	-2.34	-0.01	-1.24	-0.03
0.80	15.8	17.6	9.53	-8.53	0.074	-3.97	3.45	7.01	4.08	$-\infty$	0.00	-1.51	-0.02
0.85	17.6	11.3	11.17	-7.76	0.101	-4.15	3.45	7.10	4.43	$-\infty$	0.00	-1.84	-0.01
0.90	19.1	5.1	31.85	-6.62	0.164	-4.89	3.34	6.81	5.05	$-\infty$	0.00	-1.10	-0.04

Table 2.1: Properties for the donor stars of some of our grid models with $Z = 0.01$ and $M_{\rm i} = 1.1 M_\odot$ at their period minimum. The first three columns list the orbital period initially (at the ZAMS) in days, at Roche-lobe overflow ($P_{\rm rlof}$) in hours and the minimum period ($P_{\rm min}$) in minutes. The next 11 columns show stellar properties at $P_{\rm min}$: the age of the donor (since ZAMS), the logarithm of the mass transfer rate (expressed in $M_\odot\ {\rm yr}^{-1}$), the mass and luminosity of the donor, the logarithms of the effective temperature, the core temperature (both in K) and the central density (in g cm^{-3}), and the last four columns show the logarithms of the core and surface mass fractions of hydrogen and helium.

$P_{\rm orb}$ (min)	t (Gyr)	$\log \dot{M}_{\rm tr}$	$\log -\dot{P}_{\rm orb}$	M_2 ($M_\odot$)	$\log L/L_\odot$	$\log T_{\rm eff}$	log H	log He	log C	log N	log O
$P_{\rm ZAMS}$	0.000	—	—	1.100	0.17	3.79	-0.14	-0.59	-2.75	-3.28	-2.30
80.0	8.023	-10.11	-12.56	0.097	-2.44	3.59	-0.46	-0.19	-5.12	-2.50	-2.36
60.0	8.147	-9.97	-12.48	0.086	-2.66	3.59	-0.57	-0.14	-5.07	-2.42	-2.44
50.0	8.205	-9.81	-12.49	0.079	-2.82	3.58	-0.70	-0.10	-5.01	-2.35	-2.53
45.0	8.236	-9.72	-12.54	0.074	-2.95	3.57	-0.82	-0.08	-4.96	-2.31	-2.62
39.5	8.317	-9.67	-∞	0.056	-3.46	3.48	-1.24	-0.03	-4.90	-2.23	-2.88
40.0	11.145	-9.92	-11.86	0.124	-1.64	3.88	-0.48	-0.18	-5.22	-2.50	-2.36
30.0	11.156	-9.51	-11.68	0.122	-1.87	3.86	-0.51	-0.17	-5.23	-2.49	-2.36
20.0	11.163	-9.06	-11.41	0.120	-2.46	3.77	-0.57	-0.14	-5.18	-2.48	-2.37
15.0	11.165	-8.53	-11.26	0.117	-3.21	3.63	-0.68	-0.11	-5.11	-2.47	-2.39
11.3	11.167	-7.76	-∞	0.101	-4.15	3.45	-1.84	-0.01	-4.81	-2.31	-2.62

Table 2.2: Some properties for two of our grid models with $Z = 0.01$ and $M_{\rm i} = 1.1 M_\odot$ at selected orbital periods. *First row:* Initial (ZAMS) parameters. *Rows 2-6*: The model with $P_{\rm i} = 0.75$ d and $P_{\rm min} = 39.5$ min. *Rows 7-11*: The model with $P_{\rm i} = 0.85$ d and $P_{\rm min} = 11.3$ min. $\dot{M}_{\rm tr}$ in column 3 is expressed in $M_\odot\, yr^{-1}$ and $T_{\rm eff}$ in column 7 in Kelvin. The last five columns give the logarithm of the surface mass fractions of the elements described.

Table 2.1 lists some properties of the same nine models shown in Fig. 2.3 at their period minimum. The first five models all have minimum periods more than 1 h and more than 1% hydrogen in the core at their minimum, whereas the cores of the last four models consist for more than 99% of helium. With decreasing minimum period, the mass transfer rates increase rapidly and the luminosities of the donors decrease. In Table 2.2 we list some observational properties along the evolutionary tracks of two of our grid models with $Z = 0.01$ and $M_{\rm i} = 1.1\,M_{\odot}$.

Although we find that it is possible to reach orbital periods below 40 minutes without spiral-in, but due to magnetic capture instead, it seems that one has to select an initial period carefully in order to actually do so. We also find that it is possible to construct a model that has a minimum period as low as the observed 11.4 min in a time span smaller than the Hubble time. The question arises, however, what the chances are that such a system is indeed formed in a population of stars. In order to quantify this, we will expand our parameter space to the entire grid we calculated and do statistics on these tracks in Sect. 2.4.

2.3.3 Bifurcation models

For an initial secondary mass of $1.1\,M_{\odot}$, the grid models with initial periods of 0.85 days and 0.90 days bracket the bifurcation period. Some timescales that can explain this difference are shown in Fig. 2.4. The evolution of both models is rather similar in the beginning, except for the small difference in orbital period, that stays about constant during the main sequence. The wider system has a larger Roche lobe and thus the donor fills its Roche lobe at a slightly later stage of its evolution. At this point, the evolutionary timescale of the donor is shorter than that in the closer system, and it can form a well defined helium core. When the envelope outside this core has been reduced by mass transfer to $\simeq 0.03\,M_{\odot}$, it collapses onto the core, mass transfer stops, and magnetic braking disappears before the magnetic capture is complete. Gravitational radiation is then the only term of angular momentum loss and it is not strong enough to shrink the orbit to the ultra-short period regime within the Hubble time.

In the closer system, the evolutionary timescale of the donor is slightly larger and its helium core mass is slightly smaller. At approximately 9 Gyr mass transfer has stripped the donor to such extend that hotter layers emerge at the surface, the convective envelope of the star becomes very thin and magnetic braking is strongly reduced (see the discussion with Fig. 2.3). Fig. 2.4 shows that this happens at the moment where the gravitational radiation timescale becomes shorter than the evolutionary timescale of the donor, so that angular momentum loss remains sufficient to shrink the orbit from the hour to the minute regime.

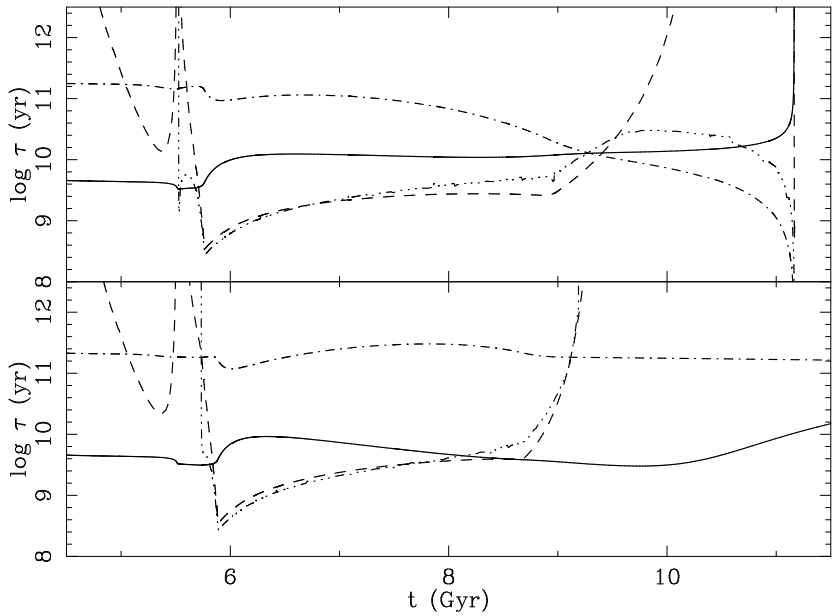

Figure 2.4: Timescales of the models that bracket the bifurcation period for 1.1 $M_\odot$. Upper panel (**a**): model with $P_\mathrm{i} = 0.85\,\mathrm{d}$. Lower panel (**b**): model with $P_\mathrm{i} = 0.90\,\mathrm{d}$. The line styles represent the different timescales: Solid line: nuclear evolution timescale $(M/M_\odot)/(L/L_\odot) \times 10^{10}\,\mathrm{yr}$, dashes: magnetic braking timescale $J_\mathrm{orb}/\dot{J}_\mathrm{MB}$, dash-dot: gravitational radiation timescale $J_\mathrm{orb}/\dot{J}_\mathrm{GR}$, dash-dot-dot-dot: mass transfer timescale $M/\dot{M}_\mathrm{tr}$. See the text for a discussion.

2.4 Statistics

2.4.1 Interpolation between models

In order to do statistics on our models, we have to interpolate between the calculated models to get a time-period track, that gives the orbital period of a system as a function of time, for a given initial orbital period P_i.

Before we can interpolate between two calculated tracks, we must first divide the tracks into similar parts of evolution. We choose three parts: i) the part between ZAMS and the beginning of RLOF, ii) the part between the beginning of RLOF and the moment where the minimum period (P_min) was reached, and iii) the part between P_min and the end of the calculation. Each of these parts is redistributed into a fixed number of data points, equally spaced in the path length of that part and determined by a polynomial interpolation of the

third degree. The path length is the integrated track in the t–$\log P$ plane, and defined as

$$\ell = \sum_i \sqrt{\left(\frac{t(i) - t(i-1)}{\Delta t}\right)^2 + \left(\frac{\log P(i) - \log P(i-1)}{\Delta \log P}\right)^2}, \qquad (2.4)$$

where $\Delta t = t_{\max} - t_{\min}$ and $\Delta \log P = \log P_{\max} - \log P_{\min}$. Thus, each part of all tracks contains the same number of points, and each point on these parts marks about the same moment in evolution in two different tracks.

Next, we interpolate between two tracks, to calculate the track for the given initial period. Because the tracks differ considerably between the shortest and longest initial period, we use linear interpolation between two adjacent tracks, that are always rather similar. Each track is thus interpolated point-by-point between each pair of corresponding points from the two adjacent tracks, to get the time and the orbital period.

Once the interpolated track is known, we interpolate within the track, to obtain the orbital period at a given moment in time. For this, we use a polynomial interpolation of the fourth degree. For some models the second part of a track consists of one point, because the beginning of RLOF marks the minimum period. For interpolations involving this point, we use a third degree polynomial interpolation.

A handful of models crash after they have stopped mass transfer, for instance the models with the highest initial period in Figs. 2.1 and 2.2. These systems will not give observable X-ray sources, but some of these tracks may be needed for the interpolation. We continued the orbital evolution of the most important of these models analytically, under the influence of gravitational radiation only, until the orbit becomes so small that the star's Roche lobe touches its surface. We consider the orbital period at which mass transfer recommences as the minimum period. We assume a constant radius of the star since the last converged model, which probably means that we overestimate the minimum period a bit in these cases.

2.4.2 Results for Z=0.01

In Sect. 2.3, we have found that we can create LMXBs with periods down to 11 minutes or perhaps even less, within a Hubble time. We also saw, however, that one has to select the initial period carefully to create a model that reaches such a low period, and that the system spends very little time on this minimum period. In order to investigate how probable it is to *observe* ultra-compact binaries, we select random points on random tracks like the ones in Figs. 2.1 and 2.2 and convert the result into a histogram. We perform this operation in the following way.

For a fixed initial secondary mass, we draw a random initial period, between 0.50 and 2.75 days, from a flat distribution in $\log P$. We then interpolate the time-period track that corresponds to this initial period, using the method described in Sect. 2.4.1. For each point on this track, an estimate for the mass transfer rate is obtained by interpolating in the logarithm of the calculated mass transfer rates. For points without mass transfer, we adapt a value of $\dot{M}_{\rm tr} = 10^{-35}\, M_\odot\, yr^{-1}$, so that we can take its logarithm. This introduces some

irregularities, like the peaks around $\log P\,(\mathrm{d}) = -0.5$ in Fig. 2.5, where interpolation between models with and without mass transfer, and interpolation between converging and diverging models play a role. This is usually only the case at orbital periods of several hours or more, and hence it is of no consequence for the ultra-compact binaries.

Once the time-period track is calculated, we draw a random moment in time, from a linear distribution between 10 and 13 Gyr, the approximate ages of globular clusters, and interpolate within the track to obtain the orbital period at that random moment. We accept only systems that have not evolved beyond their minimum period, firstly because of the negative period derivative measured for the 11.4 min system in NGC 6624, and secondly because the evolution code we use can generally not calculate far beyond the period minimum. We also estimate the mass transfer rate at that moment, again by interpolating in $\log \dot{M}_{\rm tr}$. We reject all systems with a mass transfer rate $\dot{M}_{\rm tr} < 10^{-20}\,M_\odot\,yr^{-1}$, because it is unlikely that they have any mass transfer at that moment and will therefore not be an X-ray source.

If we repeat this procedure many times, we can create a histogram that displays the expected distribution of orbital periods of a population of converging LMXBs (with all the same initial secondary masses) after 10 - 13 Gyr. The results for $1.1\,M_\odot$ and $Z = 0.01$ are shown in Fig. 2.5.

To simulate a population consisting of stars of different masses, one should interpolate between the tracks as we did for the period. The tracks are too different from each other to ensure correct results. It would require a large number of extra models to be able to interpolate between the masses correctly. Instead, we choose to add the period distributions of the different masses to simulate such a population. We do this for two different assumptions for the mass distribution: the Salpeter birth function, and a flat distribution. The results are shown in Fig. 2.6.

We see that there is little difference between the two weighing methods. This assures that although we do not know the initial distribution of the mass, it is of little influence on this result. Especially the short-period tails of the distributions are almost equal. In a sample of 10^7 systems we find one converging system with a period of about 11 minutes and 15 systems with a period of 20 minutes.

2.4.3 Results for other metallicities

The whole exercise we described in section Sect. 2.3.1, 2.4.1 and 2.4.2 is also applied to models for $Z = 0.0001$, $Z = 0.002$, and $Z = 0.02$, in order to see the effect of metallicity on the expected distributions. For $Z = 0.02$ we calculate the same initial grid as we did for $Z = 0.01$, between $P_{\rm i} = 0.5-2.75$ days for $M_{\rm i} = 0.7-1.3 M_\odot$, but $P_{\rm i} = 0.55-3.025$ days for $M_{\rm i} = 1.4$ and $1.5 M_\odot$, since these stars even at the ZAMS do not fit in an orbit with $P = 0.5$ days. For $Z = 0.002$ we use the same initial mass range, but it turns out that for $M_{\rm i} = 1.0 - 1.5 M_\odot$ the bifurcation period lies very close to or lower than 0.5 days (see Fig. 2.7). We therefore shift the minimum initial period to 0.35 days for $M_{\rm i} = 1.0, 1.4$ and $1.5 M_\odot$, and to 0.4 days for $M_{\rm i} = 1.1 - 1.3 M_\odot$. For $Z = 0.0001$, the minimum

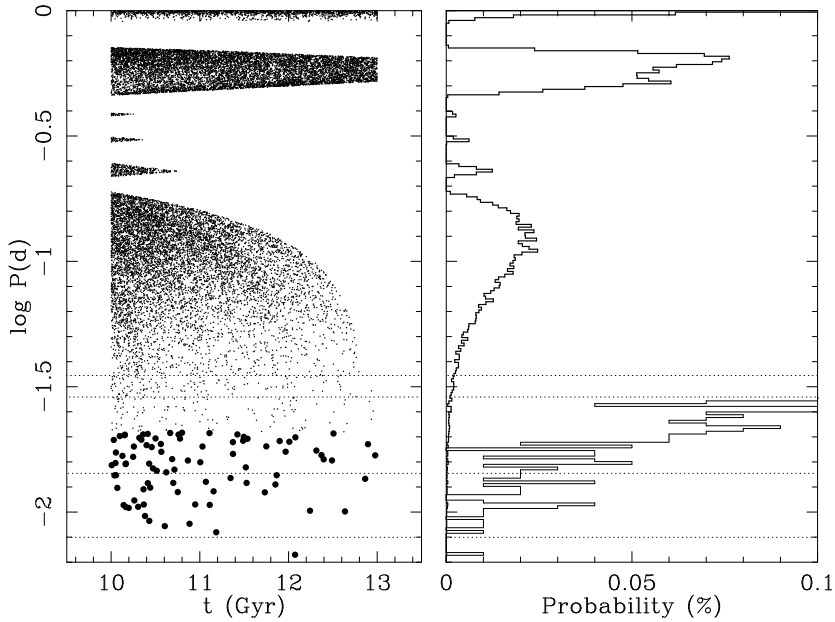

Figure 2.5: Statistics results for the 1.1 $M_{\odot}$ models. Left panel (**a**): Results from the draw of one million random initial periods and times. Each dot represents the orbital period of the selected system at the selected time. Only models that were converging and transferring mass at that time were accepted, about 10.5% of the total number. The peaks at the higher orbital periods are artefacts, caused by interpolation between models with and without mass transfer. Dots below $P = 30\,\mathrm{min}$ are plotted larger for clarity. Right panel (**b**): A histogram displaying the fraction of systems found at a certain orbital period, at any time between 10 and 13 Gyr. The $\log P$-axis was chosen to be vertical, to correspond to the vertical axis in the left panel. The thick line displays the data corresponding to the horizontal axis, the thin line is the short-period tail of the same data, multiplied by a factor of 100 in the horizontal (probability) direction. The dotted horizontal lines are the orbital periods of the four observed LMXBs mentioned in Fig 2.1.

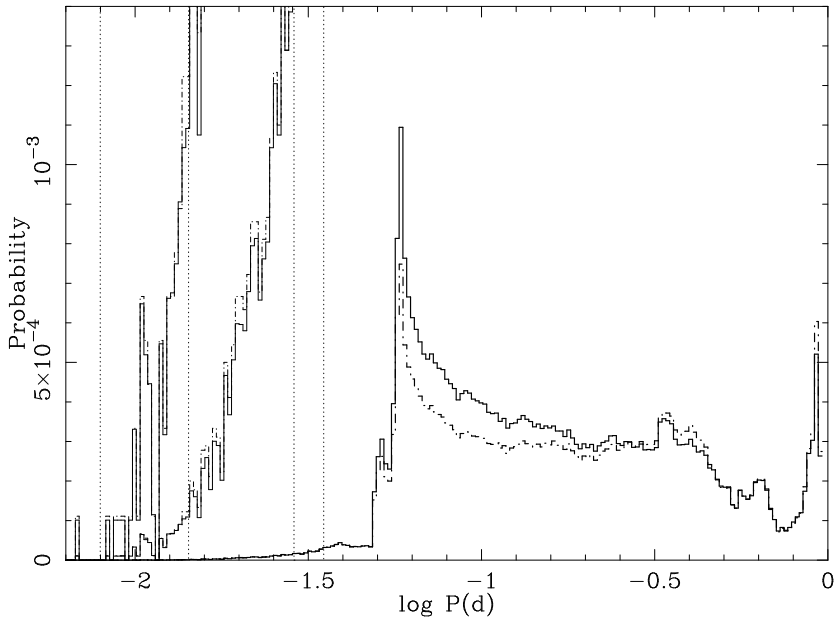

Figure 2.6: Probability distribution for all models with $Z = 0.01$. The solid line represents the sum of the distributions of the different masses weighed with the Salpeter birth function, the dash-dotted line assumes a flat distribution in mass. The thin lines below $\log P\,(d) = -1.3$ and below $\log P\,(d) = -1.7$ are the same data, multiplied with 100 and 1000 respectively. The four vertical, dotted lines show the orbital periods of the four observed LMXBs mentioned in Fig 2.1.

initial period is shifted to 0.3 d for $0.7 - 1.2\,M_\odot$ and even to $0.28\,d$ for $1.3 - 1.5\,M_\odot$. For $Z = 0.0001$ and $M_\mathrm{i} = 1.5\,M_\odot$, the initial period at which a ZAMS star fills its Roche lobe is higher than the bifurcation period. Stars with higher Z have larger radii and often do not fit in these tight orbits. We shift the upper limit for the period range from which we took random values accordingly, so that the size of the range (in $\log P$) did not change. Since the bifurcation period for the lower metallicity models lies lower, we also have to pinpoint better to calculate the interesting models around it. We therefore narrow the grid to steps of 0.01 d around the bifurcation period for $Z = 0.002$ and $Z = 0.0001$, and even down to 0.001 d for the last metallicity.

The bifurcation periods for the different masses are plotted in Fig. 2.7a. There is a trend in metallicity in the sense that the dotted line of $Z = 0.02$ could be moved down and left to fall over that of $Z = 0.01$ and further to reach that of $Z = 0.002$ and $Z = 0.0001$. Fig. 2.7b shows the minimum periods for the systems that have the bifurcation period for that mass as their initial period. The trend that is shown can be explained the fact that low mass stars with a lower metallicity reach the TAMS before the Hubble time and are therefore eligible

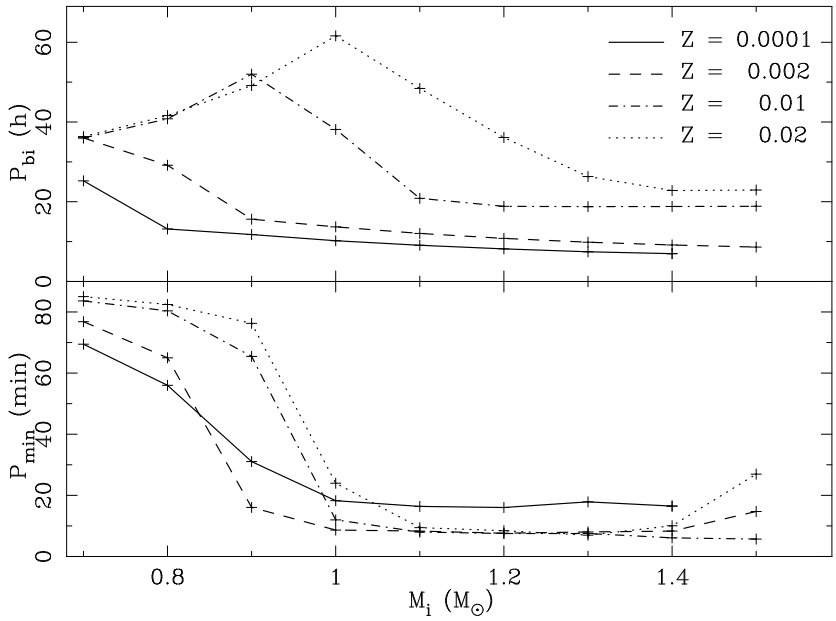

Figure 2.7: Bifurcation periods and minimum periods as a function of the initial mass for the four metallicities. *Upper panel* (**a**): The bifurcation period (in hours) between systems that converge and systems that do not converge within a Hubble time. *Lower panel* (**b**): The minimum period (in minutes) that can be reached within a Hubble time as a function of the initial secondary mass. The different line styles display the different metallicities, as indicated in the upper panel. The data point for $Z = 0.0001$, $M_{\rm i} = 1.5\,M_{\odot}$ is missing in both panels, because the bifurcation period for these systems is lower than the period at which such a donor fills its Roche lobe at ZAMS.

for magnetic capture, whereas low mass stars of higher Z do not.

The results of the statistics for $Z = 0.0001$, $Z = 0.002$ and $Z = 0.02$ are plotted in Figs. 2.8, 2.9 and 2.10 in the same way as the results for $Z = 0.01$ in Fig. 2.6, so that they can easily be compared. All four distributions are also plotted in a cumulative plot in Fig. 2.11, showing the fraction of systems with an orbital period below some value, so that they can be compared directly.

The most remarkable feature in the three distributions with the higher metallicities is the sharp drop of the number of predicted systems below $\log P\,(\mathrm{d}) = -1.25$, or about 80 minutes. This is due to the systems with low initial mass ($0.7 - 0.9 M_{\odot}$), that reach their minimum periods there because they evolve too slow to reach ultra-short periods before the Hubble time, and remain relatively long at this period. Models with $Z = 0.0001$ evolve more quickly, and although most models do not reach ultra-short periods, they are substantially lower than 80 min and can even reach 31 min in the case of $M_{\rm i} = 0.9\,M_{\odot}$. The drop

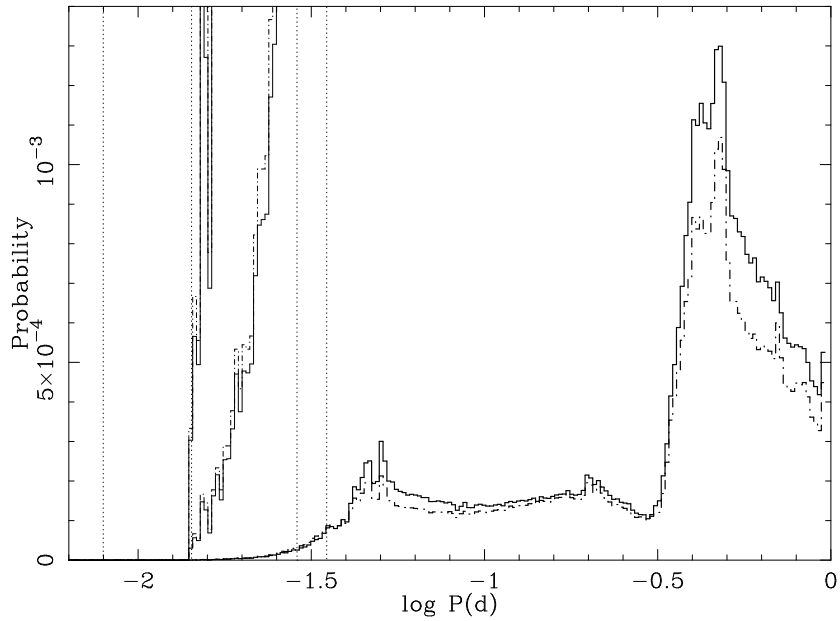

Figure 2.8: Probability distribution of the orbital periods for all models with $Z = 0.0001$. The characteristics of this plot are the same as in Fig. 2.6.

is therefore less sharp for the lowest metallicity we used.

The lower mass stars dominate in roughly the $\log P$-range $-1.25 - -0.6$, as can be seen from the fact that here the solid line for a Salpeter weighted addition of the masses that favours low mass stars is higher than the dash-dotted line for a flat mass distribution. For the ultra-short periods, there is very little difference between the two weighing methods, and we can again conclude that the exact initial mass distribution is not important for our results.

We also see that the lowest possible orbital period for an X-ray binary with $Z = 0.0001$ within the Hubble time is about a factor two smaller than for the other metallicities. This is partly due to the fact that ultra-compact binaries are less likely to be formed for this low metallicity because the initial period must be chosen more precisely. However, we find no minimum periods less than 16.0 min for this metallicity. This has probably to do with the fact that these stars are hotter and thus have a weaker magnetic field.

In a sample of 10^7 binaries with $Z = 0.0001$, we expect no converging systems with mass transfer and an orbital period of 11.4 min, and around 5 with a 20.6 min period (Fig. 2.8). For $Z = 0.002$ and $Z = 0.02$, these numbers are 7 systems with an 11.4 min period and 60 with a 20.6 min period and 4 systems with an 11.4 min period and 10 with a 20.6 min period respectively.

Fig. 2.11 shows clearly that there is some difference between the period distributions for

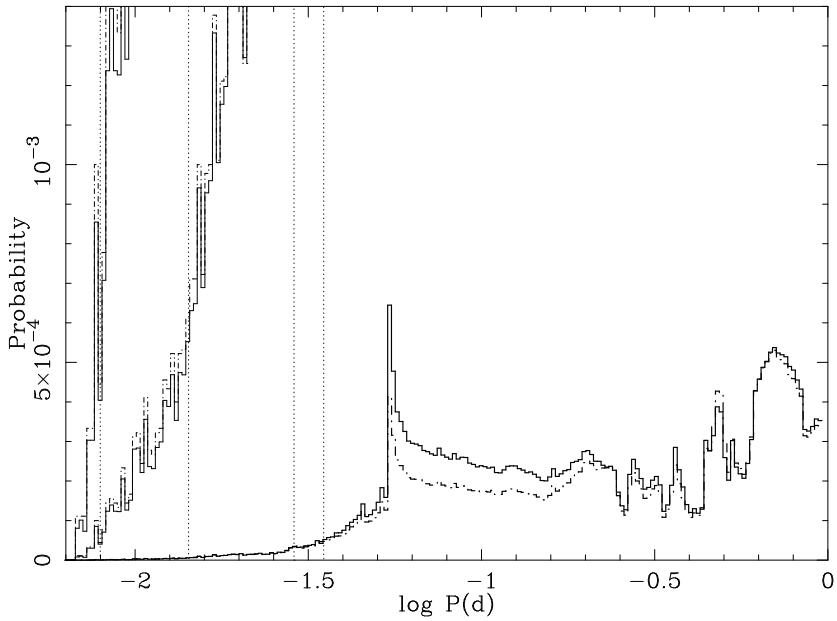

Figure 2.9: Probability distribution of the orbital periods for all models with $Z = 0.002$. The characteristics of this plot are the same as in Fig. 2.6.

the different metallicities, the largest difference being the higher period cut-off for the lowest orbital periods for $Z = 0.0001$. The largest differences for the three higher metallicities are found around 11 min, (a bit more than an order of magnitude between $Z = 0.01$ and the other two metallicities) and around 20 min (less than an order of magnitude between $Z = 0.002$ and the others). Note that the line for $Z = 0.01$ predicts for each system with an orbital period of 11 min about 100 systems with $P_{\rm orb} \lesssim 20\,{\rm min}$.

2.5 Discussion

2.5.1 The importance of converging evolution for the formation of ultra-compact binaries

To understand why the fraction of ultra-compact binaries with decreasing orbital period in our computations is so small, we note that there are three main factors contributing to this. First, only a limited range of initial orbital periods leads to strongly converging orbital evolution within the Hubble time, as listed in Table 2.3. This range of periods varies strongly with donor mass: for $Z = 0.01$ and for 1.0 and 1.1 $M_\odot$ the width is about 0.1 d; but for 1.2 and 1.3 $M_\odot$ it is only 0.003 d. This corresponds to ∼5% and ∼0.2%, respectively, of

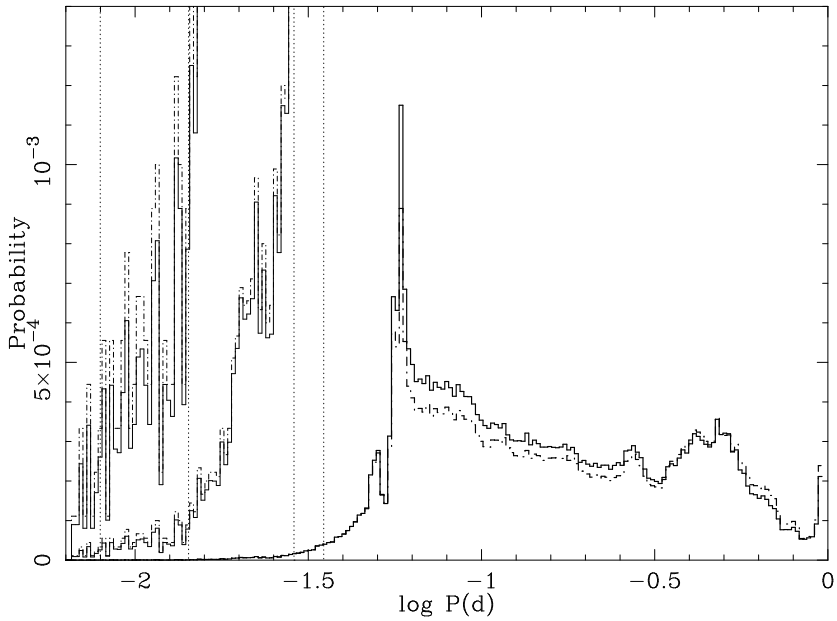

Figure 2.10: Probability distribution of the orbital periods for all models with $Z = 0.02$. The characteristics of this plot are the same as in Fig. 2.6.

the range that we consider. The reason for this rapid decrease is that the nuclear evolution time scale of the star increases much more rapidly with mass than the time scale of magnetic braking. Thus, at higher stellar mass magnetic capture can only occur for smaller initial orbital periods. Second, for each initial orbital period within the range of converging systems, only a very short time is spent at ultra-short periods while converging. Thus, the $1.1\,M_\odot$ system with initial period of 0.85 d reaches the 20 min period after 11.163 Gyr and the 11 min period after 11.167 Gyr. If we allow a range of ages of 3 Gyr, then only 0.1% of these systems will have an orbital period less than 20 min *and* a negative period derivative. If we allow also positive period derivatives, the fraction of ultra-compact binaries is somewhat higher: as can be seen in Fig. 2.2 the evolution towards longer period is comparably rapid as the evolution towards shorter period close to the minimum period. Third, as already mentioned, the range of initial periods leading to converging systems is very small for donors with $M \geq 1.2M_\odot$; hence only donors in a narrow range of initial masses contribute to ultra-short period systems. The combination of these three factors explains why so few ultra-short period systems are produced, as already surmised by Tutukov et al. (1987).

In our computations above we have assumed an initial period distribution in the range $0.5\,\mathrm{d} \lesssim P_b \lesssim 3\,\mathrm{d}$. In the galactic disk, the actual period range extends to much longer periods, and accordingly our estimates of the fraction of X-ray binaries that is observed at ultra-short periods are upper bounds, for systems evolved along the scenario that we

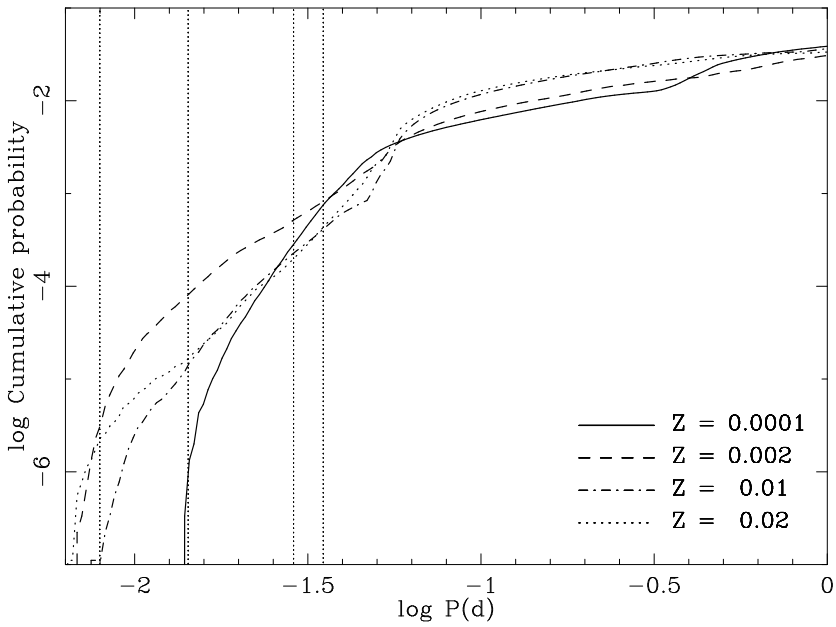

Figure 2.11: Cumulative plot for the distribution of the orbital periods for all models and all four metallicities. The different line styles represent the different metallicities as indicated in the lower right of the plot. The height of the lines shows the logarithm of the fraction of all probed systems that have an orbital period equal to or lower than the period on the horizontal axis. For all lines, a flat initial mass distribution is used. The dotted vertical lines show the observed orbital periods mentioned in Fig 2.1.

compute. This is in agreement with the absence of large numbers of X-ray binaries with periods much less than 40 minutes, in the galactic disk. If fact only one such system has recently been discovered; it may well have formed through a different mechanism, e.g. via a double spiral-in at the end of which a white dwarf becomes the donor of a neutron star (Savonije et al. 1986).

In globular clusters the binary period distribution is expected to be different from that in the galactic disk: the widest primordial binaries are dissolved and close binaries are produced in close stellar encounters. If the neutron star is exchanged into a primordial binary in a neutron-star/binary encounter, the period after the encounter scales with the pre-encounter binary period; in general the orbit after exchange will be similar in size (Sigurdsson & Phinney 1993). However, the range of periods is still expected to be wider than the range that we have considered in our computations, which therefore give an upper bound to the fraction of ultra-compact binaries. If the neutron star is captured tidally, the orbital period after capture tends to be short. The exact description of tidal capture is highly uncertain, and we will discuss the simplest description to provide a reference frame. In this description, the

M_i	$P_{i,1}$	$P_{i,2}$	$P_{rlof,1}$	$P_{rlof,2}$	R_{zams}	R_{tams}	P_{zams}	P_{tams}
1.0	1.477	1.589	0.638	0.715	0.92	1.73	0.19	2.50
1.1	0.767	0.856	0.640	0.740	1.05	1.51	0.22	2.00
1.2	0.753	0.756	0.686	0.689	1.18	1.71	0.26	2.37
1.3	0.753	0.756	0.704	0.707	1.27	2.00	0.29	2.94
1.4	0.753	0.758	0.714	0.719	1.31	2.37	0.29	3.71
1.5	0.752	0.763	0.717	0.728	1.33	2.65	0.29	4.32

Table 2.3: Comparison between the orbital periods that lead to periods less than 30 min within a Hubble time and orbital periods that result from tidal capture with a 1.4 $M_\odot$ neutron star, for different secondary masses and $Z = 0.01$. Column 1: initial secondary mass, columns 2-3: initial period range that leads to ultra-short periods, columns 4-5: RLOF-period period range that leads to ultra-short periods, columns 6-7: ZAMS and TAMS radii, columns 8-9: orbital periods for a circularised binary with capture distances of $1 \times R_{zams}$ and $3 \times R_{tams}$. Masses are in $M_\odot$, radii in $R_\odot$ and periods in days.

neutron star captures a main-sequence star if its closest approach d is within three times the radius R of that star, i.e. $d \leq 3R$ (Fabian et al. 1975). The capture rate is linear in d; thus one third of the captures is a direct hit, which completely destroys the main-sequence star. Capture may lead to a binary if $R \lesssim d \leq 3R$. The lower bound may in fact be higher, since too close a capture still does serious damage to the star (Ray et al. 1987). The orbit immediately after capture is highly eccentric, and after it circularises its semi-major axis is twice the capture distance: $a_c \simeq 2d$. Hence orbits formed by tidal capture have a semi-major axis (after circularisation) $2R \lesssim a_c \leq 6R$, or with Kepler's law:

$$0.23\,\mathrm{d}\left(\frac{R}{R_\odot}\right)^{3/2}\left(\frac{M_\odot}{M+m}\right)^{1/2} \lesssim P_b \leq 1.20\,\mathrm{d}\left(\frac{R}{R_\odot}\right)^{3/2}\left(\frac{M_\odot}{M+m}\right)^{1/2} \tag{2.5}$$

Immediately after the capture, the main-sequence star is highly perturbed, but after a thermal timescale it may settle on its equilibrium radius, and continue its evolution. The range of orbital periods depends on the radius that the star has when it is captured. In general, the period range is bounded below by the period found by entering twice the zero-age main-sequence radius into Eq. 2.5 and above by entering six times the terminal-age main-sequence radius (because a star evolved beyond this point does not evolve towards shorter periods). In Table 2.3 we list the period ranges expected in this simplest description of capture. Unless the central density of the globular cluster evolves dramatically, the probability of capture is approximately flat in time. The period after capture close to the zero-age main sequence should be compared to the initial binary period in our computations; the period after capture close to terminal-age main sequence should be compared to the period of a system close to filling its Roche lobe. In either case, we see that capture leads to a period distribution which covers an appreciable fraction of the period distribution that we cover in our computations. This means that our conclusion that only an exceedingly small fraction

of all binaries with a neutron star evolve towards periods less than 30 min holds also for tidally captured binaries.

We have taken the simplest description of tidal capture. From the above argument it is clear that changing the assumptions made about tidal capture is unlikely to change our conclusion, that evolution from magnetically driven converging evolution does not contribute significantly to the population of ultra-compact binaries. Even if tidal capture would miraculously focus the resulting orbits into the narrow range required for converging evolution, the fact would remain that each systems spends only a small fraction of its time converging from 20 min to 11 min.

If the binary in NGC 6624 were the only ultra-short-period binary in a globular cluster, one could accept an evolutionary scenario with low probability. It is thus worthy of note that our statistical argument depends critically on the observation that the 20.6 min (or 13.2 min) period of the binary in NGC 6712 is real. So far, this period has been measured only once in a single HST data set, and an independent new measurement is very desirable, to exclude definitely that the first measurement of a significant periodicity is a statistical fluke.

2.5.2 Comparison to Pylyser & Savonije

The question arises why Pylyser & Savonije (1988) and Pylyser & Savonije (1989), hereafter PS1 and PS2, did not find ultra-compact systems in their study. We tried to reproduce their models with a 1.0 $M_\odot$ compact primary and a 1.5 $M_\odot$ secondary (models A25-I25 in PS1 and A25-Z25 in PS2) because these are best documented and they find the lowest minimum period here (38 min for A25 in PS2). We calculated models with the same initial masses, mixing length ($l/H_\mathrm{p} = 1.5$), metallicity ($Z = 0.02$) and without overshooting. Figure 2.12 compares their results to our calculations as the minimum period (P_min) as a function of the period where Roche-lobe overflow starts (P_rlof).

We find the bifurcation period at much larger P_rlof, which is due to the fact that our stars rotate (about 25% of the difference, according to test calculations we have done) and increased opacities. Both effects increase the radii of our model stars, so that they must be placed in a larger orbit to fill their Roche lobe at the same stage of evolution. It seems that shifting the two solid lines of PS1 and PS2 horizontally can approximately compensate for this, but the lines must be shifted over different amounts. Hence, a gap arises between what at first sight appears to be a continuous P_rlof-range from PS1 and PS2. The fact that they find the minimum period at the limit of each range, and the fact that these two points are both at $P_\mathrm{rlof} = 0.70$ d, but give very different minimum periods (100 min and 38 min for PS1 and PS2 respectively), are supporting the evidence for the existence of this gap. The cause for the gap seems to be clear; in PS2 an accretion induced collapse (AIC) occurs when the primary reaches 1.44 $M_\odot$, whereas in PS1 no such event happens. The AIC decreases the mass of the compact object and increases the orbital period so that the further evolution can no longer be compared to that of systems without an AIC.

In our more complete series of models, shown in Fig. 2.12, the lowest minimum period we find is 7.0 min, and is reached after 12.4 Gyr.

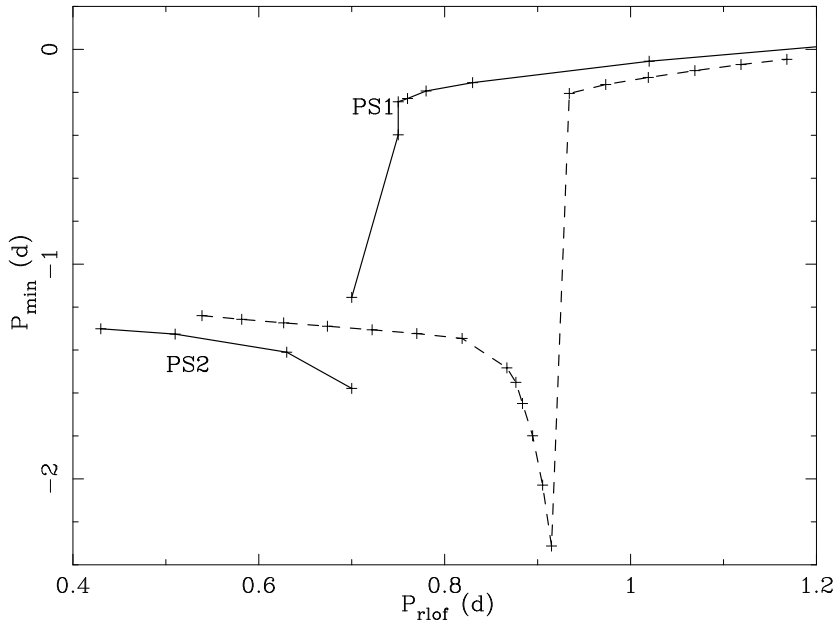

Figure 2.12: Comparison of our models (dashed line) to the models A25-I25 of PS1 and A25-Z25 of PS2 (solid lines). See the text for details.

2.5.3 Comparison to Podsiadlowski et al.

We chose the parameters of our models as similar as possible to those of Podsiadlowski et al. (2002) (see Sect. 2.2), to see if we could reproduce their results for a 1.4 $M_\odot$ neutron star and a 1.0 $M_\odot$ secondary. Indeed, the results of our calculations are qualitatively very similar to their findings in their Fig. 16 and their statement that binaries with an orbital period of 5 minutes can be achieved without a spiral-in, although we need slightly larger initial periods to get to the same minimum period. Podsiadlowski et al. (2002) display their results as a function of time since Roche-lobe overflow started, and because of this we cannot ascertain the total age of the binary at the minimum period. The red and blue model in their Fig. 16 reach minimum periods of about 9 and 7 minutes, at approximately 4.5 and 5.5 Gyr after the beginning of RLOF. We find very similar results, and in addition we find the total ages of these systems: 14 and 17 Gyr respectively. We find that it takes 13.4 Gyr to reach an orbital period of 11.4 minutes, the shortest period observed for an X-ray binary, and more than 35 Gyr to shrink the orbit to 5 minutes. We conclude that it is not possible to create systems with orbital periods less than 10 min this way, within a Hubble time.

Podsiadlowski et al. (2002) find that there is a rather large range of initial orbital periods (13 – 17.7 hr) that lead to a minimum period that is less than 30 minutes. We find for the same condition a $P_{\rm rlof}$ of 15.3 – 17.2 hr, which is considerably smaller. This is firstly

because our model stars have a slightly larger radius. Part of the explanation of the increased radius is given by the rotation of the star, although this can only account for 20% of the difference in the $P_{\rm rlof}$-range, and by the different helium abundance (Podsiadlowski et al. (2002) use $Y = 0.27$, we have $Y = 0.26$), which explains 10%. The larger radius shifts the whole $P_{\rm rlof}$-range to larger orbital period. Secondly, we limit our range to systems that reach their minimum period before the Hubble time, so that it is cut off above a certain $P_{\rm rlof}$.

What Podsiadlowski et al. (2002) call the *initial* period is the period at which RLOF initiates, and which we call $P_{\rm rlof}$. In the time before RLOF began, the magnetic braking may have played a role in shrinking the pre-RLOF orbit of the systems as listed in Table 2.3.

2.5.4 Comparison with observations and other models

The main result from our computations is that, in a population where all X-ray binaries evolve from close detached binaries of a main-sequence star and a neutron star, systems with orbital periods less than 30-40 minutes and with decreasing orbital periods are very rare. If we accept that the orbital period of the X-ray source in NGC 6624 is decreasing intrinsically (and not just observationally due to gravitational acceleration), we must accept that it is a statistical fluke, or look for a different origin.

In this respect it would be important to know more about the orbital periods and their derivatives of other X-ray sources in globular clusters. A very short orbital period is detected for just one other bright X-ray source, in NGC 6712, as a regular variation of 0.044(7) mag in one series of 53 F300W (wide U) filter HST observations with WFPC2 in 1995; aliasing allows two solutions at 13.2 or 20.6 minutes (Homer et al. 1996). Homer et al. (1996) opt for the longer period, on the basis of the low X-ray luminosity that reflects a low mass-transfer rate and a model in which the donor to the neutron star is a white dwarf (Verbunt 1987). We note that the same choice for the longer period would follow for the magnetic-capture model. The period derivative of the source in NGC 6712 is not known. The argument that as many as half of the bright X-ray sources in globular clusters have ultra-short periods is based on the similarity of various properties of those X-ray sources with the properties of the X-ray sources in NGC 6624 and NGC 6712. This argument is correct only if the X-ray source in NGC 6712 indeed has an ultra-short period. It is therefore important that this period is confirmed; which will also settle between the aliases of 13.2 and 20.6 minutes.

Measurement of the period derivative will be very difficult. It is therefore of interest to know how many ultra-compact binaries one would expect irrespective of their period derivative, in the magnetic capture model. Alas, our computations stop a short time after the minimum period, so that we do not have an accurate estimate of the time spent at positive period derivative. Nonetheless, inspection of our results as reflected in Fig. 2.1 shows that the evolution away from the minimum period is only slightly slower than the evolution towards it. Thus, the number of systems expected at the shortest period range of between 10-30 minutes would only be a factor few higher than the number in the same period range with decreasing period only. This implies that the presence of even two systems with periods less than 30 minutes among 13 globular cluster systems excludes the magnetic-capture scenario

as the dominant formation process. The conclusion is true a fortiori if more such systems are discovered.

A donor in an ultra-compact system can also be a helium-burning star. To bring such a small star into contact, a spiral-in must have occurred (Savonije et al. 1986). The progenitor of such a helium-burning star would be more massive than the main-sequence star found in globular clusters, and Verbunt (1987) argued that this excludes such donors for sources in globular clusters. However, more massive stars can be made in direct collisions: if such a more massive star ends up in a binary with a neutron star, further evolution can lead to a helium-burning donor in an ultra-compact system. This scenario may gain in importance if tidal capture is indeed less efficient, as indicated by a high fraction of systems with ultra-short periods. It allows negative derivatives of the orbital period.

Since the measurement of the intrinsic derivative of the orbital period is so difficult, it is useful to look for other observational properties that can discriminate between the different origins of an ultra-compact binary. With this in mind, we refer to Table 2.2 where some properties of ultra-short-period systems are listed that follow for the magnetic-capture model, in particular the mass-transfer rate at various periods, and the abundances of the more important elements. A pure white-dwarf donor, whittled down to a mass less than $0.1\,M_{\odot}$, would have no hydrogen if it was a helium white dwarf; and no hydrogen and no helium if it was a carbon-oxygen white dwarf. Therefore, if hydrogen is discovered in the spectrum of an ultra-compact X-ray binary, this indicates evolution through magnetic capture and the orbital period must still be decreasing. Close to the minimum period the hydrogen abundance at the surface goes to zero and thus is no longer discriminant between models.

Acknowledgements We thank P.P. Eggleton for making available to us the latest version of his binary evolution code. We also thank F. Rasio for his suggestions to improve this chapter.

Chapter 3

Reduced magnetic braking and the magnetic capture model for the formation of ultra-compact binaries

M.V. van der Sluys, F. Verbunt and O.R. Pols

Astronomy and Astrophysics, v.440, p.973–979 (2005)

Abstract A binary in which a slightly evolved star starts mass transfer to a neutron star can evolve towards ultra-short orbital periods under the influence of magnetic braking. This is called magnetic capture. In Chapter 2 we showed that ultra-short periods are only reached for an extremely small range of initial binary parameters, in particular orbital period and donor mass. Our conclusion was based on one specific choice for the law of magnetic braking, and for the loss of mass and angular momentum during mass transfer. In this chapter we show that for less efficient magnetic braking it is impossible to evolve to ultra-short periods, independent of the amount of mass and associated angular momentum lost from the binary.

3.1 Introduction

In Chapter 2 we examined the process of magnetic capture: a slightly evolved main-sequence star in a binary that transfers mass to a neutron-star companion while the orbital period shrinks to the ultra-short-period regime (less than about 40 minutes). To facilitate comparison with earlier work, we used the same law for magnetic braking, and the same assumption about the loss of mass and angular momentum during mass transfer as Podsiadlowski et al. (2002). Specifically, we used the law for magnetic braking as postulated by Verbunt & Zwaan (1981), with the extra requirement that a sufficiently large convective zone is present near the surface of the star, and we assumed that half of the transferred mass leaves the binary with the specific angular momentum of the neutron star. We concluded that ultra-short periods are reached within the Hubble time only by binaries within very narrow ranges of initial orbital periods and donor masses. In this chapter we investigate how this conclusion changes if we vary the assumptions on the strength of magnetic braking and on the loss of mass and angular momentum from the system.

Section 3.2 briefly describes the stellar evolution code used and especially the laws for magnetic braking and system mass loss that we implemented. We then show which grids of models were calculated and how the statistical study was performed in Sect. 3.3. The results are presented in Sect. 3.4 and discussed in Sect. 3.5. In Sect. 3.6 we summarise our conclusions.

3.2 Binary evolution code

3.2.1 The stellar evolution code

We calculate our models using the STARS binary stellar evolution code, originally developed by Eggleton (1971, 1972) and with updated input physics as described in Pols et al. (1995). Opacity tables are taken from OPAL (Iglesias et al. 1992), complemented with low-temperature opacities from Alexander & Ferguson (1994). For more details, see Sect. 2.2.

3.2.2 Angular momentum losses

Loss of angular momentum is essential to shrink the orbit of a binary in which the less massive star transfers mass to its more massive companion. We consider three sources of angular momentum loss.

For short periods, gravitational radiation is a strong source of angular momentum loss. We use the standard description

$$\frac{dJ_{\rm GR}}{dt} = -\frac{32}{5}\,\frac{G^{7/2}}{c^5}\,\frac{M_1^2\,M_2^2\,(M_1+M_2)^{1/2}}{a^{7/2}} \tag{3.1}$$

(Peters 1984).

The second mechanism of angular momentum loss from the system is by non-conservative mass transfer. We assume that only a fraction β of the transferred mass is accreted by the neutron star. The remainder is lost from the system, carrying away a fraction α of the specific orbital angular momentum of the neutron star:

$$\frac{dJ_{\rm ML}}{dt} \;=\; -\alpha\,(1-\beta)\,a_1^2\,\omega\,\dot{M}_2, \tag{3.2}$$

where a_1 is the orbital radius of the neutron star and ω is the angular velocity.

To keep the models simple, we applied no regular stellar wind to our models, so that all mass loss from the system and associated angular momentum loss result from the non-conservative mass transfer described above.

The third source of angular momentum loss in this study is magnetic braking. Verbunt & Zwaan (1981) postulated a law for magnetic braking

$$\frac{dJ_{\rm MB}}{dt} \;=\; -3.8\times10^{-30}\,\eta\,M\,R^4\,\omega^3\,{\rm dyn\,cm}, \tag{3.3}$$

on the basis of the observations by Skumanich (1972) that the equatorial rotation velocity v_e of main-sequence G stars decreases with the age t of the star as $v_e \propto t^{-0.5}$. In Chapter 2 we assumed $\eta = 1$, after Rappaport et al. (1983). More recent measurements of rotation velocities of stars in the Hyades and Pleiades, however, show that M stars have a wide range of rotation velocities that is preserved as they age (Terndrup et al. 2000). This indicates that magnetic braking is less strong for low mass stars than assumed in Eq. 3.3 with $\eta = 1$. Also, observational evidence indicates that coronal and chromospheric activity, and with it magnetic braking, saturate to a maximum level at rotation periods less than about 3 days (*e.g.* Vilhu 1982; Vilhu & Rucinski 1983). Verbunt (1984) showed that to explain a braking with the strength of Eq. 3.3 for a solar-type star, the star must have a magnetic field in excess of ~ 200 G for a slow rotator, and in addition a stellar wind loss in excess of $5\times10^{-10}M_\odot$/yr for a fast rotator (for which the corotation velocity of the wind matter is much higher than the escape velocity – see also Mochnacki (1981)). A smaller field or less wind (for the fast rotator) automatically leads to a lower braking.

Many theoretical descriptions of angular momentum loss due to a magnetized wind can be found in the literature (among others Kawaler 1988; Stepien 1995; Eggleton & Kiseleva-Eggleton 2002; Ivanova & Taam 2003). These prescriptions depend on properties of the star (for instance wind mass loss rate, magnetic field strength, corona temperature) that are poorly known from observations for main-sequence stars and even less for evolving stars. These angular momentum prescriptions vary in strength and dependence on the stellar parameters. We have selected two different semi-empirical prescriptions to investigate the effect of reduced braking on the mechanism of magnetic capture. In Sect. 3.5 we will show that these two different implementations of magnetic braking dominate the evolution of the binary in two completely different phases of their life.

First, we retain the functional dependence of the braking on stellar mass and radius given by Eq. 3.3, but arbitrarily reduce the strength by taking $\eta = 0.25$ (reduced braking)

and $\eta = 0$ (no braking). Second, we use a new law for magnetic braking, derived on the basis of the ranges of rotation velocities in the Hyades and Pleiades, which includes saturation at a critical angular rotation velocity $\omega_{\rm crit}$ (Sills et al. 2000):

$$\begin{aligned} \frac{dJ_{\rm MB}}{dt} &= -K \left(\frac{R}{R_\odot}\right)^{0.5} \left(\frac{M}{M_\odot}\right)^{-0.5} \omega^3, \quad \omega \leq \omega_{\rm crit} \\ \frac{dJ_{\rm MB}}{dt} &= -K \left(\frac{R}{R_\odot}\right)^{0.5} \left(\frac{M}{M_\odot}\right)^{-0.5} \omega\, \omega_{\rm crit}^2, \; \omega > \omega_{\rm crit} \end{aligned} \tag{3.4}$$

From Andronov et al. (2003) we take the value $K = 2.7 \times 10^{47}$ g cm^2 s that reproduces the angular velocity of the Sun at the age of the Sun. Krishnamurthi et al. (1997) require a mass-dependent value for $\omega_{\rm crit}$ and they scale this quantity inversely with the turnover timescale for the convective envelope $\tau_{\rm to}$ of the star at an age of 200 Myr:

$$\omega_{\rm crit} = \omega_{\rm crit,\odot} \frac{\tau_{\rm to,\odot}}{\tau_{\rm to}} \tag{3.5}$$

They use a fixed value for $\omega_{\rm crit}$, because they consider main-sequence stars and the value of $\tau_{\rm to}$ does not change much during this evolution period. However, we consider donor stars in a binary system that change substantially during their evolution and hence use the instantaneous value for $\tau_{\rm to}$. This convective turnover timescale is determined by the evolution code by integrating the inverse velocity of convective cells, as given by the mixing-length theory (Böhm-Vitense 1958), over the radial extent of the convective envelope. We further use a value of $\omega_{\rm crit,\odot} = 2.9 \times 10^{-5}$ Hz, equivalent to $P_{\rm crit,\odot} = 2.5$ d (Sills et al. (2000) find that a value for $\omega_{\rm crit,\odot}$ of around 10 times the current solar angular velocity is needed to reproduce observational data of young clusters with a rigidly rotating model), and $\tau_{\rm to,\odot} = 13.8$ d, the value that the evolution code gives for a $1.0\,M_\odot$ star at the age of 4.6 Gyr.

In both prescriptions (Eqs. 3.3 and 3.4) we follow Podsiadlowski et al. (2002) and reduce the magnetic braking by an ad hoc term

$$\exp(1 - 0.02/q_{\rm conv}) \quad \text{if } q_{\rm conv} < 0.02, \tag{3.6}$$

where $q_{\rm conv}$ is the fractional mass of the convective envelope. In this way we account for the fact that stars with a small or no convective mantle do not have a strong magnetic field and will therefore experience little or no magnetic braking. Notice that Eq. 3.5 alone predicts that stars with higher mass have a higher $\omega_{\rm crit}$, because they have a higher surface temperature, hence a smaller convective mantle and a shorter $\tau_{\rm to}$. The application of the term in Eq. 3.6 prevents that these stars experience unrealistically strong magnetic braking.

3.3 Creating theoretical period distributions

3.3.1 Binary models

Using the binary evolution code described in Sect. 3.2, with the non-saturated magnetic-braking law of Eq. 3.3 we calculated grids of models for Z=0.01, the metallicity of the

globular cluster NGC 6624, and Y=0.26. We choose initial masses between 0.7 and 1.5 $M_\odot$ with steps of 0.1 $M_\odot$. For each mass we calculated models with initial periods (P_i) between 0.5 and 2.5 days with steps of 0.5 d for all masses and dropped the lower limit for the initial period where necessary, down to 0.25 d. Around the bifurcation period between converging and diverging systems, where the shortest orbital periods occur, we narrow the steps in P_i to 0.05 or sometimes even 0.02 d.

Another series of models was calculated with a similar grid of initial masses and periods, but with the magnetic-braking law of Eq. 3.4 that includes saturation of the magnetic field strength at high angular velocities.

3.3.2 Statistics

In order to create a theoretical period distribution for a population of stars, we proceed as described in Sect. 2.4. First, we draw a random initial period (P_i) and calculate the time-period track for this P_i by interpolation from the two bracketing calculated tracks. Second, we pick a random moment in time and interpolate within the obtained time-period track to get the orbital period of the system at that moment in time. The system is accepted if mass transfer is occurring and the period derivative is negative. The details of this interpolation are described in Sect. 2.4.1. We do this 10^6 times for each mass to produce a theoretical orbital-period distribution for a given initial mass and given ranges in $\log P_i$ and time.

To simulate the period distribution for a population of stars with an initial mass distribution, we add the distributions of different masses. In Sect. 2.4.2 we show that the result depends very little on the weighting, so that we simulate a flat distribution in initial mass.

3.4 Results

3.4.1 Reduced magnetic braking

We have calculated three grids of models as described in Sect. 3.3.1 with the non-saturated magnetic-braking law given by Eq. 3.3. We have given the three grids different braking strengths by changing the value for η. We used the values $\eta = 1.0$ (as in Chapter 2), $\eta = 0.25$ and $\eta = 0.0$. For the last set, there is no magnetic braking and the angular momentum loss comes predominantly from gravitational radiation. For all models in these grids, half of the transferred mass is ejected from the system with the specific angular momentum of the neutron star, i.e. we used $\alpha = 1$ and $\beta = 0.5$ in Eq. 3.2. Figure 3.1 shows time-period tracks for models from the three grids with selected initial orbital periods and $M_i = 1.1\,M_\odot$.

The figure shows clearly that initially similar models evolve in different ways, but only after mass transfer has started. This is because a low-metallicity main-sequence 1.1 $M_\odot$ star has a high surface temperature, hence a small convective envelope ($q_{\rm conv} \approx 10^{-3}$) and therefore effectively no magnetic braking at that stage (see Eq. 3.6). After mass transfer starts, the surface temperatures drop and the differences in magnetic braking strength become apparent. It is obvious that a model that experiences weaker magnetic braking may

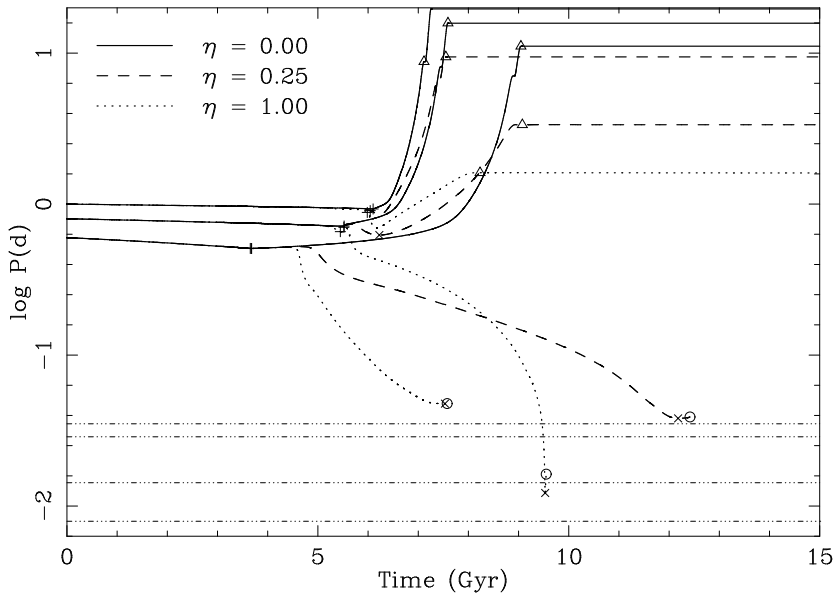

Figure 3.1: Time-period tracks for $Z = 0.01$, $M_{\rm i} = 1.1\,{\rm M}_{\odot}$ with $P_{\rm i}$ = 0.6 d, $P_{\rm i}$ = 0.8 d, and $P_{\rm i}$ = 1.0 d. Each model is shown for three different values of η: 0.0 (solid lines), 0.25 (dashed lines) and 1.0 (dotted lines). The symbols mark special points in the evolution: $+$ marks the start of Roche-lobe overflow (RLOF), $\times$ the minimum period, $\triangle$ the end of RLOF and O marks the end of the calculation. The four dash-dotted horizontal lines show the orbital periods of the closest observed LMXBs in globular clusters: 11.4 and 20.6, and in the galactic disk: 41 and 50 minutes.

diverge where a similar model with stronger braking converges, and that models with weak magnetic braking converge slower than models with strong magnetic braking.

For each grid of models we produce a statistical sample as explained in Sect. 3.3.2. The results are period distributions for three populations of stars with initial masses between 0.7 and 1.5 $M_{\odot}$ and ages between 10 and 13 Gyr. The distributions are compared in Fig. 3.2.

The most striking difference in the period distributions for the three values of η is the shortest orbital period produced in the magnetic capture model. In models with reduced magnetic braking the orbits do not converge to ultra-short periods before the Hubble time, and the cut-off at the low-period end of the distribution accordingly lies at a higher period. This is also the reason why there are more systems with orbital periods of around 0.1 d for $\eta = 0.0$ than for $\eta = 1.0$; the missing models with stronger braking have already converged to lower orbital periods, or beyond the period minimum.

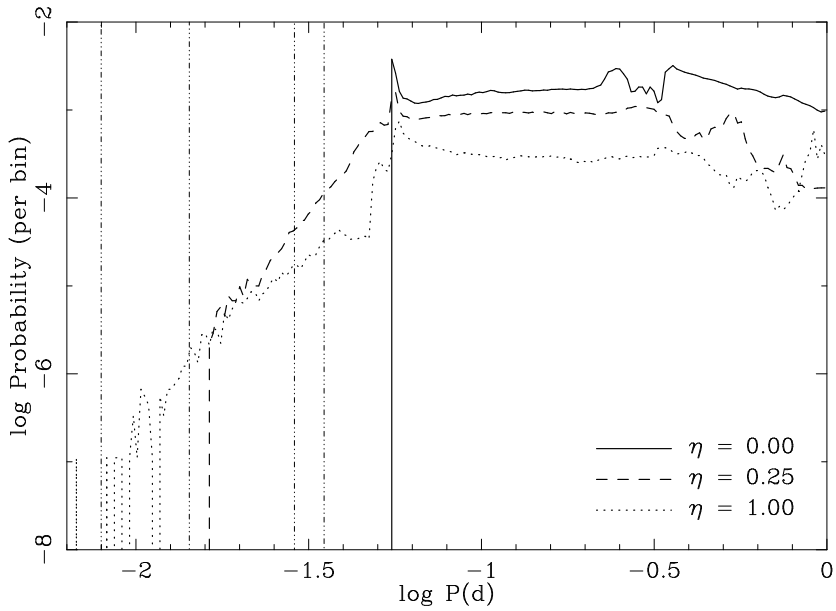

Figure 3.2: Period distributions for the magnetic capture model for η = 0.0 (solid lines), 0.25 (dashed lines) and 1.0 (dotted lines). It is clear that the cut-off for lower orbital periods strongly depends on the strength of the magnetic braking. The vertical axis displays the logarithm of the probability that an X-ray binary with a certain orbital period is found. The four vertical dash-dotted lines show the same observed orbital periods as the horizontal lines in Fig. 3.1. The probability is computed by distributing the accepted periods into bins of width $\Delta \log P = 0.011$ and dividing the number in each bin by the total number of systems.

3.4.2 Saturated magnetic braking

We have calculated one grid of models described in Sect. 3.3.1 with the saturated magnetic-braking law given by Eq. 3.4. In this prescription the magnetic field saturates at a certain critical angular velocity $\omega_{\rm crit}$, that depends on the convective turnover timescale of the donor star, as shown in Eq. 3.5. At an angular velocity higher than $\omega_{\rm crit}$, the magnetic braking scales linearly with ω rather than cubically. As the typical initial critical spin *period* is a few days, this is long compared to the initial orbital and – since the spins and orbits of our models are generally synchronised – spin period, and therefore replacing the prescription of Eq. 3.3 by that of Eq. 3.4 can be expected to have an effect similar to lowering the strength of the magnetic braking, as we did in Sect. 3.4.1. Because we will see in Sect. 3.4.3 that the shortest orbital periods are reached for models with conservative mass transfer, all models in this grid have $\beta = 1.0$ in Eq. 3.2.

Figure 3.3 compares the tracks of $1.1 M_\odot$ models from this grid with tracks taken from

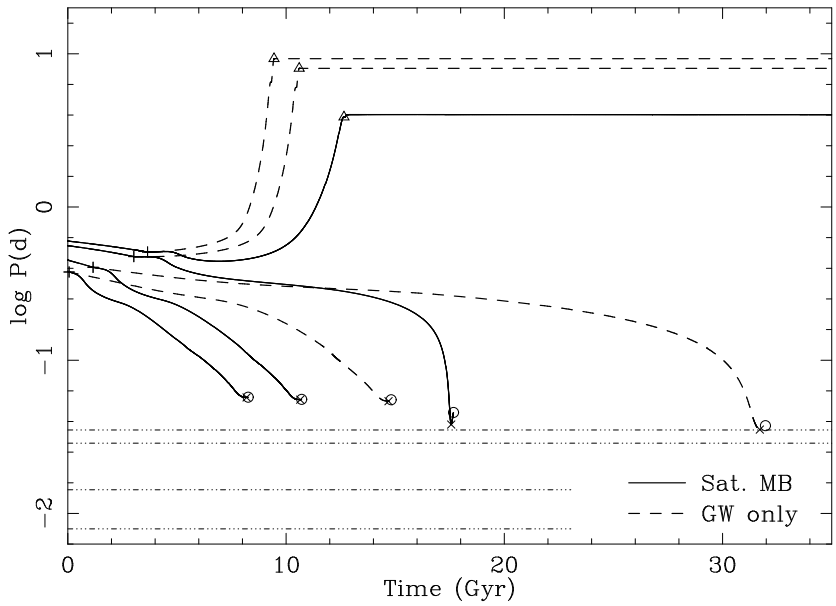

Figure 3.3: Time-period tracks for $Z = 0.01$, $M_{\rm i} = 1.1\,{\rm M}_{\odot}$ with $P_{\rm i}$ = 0.38 d (the shortest possible $P_{\rm i}$ for this model), $P_{\rm i}$ = 0.45 d, $P_{\rm i}$ = 0.56 d, and $P_{\rm i}$ = 0.60 d. Each model is shown for a magnetic braking law according to Eq. 3.4 (Sat. MB, solid lines) and no magnetic braking, but gravitational waves only (GW only, dashed lines). The symbols and horizontal dash-dotted lines are as in Fig. 3.1. Note that the time axis extends far beyond the Hubble time.

Sect. 3.4.3 with conservative mass transfer and without magnetic braking, i.e. $\beta = 1.0$ and $\eta = 0.0$. We see similar differences between the two sets of models as seen in Fig. 3.1, but the magnetic braking is clearly too weak to evolve the systems to less than 75 min within the Hubble time.

We performed statistics on the model as described in Sect. 3.3.2; the result is displayed in Fig. 3.4 and compared to the period distribution for a grid of models with $\beta = 1.0$ and $\eta = 0.0$.

3.4.3 The influence of mass loss

In Chapter 2 we have assumed that half of the transferred mass in our models is lost by the accretor and leaves the system with the specific angular momentum of the accretor. To see what influence this assumption has on the results of our study, we calculated a number of models with conservative mass transfer, so that $\beta = 1.0$ in Eq. 3.2. We calculated two sets of conservative models, one set without magnetic braking ($\eta = 0$ in Eq. 3.3) and one set with full braking ($\eta = 1$). The time-period tracks of selected models are compared to

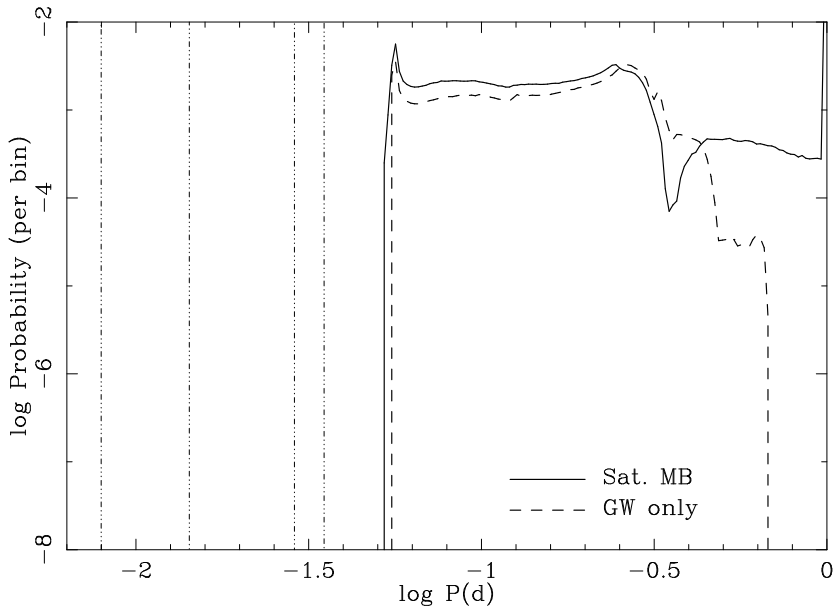

Figure 3.4: Period distribution for the magnetic capture model using the magnetic braking law described in Eq. 3.4 (Sat. MB, solid line) compared to the period distribution for models without braking, but with gravitational waves only (GW only, dashed line). The four vertical dash-dotted lines show the same observed orbital periods as the horizontal lines in Fig. 3.1. The probability is calculated in the same way as in Fig. 3.2.

previous models with $\beta = 0.5$ in Figs. 3.5 and 3.6.

Figure 3.5 shows that the time-period tracks of models with gravitational waves as the dominant angular momentum loss source are changed noticeably by a change in β. Converging models reach their minimum period much earlier for conservative models than for non-conservative models. The reason for this is that mass loss from the binary according to Eq. 3.2 leads to a widening of the binary for the value of α we use. However, even for the shortest possible initial period (0.38 d), and therefore the earliest possible period minimum for these systems, the time of the minimum shifts from 19.9 Gyr to 14.7 Gyr with a period of 78 min. The conclusion is that this effect makes no difference to the number or distribution of ultra-compact binaries.

For models with magnetic braking, the differences between the two sets of models is much smaller, as shown in Fig. 3.6. The reason for this is that the orbital evolution is completely dominated by the strong magnetic braking, so that changes in less important terms, like the amount of mass loss from the system and the associated angular momentum loss, are of very little influence. The models with full magnetic braking *can* produce ultra-compact binaries within the Hubble time; the distribution of ultra-short periods in these models is

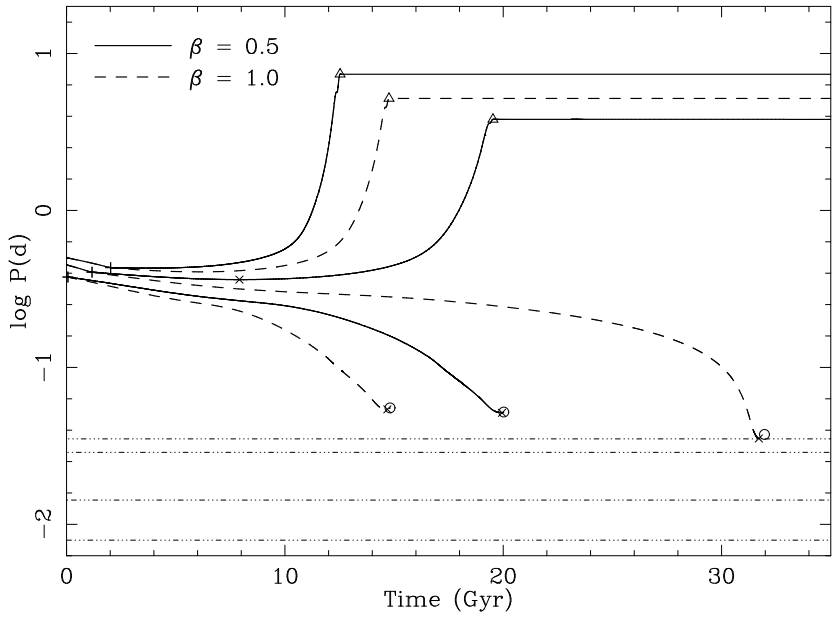

Figure 3.5: Time-period tracks for $Z = 0.01$, $M_{\rm i} = 1.1\,{\rm M}_{\odot}$ with $P_{\rm i}$ = 0.38 d (the shortest possible P_i), $P_{\rm i}$ = 0.45 d and $P_{\rm i}$ = 0.50 d. Each model is shown for two different values of β ($\beta = 0.5$, solid lines and $\beta = 1.0$, dashed lines) and has no magnetic braking ($\eta = 0.0$). The symbols and horizontal dash-dotted lines are as in Fig. 3.1.

slightly affected by a change in β (see Fig. 3.6), but not enough to change the overall conclusion of Chapter 2.

3.5 Discussion

It is clear that the magnetic capture scenario to create ultra-compact binaries depends very strongly on the strength of the magnetic braking used. By simply scaling down the Verbunt & Zwaan (1981) prescription for magnetic braking, the results are, as can be expected intuitively,

- The bifurcation period between converging and diverging systems decreases, which means that only models with a lower initial orbital period will converge.
- The rate at which a system converges is lower, so that minimum periods are reached at a later time. This can imply that ultra-compact periods occur only after a Hubble time.

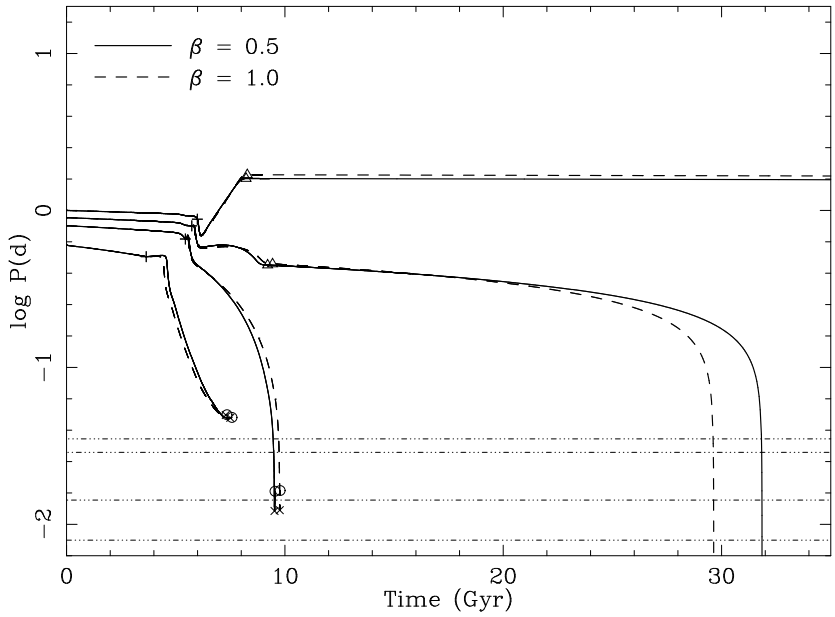

Figure 3.6: Time-period tracks for $Z = 0.01$, $M_{\rm i} = 1.1\,{\rm M}_{\odot}$ with $P_{\rm i}$ = 0.6 d, $P_{\rm i}$ = 0.8 d, $P_{\rm i}$ = 0.9 d, and $P_{\rm i}$ = 1.0 d. Each model is shown for two different values of β ($\beta = 0.5$, solid lines and $\beta = 1.0$, dashed lines) and has full magnetic braking ($\eta = 1.0$). The symbols and horizontal dash-dotted lines are as in Fig. 3.1.

- Because reaching the minimum period takes much longer, a small offset in the initial period has much more impact on the evolution of the system. Because of this, the initial period range that leads to ultra-compact systems for a certain initial mass is much smaller and thus the chances of actually producing an ultra-compact system decrease.

If we use a slightly more sophisticated, saturated magnetic braking law, the results are qualitatively similar to decreasing the magnetic braking strength. Because of the different dependencies of the two different magnetic braking laws on the mass and radius of the star in Eqs. 3.3 and 3.4, the two prescriptions take effect at completely different parts of the evolution. To illustrate this, we picked three models with an initial mass of 1 $M_{\odot}$ that evolve to the same minimum period (28 min) at about the same mass (0.06–0.07 $\rm M_{\odot}$). The three models have different magnetic braking laws implemented and are given different initial periods to reach the desired $P_{\rm min}$: the first model uses braking according to Eq. 3.3 and $P_{\rm i} = 1.485\,$d so that the period minimum is reached after 11.7 Gyr. The second model loses angular momentum according to the saturated magnetic braking law in Eq. 3.4. It has $P_{\rm i} = 1.109\,$d and needs 20.1 Gyr. The third model has no magnetic braking but only gravitational waves to lose angular momentum. It needs the shortest initial period (0.4998 d)

and longest evolution time (42 Gyr) to reach the desired minimum period.

The three models are compared in Fig. 3.7. The data are shown as a function of the total mass of the donor, starting with the onset of Roche-lobe overflow. Fig. 3.7a displays the orbital evolution of the three models. Due to loss of angular momentum, the orbital periods at the start of mass transfer are already significantly shorter than the periods P_i at the ZAMS. The model with the magnetic braking law of Eq. 3.3 has the longest orbital period at the onset of RLOF, but shrinks fast and coincides with the model without magnetic braking in the end. The dashed line of the model with the saturated magnetic braking from Eq. 3.4 intersects the solid line twice before the period minimum, indicating that braking starts out weaker, but ends stronger than the canonical magnetic braking of Eq. 3.3. This is clearly seen in Fig. 3.7b, where for each model two competing time scales are plotted: the time scale in which the mass transfer from the less massive to the more massive component would expand the orbit if it were the only process going on, and the timescale in which angular momentum loss (the sum of gravitational radiation and magnetic braking) would shrink the orbit if nothing else would happen. In order to obtain the timescale at which the orbital period changes (τ_P) due to angular momentum loss ($\dot{J}$), we use the fact that the total angular momentum of a binary scales with the cubed root of the orbital period ($J_{\rm orb} \propto P_{\rm orb}^{1/3}$) and thus

$$\tau_P \;=\; \frac{P_{\rm orb}}{\dot{P}_{\rm orb}} \;=\; \frac{P_{\rm orb}}{\frac{dP}{dJ}\,\dot{J}_{\rm orb}} \;=\; \frac{J_{\rm orb}}{3\,\dot{J}_{\rm orb}}. \tag{3.7}$$

To calculate τ_P due to angular momentum loss we substitute for $\dot{J}_{\rm orb}$ in Eq. 3.7 the sum of the angular momentum losses due to gravitational radiation and magnetic braking. The period derivative due to conservative mass transfer from star 1 to star 2, assuming no angular momentum loss, is given by:

$$\dot{P}_{\rm orb} \;=\; 3P_{\rm orb}\,\frac{M_1 - M_2}{M_1\,M_2}\,\dot{M}_1 \tag{3.8}$$

which can be substituted into Eq. 3.7 to get τ_P. Depending on which of the two timescales is shorter, the orbit will expand or shrink. At the period minimum, the two lines for each model intersect. The figure shows that the timescales for the model with the canonical magnetic braking and the model with gravitational radiation only coincide around the period minimum. This happens because at these short orbital periods the models with canonical braking have very weak magnetic braking due to their small masses and radii (see Eq. 3.3) and therefore gravitational wave emission dominates the orbital evolution. It can be clearly seen in the figure that the timescales for the model with saturated magnetic braking are almost two orders of magnitude shorter than for the two other models and the orbital evolution is driven by the strong magnetic braking. Figure 3.7c shows the true period derivatives of the three models, which could have been inferred from the difference between the lines in Fig. 3.7b. It shows clearly that the orbit changes fastest for the model with canonical magnetic braking in the first part of the evolution, but faster for the model with the saturated magnetic braking law when the donor mass drops below about 0.2 $M_\odot$. Interestingly, the

model with saturated magnetic braking is in the saturated regime during all of the evolution, so that the difference in strength comes from the different dependence on the mass and radius of the donor. The deep dips in Fig. 3.7c are the period minima where $\dot{P}$ changes sign. Figure 3.7 illustrates that the two magnetic braking prescriptions that we use work at completely different phases of the evolution of the model. The canonical braking model of Eq. 3.3 acts mainly in the first part of the mass transfer phase, well before the period minimum, up to the point where the orbital period has decreased enough for gravitational radiation to take over as the main angular momentum loss mechanism and evolve the orbit to the ultra-short period regime. The saturated magnetic braking prescription of Eq. 3.4 is only slightly stronger than the gravitational radiation in the first part of the evolution, but becomes orders of magnitude stronger at shorter orbital periods and evolves to the ultra-compact binary state without any significant contribution in the angular momentum loss from gravitational radiation. Despite these large differences, there is little influence on the outcome of our statistical study. We therefore conclude that our study is independent of the the details of the magnetic braking, and that the use of other theoretical or semi-empirical laws mentioned in Sect. 3.2 will lead to similar results.

3.6 Conclusions

In Chapter 2 we showed that for magnetic braking according to Verbunt & Zwaan (1981) the formation of ultra-short-period binaries via magnetic capture is possible, albeit very improbable, within the Hubble time. In this chapter we find that for less strong magnetic braking, in better agreement with recent observations of single stars, the formation of ultra-short-period binaries via magnetic capture is even less efficient. Specifically, for magnetic braking reduced to 25% of the standard prescription (according to Eq. 3.3), the shortest possible period is 23 min; for saturated magnetic braking (according to Eq. 3.4) the shortest possible period is essentially the same as without magnetic braking, about 70 min.

Loss of mass and associated angular momentum from the binary in general widens the orbit and thereby delays the formation of ultra-compact binaries. However, this effect is only noticeable in the absence of magnetic braking.

An attractive feature of the magnetic capture model is its ability to explain the negative period derivative of the 11-minute binary in the globular cluster NGC 6624 (Van der Klis et al. 1993b; Chou & Grindlay 2001). Since we find that for a more realistic magnetic braking law it is impossible to create ultra-compact binaries via magnetic capture at all, it becomes less likely that the negative period derivative is intrinsic. Van der Klis et al. (1993a) show that an apparent negative period derivative can be the result of acceleration of the binary in the cluster potential. According to measurements with the HST the projected position of the binary is very close to the cluster centre, which makes a significant contribution of gravitational acceleration to the observed period derivative more likely (King et al. 1993).

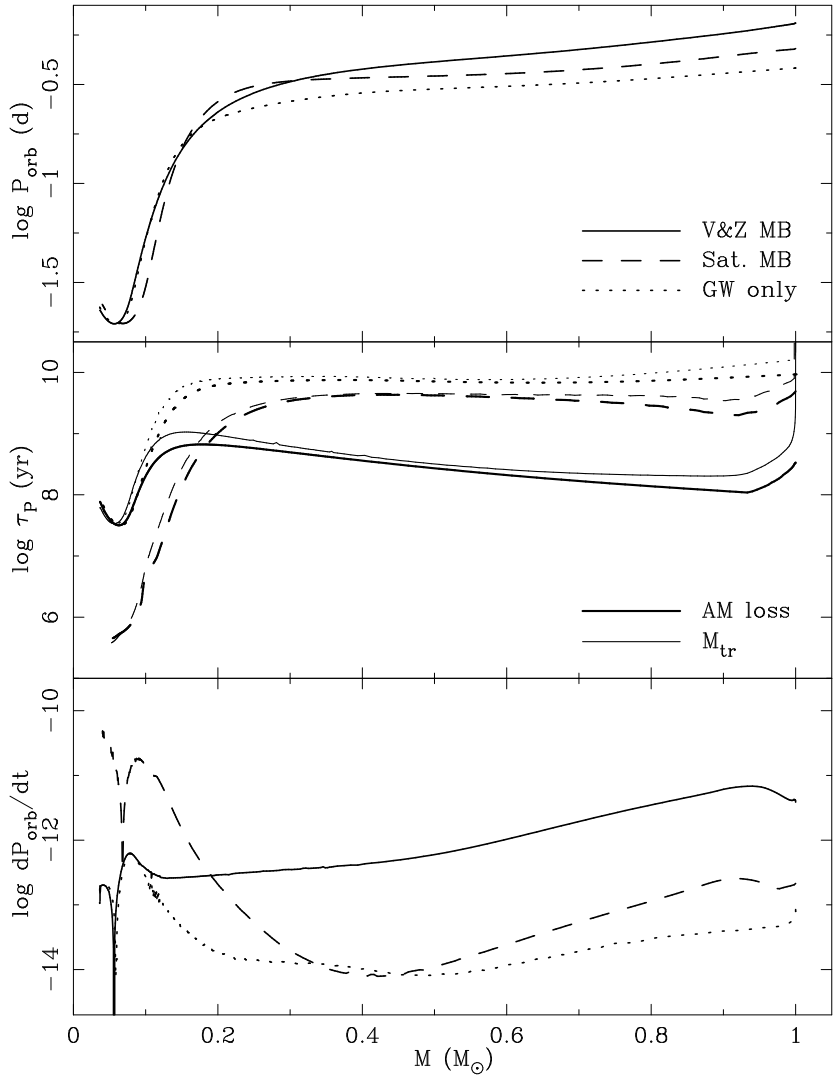

Figure 3.7: *Upper panel* (**a**): The logarithm of the orbital period. The line styles show the different models: with magnetic braking according to Eq. 3.3 (V&Z MB, solid line), with magnetic braking according to Eq. 3.4 (Sat. MB, dashed line) and without magnetic braking (GW only, dotted line). *Middle panel* (**b**): The logarithm of the timescales of orbital shrinkage due to angular momentum loss (AM loss, thick lines) and orbital expansion due to the mass transfer (M_{tr}, thin lines). The line styles represent the different models as in (a). *Lower panel* (**c**): The logarithm of (the absolute value of) the orbital period derivative in dimensionless units. The line styles are as in (a).

Chapter 4

On the possibility of a helium white dwarf donor in the presumed ultracompact binary 2S 0918–549

J.J.M. in 't Zand, A. Cumming, M.V. van der Sluys, F. Verbunt and O.R. Pols

Astronomy and Astrophysics, v.441, p.675–684 (2005)

Abstract 2S 0918–549 is a low-mass X-ray binary (LMXB) with a low optical to X-ray flux ratio. Probably it is an ultracompact binary with an orbital period shorter than 60 min. Such binaries cannot harbor hydrogen-rich donor stars. As with other (sometimes confirmed) ultracompact LMXBs, 2S 0918–549 is observed to have a high neon-to-oxygen abundance ratio (Juett et al. 2001) which has been used to argue that the companion star is a CO or ONe white dwarf. However, type-I X-ray bursts have been observed from several of these systems implying the presence of hydrogen or helium on the neutron star surface. In this chapter, we argue that the companion star in 2S 0918–549 is a helium white dwarf We first present a Type I X-ray burst from 2S 0918–549 with a long duration of 40 minutes. We show that this burst is naturally explained by accretion of pure helium at the inferred accretion rate of ~ 0.01 times the Eddington accretion rate. At higher accretion rates of ~ 0.1 Eddington, hydrogen is required to explain long duration bursts. However, at low rates the long duration is due to the large amount of helium that accumulates prior to the burst. We show that it is possible to form a helium white dwarf donor in an ultracompact binary if accretion starts during the first ascent of the giant branch, when the core is made of predominantly helium. Furthermore, this scenario naturally explains the high neon-to-oxygen ratio, without requiring a CO or ONe white dwarf companion. The only observational aspect of 2S 0918–549 that we cannot explain is the absence of helium lines in the optical spectrum. Model calculations of optical accretion disk spectra need to be carried out in order to obtain limits on the helium abundance.

4.1 Introduction

2S 0918–549 is a low-mass X-ray binary (LMXB) in which a Roche-lobe filling low-mass star orbits a neutron star and the liberation of gravitational energy of the in-falling matter produces X-rays. It is a particularly interesting example of a LMXB for three reasons. First, it has an optical to X-ray flux ratio which suggests that it is an ultracompact binary with an orbital period less than $\sim$60 min and a companion donor star that can only fit within the Roche lobe if it is hydrogen depleted (Juett et al. 2001, based on relations established by Van Paradijs & McClintock 1994). This was recently confirmed through optical spectroscopy which revealed the lack of lines from hydrogen and helium (Nelemans et al. 2004). It suggests that the companion star is a C-O or O-Ne white dwarf (cf., Nelson, Rappaport, & Joss 1986).

Second, it has an X-ray luminosity which is low for an active LMXB, namely less than or equal to 1% of the Eddington limit for a canonical (1.4 $M_{\odot}$, 10 km radius) neutron star (Jonker et al. 2001).

Third, 2S 0918–549 appears to have an unusually high Ne/O abundance ratio, a characteristic which it shares with three other non-pulsating LMXBs out of 56 cases investigated by Juett et al. (2001). Juett et al. propose that this is related to a degenerate donor in the suggested ultracompact nature of the binary. This proposition is supported by detections of orbital periods in two of the other three (18 min in 4U 1543–624, see Wang & Chakrabarty 2004; 21 min in 4U 1850–087, see Homer et al. 1996), although those detections need corroboration since they were made only once in each case. Recently, it was observed for two of these high Ne/O systems that the Ne/O ratio changed while for another previously not measured ultracompact system the Ne/O ratio was not high (Juett & Chakrabarty 2003, 2005). This indicates that the interpretation of Ne/O in terms of donor evolutionary status is less straightforward and is possibly biased by ionisation effects. For 2S 0918–549, nevertheless, the Ne/O ratio was found be consistently 2.4 times the solar value, as measured with ASCA, Chandra-LETGS and XMM-Newton observations, while the flux changed almost by an order of magnitude.

Three of the four LMXBs with a possibly high Ne/O-ratio exhibit sporadic type-I X-ray bursts which are due to thermonuclear flashes in the upper layers of a neutron star. Two have been reported from 4U 0614+09 (Swank et al. 1978; Brandt et al. 1992), four from 4U 1850–087 (Swank et al. 1976; Cominsky et al. 1977; Hoffman et al. 1980; Cominsky 1981) and three from 2S 0918–549 (Jonker et al. 2001; Cornelisse et al. 2002; Galloway et al. 2006). We here report four additional bursts from the latter. Additional bursts for the other systems were also detected, particularly with HETE-II (see for instance Nakagawa et al. 2004), but these are not published in detail yet. The one source never seen bursting is 4U 1543–624.

As noted by Juett & Chakrabarty (2003) and Nelemans et al. (2004), there is a puzzling contradiction between the characteristics (or mere presence) of these bursts and the suggested hydrogen or helium depletion in the donor stars. The bursts detected from these systems last between 10 and a few hundred seconds, suggesting a high hydrogen and helium

content in the flash fuel. The question is: where does the hydrogen and helium come from if not from the donor star? The problem is more severe for hydrogen than for helium because in an evolved donor star like in an ultracompact system the hydrogen can reside only in the outer layers that were lost being outside the Roche lobe. Juett et al. and Nelemans et al. suggest that spallation of accreted elements may be important (e.g., Bildsten, Salpeter, & Wasserman 1992). However, it is not trivial to invoke spallation. Spallation requires hydrogen nuclei (protons) to bombard the higher-up Coulomb-stopped heavy nuclei and create lighter elements, but the problem is that protons are in short supply. A definite assessment of the viability of this process needs to come from new calculations that also take into account non-radial accretion (e.g., Bildsten, Chang, & Paerels 2003) and high metal abundances.

In this chapter we present (in Sections 4.2 and 4.3) measurements of an extraordinary burst from 2S 0918–549 which was detected with the Wide Field Cameras (WFCs; Jager et al. 1997) on board BeppoSAX (Boella et al. 1997a). It is the longest of all bursts observed from any (presumed) ultracompact, lasting over half an hour. Commonly, long burst durations (for example, bursts from the regular burster GS 1826–24; Ubertini et al. 1999; Galloway et al. 2004) are explained by a high hydrogen fuel content. The protons are captured by the ashes of unstable helium burning and initiate a relatively slow beta decay process (the rp process) that is responsible for the burst longevity (e.g., Fujimoto et al. 1981). However, at the low accretion rate of $\sim$ 1% Eddington appropriate for 2S 0918–549, the conditions at the time of ignition of the flash are different. Because the fuel accumulates slowly, any hydrogen has time to stably burn away, leaving a thick layer of helium which ignites and burns in a long duration and energetic burst. In fact, given the likely ultracompact nature of this source, we argue that the long duration burst is due to accretion of pure helium from a helium white dwarf companion. As we show in section 4.5.1, 2S 0918–549 provides the rarely seen circumstances for a long duration helium flash to be possible, being a persistent X-ray source at a fairly low mass accretion rate. We investigate in section 4.5.2 evolutionary paths to arrive at the implied helium-rich donor star and find a likely path leading to a helium white dwarf. What is more, this star is predicted to have a Ne/O overabundance ratio which confirms the observations. Thus, a model in which the companion star is a helium white dwarf explains many peculiar details about 2S 0918–549. One detail which is not explained concerns the lack of helium lines in the optical spectrum.

4.2 Synopsis of X-ray bursts from 2S 0918–549

Thus far three X-ray bursts were reported from 2S 0918–549, Jonker et al. (2001), Cornelisse et al. (2002) and Galloway et al. (2006). The first two bursts have similar bolometric peak fluxes of 8.8 and 9.4×10^{-8} erg cm^{-2} s^{-1}, but the decay times differ by a factor of 3 (see Table 4.1). The third burst as identified by Galloway is an order of magnitude fainter. We carried out archival searches in BeppoSAX/WFC data (net exposure 9.2 Msec), RXTE/ASM (2.6 Msec for an effective exposure time of 70 s per dwell), and RXTE/PCA data ($\sim$300 ksec, including data from AO9), and found 2 more bursts in ASM and 2 in WFC data. No reports of bursts were made from observations with Einstein, EXOSAT, ROSAT,

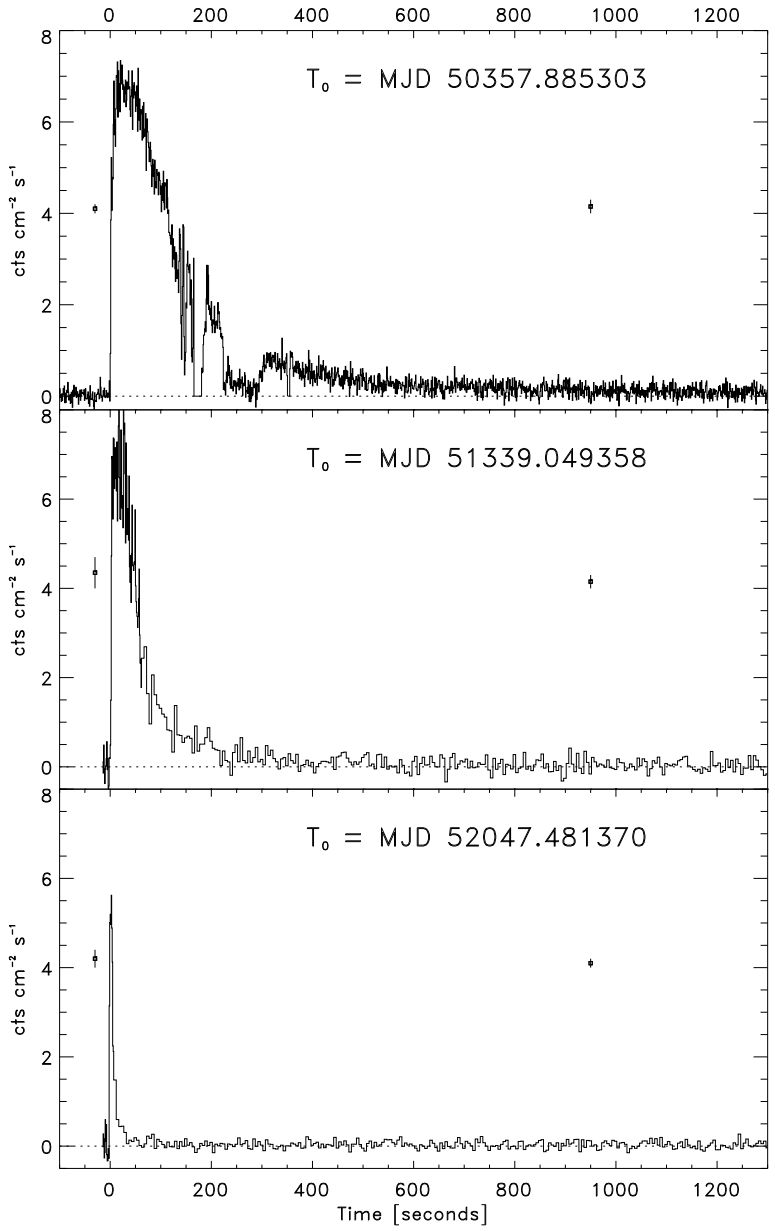

Figure 4.1: 2–28 keV light curves of the three WFC-detected bursts at varying time resolution. Typical error bars are indicated at the left and right of each panel.

No	Date	Instr.	Peak flux	Persistent flux (Crab units*)	τ (sec)
1	1996 Oct 1	WFC	3.7(3)	0.0048(5)	117(2)
2†	1999 Jun 10	WFC	3.3(3)	0.0037(5)	29(4)
3‡	2000 May 12	PCA	> 3.2	< 0.0146	8.95(5)
4	2001 May 18	WFC	2.5(3)	0.0094(5)	5.8(4)
5	2001 Sep 29	ASM	2.9(1)	0.0061(7)¶	25(3)
6	2003 Aug 5	ASM	2.1(1)	0.0080(8)¶	22(10)$^\times$
7*	2004 Jun 18	PCA	0.26(1)	0.0126(3)	12.5(5)

*For a burst peak spectrum as determined in this chapter for the first burst, one Crab unit translates to a bolometric flux of 2.7×10^{-8} erg cm^{-2} s^{-1}. For the persistent flux, one may adhere to a 2–10 keV flux of 2.0×10^{-8} erg cm^{-2} s^{-1} (the bolometric correction is less certain in that case).

†Cornelisse et al. (2002). This burst was erroneously dated four days earlier in that paper.

‡Jonker et al. (2001)

*Galloway et al. (2006) (this paper mentioned 2 more faint bursts from 2S 0918–549, but the data do not allow confirmation as type-I X-ray bursts

¶These are 14-d averages.

$^\times$This burst was only partly observed. The observation stopped 18 s after burst onset.

Table 4.1: List of X-ray bursts from 2S 0918–549. Bursts 2, 3 and 7 have been published before. Values between parentheses represent uncertainties in the last digit.

ASCA, BeppoSAX, Chandra and XMM-Newton within a total of approximately 170 ksec. We derive an average burst rate (from simple division of the exposure time by the number of bursts) of once every 20 days, but note that the WFCs and ASM are not sensitive enough to detect the fainter bursts. Based on PCA data alone, the average burst rate is once every 2 ± 1 d. Table 4.1 reports the main characteristics of all 7 bursts.

Except for the last, all bursts are fairly bright with bolometric peak fluxes that translate to between 6×10^{-8} and 10^{-7} erg cm^{-2} s^{-1}. Cornelisse et al. (2002), equalizing the peak flux of the second burst to the Eddington limit of a hydrogen-rich photosphere, derive a distance of 4.2 kpc with an uncertainty of 30%. This is in contrast to an earlier distance estimate, from optical measurements, of 15 kpc by Chevalier & Ilovaisky (1987) which is derived assuming the optical counterpart to be as luminous as in other LMXBs. Therefore, the counterpart must be considerably sub-luminous which is indicative of a small accretion disk and short orbital period of at most 60 min (Juett et al. 2001).

In Fig. 4.1 the three bursts detected with the WFC are plotted on identical scales. This illustrates the diversity of the bursts. In particular it illustrates the longevity of the first burst. In Fig. 4.2 the flux scale is blown up for this burst and it is clear that it persists for at least

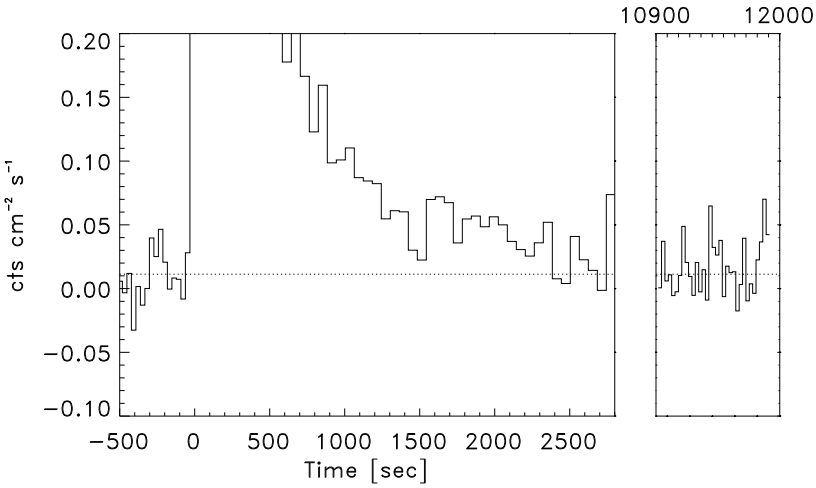

Figure 4.2: 2–28 keV light curve of the long burst, zooming in at low flux levels and with a time resolution of 30 s. The dotted line indicates the out-of-burst persistent flux level. There are no data during times between the two panels.

approximately 2500 s. The second burst lasts 10 times as short, the third burst nearly 100 times as short, the bright PCA-detected burst about 25 times (Jonker et al. 2001).

4.3 Analysis of the long burst

The long burst started on October 1, 1996, at 21:14:51 UT, rose to peak levels within 1 s and carried on for approximately 40 min before it disappeared in the background noise (at a level ≈350 times below the burst peak; see Fig. 4.2). The e-folding decay time over the first 200 s is 117 ± 2 s. This is the longest decay time of all 2427 type-I X-ray bursts measured with the WFCs that are not superbursts (In 't Zand et al. 2004a; Kuulkers 2004), except for one burst from SLX 1737–282 (In 't Zand et al. 2002) which exhibited a decay time of 600 s.

The off-axis angle of 2S 0918–549 in the WFC field of view during the long burst was near to optimum. The source illuminated 90% of the available sensitive detector area. However, the observation was plagued by high telemetry rates due to a bright source within the concurrent narrow-field instruments, which resulted in sporadic WFC data drop outs. Two drop outs occurred during the long X-ray burst, from 165 to 180 sec after burst onset and from 350 to 354 sec.

There are two more conspicuous features in the time profile of the long burst, see Fig. 4.3: two minutes after the burst onset a 30 s period of strong variability is observed, with dips and peaks that grow above the flux before that. Two minutes later the flux suddenly (within 2 s) decreases by a factor of about four. Subsequently it remains on a decay-

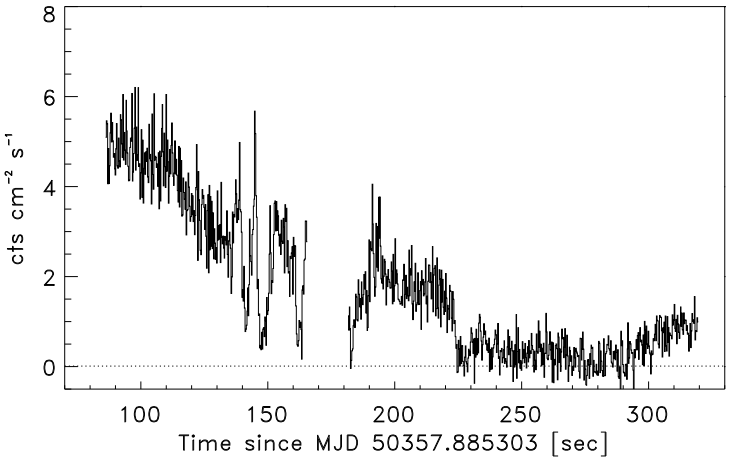

Figure 4.3: 2–28 keV light curve of the long burst, zooming in on the period of strong variability at a time resolution of 0.25 s.

ing track. After a little over 70 s it rises back to the extrapolated pre-drop downward trend and continues its decay. Since several data drop outs occurred during this observation we checked whether this drop in flux could be due to telemetry overflow. We studied the flux history of another bright source in the field of view, Vela X-1, and that of the remaining background. These showed no flux decrease whatsoever, in contrast to during the data drop out periods. We conclude that the flux decrease during the burst is genuinely associated with 2S 0918–549.

We modeled the spectrum of the long burst with black body radiation and present the results in Fig. 4.4. The burst starts with a strong photospheric radius expansion phase which ends after a few seconds. Subsequently the bolometric flux remains at a level of about 10^{-7} erg cm^{-2} s^{-1} for one minute during which the temperature rises and the radius shows a slow instead of fast decrease. This suggests that the photosphere is continuously injected with fresh (radiation) energy since the fall-back time of the atmosphere is much shorter. Thereafter the burst decays in an ordinary fashion for about 3 minutes with decreasing temperatures and constant radii. This suggests cooling by a fairly thick layer. Four minutes after the burst onset the flux suddenly (within 2 s) drops by a factor of 4. The flux remains low for 73 s after which it slowly rises during 20 s and resumes the pre-drop decay. The e-folding decay time then is 236 ± 11 s. The cause of the dip can be modeled in two ways: either through a variation of $N_{\rm H}$ ($\chi^2_\nu = 0.85$ for $\nu = 78$ for simultaneously fitting the 3 spectra of the dip [exposure time 71 s], the rise out of the dip [14 s], and a period afterwards [41 s]) or through a variation of the emission area ($\chi^2_\nu = 0.82$ for $\nu = 78$). Fig. 4.4 shows the results of the latter model. The implied reduction in emission area is a factor of 6 (or 2.5 in radius). When modeled through an increase of the absorption, the implied maximum column density is $N_{\rm H} = 8.3^{+2.9}_{-2.5} \times 10^{22}$ cm^{-2} (90% confidence; compare with

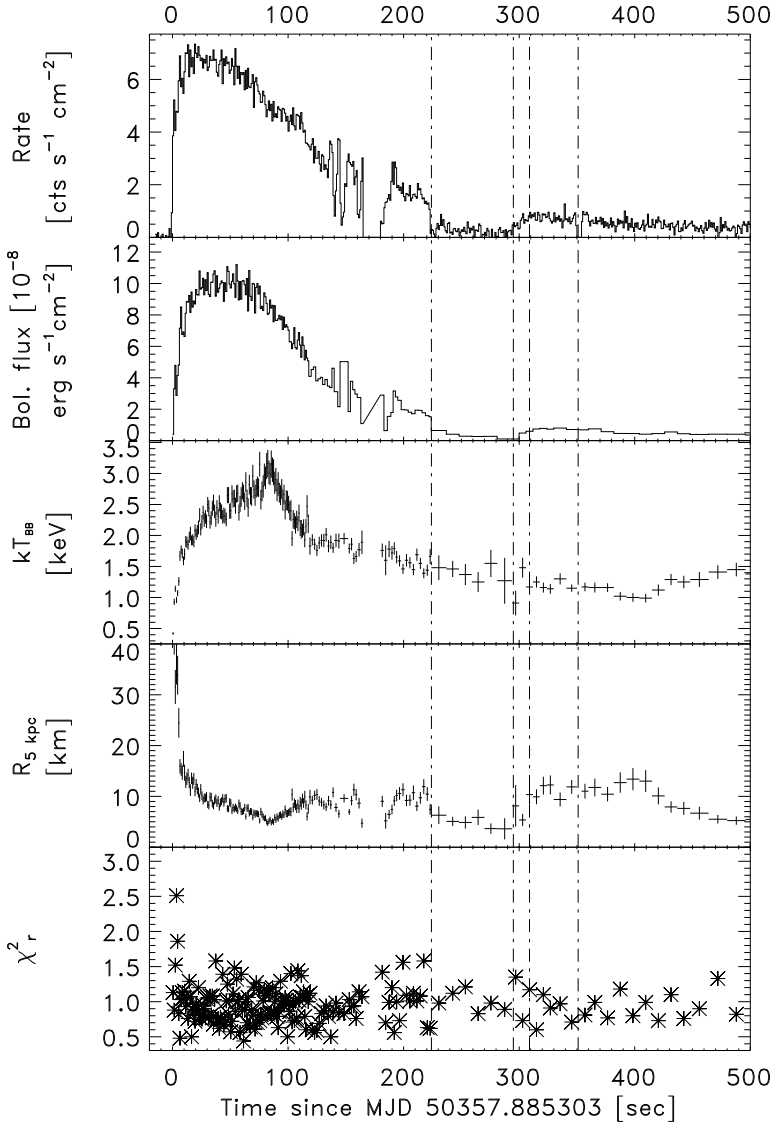

Figure 4.4: **a**): Time history of observed photon flux. **b**): Bolometric flux of modeled black body radiation. **c**): Colour temperature of black body radiation. **d**): Sphere-equivalent radius of bb radiation for a distance of 5 kpc (the first data point of 208 ± 25 km is outside the plot borders). **e**): χ^2_ν of fits. The vertical lines indicate time intervals for further spectroscopy of the dip (see Fig. 4.5).

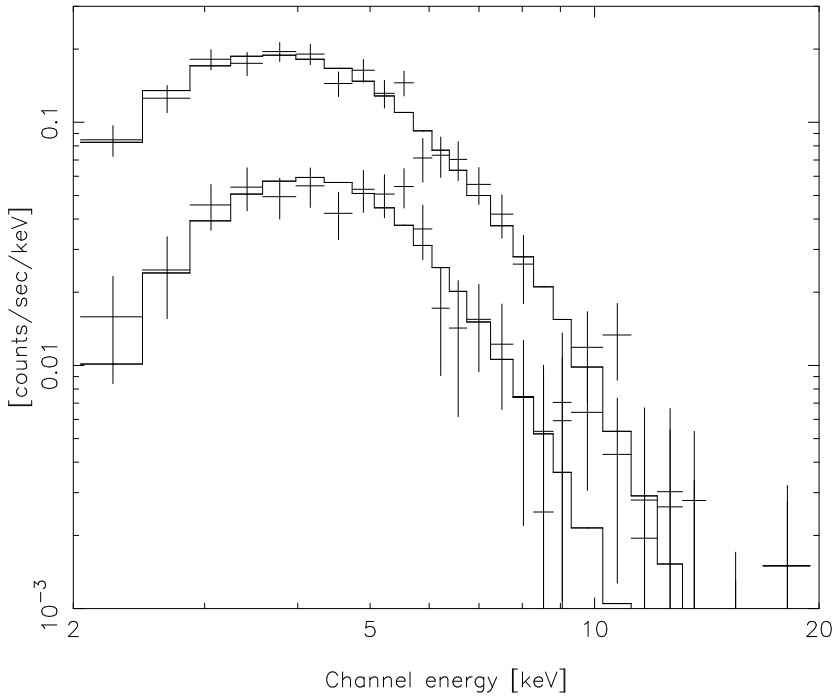

Figure 4.5: Spectra of the 71 s lower-flux interval (lower spectrum; first interval between vertical lines in Fig. 4.4) and the 41 s interval after the dip (upper spectrum; last interval in Fig. 4.4). The crosses indicate the measurements (vertical lengths indicate 1σ error intervals; histograms indicate the fitted model with free $N_{\rm H}$ and fixed radius).

$N_{\rm H} = 4.2 \times 10^{21}$ cm^{-2} outside the dip).

If one equalizes the peak bolometric flux to the Eddington limit of a canonical $1.4\,M_{\odot}$ neutron star, the implied distance is 4.1 kpc for a hydrogen-rich photosphere and 5.4 kpc if it is hydrogen-poor.

Ignoring the behavior of the source during the dip and data drop outs, the total bolometric energy output for a distance of 5.4 kpc is estimated to be $(0.9 \pm 0.4) \times 10^{41}$ erg. This is a factor of of at least 3 smaller than any of the 13 superbursts observed so far (cf, Kuulkers 2004; In 't Zand et al. 2004b) but similar to the most energetic non-super X-ray burst (from SLX 1737–282, In 't Zand et al. 2002).

What is the cause of the 1.2 min drop during the decay phase? The profile of the flux history looks strikingly similar to a partial eclipse. However, this is inconceivable because 1) the radiating surface is so small that a *partial* eclipse seems very unlikely, and 2) eclipses have never been seen in 2S 0918–549 down to very good limits (e.g., Juett & Chakrabarty 2003).

The effect looks a bit like the few-second long dip seen in the superburst from 4U 1820–303 (Strohmayer & Brown 2002). There it was attributed to the combination of photospheric radius expansion and a clean sweep of the normally X-radiating inner accretion disk. This explanation is inconsistent with the temperature evolution seen in 2S 0918–549. Still, it seems likely that the dip is related to a perhaps more moderate change in the accretion flow geometry induced by the radiation pressure of the luminous flash. An indication of that is provided by the strong variability in the minute before the dip.

4.4 Flux history of persistent emission

Given the wide variety of burst durations, it is of interest to test whether there is a connection with a varying mass accretion rate. Therefore, we studied data relating to the persistent flux history. 2S 0918–549 is quite faint for monitoring devices such as the WFC or the RXTE All-Sky Monitor (Levine et al. 1996). This hampers accurate measurements on time scales below a few weeks. In Fig. 4.6, the 2–12 keV flux history is plotted as measured with the RXTE ASM with a 14 d binning time. On that time scale the flux ranges between 0.3 and 1.0 ASM c s^{-1} which, for a Crab-like spectrum, translates to a 2–10 keV flux of $(1-3)\times 10^{-10}$ erg cm^{-2} s^{-1}. We note that no flares were observed on shorter time scales above a limit of roughly 0.1 Crab units, except for the bursts. In the same plot the times of the 7 bursts are indicated. The long (first) burst distinguishes itself from the other bursts by occurring during a somewhat tranquil low state of the source.

There has been one broad-band X-ray measurement of the source, by the BeppoSAX Narrow Field Instruments (Boella et al. 1997a) on 1998 April 22. Broad-band coverage was obtained through the Low-Energy Concentrator Spectrometer (LECS, Parmar et al. 1997, 0.1–3.0 keV, 16 ksec exposure time), the Medium Energy Concentrator Spectrometer (MECS, Boella et al. 1997b, 1.6–10.0 keV, 28 ksec) and the Phoswhich Detector System (PDS, Frontera et al. 1997, 15–200 keV, 12 ksec). The LECS and MECS provided imaging data, while the PDS operated with a collimator that rocked between on-source and background pointings 240′ from the source position. We verified that no bright X-ray source was contained in the background pointings.

We employed standard extraction and data analysis techniques (e.g., In 't Zand et al. 1999) and restricted further analysis to those photon energies where there is a significant detection (extending from 0.3 to 120 keV). The LECS and MECS extraction radii were 4′, a LECS/MECS and PDS/MECS normalization factor was left free during spectral fits, LECS and MECS background spectra were determined from independent long observations on empty fields, and no systematic uncertainty was included. Various models were tested against the data; two have a satisfactory result. These are presented in Table 4.2. The power-law fit is shown in Fig. 4.7. We tested a pure Comptonised model (model `comptt` in `XSPEC`, Arnaud 1996; Titarchuk 1994; Hua & Titarchuk 1995; Titarchuk & Lyubarskij 1995), and a simple power law. Both models were absorbed (following the model by Morrison & McCammon 1983) and a black body component was included describing the 0.7 keV feature discussed by Juett et al. (2001). The fit results are consistent with those obtained

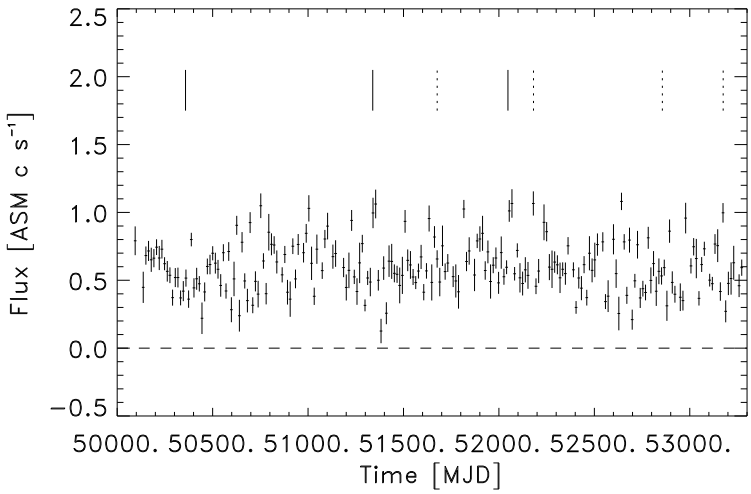

Figure 4.6: RXTE/ASM 2–12 keV light curve with bin time of 14 d and eliminating all data points from SSC3 and with an error in excess of 0.15 c s^{-1}. The vertical lines in the top indicate the times when bursts were detected (solid lines WFC, dashed lines RXTE PCA (1st and last) and ASM).

by Juett & Chakrabarty (2003). The (absorbed) 2–10 keV flux is consistent with the ASM measurements. The unabsorbed 0.1–200 keV flux is the same in both cases.

The 0.1–200 keV flux is of $(6.0 \pm 0.5) \times 10^{-10}$ erg cm^{-2} s^{-1} is less than 1% of the bolometric burst peak flux of $(1.0 \pm 0.1) \times 10^{-7}$ erg cm^{-2} s^{-1} which is thought to be the Eddington limit. For a distance of 4.1–5.4 kpc the 0.1–200 keV luminosity is $(1.2 - 2.1) \times 10^{36}$ erg s^{-1}. The ASM light curve suggests that the source never becomes brighter than roughly twice this value, on time scales of weeks. The 2–10 keV absorbed flux is also consistent with similar measurements since the 1970s as compiled by Juett & Chakrabarty (2003) which range between 0.9 and 2.7×10^{-10} erg cm^{-2} s^{-1}, except for an ASCA measurement on 1995 May 2 (MJD 49839; 17 months before the first burst) when the flux was 7.0×10^{-10} erg cm^{-2} s^{-1}. We note that an analysis of the near-to-continuous BATSE data set on 2S 0918–549 by Harmon et al. (2004) does not discuss a peak in 1995.

2S 0918–549 has never been seen in an off state, despite extensive coverage since the early 1970s. It is therefore not an X-ray transient. The reason that it is persistent while the luminosity is rather low is possibly related to the presumed ultracompact nature. A smaller orbit generally implies a smaller accretion disk. Therefore, the disk will remain completely photo-ionised at lower accretion rates and the accretion will sustain all the way to the neutron star rather than turn off due to an accretion disk instability (White et al. 1984;

Model	power law + black body
$N_{\rm H}$	$(3.1 \pm 0.3) \times 10^{21}$
bb kT	0.51 ± 0.03 keV
Γ	2.07 ± 0.05
χ^2_ν	1.21 (133 dof)
Unabs. 0.1–200 keV flux	$(6.4 \pm 0.5) \times 10^{-10}$ erg cm^{-2} s^{-1}
Abs. 2–10 keV flux	$(1.37 \pm 0.02) \times 10^{-10}$ erg cm^{-2} s^{-1}
Model	comptt + black body
$N_{\rm H}$	$(2.8 \pm 0.3) \times 10^{21}$
bb kT	0.51 ± 0.03 keV
$kT_{\rm plasma}$	34^{+110}_{-17} keV
τ (spherical geometry)	1 ± 0.5
$\chi^2_{\rm r}$	1.20 (131 dof)
Unabs. 0.1–200 keV flux	$(5.5 \pm 0.5) \times 10^{-10}$ erg cm^{-2} s^{-1}
Abs. 2–10 keV flux	$(1.37 \pm 0.02) \times 10^{-10}$ erg cm^{-2} s^{-1}

Table 4.2: Spectral parameters of acceptable model fits to the NFI spectrum. Γ is the photon index. Errors are for 90% confidence.

Van Paradijs 1996; Deloye & Bildsten 2003).

4.5 Discussion

4.5.1 Short and long helium bursts

In general, the longevity of an X-ray burst is determined by the duration of the nuclear burning, and by the thickness and composition (through thermal conductivity) of the layer where the burning deposits heat. Whereas helium and carbon burn very rapidly, hydrogen burning involves slow beta decays, and so can prolong the energy generation. Slow hydrogen burning via the rp-process (Wallace & Woosley 1981) is believed to power the minutes long tails of bursts from GS 1826–24 (Galloway et al. 2004). For accretion rates ~ 0.1 times Eddington, appropriate for most X-ray burst sources, this has led to the identification of "short" duration bursts (~ 10 s) with helium-dominated flashes, and long duration (~ 100 s) bursts with hydrogen-dominated flashes. In this picture, the long duration burst from 2S 0918–549 is difficult to explain because we expect the companion to be hydrogen deficient. However, at low accretion rates, long bursts can arise because of very thick fuel layers that accumulate between bursts. These thick layers have a long cooling time, leading to long burst durations. In this section, we show that the long burst from 2S 0918–549 is naturally explained by accretion of pure helium at the observed rate of 0.01 of the Eddington accretion rate.

The observed burst energy of $E_{\rm nuc} = 10^{41}$ ergs implies an ignition column depth of $y = E_{\rm nuc}(1+z)/4\pi R^2 Q_{\rm nuc} \approx 7 \times 10^9$ g cm^{-2}, where $Q_{\rm nuc} \approx 1.6$ MeV per nucleon

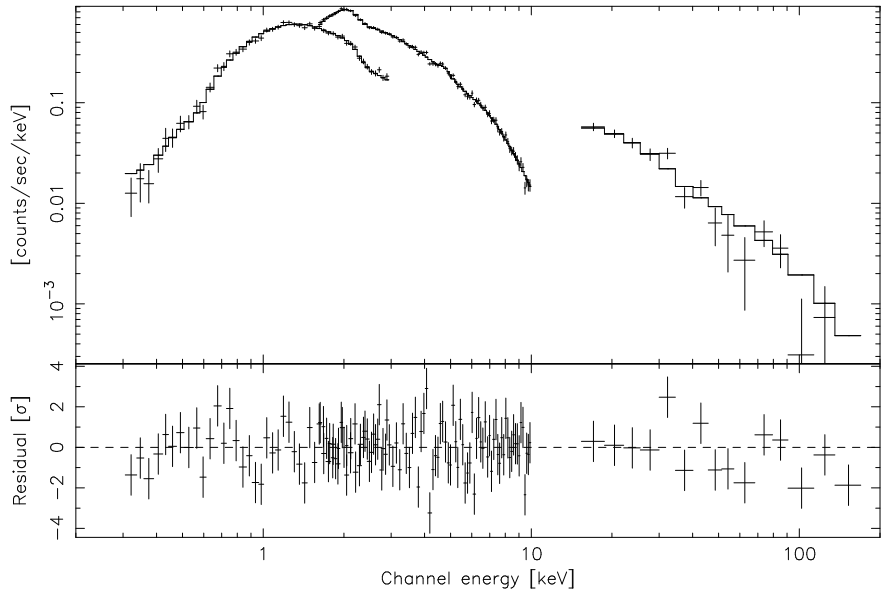

Figure 4.7: Top panel: from left to right LECS, MECS and PDS spectrum (crosses with vertical lines depicting 1σ error bars) and best fit result for power law and black body model (histogram). Bottom panel: fit residuals.

is the energy release for helium burning to iron group nuclei, R is the neutron star radius, and z is the gravitational redshift (we assume $R = 10$ km and $z = 0.31$, appropriate for a $1.4\,M_\odot$ neutron star). We have calculated the ignition depth for pure helium following the ignition calculations of Cumming & Bildsten (2000). The calculation involves finding the temperature profile of the accumulating fuel layer, and adjusting the layer thickness until the criterion for unstable ignition is met at the base. Since hydrogen burning is not active for pure helium accretion, the temperature profile of the layer is set by the heat flux emerging from the neutron star crust. We write this heat flux as $\dot{m}Q_b$ erg cm^{-2} s^{-1}, where $\dot{m}$ is the mass accretion rate per unit area, and Q_b is the energy per gram released in the crust by pycnonuclear reactions that flows outwards. For low $\dot{m}$, Brown (2000) found that almost all of the ≈ 1.4 MeV per nucleon released in the crust comes out through the surface[1] (see Fig. 11 of Brown 2000). For $Q_b \approx 1$ MeV per nucleon or $Q_b \approx 10^{18}$ erg g^{-1}, and using the Eddington accretion rate $\dot{m}_{\rm Edd} \approx 10^5$ g cm^{-2} s^{-1}, we find $F_b \approx 10^{21}$ erg cm^{-2} s^{-1} for accretion at $\dot{m} = 0.01\,\dot{m}_{\rm Edd}$. Figure 4.8 shows the ignition column depth and predicted burst energy as a function of base flux. For a base flux of 10^{21} erg cm^{-2} s^{-1}, we find an ignition column depth of $y \approx 10^{10}$ g cm^{-2}, in good agreement with the value inferred from

[1] We expect that the value of Q_b will depend on the thermal properties of the neutron star interior, for example, the core temperature and crust thermal conductivity. We will investigate the dependence of the ignition conditions on these factors in a future paper.

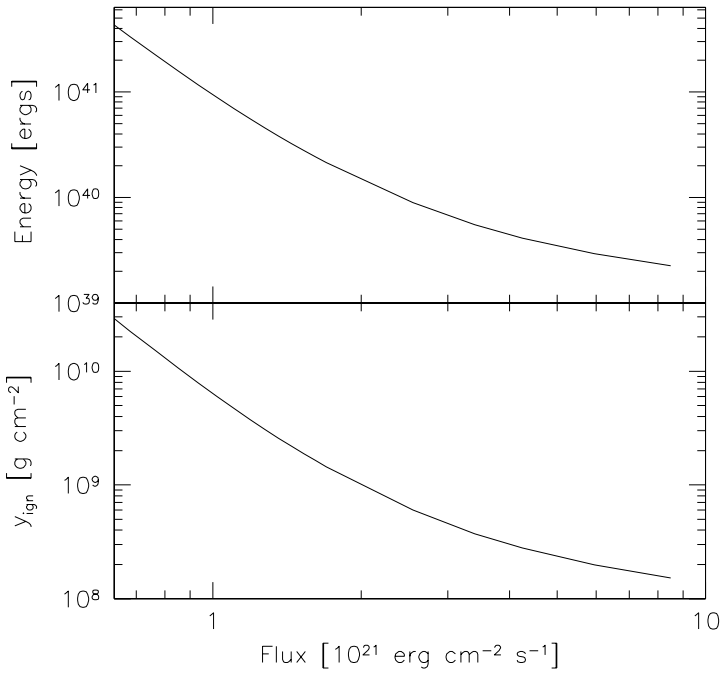

Figure 4.8: Ignition thicknesses and flash energies as a function of heat flux.

the burst energetics.

Additional constraints come from the burst light curve and the recurrence time. Figure 4.9 shows the observed light curve compared with theoretical cooling models calculated following Cumming & Macbeth (2004). In these models, the burning is assumed to take place instantaneously, since helium burning is extremely rapid. We then follow the cooling of the hot layer using a time-dependent thermal diffusion code. We show two curves with a total energy release of 10^{41} ergs, with column depths 7×10^9 and 10^{10} g cm^{-2}. The observed decay is well-reproduced by these models. Unfortunately, the recurrence time of the long burst is not well constrained by observations although the suggestion is that it is long. The expected recurrence time from the ignition models is $y/\dot{m} = 116$ days $(y/10^{10}$ g cm$^{-2})(\dot{m}/10^3$ g cm^{-2} s$^{-1})^{-1}$. 2S 0918–549 was almost continuously observed with the WFCs for 4 days prior to the burst, but there were two data gaps so that the lower limit to the recurrence time is only 1.1 days. In the 87.3 d period prior to

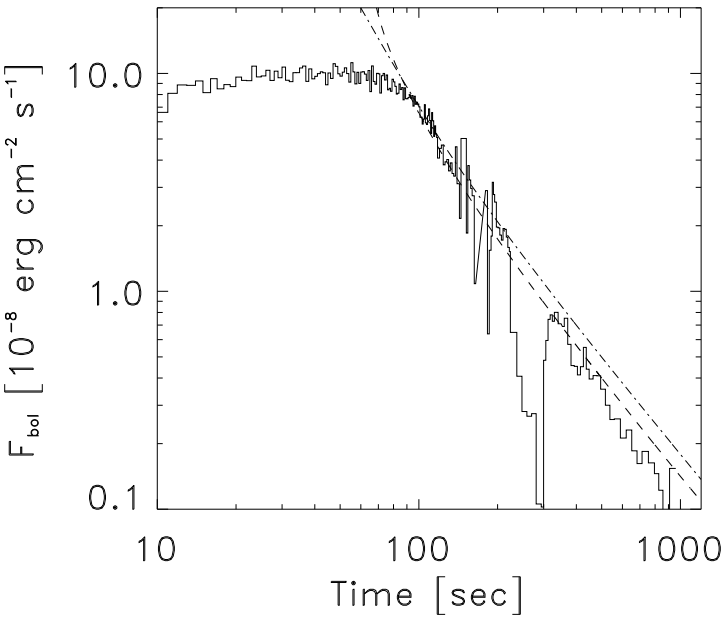

Figure 4.9: Comparison of the observed decay of the bolometric black body flux (histogram) with a theoretical model (Cumming & Macbeth 2004) for the cooling rate of a column of depth 7×10^9 g cm^{-2} and a nuclear energy release of 1.6×10^{18} erg g^{-1} which is expected for helium burning to iron (dashed curve). To illustrate the dependence on these two parameters a model is shown with the same energy output (10^{41} erg) but for a column depth of 1×10^{10} g cm^{-2} and an energy release of 1.0×10^{18} erg g^{-1} (dashed-dotted curve).

the long burst, 15.6 d of effective exposure time were collected with no burst detections. The only other X-ray experiment with coverage of 2S 0918–549 in 1996 is the All-Sky Monitor on RXTE, also without burst detections.

We have assumed that the accreted material is pure helium. If the accreted material contains carbon, carbon ignition is also possible. However, the burst energy in that case would be $\gg 10^{42}$ ergs, and recurrence time > 10 years (Cumming & Bildsten 2001). If hydrogen is included in the accreted material, additional heating arises because of CNO burning. Our steady-state accumulation models are only applicable if the temperature is large enough during accumulation ($\gtrsim 8\times10^7$ K) that the temperature-independent hot CNO cycle operates. Assuming this to be the case, we find that accretion of solar composition material at a rate 10^3 g cm^{-2} s^{-1} gives an ignition depth smaller than the pure helium case,

6×10^8 g cm^{-2}, and energy release $\approx 10^{40}$ ergs (in this model, only the upper 10% by mass of the layer contains hydrogen). In fact, depending on the accretion history, CNO burning may be much less than the hot CNO value. Narayan & Heyl (2003) calculate steady-state models with detailed CNO burning, and find ignition column depths of $\approx 3 \times 10^9$ g cm^{-2} for $\dot{m} = 0.01\ \dot{m}_{\rm Edd}$. Therefore, the burst properties may be similar to those observed if some hydrogen is present. However, we do not expect this because of the likely ultracompact nature of this source.

If the long burst is indeed a helium burst and the other bursts are as well, then the widely varying burst duration must be directly related to the layer thickness. The ignition condition predicts that the ignition thickness decreases with increasing temperature. This implies that the temperature increases from burst 1 to 4 and then decreases again. If the hot CNO cycle is not active, the heat flux from the core/crust and the composition of the outer 100 m of the NS determines the temperature (Brown et al. 2002). Since the time scale of variation of the crust temperature is expected to be much longer than the burst interval time (years rather than months), the suggestion is there that the composition of the layer changes between bursts. Given the limited accuracy of our measurements we are unable to test this quantitatively. Temperature variability of roughly a factor of 2 to 3 would be needed to explain a variety of burst durations of a factor of 10 to 100. The ASM data suggest that the accretion rate shows more variability during the six shorter bursts. Perhaps this explains the earlier ignition and presence of shorter (less energetic) bursts, much as was observed in KS 1731–260 by Cornelisse et al. (2003); Cornelisse (2004).

4.5.2 Evolutionary considerations

Since the surface layers of the donor are the source of the matter flowing through the accretion disk onto the neutron star, we may conclude that these surface layers are deficient in hydrogen (from the optical spectrum of the disk and the presumed ultracompact nature), do contain helium (from the X-ray bursts), and have an enhanced Ne/O abundance ratio (from the X-ray spectrum). This information is useful to discriminate between different evolutionary scenarios.

The evolutionary path of a binary in which a neutron star accretes matter from a companion depends to a large extent on the evolutionary state of the donor at the moment at which mass transfer starts. If mass transfer starts on the main sequence, the orbit shrinks to a minimum of around 70–80 min, and then expands again. At all times during the evolution, the transferred mass consists mainly of hydrogen. It has been suggested that strong magnetic braking may cause the orbit to shrink even if mass transfer is initiated after the donor has evolved a little beyond the terminal age main sequence (Tutukov et al. 1985). The decrease of the orbital period may then proceed to periods less than 70–80 min before the orbit expands again. Even though the hydrogen contents of the transferred mass drop at the shortest periods, the transferred mass is hydrogen rich throughout the evolution in this case also (see e.g. Tables 2.1 and 2.2). In Chapter 2 and 3 we showed that this path to ultrashort periods demands both very special initial conditions and very strong magnetic braking, and

thus is unlikely to be important.

If mass transfer starts during shell burning as the star ascends the giant branch, it will lead to long periods if the mass transfer is stable, and eventually to a wide binary of a neutron star an an undermassive white dwarf (e.g. Webbink et al. 1983). However, if the mass transfer is unstable, a spiral-in may ensue, and lead to a close binary of the core of the giant and the neutron star. Mass transfer is increasingly likely to be unstable if the donor star has higher mass, and is further evolved along the giant branch and hence its envelope is fully convective. The post-spiral-in close binary evolves to even shorter periods through loss of angular momentum via gravitational radiation, which may bring the core of the giant, by then cooled into a white dwarf, into contact with the Roche lobe, after which mass transfer starts again. If the spiral-in started with the donor in a phase of hydrogen shell burning, the white dwarf is a helium white dwarf. Donors in a phase of helium and carbon shell burning would lead to carbon-oxygen and neon-magnesium-oxygen white dwarfs, respectively. Mass transfer from the white dwarf to the neutron star is dynamically unstable if the white dwarf has a mass which is too high. The precise limit is somewhat uncertain, depending on the amount of mass and angular momentum loss, but is probably near 0.4–0.5 $M_\odot$ (see e.g. Yungelson et al. 2002). This limit excludes neon-magnesium-oxygen white dwarfs as well as the more massive carbon-oxygen white dwarfs. Only low-mass carbon-oxygen white dwarfs and helium white dwarfs are possible stable donors for a neutron star.

Mass transfer in a system with a white dwarf donor is a very strong function of the mass of the white dwarf. Immediately after contact, at a period on the order of a few minutes, the mass transfer is highly super-Eddington, and the white dwarf mass decreases rapidly. The orbit expands, and the donor mass decreases quickly until the binary has a mass transfer rate that is sufficiently low to be sustained for a longer period of time. The shortest orbital period observed for a system with a neutron star and white dwarf donor is 11 min. A rough estimate of the mass of the donor M as a function of orbital period P_b can be made by combining the mass-radius relation of a white dwarf with the equation giving the size of the Roche lobe for the less massive star in a binary: this gives $M/M_\odot \sim (50\,\mathrm{s}/P_b)$. Thus, the 11 min binary has a donor with mass less than $0.1 M_\odot$ (Verbunt 1987), and the other ultrashort period systems with known orbital periods have donors of smaller masses still. This implies that the composition of the mass being transferred to the neutron star in these binaries is that of the innermost material of the initial white dwarf.

We illustrate the compositions of the helium and carbon-oxygen white dwarfs by means of the core of a model star of 1.5 $M_\odot$ in Fig. 4.10 and Table 4.3. These compositions were computed with the evolution code of Eggleton (1971, 1972) with updated input physics as described in Pols et al. (1995). We do not expect mass loss to have any effect, because the profiles in the inner core have already been established by the time mass loss becomes important. Mass transfer from the white dwarf donor can cause its mantle to become convective, especially near and beyond the period minimum. However, since the core of the star is very homogeneous (Fig. 4.10), this has little influence on the surface abundances. The demand that the mass transferred in 2S 0918–549 contains helium is obviously compatible

with a donor consisting of the inner $\lesssim 0.1 M_\odot$ of an initial helium white dwarf; however, it is not compatible with a donor consisting of the inner $\lesssim 0.1 M_\odot$ of an initial carbon-oxygen white dwarf. As shown by Fig. 4.10 the helium content of the central mass of a carbon-oxygen white dwarf is zero (it is at the minimum allowed for computational stability in the evolution code, 10^{-12}). From this, one would have to conclude that the donor at the onset of mass transfer was a helium white dwarf, rather than a carbon-oxygen white dwarf.

This conclusion is strengthened when we consider the neon and oxygen abundances. In the helium core, the neon abundance is still at the zero-age main-sequence composition of the progenitor star, not affected by nuclear evolution (Fig. 4.10). The oxygen abundance, however, is lower in the helium core as oxygen is converted into nitrogen in the CNO cycle (Iben 1967). The depletion of oxygen is stronger in more massive progenitors, because the CNO cycle takes place at higher temperatures (see Table 4.4). Thus the Ne/O abundance ratio is predicted to be high if the donor in 2S 0918–549 consists of the central mass of a helium white dwarf. We point out that there is no observational evidence that the mass fraction of neon is enhanced since a complete measurement of the abundance of all expected elements, particularly helium and carbon, is lacking; only the abundance ratios Ne/O and Ne/Fe have been measured (Juett & Chakrabarty 2003). Neither is there conclusive observational evidence for an increased oxygen abundance, even when considering the optical spectrum which does suggest the presence of oxygen (and carbon) lines but with insufficient significance to prove the presence (Nelemans et al. 2004).

In a carbon-oxygen white dwarf both neon and oxygen are more abundant, but oxygen more so than neon (Fig. 4.10). The increase in neon abundance is caused by the conversion of ^{14}N, produced by the CNO cycle, into ^{22}Ne during core He-burning.[2] However, this is dwarfed by the production of oxygen by helium burning. The possibility exists, if the white dwarf has time to cool enough for crystallisation to take place, that ^{22}Ne settles in the centre (Yungelson et al. 2002) and reaches there the so-called azeotropic mass fraction, which is between 0.05 and 0.09 (Isern et al. 1991). This is not enough, however, to increase the Ne/O ratio above the solar value. Taking into account that the azeotropic Ne abundance may be underestimated by up to a factor three, the Ne/O ratio might be barely reconciled with the observed value, as noted by Yungelson et al. (2002). Nevertheless, if the donor in 2S 0918–549 consists of the central mass of a carbon-oxygen white dwarf the Ne/O abundance ratio is expected to be rather low. Conversely, the Ne/O ratio observed for 2S 0918–549 is naturally explained if its donor is the central mass of a helium white dwarf, rather than a carbon-oxygen white dwarf.

The helium core denuded by a spiral-in undergoes helium burning if its mass is higher than about $0.34\,M_\odot$ before it becomes degenerate, which will be the case for stars with initial mass higher than $2.25\,M_\odot$ (see Table 4.4). In this case a hybrid white dwarf may be formed, with a carbon-oxygen core and a helium mantle. When this white dwarf transfers mass to a neutron star, it will rapidly lose its helium mantle; at orbital periods in excess of

[2] The nuclear network in the evolution code does not follow the ^{22}Ne abundance directly, but instead the burnt ^{14}N is added to the ^{20}Ne abundance assuming particle number conservation (see Pols et al. 1995). The total neon mass fraction we find is therefore slightly underestimated.

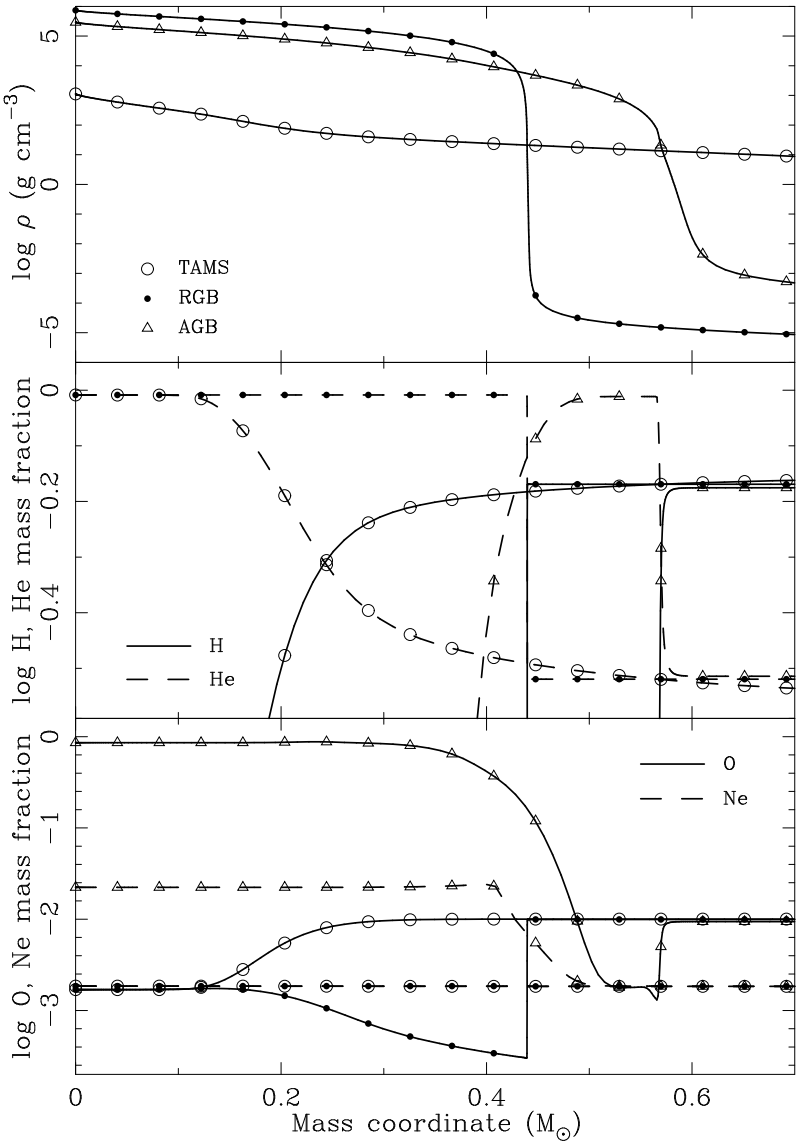

Figure 4.10: Three structure plots for different moments in the evolution of a 1.5 $M_\odot$ model. Only the central 0.7 $M_\odot$ is shown, as a function of the mass coordinate. *Upper panel* (**a**): Logarithm of the mass density. *Middle panel* (**b**): Logarithm of the hydrogen (solid lines) and helium (dashed lines) mass fraction. *Lower panel* (**c**): Logarithm of the oxygen (solid lines) and neon (dashed lines) mass fraction. The symbols on the lines indicate the model, as shown in the upper panel.

Model	Age	M_{He}	M_{CO}	$(Ne/O)_c$	$(Ne/O)_c/(Ne/O)_{in}$
TAMS	2.5949	0.166	0.000	1.093	5.97
RGB	2.8495	0.440	0.000	1.093	5.97
AGB	2.9852	0.568	0.379	0.0260	0.142

Table 4.3: Properties of the 1.5 $M_\odot$ model at the moments the structure plots of Fig. 4.10 were made. The age is in Gyr, the helium and carbon-oxygen core masses in $M_\odot$. The last two columns give the mass fraction ratio Ne/O in the core, and the ratio of this number to the initial (ZAMS or ISM) Ne/O ratio.

M	$M_{He-core}$	$(Ne/O)_c/(Ne/O)_{in}$	
		RGB	AGB
1.00	0.00 – 0.47	2.25	0.14
1.50	0.15 – 0.47	5.97	0.15
2.00	0.23 – 0.39	9.03	0.14
2.25	0.30 – 0.34	10.2	0.13
2.50	0.34 – 0.36	11.3	0.13
3.00	0.38 – 0.42	12.9	0.14
4.00	0.63 – 0.64	16.3	0.15
5.00	0.85 – 0.85	19.0	0.16

Table 4.4: Helium core masses and core abundances for model stars with masses between 1.0 and 5.0 $M_\odot$. The second column gives the range of helium core masses (in $M_\odot$) that are obtained between the formation of the core and core helium ignition. The third and fourth column give the Ne/O abundance of the core, relative to the initial (ISM) Ne/O abundance, for the helium core (RGB) and carbon-oxygen core (AGB) respectively.

11 min no helium is left.

Thus, a helium white dwarf is the most promising donor in the 2S 0918–549 system. Such a donor is formed when a star with initial mass less than 2.25 $M_\odot$ enters a spiral-in phase on its first ascent of the giant branch. Based on the work by Deloye & Bildsten (2003), the observed mass accretion rate predicts for a He WD donor an orbital period between 25 and 30 minutes. These results are in general agreement with calculations by Belczynski & Taam (2004) who predict that of all ultracompact binaries with a neutron star accretor, 60% may have a helium white dwarf donor. Furthermore, our calculations suggest that AM CVn systems, ultracompact binaries in which the accretor is a white dwarf, should show an enhanced Ne/O ratio if they have a helium white dwarf companion. Indeed, such an enhancement was recently observed in the AM CVn system GP Com (Strohmayer 2004).

4.6 Conclusion

In conclusion, we have shown that the properties of the long X-ray burst from 2S 0918–549 and the enhanced Ne/O abundance ratio are both consistent with the companion star being a helium white dwarf. This scenario would seem to be at odds with the presence of C and O lines and the absence of He lines in the optical spectrum. However, the evidence for C and O lines is inconclusive. Nelemans et al. (2004) find that the case is less clear for 2S 0918–549 than for 4U 0614+091 and 4U 1543–624 due to the relative faintness of the optical counterpart, and confirmation through deeper observations would be desirable. In addition, non-LTE effects may be important. This is the case in the UV, where Werner et al. (2004) calculated accretion disk models for the UV spectrum and found the He II 1640A line depth to be rather weak even for large helium abundances. Therefore, as yet we regard all X-ray and optical measurements of 2S 0918–549 to be consistent with a helium white dwarf donor star.

Acknowledgements We thank Ron Remillard for providing the high time-resolution data of the two bursts detected with the RXTE/ASM, and Lars Bildsten, Deepto Chakrabarty, Edward Brown, Duncan Galloway, Peter Jonker and Gijs Nelemans and for useful discussions. JZ acknowledges support from the Netherlands Organization for Scientific Research (NWO). AC acknowledges support from McGill University startup funds, an NSERC Discovery Grant, Le Fonds Québécois de la Recherche sur la Nature et les Technologies, and the Canadian Institute for Advanced Research. Gerrit Wiersma, Jaap Schuurmans, Nuovo Telespazio and the ASI Science Data Center are thanked for continued support.

Chapter 5

Modelling the formation of double white dwarfs

M.V. van der Sluys, F. Verbunt and O.R. Pols

Submitted to Astronomy and Astrophysics

Abstract We investigate the formation of the ten double-lined double white dwarfs that have been observed so far. A detailed stellar evolution code is used to calculate grids of single-star and binary models and we use these to reconstruct possible evolutionary scenarios. We apply various criteria to select the acceptable solutions from these scenarios. We confirm the conclusion of Nelemans et al. (2000) that formation via conservative mass transfer and a common envelope with spiral-in based on energy balance or via two such spiral-ins cannot explain the formation of all observed systems. We investigate three different prescriptions of envelope ejection due to dynamical mass loss with angular-momentum balance and show that they can explain the observed masses and orbital periods well. Next, we demand that the age difference of our model is comparable to the observed cooling-age difference and show that this puts a strong constraint on the model solutions. One of these solutions explains the DB-nature of the oldest white dwarf in PG 1115+116 along the evolutionary scenario proposed by Maxted et al. (2002a), in which the helium core of the primary becomes exposed due to envelope ejection, evolves into a giant phase and loses its hydrogen-rich outer layers.

5.1 Introduction

Ten double-lined spectroscopic binaries with two white-dwarf components are currently known. These binaries have been systematically searched for to find possible progenitor systems for Type Ia supernovae, for instance by the SPY (ESO SN Ia Progenitor surveY) project (*e.g.* Napiwotzki et al. 2001, 2002). Short-period double white dwarfs can lose orbital angular momentum by emitting gravitational radiation and if the total mass of the binary exceeds the Chandrasekhar limit, their eventual merger might produce a supernova of type Ia (Iben & Tutukov 1984).

The observed binary systems all have short orbital periods that, with one exception, range from an hour and a half to a day or two (see Table 5.1), corresponding to orbital separations between 0.6 $R_\odot$ and 7 $R_\odot$. The white-dwarf masses of 0.3 $M_\odot$ or more indicate that their progenitors were (sub)giants with radii of a few tens to a few hundred solar radii. This makes a significant orbital shrinkage (spiral-in) during the last mass-transfer phase necessary and fixes the mechanism for the last mass transfer to common-envelope evolution. In such an event the envelope of the secondary engulfs the oldest white dwarf due to dynamically-unstable mass transfer. Friction then causes the two white dwarfs to spiral in towards each other while the envelope is expelled. The orbital energy that is freed due to the spiral-in provides for the necessary energy for the expulsion (Webbink 1984).

The first mass transfer phase is usually thought to be either another spiral-in or stable and conservative mass transfer. The first scenario predicts that the orbit shrinks appreciably during the mass transfer whereas the second suggests a widening orbit. Combined with a core mass–radius relation (*e.g.* Refsdal & Weigert 1970) these scenarios suggest that the mass ratio $q_2 \equiv M_2/M_1$ of the double white dwarfs is much smaller than unity in the first scenario and larger than unity in the second scenario. The observed systems all have mass ratios between 0.70 and 1.28 (Table 5.1), which led Nelemans et al. (2000) to conclude that a third mechanism is necessary to explain the evolution of these systems. They suggested envelope ejection due to dynamical mass loss based on angular-momentum balance, in which little orbital shrinkage takes place. They used analytical approximations to reconstruct the evolution of three double white dwarfs and concluded that these three systems can only be modelled if this angular-momentum prescription is included.

In this chapter we will use the same method as Nelemans et al. (2000), to see if a stable-mass-transfer episode followed by a common envelope with spiral-in can explain the observed double white dwarfs. We will improve on their calculations in several respects. First, we extend the set of observed binaries from 3 to 10 systems. Second, we take into account progenitor masses for the white dwarf that was formed last up to $10\,M_\odot$ and allow them to evolve beyond core helium burning to the asymptotic giant branch. Nelemans et al. (2000) restricted themselves to progenitor masses of $2.3\,M_\odot$ or less and did not allow these stars to evolve past the helium flash. This was justified because the maximum white-dwarf mass that should be created by these progenitors was $0.47\,M_\odot$, the maximum helium-core mass of a low-mass star and less than the minimum mass for a CO white dwarf formed in a spiral-in (see Fig. 5.1). The most massive white dwarf in our sample is $0.71\,M_\odot$ and cannot

have been created by a low-mass star on the red-giant branch. Third, we use more sophisticated stellar models to reconstruct the evolution of the observed systems. This means that the radius of our model stars does not depend on the helium-core mass only, but also on total mass of the star (see Fig. 5.1). Furthermore, we can calculate the binding energy of the hydrogen envelope of our models so that we do not need the envelope-structure parameter $\lambda_{\rm env}$ and can calculate the common-envelope parameter $\alpha_{\rm ce}$ directly. Last, because we use a full binary-evolution code, we can accurately model the stable mass transfer rather than estimate the upper limit for the orbital period after such a mass-transfer phase. This places a strong constraint on the possible stable-mass-transfer solutions. The evolution code also takes into account the fact that the core mass of a donor star can grow appreciably during stable mass transfer, a fact that alters the relation between the white-dwarf mass and the radius of the progenitor mentioned earlier for the case of stable mass transfer.

Our research follows the lines of Nelemans et al. (2000), calculating the evolution of the systems in reverse order, from double white dwarf, via some intermediate system with one white dwarf, to the initial ZAMS binary. In Sect. 5.2 we list the observed systems that we try to model. The stellar evolution code that we use to calculate stellar models is described in Sect. 5.3. In Sect. 5.4 we present several grids of single-star models from which we will use the helium-core mass, stellar radius and envelope binding energy to calculate the evolution during a spiral-in. We show a grid of 'basic' models with standard parameters and describe the effect of chemical enrichment due to accretion and the wind mass loss. We find that these two effects may be neglected for our purpose. In Sect. 5.5 we use the single-star models to calculate spiral-in evolution for each observed binary and each model star in our grid and thus produce a set of progenitor binaries. Many of these systems can be rejected based on the values for the common-envelope parameter or orbital period. The remainder is a series of binaries consisting of a white dwarf and a giant star that would cause a common envelope with spiral-in and produce one of the observed double white dwarfs. In Sect. 5.6 we model the first mass-transfer scenario that produces the systems found in Sect. 5.5 to complete the evolution. We consider three possible mechanisms: stable and conservative mass transfer, a common envelope with spiral-in based on energy balance and envelope ejection based on angular-momentum balance. We introduce two variations in the latter mechanism and show that they can explain the observed binaries. In addition, we show that the envelope-ejection scenario based on angular-momentum balance can also explain the second mass-transfer episode. In Sect. 5.6.4 we include the observed age difference in the list of parameters our models should explain and find that this places a strong constraint on our selection criteria. In Sect. 5.7 we compare this study to earlier work and discuss an alternative formation scenario for PG 1115+116. Our conclusions are summed up in Sect. 5.8.

5.2 Observed double white dwarfs

At present, ten double-lined spectroscopic binaries consisting of two white dwarfs have been observed. The orbital periods of these systems are well determined. The fact that both components are detected makes it possible to constrain the mass ratio of the system from

the radial-velocity amplitudes. The masses of the components are usually determined by fitting white-dwarf atmosphere models to the observed effective temperature and surface gravity, using mass–radius relations for white dwarfs. The values thus obtained are clearly better for the brightest white dwarf but less well-constrained than the values for the period or mass ratio. It is also harder to estimate the errors on the derived mass. In the publications of these observations, the brightest white dwarf is usually denoted as 'star 1' or 'star A'. Age determinations suggest in most cases that the brightest component of these systems is the youngest white dwarf. These systems must have evolved through two mass-transfer episodes and the brightest white dwarf is likely to have formed from the originally less massive component of the initial binary (consisting of two ZAMS stars). We will call this star the secondary or 'star 2' throughout this chapter, whereas the primary or 'star 1' is the component that was the initially more massive star in the binary. The two components will carry these labels throughout their evolution, and therefore white dwarf 1 will be the oldest and usually the faintest and coldest of the two observed components. The properties of the ten double-lined white-dwarf systems are listed in Table 5.1. For our calculations we will use the parameters that are best determined from the Table: $P_{\rm orb}$, q_2 and M_2. For M_1 we will *not* use the value listed in Table 5.1, but the value M_2/q_2 instead. We hereby ignore the observational uncertainties in q_2, because they are small with respect to the uncertainties in the mass. In Sects. 5.5 and 5.6 we will use a typical value of $0.05\,M_\odot$ (Maxted et al. 2002b) for the uncertainties in the estimate of the secondary mass.

Although the cooling-age determinations are strongly dependent on the cooling model used, the thickness of the hydrogen layer on the surface and the occurrence of shell flashes, the cooling-age *difference* is thought to suffer less from systematic errors. The values for $\Delta\tau$ in Table 5.1 have an estimated uncertainty of 50% (Maxted et al. 2002b). The age determinations of the components of WD 1704+481a suggest that star 2 may be the oldest white dwarf, although the age difference is small in both absolute (20 Myr) and relative ($\approx 3\%$) sense (Maxted et al. 2002b). Because of this uncertainty we will introduce an eleventh system with a reversed mass ratio. This new system will be referred to as WD 1704+481b or 1704b and since we assume that the value for M_2 is better determined, we will use the following values for this system: $M_1 = 0.39\,M_\odot$, $q_2 = 1.43 \pm 0.06$ and $M_2 \equiv q_2 M_1 = 0.56\,M_\odot$.

5.3 The stellar evolution code

We calculate our models using the STARS binary stellar evolution code, originally developed by Eggleton (1971, 1972) and with updated input physics as described in Pols et al. (1995). Opacity tables are taken from OPAL (Iglesias et al. 1992), complemented with low-temperature opacities from Alexander & Ferguson (1994).

The equations for stellar structure and composition are solved implicitly and simultaneously, along with an adaptive mesh-spacing equation. Because of this, the code is quite stable numerically and relatively large timesteps can be taken. As a result of the large timesteps and because hydrostatic equilibrium is assumed, the code does not easily pick up short-time-scale instabilities such as thermal pulses. We can thus quickly evolve our models

Name	$P_{\rm orb}$ (d)	$a_{\rm orb}$ ($R_\odot$)	M_1 ($M_\odot$)	M_2 ($M_\odot$)	$q_2 = M_2/M_1$	τ_2 (Myr)	$\Delta\tau$ (Myr)	Ref/Note
WD 0135–052	1.556	5.63	0.52 ± 0.05	0.47 ± 0.05	0.90 ± 0.04	950	350	1,2
WD 0136+768	1.407	4.98	0.37	0.47	1.26 ± 0.03	150	450	3,10
WD 0957–666	0.061	0.58	0.32	0.37	1.13 ± 0.02	25	325	3,5,6,10
WD 1101+364	0.145	0.99	0.33	0.29	0.87 ± 0.03	135	215	4,(10)
PG 1115+116	30.09	40.0	0.7	0.7	0.84 ± 0.21	60	160	8,9
WD 1204+450	1.603	5.72	0.52	0.46	0.87 ± 0.03	40	80	6,10
WD 1349+144	2.209	6.65	0.44	0.44	1.26 ± 0.05	—	—	12
HE 1414–0848	0.518	2.93	0.55 ± 0.03	0.71 ± 0.03	1.28 ± 0.03	1000	200	11
WD 1704+481a	0.145	1.13	0.56 ± 0.07	0.39 ± 0.05	0.70 ± 0.03	725	-20	7,a
HE 2209–1444	0.277	1.89	0.58 ± 0.08	0.58 ± 0.03	1.00 ± 0.12	900	500	13

Table 5.1: Observed double white dwarfs discussed in this chapter. The table shows for each system the orbital period $P_{\rm orb}$, the orbital separation $a_{\rm orb}$, the masses M_1 and M_2, the mass ratio $q_2 = M_2/M_1$, the estimated cooling age of the youngest white dwarf τ_2 and the difference between the cooling ages of the components $\Delta\tau$. M_1 is the mass of the oldest white dwarf and thus presumably the original primary. The errors on the periods are smaller than the last digit. The values for $a_{\rm orb}$ are calculated by the authors and meant to give an indication. References: (1) Saffer et al. (1988), (2) Bergeron et al. (1989), (3) Bragaglia et al. (1990), (4) Marsh (1995), (5) Moran et al. (1997), (6) Moran et al. (1999), (7) Maxted et al. (2000), (8) Bergeron & Liebert (2002), (9) Maxted et al. (2002a), (10) Maxted et al. (2002b), (11) Napiwotzki et al. (2002), (12) Karl et al. (2003a), (13) Karl et al. (2003b). Note: (a) WD 1704+481a is the close pair of a hierarchical triple. It seems unclear which of the two stars in this pair is the youngest (see the text).

up the asymptotic giant branch (AGB), without having to calculate a number of pulses in detail. We thus assume that such a model is a good representation of an AGB star.

Convective mixing is modelled by a diffusion equation for each of the composition variables, and we assume a mixing-length to scale-height ratio $l/H_{\rm p} = 2.0$. Convective overshooting is taken into account as in Schröder et al. (1997), with a parameter $\delta_{\rm ov} = 0.12$ which corresponds to overshooting lengths of about 0.3 pressure scale heights ($H_{\rm p}$) and is calibrated against accurate stellar data from non-interacting binaries (Schröder et al. 1997; Pols et al. 1997). The code circumvents the helium flash in the degenerate core of a low-mass star by replacing the model at which the flash occurs by a model with the same total mass and core mass but a non-degenerate helium core in which helium was just ignited. The masses of the helium and carbon-oxygen cores are defined as the mass coordinates where the abundances of hydrogen and helium respectively become less than 10%. The binding energy of the hydrogen envelope of a model is calculated by integrating the sum of the internal and gravitational energy over the mass coordinate, from the helium-core mass $M_{\rm c}$ to the surface of the star $M_{\rm s}$:

$$U_{\rm b,e} = \int_{M_{\rm c}}^{M_{\rm s}} \left(U_{\rm int}(m) - \frac{Gm}{r(m)} \right) {\rm d}m \tag{5.1}$$

The term $U_{\rm int}$ is the internal energy per unit of mass, that contains terms such as the thermal energy and recombination energy of hydrogen and helium.

We use a version of the code (see Eggleton & Kiseleva-Eggleton 2002) that allows for non-conservative binary evolution. We use the code to calculate the evolution of both single stars and binaries in which both components are calculated in full detail. With the adaptive mesh, mass loss by stellar winds or by Roche-lobe overflow (RLOF) in a binary is simply accounted for in the boundary condition for the mass. The spin of the stars is neglected in the calculations and the spin-orbit interaction by tides is switched off. The initial composition of our model stars is similar to solar composition: $X = 0.70, Y = 0.28$ and $Z = 0.02$.

5.4 Giant branch models

As we have seen in Sect. 5.1, each of the double white dwarfs that are observed today must have formed in a common-envelope event that caused a spiral-in of the two degenerate stars and expelled the envelope of the secondary. The intermediate binary system that existed before this event, but after the first mass-transfer episode, consisted of the first white dwarf (formed from the original primary) and a giant-branch star (the secondary). This giant is thus the star that caused the common envelope and in order to determine the properties of the spiral-in that formed each of the observed systems, we need a series of giant-branch models. In this section we present a grid of models for single stars that evolve from the ZAMS to high up the asymptotic giant branch (AGB). For each time step we saved the total mass of the star, the radius, the helium-core mass and the binding energy of the hydrogen envelope of the star.

In an attempt to cover all possibilities, we need to take into account the effects that can change the quantities mentioned above. We consider the chemical enrichment of the secondary by accretion in a first mass-transfer phase and the effect a stellar-wind mass loss may have. For each of these changes, we compare the results to a grid of 'basic' models with default parameters. We keep the overshooting parameter $\delta_{\rm ov}$ constant for all these grids, because this effect is unimportant for low-mass stars ($M \lesssim 2.0\,M_\odot$) and its value is well calibrated for intermediate-mass stars (see Sect. 5.3).

5.4.1 Basic models

In order to find the influence of the effects mentioned above, we want to compare the models including these effects to a standard. We therefore calculated a grid of stellar models, from the zero-age main sequence to high up the asymptotic giant branch (AGB), with default values for all parameters. These models have solar composition and no wind mass loss. We calculated a grid of 199 single-star models with these parameters with masses between 0.80 and 10.0 $M_\odot$, with the logarithm of their masses evenly distributed. Model stars with masses lower than about 2.05 $M_\odot$ experience a degenerate core helium flash and are at that point replaced by a post-helium-flash model as described in Sect. 5.3. Because of the large timesteps the code can take, the models evolve beyond the point on the AGB where the carbon-oxygen core (CO-core) mass has caught up with the helium-core mass and the first thermal pulse should occur.

Figure 5.1 shows the radii of a selection of our grid models as a function of their helium-core masses. We used different line styles to mark different phases in the evolution of these stars, depending on their ability to fill their Roche lobes or cause a spiral-in and the type of star a common envelope would result in. The solid lines show the evolution up the first giant branch (FGB), where especially the low-mass stars expand much and could cause a common envelope with spiral-in, in which a helium white dwarf would be formed. Fig. 5.1a shows that low-mass stars briefly contract for core masses around 0.3 $M_\odot$. This is due to the first dredge-up, where the convective envelope deepens down to just above the hydrogen burning shell and increases the hydrogen abundance there. The contraction happens when the hydrogen-burning shell catches up with this composition discontinuity. After ignition of helium in the core, all stars shrink and during core helium burning and the first phase of helium fusion in a shell, their radii are smaller than at the tip of the FGB. This means that these stars could never start filling their Roche lobes in this stage. These parts of the evolution are plotted with dotted lines. Once a CO core is established, the stars evolve up the AGB and eventually get a radius that is larger than that on the FGB. The stars are now capable of filling their Roche lobes again and cause a common envelope with spiral-in. In such a case we assume that the whole helium core survives the spiral-in and that the helium burning shell will convert most of the helium to carbon and oxygen, eventually resulting in a CO white dwarf, probably with an atmosphere that consists of a mixture of hydrogen and helium. This part of the evolution is marked with dashed lines. Fig. 5.1b shows that the most massive models in our grid have a decreasing helium-core mass at some point

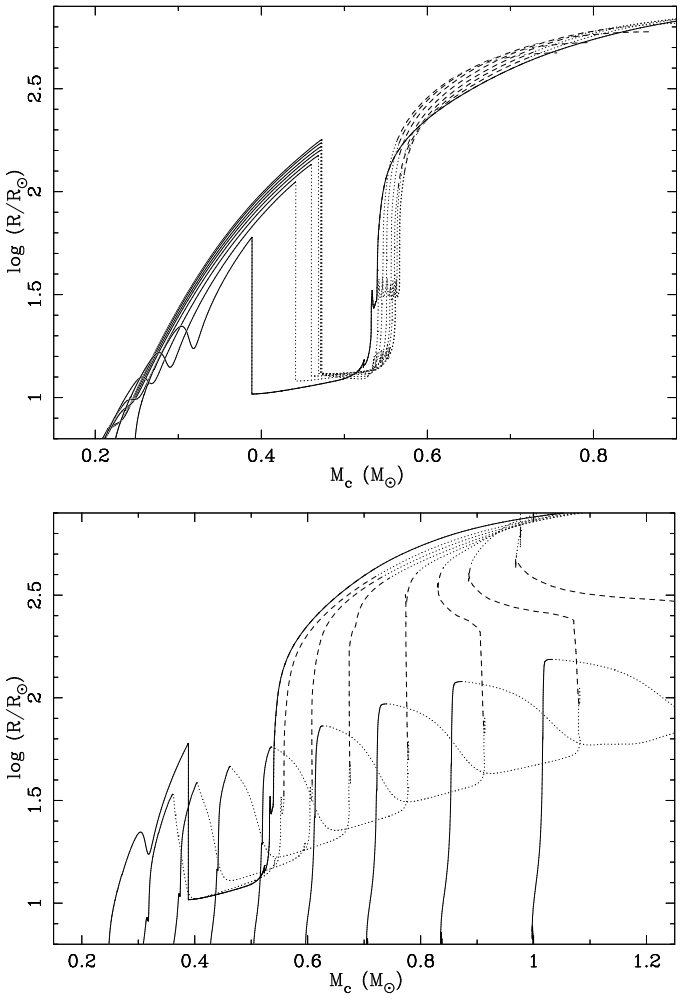

Figure 5.1: Core-mass–radius relations for the 'basic' models, as described in the text. The lines show the logarithm of the radius of the stars as a function of the helium-core mass. *Upper panel* (**a**): grid models with low masses: 0.91, 1.01, 1.14, 1.30, 1.48, 1.63, 1.81 and 2.00 $M_{\odot}$. *Lower panel* (**b**): grid models with high masses: 2.00, 2.46, 2.79, 3.17, 3.60, 4.09, 4.65, 5.28 and 6.00 $M_{\odot}$. The 2 $M_{\odot}$ model is plotted in both panels throughout as a solid line for easier comparison. The other models are shown as solid lines on the first giant branch (FGB), where they could cause a common envelope with a spiral-in and create a helium white dwarf. The dashed lines show the asymptotic giant branch (AGB), where a spiral-in would lead to the formation of a carbon-oxygen white dwarf. Dotted lines are parts of the evolution where the stars either are smaller than at the tip of the FGB (at lower radii) or where their envelope binding energies become positive on the AGB (at large radii).

on the AGB. This happens at the so-called second dredge-up, where the convective mantle extends inward, into the helium core and mixes some of the helium from the core into the mantle, thereby reducing the mass of the core. Models with masses between about 1.2 and 5.6 $M_\odot$ expand to such large radii that the binding energy of their hydrogen envelopes become positive. In Sect. 5.5 we are looking for models that can cause a spiral-in based on energy balance in the second mass-transfer phase, for which purpose we require stars that have hydrogen envelopes with a negative binding energy. A positive binding energy means that there is no orbital energy needed for the expulsion of the envelope and thus the orbit will not shrink during a common envelope caused by such a star. We have hereby implicitly assumed that the recombination energy is available during common-envelope ejection.

To give some idea what kind of binaries can cause a spiral-in and could be the progenitors of the observed double white dwarfs, we converted the radii of the stars displayed in Fig. 5.1 into orbital periods of the pre-common-envelope systems. To do this, we assumed that the Roche-lobe radius is equal to the radius of the model star, and that the mass of the companion is equal to the mass of the helium core of the model. This is justified by Table 5.1, where the geometric mean of the mass ratios is equal to 1.03. The result is shown in Fig. 5.2.

In Sect. 5.5 we will need the efficiency parameter $\alpha_{\rm ce}$ of each common-envelope model to judge whether that model is acceptable or not. In order to calculate this parameter we must know the binding energy of the hydrogen envelope of the progenitor star (see Eq. 5.4), that is provided by the evolution code as shown in Eq. 5.1. The envelope binding energy is therefore an important parameter and we show it for a selection of models in Fig. 5.3, again as a function of the helium-core mass. Because the binding energy is usually negative, we plot the logarithm of $-U_{\rm b,e}$. The phases where the envelope binding energy is non-negative are irrelevant for our calculations of $\alpha_{\rm ce}$ and therefore not shown in the Figure.

Many common-envelope calculations in the literature use the so-called envelope-structure parameter $\lambda_{\rm env}$ to estimate the envelope binding energy from basic stellar parameters in case a detailed model is not available

$$U_{\rm b,e} = -\frac{G\,M_*\,M_{\rm env}}{\lambda_{\rm env}\,R_*}. \tag{5.2}$$

De Kool et al. (1987) suggest that $\lambda_{\rm env} \approx 0.5$. Since we calculate the binding energy of the stellar envelope accurately, we can invert Eq. 5.2 and calculate $\lambda_{\rm env}$ (see also Dewi & Tauris 2000). Figure 5.4 shows the results of these calculations as a function of the helium core mass, for the same selection of models as in Fig. 5.3. We see that a value of $\lambda_{\rm env} = 0.5$ is a good approximation for the lower FGB of a low-mass star, or the FGB of a higher-mass star. A low-mass star near the tip of the first giant branch has a structure parameter between 0.5 and 1.5 and for most stars $\lambda_{\rm env}$ increases to more than unity rather quickly, especially when the stars expand to large radii and the binding energies come close to zero.

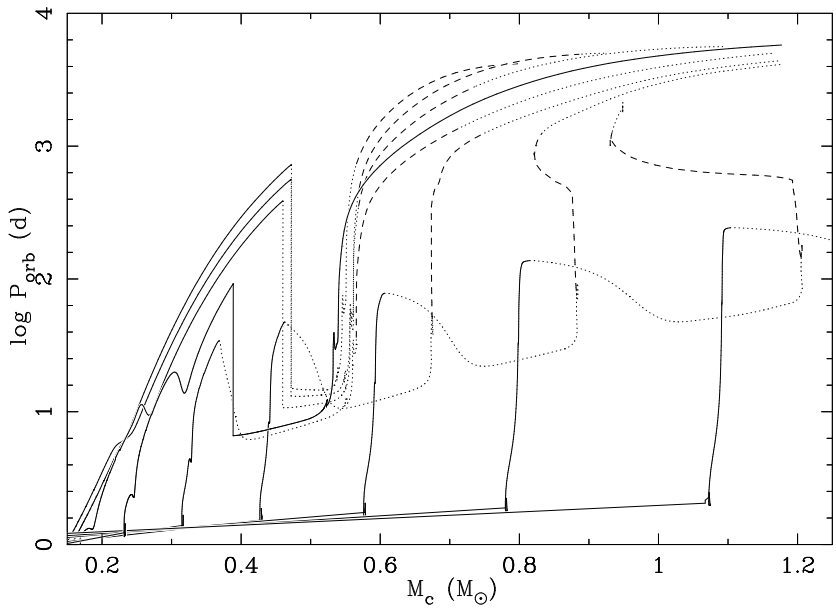

Figure 5.2: Helium-core-mass–orbital period tracks for the 'basic' models. The lines show the logarithm of the orbital period at which the Roche lobe is filled for grid models with masses of 1.01, 1.27, 1.59, 2.00, 2.52, 3.17, 3.99, 5.02 and 6.32 $M_\odot$. The period was obtained from the radius of the model star, under the assumption that it fills its Roche lobe and the companion has a mass equal to the helium-core mass of the model. This way, the system would undergo a spiral-in that would lead to a binary with mass ratio $q = 1$. The line styles have the same meaning as in Fig. 5.1.

5.4.2 Chemical enrichment by accretion

The secondary that causes the common envelope may have gained mass by accretion during the first mass-transfer phase. If this mass transfer was stable, the secondary has probably accreted much of the envelope of the primary star. The deepest layers of the envelope of the donor are usually enriched with nuclear burning products, brought up from the core by a dredge-up process. This way, the secondary may have been enriched with especially helium which, in sufficiently large quantities, can have an appreciable effect on the opacity in the envelope of the star and thus its radius. This would change the core-mass–radius relation of the star and the common envelope it causes.

To see whether this effect is significant, we considered a number of binary models that evolved through stable mass transfer to produce a white dwarf and a main-sequence secondary. The latter had a mass between 2 and 5 $M_\odot$ in the cases considered, of which 50–60% was accreted. We then took this secondary out of the binary and let it evolve up the asymptotic giant branch, to the point where the code picks up a shell instability and termi-

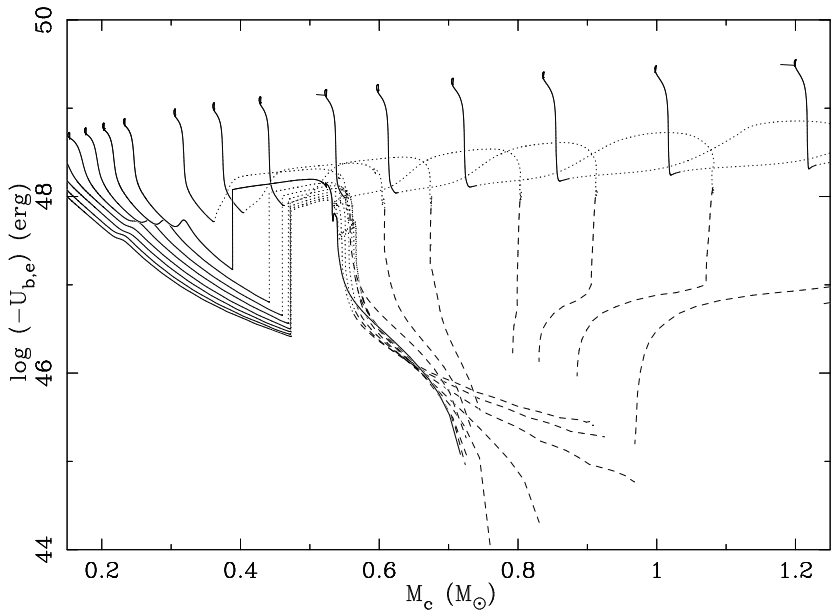

Figure 5.3: The logarithm of the binding energy of the 'basic' model stars as a function of the helium-core mass. The grid models with masses of 0.91, 1.01, 1.14, 1.30, 1.48, 1.63, 1.81, 2.00, 2.46, 2.79, 3.17, 3.70, 4.09, 4.65, 5.28, 6.00 and 6.82 $M_{\odot}$ are shown. The 2.00 $M_{\odot}$ model is drawn as a solid line, the line styles for the other models have the same meaning as in Fig. 5.1. The parts where the envelope binding energy is zero (before a helium core develops) or positive are not shown.

nates. We then compared this final model to a model of a single star with the same mass, but with solar composition, that was evolved to the same stage. In all cases the core mass–radius relations coincide with those in Fig. 5.1. When we compared the surface helium abundances of these models, after one or two dredge-ups, we found that although the abundances were enhanced appreciably since the ZAMS, they were enhanced with approximately the same amount and the relative difference of the helium abundance at the surface between the different models was always less than 1.5%. In some cases the model that had accreted from a companion had the lower surface helium abundance.

The small amount of helium enrichment due to accretion gives rise to such small changes in the core mass–radius relation, that we conclude that this effect can be ignored in our common-envelope calculations in Sect. 5.5.

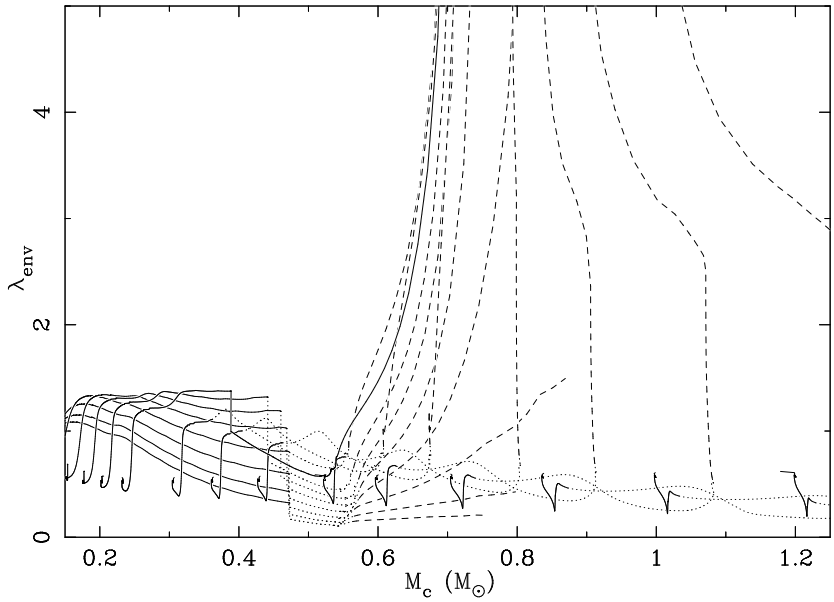

Figure 5.4: The envelope-structure parameter $\lambda_{\rm env}$ for the 'basic' models, as a function of the helium-core mass. The same grid models are shown as in Fig. 5.3. The meaning of the line styles is explained in the caption of Fig. 5.1.

5.4.3 Wind mass loss

The mass loss of a star by stellar wind can change the mass of a star appreciably before the onset of Roche-lobe overflow, and the mass loss can influence the relation between the core mass and the radius of a star. From Fig. 5.1 it is already clear that this relation depends on the total mass of the star. In this section, we would therefore like to find out whether a conservative model star of a certain total mass and core mass has the same radius and envelope binding energy as a model with the same total mass and core mass, but that started out as a more massive star, has a strong stellar wind and just passes by this mass on its evolution down to even lower masses. We calculated a small grid of models with ten different initial masses between 1.0 $M_\odot$ and 8.0 $\mathrm{M}_\odot$, evenly spread in $\log M$ and included a Reimers type mass loss (Reimers 1975) of variable strength:

$$\dot{M}_{\rm rml} \;=\; -4\times10^{-13}\,M_\odot\,{\rm yr}^{-1}\,C_{\rm rml}\,\left(\frac{L}{L_\odot}\right)\left(\frac{R}{R_\odot}\right)\left(\frac{M}{M_\odot}\right)^{-1}, \qquad (5.3)$$

where we have used the values $C_{\rm rml}$ = 0.2, 0.5 and 1.0. The basic models of Sect. 5.4.1 are conservative and therefore have $C_{\rm rml} = 0$. The effect of these winds on the total mass of the model stars in our grid is displayed in Fig. 5.5. It shows the fraction of mass lost at the tip of the first giant branch (FGB) and the 'tip of the asymptotic giant branch' (AGB). The first

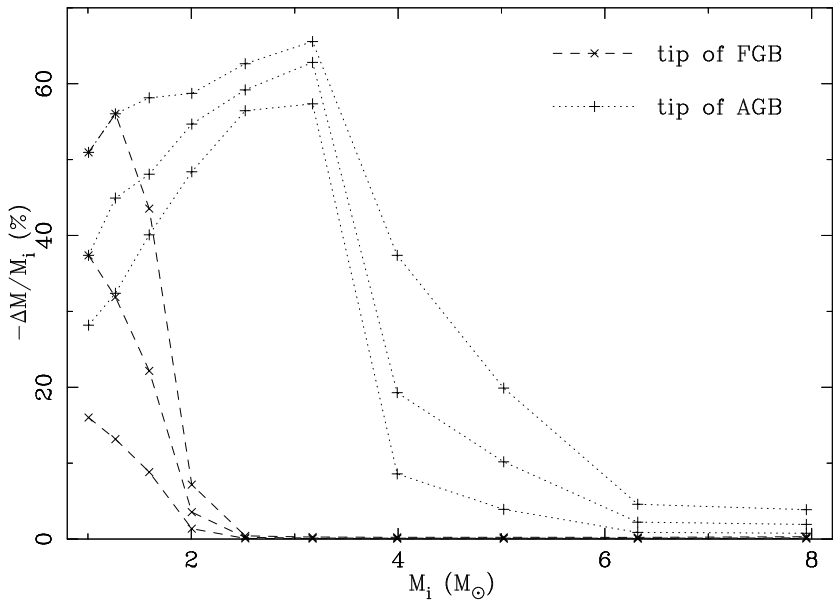

Figure 5.5: The fraction of mass lost at two moments in the evolution of a star as a function of its initial mass, for the three different wind strengths ($C_{\rm rml}$ = 0.2, 0.5 and 1.0) used in the grid. This fraction is shown for the tip of the FGB (dashed lines and crosses), and the 'tip of the AGB' (dotted lines and plusses). See the text for details.

moment is defined as the point where the star reaches its largest radius before helium ignites in the core, the second as the point where the radius of the star reaches its maximum value while the envelope binding energy is still negative. Values for both moments are plotted in Fig. 5.5 for each non-zero value of $C_{\rm rml}$ in the grid. For the two models with the lowest masses the highest mass-loss rates are so high that the total mass is reduced sufficiently on the FGB to keep the star from igniting helium in the core, and the lines in the plot coincide. Stars more massive than 2 $M_\odot$ have negligible mass loss on the FGB, because they have non-degenerate helium cores so that they do not ascend the FGB as far as stars of lower mass. Their radii and luminosities stay relatively small, so that Eq. 5.3 gives a low mass loss rate. For stars of 4 $M_\odot$ or more, the mass loss is diminutive and happens only shortly before the envelope binding energy becomes positive. We can conclude that for these stars the wind mass loss has little effect on the core mass–radius relation.

The core mass–radius relations for a selection of the models from our wind grid are shown in Fig. 5.6. The Figure compares models without stellar wind with models that have the strongest stellar wind in our grid ($C_{\rm rml} = 1.0$). Models with the other wind strengths would lie between those shown, but are not plotted for clarity. The greatest difference in Fig. 5.6 is in the 1.0 $M_\odot$ model. The heavy mass loss reduces the total mass of the star to

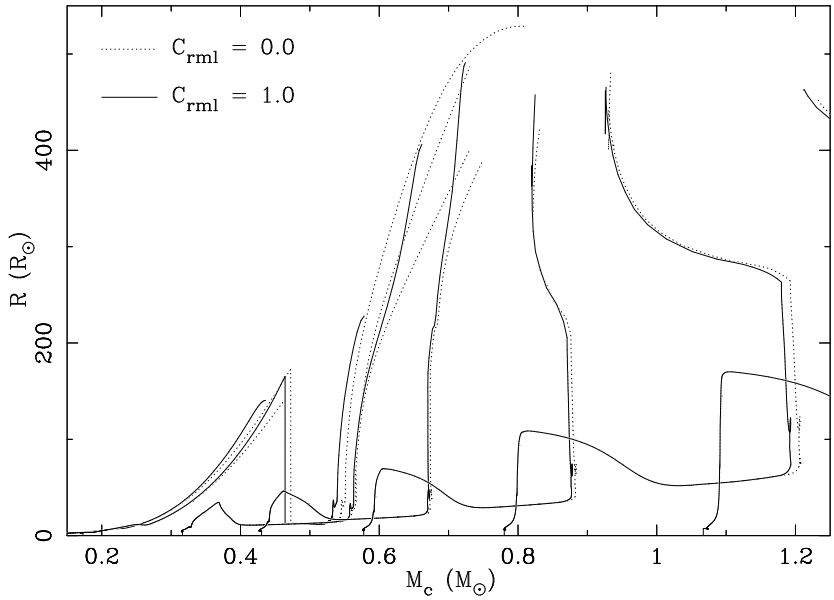

Figure 5.6: Comparison of a selection from the small grid of models with a stellar wind. The models displayed have masses of 1.0, 1.6, 2.5, 3.2, 4.0, 5.0 and 6.3 $M_\odot$. The wind strength parameters are $C_{\rm rml}$ = 0.0 (dotted lines) and $C_{\rm rml}$ = 1.0 (solid lines, the strongest mass loss in the grid). Stars with mass loss are usually larger, but for models of 4.0 $M_\odot$ or more this effect becomes negligible. The 1.0 $M_\odot$ model loses so much mass that it never ignites helium in the core.

0.49 $M_\odot$ on the first giant branch, so that the star is not massive enough to ignite helium in the core. Fig. 5.6 shows that models with mass loss are larger than conservative models for the same core mass, as one would expect from Fig. 5.1. This becomes clear on the FGB for stars that have degenerate helium cores, because they have large radii and luminosities and lose large amounts of mass there. For stars more massive than about 2 $M_\odot$ the mass loss becomes noticeable on the AGB. Stars of 4 $M_\odot$ or more show little difference in Fig. 5.6. The envelope binding energies have similar differences in the same mass regions.

The question is whether the properties of the model with reduced mass due to the wind are the same as those for a conservative model of that mass. In order to answer this question, we have compared the models from the 'wind grid' to the basic, conservative models. As the wind reduces the total mass of a model star, it usually reaches masses that are equal to that of several models in the conservative grid. As this happens, we interpolate linearly within the mass-losing model to find the exact moment where its mass equals the mass of the conservative model. We then use the helium-core mass of the interpolated mass-losing model to find the moment where the conservative model has the same core mass and we

calculate its radius and envelope binding energy, again by linear interpolation. This way we can compare the two models at the moment in evolution where they have the same total mass and the same core mass. This comparison is done in Fig. 5.7. Figure 5.7a directly compares the radii of the two sets of models, in Fig. 5.7b the ratio of the two radii is shown.

Of the data points in Fig. 5.7b 83% lie between 0.9 and 1.1 and 61% between 0.95 and 1.05. For the wind models with $C_{\rm rml} = 0.2$ these numbers are 99% and 97%, and for the models with $C_{\rm rml} = 0.5$ they are 94% and 85% respectively. As can be expected, the models that have a lower — and perhaps a more realistic — mass-loss rate compare better to the conservative models. We see in Fig. 5.7a that many of the points that lie farther from unity need only a small shift in core mass to give a perfect match. This shift is certainly less than $0.05\,M_\odot$, which is what we will adopt for the uncertainty of the white-dwarf masses in Sect. 5.5. We conclude here that there is sufficient agreement between a model that reaches a certain total mass because it suffers from mass loss and a conservative model of the same mass. The agreement is particularly good for stars high up on the FGB or AGB, where the density contrast between core and envelope is very large.

5.5 Second mass-transfer phase

For the formation of two white dwarfs in a close binary system, two phases of mass transfer must happen. We will call the binary system before the first mass transfer the *initial binary*, with masses and orbital period $M_{1\rm i}$, $M_{2\rm i}$ and $P_{\rm i}$. If one considers mass loss due to stellar wind before the first mass-transfer episode, these parameters are not necessarily equal to the ZAMS parameters, especially for large 'initial' periods. The binary between the two mass-transfer phases is referred to as the *intermediate binary* with $M_{1\rm m}$, $M_{2\rm m}$ and $P_{\rm m}$. After the two mass-transfer episodes, we obtain the *final binary* with parameters $M_{1\rm f}$, $M_{2\rm f}$ and $P_{\rm f}$, that should correspond to the values that are now observed and listed in Table 5.1. The subscripts '1' and '2' are used for the initial primary and secondary as defined in Sect. 5.2.

In the first mass transfer, the primary star fills its Roche lobe and loses mass, that may or may not be accreted by the secondary. This leads to the formation of the intermediate binary, that consists of the first white dwarf and a secondary of unknown mass. In the second mass-transfer phase, the secondary fills its Roche lobe and loses its envelope. The second mass transfer results in the observed double white dwarf binaries that are listed in Table 5.1 and must account for significant orbital shrinkage. This is because the youngest white dwarf must have been the core of its progenitor, the secondary in the intermediate binary. Stars with cores between 0.3 and 0.7 $M_\odot$ usually have radii of several tens to several hundreds of solar radii, and the orbital separation of the binaries they reside in must be even larger than that. The orbital separation of the observed systems is typically only in the order of a few solar radii (Table 5.1). Giant stars with large radii have deep convective envelopes and when such a star fills its Roche lobe, the ensuing mass transfer will be unstable and occur on a very short, dynamical timescale, especially if the donor is much more massive than its companion. It is thought that the envelope of such a star can engulf its companion and this event is referred to as a *common envelope*. The companion and the core of the donor orbit

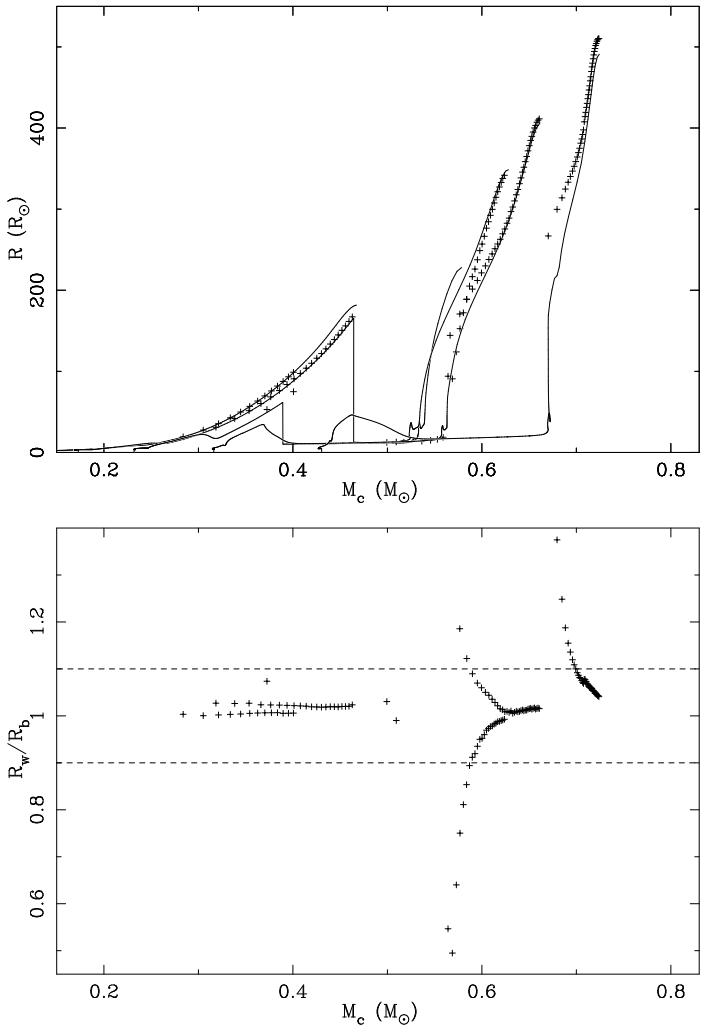

Figure 5.7: Comparison of a selection of grid models with $C_{\rm rml} = 1.0$ with initial masses of 1.3, 1.6, 2.0, 2.5 and 3.2 $M_\odot$ to the basic models ($C_{\rm rml} = 0.0$). *Upper panel* (**a**): Comparison of the radius of the models with a stellar wind (solid lines) and the radius of a basic model with the same mass and core mass (plusses). *Lower panel* (**b**): The fraction of the radius of the wind model $R_{\rm w}$ over the radius of the basic model $R_{\rm b}$ with the same total and core mass. Each data point corresponds to a point in the upper panel. Of the data points in the upper panel, 7 out of 143 (5%) lie outside the plot boundaries in the lower panel. The dashed lines show the region where agreement is better than 10%, where 83% of the data points lie. The 1.0 $M_\odot$ model was left out because there are only a few basic models with lower mass, the higher-mass models were left out because they lose very little mass (see Fig. 5.5).

inside the common envelope and drag forces will release energy from the orbit, causing the orbit to shrink and the two degenerate stars to spiral in. The freed orbital energy will heat the envelope and eventually expel it. This way, the hypothesis of the common envelope with spiral-in can phenomenologically explain the formation of close double-white-dwarf binaries.

5.5.1 The treatment of a spiral-in

In order to estimate the orbital separation of the post-common envelope system quantitatively, it is often assumed that the orbital energy of the system is decreased by an amount that is equal to the binding energy of the envelope of the donor star (Webbink 1984):

$$U_{\rm b,e} = -\alpha_{\rm ce}\left[\frac{GM_{\rm 1f}M_{\rm 2f}}{2a_{\rm f}} - \frac{GM_{\rm 1m}M_{\rm 2m}}{2a_{\rm m}}\right]. \tag{5.4}$$

The parameter $\alpha_{\rm ce}$ is the *common-envelope parameter* that expresses the efficiency by which the orbital energy is deposited in the envelope. Intuitively one would expect that $\alpha_{\rm ce} \approx 1$. However, part of the liberated orbital energy might be radiated away from the envelope during the process, without contributing to its expulsion, thereby lowering $\alpha_{\rm ce}$. Conversely, if the common-envelope phase would last long enough that the donor star can produce a significant amount of energy by nuclear fusion, or if energy is released by accretion on to the white dwarf, this energy will support the expulsion and thus increase $\alpha_{\rm ce}$.

In the forward calculation of a spiral-in the final orbital separation $a_{\rm f}$ depends strongly on the parameter $\alpha_{\rm ce}$, which must therefore be known. In this section we will try to establish the binary systems that were the possible progenitors of the observed double white dwarfs and we will therefore perform *backward* calculations. The advantage of this is that we start as close as possible to the observations thus introducing as little uncertainty as possible. The problem with this strategy is that we do not know the mass of the secondary progenitor beforehand. We will have to consider this mass as a free parameter and assume a range of possible values for it. The grid of single-star models of Sect. 5.4 provides us with the total mass, core mass, radius and envelope binding energy at every moment of evolution, for a range of total masses between 0.8 and 10 $M_\odot$. It is then not necessary to know the common-envelope parameter, and we can even calculate the $\alpha_{\rm ce}$ that is needed to shrink the orbit of a model with a given mass to the observed period of the double white dwarf from the binding energy. We make two assumptions about the evolution of the two stars during the common envelope to perform these backward calculations:

1. the core mass of the donor does not change,
2. the mass of the companion does not change.

The first assumption will be valid if the timescale on which the common envelope takes place is much shorter than the nuclear-evolution timescale of the giant donor. This is certainly true, since the mass transfer occurs on the dynamical timescale of the donor. The

second assumption is supported firstly by the fact that the companion is a white dwarf, a degenerate object that has a low Eddington accretion limit and is furthermore difficult to hit directly by a mass stream from the donor. The white dwarf could accrete matter in the Bondi-Hoyle fashion (Bondi & Hoyle 1944). This would not change the mass of the white dwarf significantly but could release appreciable amounts of energy. Secondly, a common envelope is established very shortly after the beginning of the mass transfer, so that the mass stream disappears and the white dwarf is orbiting inside the fast-expanding envelope rather than accreting mass from the donor. In the terminology used here, the second assumption can be written as $M_{1\mathrm{m}} = M_{1\mathrm{f}}$.

From the two assumptions above it follows that the mass of the second white dwarf, the one that is formed in the spiral-in, is equal to the helium-core mass of the donor at the moment it fills its Roche lobe. There is therefore a unique moment in the evolution of a given model star at which it could cause a common envelope with spiral-in and produce a white dwarf of the proper mass. Recall from Fig. 5.1b that although the second dredge-up reduces notably the helium-core mass of the more massive models in the grid, there is no overlap in core mass in the phases where the star could fill its Roche lobe on the first giant branch (solid lines) or asymptotic giant branch (dashed lines). The moment where the model star could produce a white dwarf of the desired mass in a common envelope with spiral-in is therefore defined by two conditions:

1. the helium-core mass of the model reaches the mass of the white dwarf,
2. the model star has its largest radius so far in its evolution.

The second restriction is necessary because stars can shrink appreciably during their evolution, as noted in Sect. 5.4.1. If the core of a model star obtains the desired mass at a point in the evolution where the star is smaller than it has been at some point in the past, then the star cannot fill its Roche lobe at the right moment to produce a white dwarf of the proper mass and therefore this star cannot be the progenitor of the white dwarf. This way, each model star has at most one moment in its evolution where it could fill its Roche lobe and produce the observed double white dwarf. If such a moment does not exist, the model star is rejected as a possible progenitor of the second white dwarf.

If the model star could be the progenitor of the youngest white dwarf in the observed system, the computer model gives us the radius of the donor star, that must be equal to the Roche-lobe radius. Under the assumption that the mass of the first white dwarf does not change in the common envelope, the mass ratio of the two stars $q_{2\mathrm{m}} \equiv M_{2\mathrm{m}}/M_{1\mathrm{m}}$ and the Roche-lobe radius of the secondary star R_{Rl2m} give us the orbital separation before the spiral-in a_{m}, where we use the fit by Eggleton (1983)

$$R_{\mathrm{Rl2m}} \;=\; a_{\mathrm{m}}\,\frac{0.49\,q_{2\mathrm{m}}^{2/3}}{0.6\,q_{2\mathrm{m}}^{2/3}+\ln\left(1+q_{2\mathrm{m}}^{1/3}\right)}, \quad 0<q_{2\mathrm{m}}<\infty. \tag{5.5}$$

Kepler's law finally provides us with the orbital period P_{m} of the intermediate system. The stellar model also gives the binding energy of the envelope of the donor $U_{\mathrm{b,e}}$ at the onset of

the common envelope and we can use Eq. 5.4 to determine the common-envelope parameter $\alpha_{\rm ce}$. We will use $\alpha_{\rm ce}$ to judge the validity of the model star to be the progenitor of the second white dwarf. There are several reasons why a numerical solution can be rejected. Firstly, the proposed donor could be a massive star with a relatively small radius. Then $a_{\rm m}$ will be small and it might happen that $a_{\rm m} < a_{\rm f} \frac{M_{2\rm m}}{M_{2\rm f}}$, so that $\alpha_{\rm ce} < 0$. This means that energy is needed to change the orbit from $a_{\rm m}$ to $a_{\rm f}$, or even that $a_{\rm m} < a_{\rm f}$ and a spiral-in (if it can be called that) to the desired orbit will not lead to expulsion of the common envelope. Secondly, as mentioned above, $\alpha_{\rm ce}$ is expected to be close, though not necessarily equal, to unity. However if the parameter is either much smaller or much larger than 1, we will consider the spiral-in to be 'physically unbelievable'. We arbitrarily chose the boundaries between which $\alpha_{\rm ce}$ must lie for a believable spiral-in to be a factor of ten either way: $0.1 \leq \alpha_{\rm ce} \leq 10$. We think that the actual value for $\alpha_{\rm ce}$ should be more constrained than that because common-envelope evolution is thought to last only a short time so that there is little time to generate or radiate large amounts of energy, but keep the range as broad as it is to be certain that all possible progenitor systems are considered in our sample.

5.5.2 Results of the spiral-in calculations

We will now apply the stellar models of Sect. 5.4.1 as described in the previous section to calculate potential progenitors to the observed double white dwarfs as listed in Table 5.1. As input parameters we took the values $P_{\rm f} = P_{\rm orb}$ and $M_{2\rm f} = M_2$ from the table, and assumed that $M_{1\rm f} \equiv M_2/q_2$, where q_2 is the observed mass ratio listed in Table 5.1. We thus ignore for the moment any uncertainty in the observed masses. Figure 5.8 shows the orbital period $P_{\rm m}$ as a function of the secondary mass $M_{2\rm m}$. Each symbol is a solution to the spiral-in calculations and represents an intermediate binary system that consists of the first white dwarf of mass $M_{1\rm m} = M_{1\rm f}$, a companion of mass $M_{2\rm m}$ and an orbital period $P_{\rm m}$. The secondary of this system will fill its Roche lobe at the moment when its helium-core mass is equal to the mass of the observed white dwarf $M_{2\rm f}$, and can thus produce the observed double-white-dwarf system with a common-envelope parameter that lies between 0.1 and 10.

The solutions for each system in Fig. 5.8 seem to lie on curves that roughly run from long orbital periods for low-mass donors to short periods for higher-mass secondaries. This is to be expected, partially because higher-mass stars have smaller radii at a certain core mass than stars of lower mass (see Fig. 5.1) and thus fill their Roche lobes at shorter orbital periods, but mainly because the orbital period of a Roche-lobe filling star falls off approximately with the square root of its mass. The Figure also shows gaps between the solutions, for instance for WD 0957–666 and WD 1704+481a, between progenitor masses $M_{2\rm m}$ of about 2 and 2.5 $M_\odot$. These gaps arise because the low-mass donors on the left side of the gap ignite helium degenerately when the core mass is $0.47\,M_\odot$, after which the star shrinks, whereas for stars with masses close to $2\,M_\odot$ helium ignition is non-degenerate and occurs at lower core masses, reaching a minimum for stars with a mass of $2.05\,M_\odot$, where helium ignition occurs when the helium-core mass amounts to $0.33\,M_\odot$ (see Fig. 5.1). Thus, for

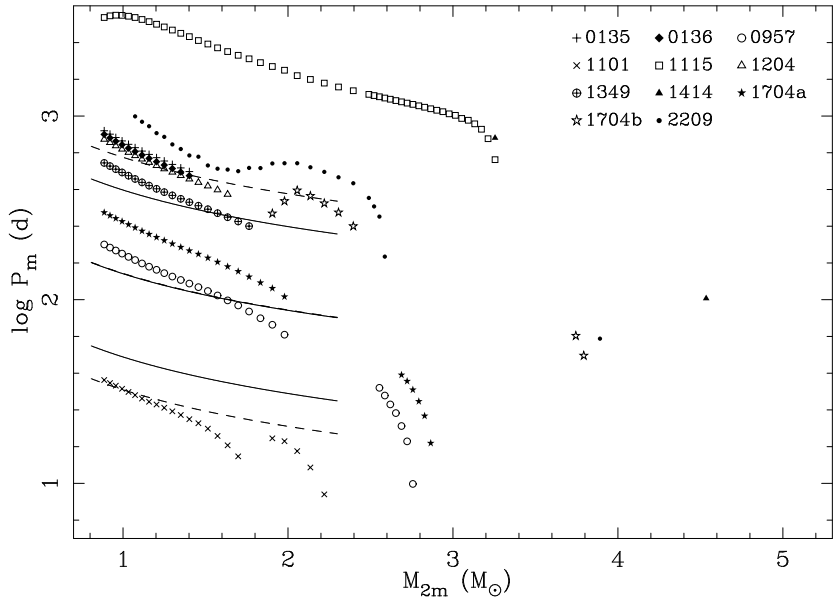

Figure 5.8: Results of the spiral-in calculations, each individual symbol is a solution of the calculations and thus represents one pre-CE binary. The figure shows the logarithm of the orbital period of the intermediate binary $P_{\rm m}$ as a function of the secondary mass $M_{2\rm m}$. Different symbols represent different observed systems, as explained in the legend. System 1704a is the system listed in Table 5.1, 1704b is the same system, but with the reverse mass ratio. For solutions with $M_{2\rm m} < 2.5\,M_\odot$, only every third solution is plotted for clarity. Around $M_{2\rm m} = 1.2$ and $\log P_{\rm m} = 2.8$ the symbols of WD 0135–052, WD 0136+768 and WD 1204+450 overlap due to the fact that they have similar white-dwarf masses. For comparison we show the lines of the solutions for (top to bottom) WD 0136+768, WD 0957–666 and WD 1101+364 taken from Nelemans et al. (2000), as described in the text.

white dwarfs with masses between 0.33 and $0.47\,M_\odot$ there is a range of masses between about 1.5 and $3\,M_\odot$ for which the progenitor has just ignited helium in the core, and thus shrunk, when it reaches the desired helium-core mass.

The dip and gap in Fig. 5.8 for WD 1101+364 (with $M_{2\rm f} \approx 0.29 M_\odot$) around $M_{2\rm m} = 1.8\,M_\odot$ can be attributed to the first dredge-up that occurs for low-mass stars ($M < 2.2\,M_\odot$) early on the first giant branch. Stars with these low masses shrink slightly due to this dredge-up that occurs at core masses between about 0.2 and $0.33\,M_\odot$, the higher core masses for the more massive stars (see Fig. 5.1a). Stars at the low-mass ($M_{2\rm m}$) side of the gap obtain the desired core mass just after the dredge-up, are relatively small and fill their Roche lobes at short periods. Stars with masses that lie in the gap reach that core mass while shrinking and cannot fill their Roche lobes for that reason. Stars at the high-mass end of the gap fill their Roche lobes just before the dredge-up so that this happens when they are relatively

large and therefore this happens at longer orbital periods.

For comparison we display as solid lines in Fig. 5.8 the results for the white-dwarf systems WD 0136+768, WD 0957–666 and WD 1101+364 (from top to bottom), as found by Nelemans et al. (2000) and shown in their Fig. 1. The differences between their and our results stem in part from the fact that the values for the observed masses have been updated by observations since their paper was published. To compensate for this we include dashed lines for the two systems for which this is the case. The dashed lines were calculated with their method but the values for the observed masses as listed in this chapter. By comparing the lines to the symbols for the same systems, we see that they lie in the same region of the plot and in the first order approach they give about the same results. However, the slopes in the two sets of results are clearly different. This can be attributed to the fact that Nelemans et al. (2000) used a power law to describe the radius of a star as a function of its core mass only. The change in orbital period with mass in their calculations is the result of changing the total mass in Kepler's law. Furthermore, they assumed that all stars with masses between 0.8 and 2.3 $M_\odot$ have a solution, whereas we find limits and gaps, partially due to the fact that we take into account the fact that stars shrink and partially because in Fig. 5.8 only solutions with a restricted $\alpha_{\rm ce}$ are allowed. On the other hand, we allow stars more massive than 2.3 $M_\odot$ as possible progenitors.

In Fig. 5.9, we display the common-envelope parameter $\alpha_{\rm ce}$ for a selection of the solutions with $0.1 \leq \alpha_{\rm ce} \leq 10$ as a function of the unknown intermediate secondary mass $M_{2\rm m}$. Each of the plot symbols has a corresponding symbol in Fig. 5.8. To produce these two figures, we have so far implicitly assumed that the masses of the two components are exact, so that there is at most one acceptable solution for each progenitor mass. This is of course unrealistic and it might keep us from finding an acceptable solution. At this stage we therefore introduce an uncertainty on the values for M_2 in Table 5.1 and take $M_{2\rm f} = M_2 - 0.05\,M_\odot, M_2 - 0.04\,M_\odot, \ldots, M_2 + 0.05\,M_\odot$. Meanwhile we assume that the mass ratio and orbital period have negligible observational error, because these errors are much smaller than those on the masses, and obtain the mass for the first white dwarf from $M_{1\rm f} = M_{2\rm f}/q_2$. Thus we have 11 pairs of values for $M_{1\rm f}$ and $M_{2\rm f}$ for each observed system, which we use as input for our spiral-in calculations. The results are shown in Fig. 5.10.

If we compare Fig. 5.8 and Fig. 5.10, we see that the wider range in input masses results in a wider range of solutions, similar to those we found in Fig. 5.8, but extended in orbital period. This can be understood intuitively, since lowering the white-dwarf mass demands a lower helium-core mass in the progenitor and thus a less evolved progenitor with a smaller radius at the onset of Roche-lobe overflow. Conversely, higher white-dwarf masses need more evolved progenitors that fill their Roche lobes at longer orbital periods. The introduction of this uncertainty clearly results in a larger and more realistic set of solutions for the spiral-in calculations and therefore should be taken into account.

Each system in Fig. 5.10 is a possible progenitor of one of the ten observed double white dwarfs listed in Table 5.1. We now turn to the question whether and how these intermediate systems can be produced.

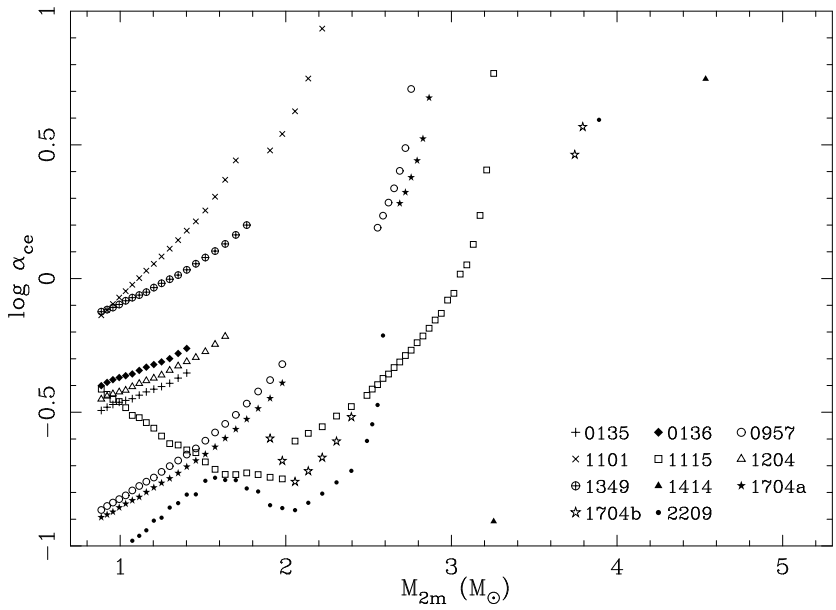

Figure 5.9: The logarithm of the common-envelope parameter $\alpha_{\rm ce}$ for the solutions of the spiral-in calculations shown in Fig. 5.8. Different symbols represent different observed systems. For $M_{2\rm m} < 2.5\,M_\odot$ every third solution is plotted only.

5.6 First mass-transfer phase

The solutions of the spiral-in calculations we found in the previous section are in our nomenclature *intermediate binaries*, that consist of one white dwarf and a non-degenerate companion. In this section we will look for an initial binary that consists of two zero-age main-sequence (ZAMS) stars of which the primary evolves, fills its Roche lobe, loses its hydrogen envelope, possibly transfers it to the secondary, so that one of the intermediate binaries of Fig. 5.10 is produced. The nature of this first mass transfer is a priori unknown. In the following subsections we will consider (1) stable and conservative mass transfer that will result in expansion of the orbit in most cases, (2) a common envelope with spiral-in based on energy balance (see Eq. 5.4) that usually gives rise to appreciable orbital shrinkage and (3) envelope ejection due to dynamically unstable mass loss based on angular-momentum balance, as introduced by Paczyński & Ziółkowski (1967) and already used by Nelemans et al. (2000) for the same purpose, which can take place without much change in the orbital period.

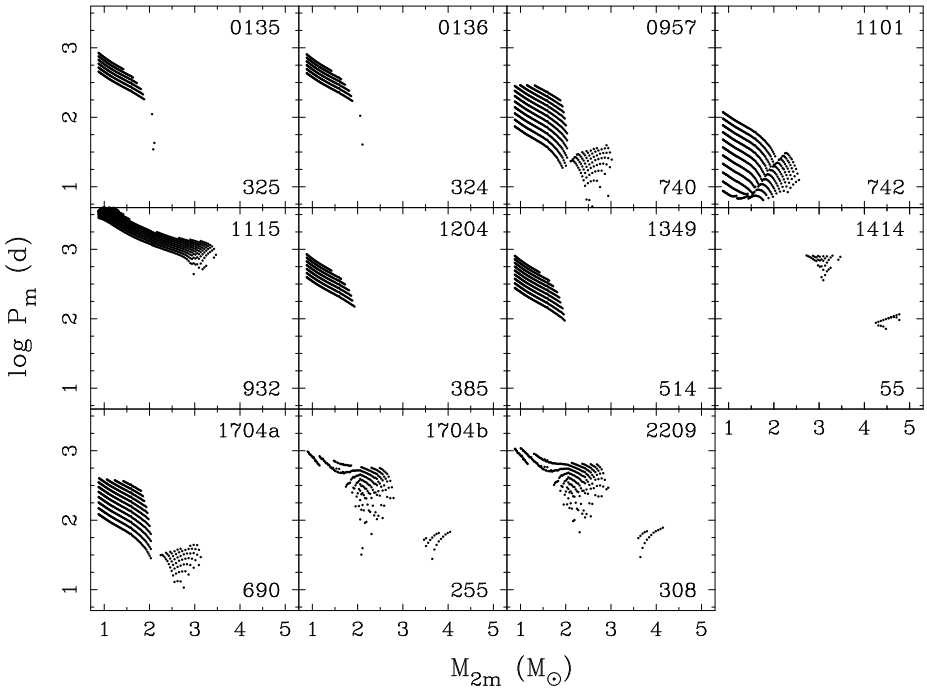

Figure 5.10: Results of the spiral-in calculations. This figure is similar to Fig. 5.8 and shows the orbital period of the pre-CE system as a function of the secondary mass. The solutions for each system are plotted in a separate panel, as labelled in the upper-right corner. All solutions with acceptable $\alpha_{\rm ce}$ are plotted. The number of solutions for each system is shown in the lower-right corner. We assumed an uncertainty in $M_{2\rm f}$ of $0.05\,M_\odot$ and calculated $M_{1\rm f}$ using q_2.

5.6.1 Conservative mass transfer

In this section we will find out which of the spiral-in solutions of Fig. 5.10 may be produced by stable, conservative mass transfer. We use the binary evolution code described in Sect. 5.3. For simplicity, we ignore stellar wind and the effect of stellar spin on the structure of the star. Because we assume conservative evolution, the total mass of the binary is constant, so that $M_{1\rm i} + M_{2\rm i} = M_{1\rm m} + M_{2\rm m}$, where the last two quantities are known. Also, we ignore angular momentum exchange between spin and orbit by tidal forces, so that the orbital angular momentum is conserved. This implies that

$$\frac{P_{\rm m}}{P_{\rm i}} = \left(\frac{M_{1\rm i}\, M_{2\rm i}}{M_{1\rm m}\, M_{2\rm m}} \right)^3 . \tag{5.6}$$

Because of the large number of possible intermediate systems we will first remove all

such systems for which it can a priori be shown that they cannot be produced by conservative mass transfer. These systems have orbital periods that are either too short or too long to be formed this way. We can find a lower limit to the intermediate period as a function of secondary mass $M_{2\mathrm{m}}$ using the fact that the total mass of the initial system must be equal to the sum of the mass of the observed white dwarf M_1 and $M_{2\mathrm{m}}$. We distributed this mass equally over two ZAMS stars and set the Roche-lobe radii equal to the two ZAMS radii. By substituting the initial and desired masses in Eq. 5.6 we find a lower limit to the period of the intermediate binary, which we will call P_{min}.

An upper limit to the intermediate period P_{m} can also be obtained. In order to do this, we note that the maximum orbital period after conservative mass transfer for a given binary mass is obtained for an optimum initial mass ratio $q_{2\mathrm{i,opt}} = 0.62$ (Nelemans et al. 2000). We can therefore calculate the masses $M_{1\mathrm{i,opt}}$ and $M_{2\mathrm{i,opt}}$ of the initial binary that evolves to that maximum intermediate period by distributing the total system mass ($M_1 + M_{2\mathrm{m}}$) according to the mass ratio $q_{2\mathrm{i,opt}}$. The optimum initial period is the maximum period at which stable mass transfer can still occur in a binary with masses $M_{1\mathrm{i,opt}}$ and $M_{2\mathrm{i,opt}}$. This is the orbital period at which the donor star fills its Roche lobe just before it reaches the base of the giant branch (BGB). We use the conditions by Hurley et al. (2000) who define this point as the moment where the mass of the convective envelope M_{CE} exceeds a certain fraction of the total mass of the hydrogen envelope M_{E} for the first time:

$$\begin{array}{lll} M_{\mathrm{CE}} & = \frac{2}{5} M_{\mathrm{E}}, & M_{1\mathrm{i,opt}} \leq 1.995\, M_{\odot}, \\ M_{\mathrm{CE}} & = \frac{1}{3} M_{\mathrm{E}}, & M_{1\mathrm{i,opt}} > 1.995\, M_{\odot}, \end{array} \tag{5.7}$$

for $Z = 0.02$. We then find from our grid of Sect. 5.4 the two single-star models with masses that bracket $M_{1\mathrm{i,opt}}$ and interpolate within these models to find the radii of these stars where the condition of Eq. 5.7 is fulfilled for the first time. Subsequently, we interpolate again between these two bracketing models to find the radius of the star with the desired mass at the base of the giant branch (R_{BGB}). By assuming that this radius is equal to the Roche-lobe radius and using Eq. 5.5, the initial masses and period that lead to the maximum intermediate period are known and we can use Eq. 5.6 to find this upper limit to the intermediate period, which we will call P_{max}, as a function of the secondary mass. All intermediate systems that result from our spiral-in calculations and have longer orbital periods than P_{max} cannot result from conservative mass transfer.

The lower and upper limits for the orbital period between which a conservative solution must lie for WD 0957–666 are shown in Fig. 5.11 together with the intermediate systems found from the spiral-in calculations. Black dots represent solutions that lie between the limits and could match the outcome of a conservative model, grey dots lie outside these limits and cannot be created by conservative mass transfer. There is a slight difference between the dashed lines and the division between filled and open symbols in the Figure, because the spiral-in solutions are shown with the uncertainty in the masses described in the previous section, whereas the period limits are only shown for the measured M_2 and q_2 (see Table 5.1) for clarity.

After selecting the spiral-in solutions that lie between these period limits for all eleven systems, we find that such solutions exist for only six of the observed binaries, as shown in

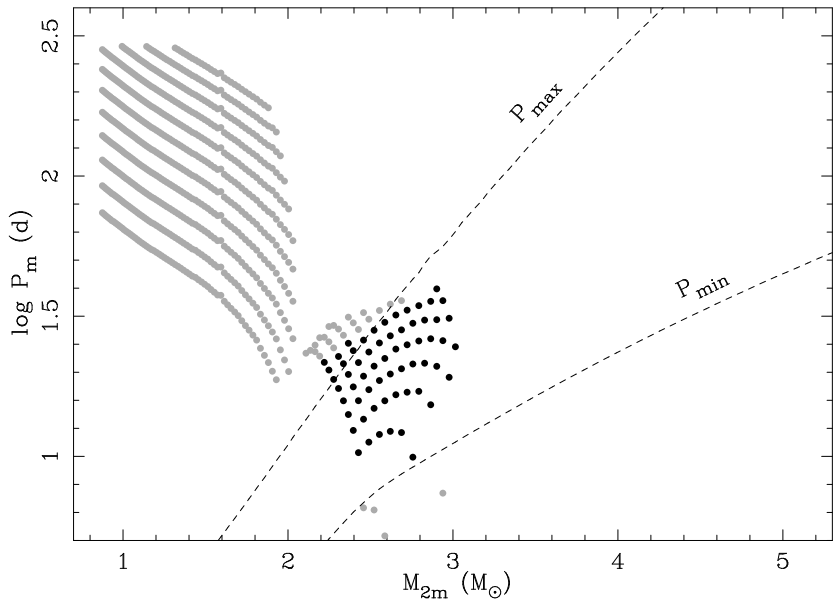

Figure 5.11: Results of the spiral-in calculations for WD 0957–666 with period limits for a conservative first mass transfer. This figure contains the same data as the third panel in Fig. 5.10 (symbols) plus the period limits $P_{\rm min}$ and $P_{\rm max}$ (dashed lines). The solutions that lie between these limits are shown in black, the others in grey. See the main text for details.

Fig. 5.12. We tried to model these intermediate systems with the binary evolution code described in Sect. 5.3. Because of the large number of allowed spiral-in solutions for WD 0957–666 and WD 1101+364, we decided to model about half of the solutions for these two systems and all of the solutions for the other four. Because we assume that during this part of the evolution mass and orbital angular momentum are conserved, the only free parameter is the initial mass ratio $q_{\rm 1i} \equiv M_{\rm 1i}/M_{\rm 2i}$. For each of the spiral-in solutions we selected, we chose five different values for $q_{\rm 1i}$, evenly spread in the logarithm: 1.1, 1.3, 1.7, 2.0 and 2.5. The total number of conservative models that we calculated is 570, of which 270 resulted in a double white dwarf. The majority of the rest either experienced dynamical mass transfer or evolved into a contact system. A few models were discarded because of numerical problems. The results of the calculations for the conservative first mass transfer are compared to the solutions of the spiral-in calculations in Fig. 5.13.

The systems that result from our conservative models generally have longer orbital periods than the intermediate systems that we are looking for. This means that stable mass transfer in the models continues beyond the point where the desired masses and orbital period are reached. The result is that $M_{\rm 1m}$ is too small and that $M_{\rm 2m}$ and $P_{\rm m}$ are too large. The reason that mass transfer continues is that the donor star is not yet sufficiently evolved:

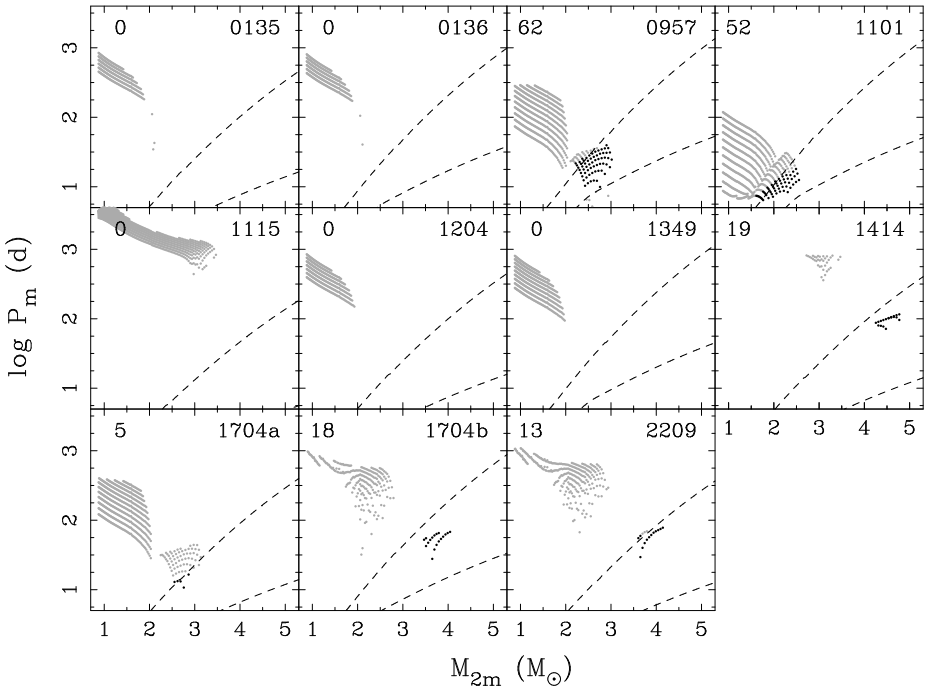

Figure 5.12: Results of the spiral-in calculations with period limits for conservative mass transfer as in Fig. 5.11, but for all systems. The number in the upper left corner of each panel is the number of systems that lie between the period limits.

the helium core is still small and there is sufficient envelope mass to keep the Roche lobe filled. White dwarfs of higher mass would result from larger values of $q_{1\mathrm{i}}$. This way, the initial primary is more massive and the initial period is longer, so that the star fills its Roche lobe at a slightly later stage in evolution. Both effects increase the mass of the resulting white dwarf. However, if once chooses the initial mass ratio too high, the system evolves into a contact binary or, for even higher $q_{1\mathrm{i}}$, mass transfer becomes dynamically unstable. In both cases the required intermediate system will not be produced. These effects put an upper limit to the initial mass ratio for which mass transfer is still stable, and thus an upper limit to the white-dwarf mass that can be produced with stable mass transfer for a given system mass. Our calculations show that conservative models with an initial mass ratio of 2.5 produce no double white dwarfs. Apparently this value of $q_{1\mathrm{i}}$ is beyond the upper limit. The solutions in Fig. 5.14 with a final mass ratio close to or in agreement with the observations come predominantly from the models with initial mass ratios of 1.7 and 2.0.

Because small deviations in the masses and orbital period of the intermediate systems can still lead to acceptable double white dwarfs, we monitor the evolution of these systems to the point where the secondary fills its Roche lobe and determine the mass of the second

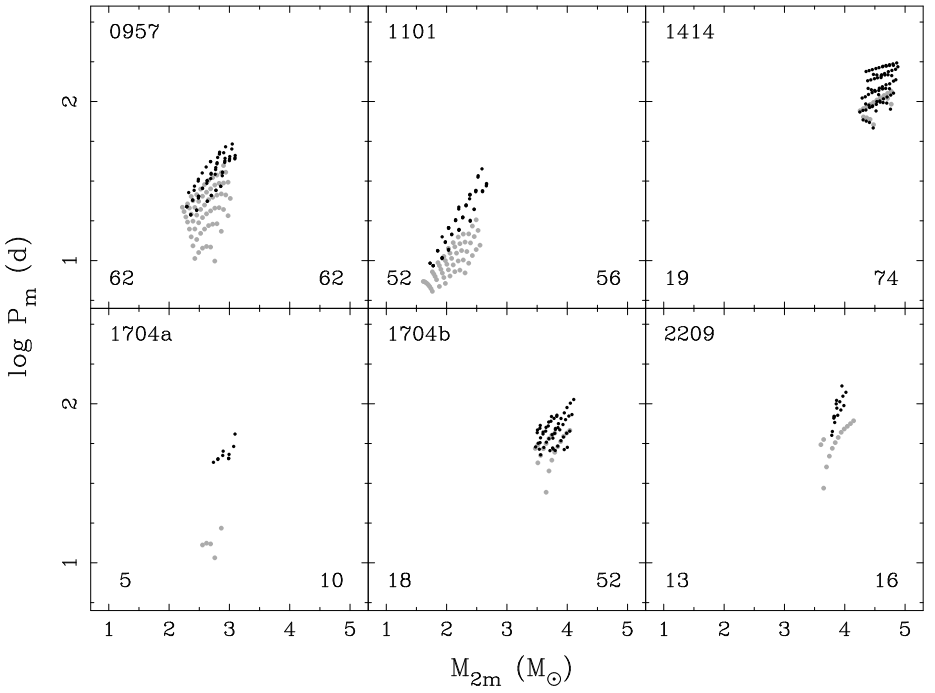

Figure 5.13: Results of the spiral-in calculations (grey symbols), obtained as in Fig. 5.11, and the solutions of calculations of conservative evolution (black symbols). Only the six systems shown have spiral-in solutions within the period limits (see Fig. 5.12). The numbers in the lower left and lower right corners are the numbers of plotted spiral-in solutions and conservative solutions respectively.

white dwarf $M_{2\mathrm{f}}$ from the helium-core mass of the secondary at that point. Because the secondary in the intermediate binary is slightly too massive in most cases, it is smaller at a given core mass (see Fig. 5.1) so that the mass of the second white dwarf becomes larger than desired. Combined with an undermassive first white dwarf this results in a too large mass ratio $q_{2\mathrm{f}}$. This is shown in Fig. 5.14, where the values for $q_{2\mathrm{f}}$ for our conservative models are compared to the observations. The Figure also shows the difference in age of the system between the moment where the second white dwarf was formed and the moment when the first white dwarf was formed ($\Delta\tau$). This difference should be similar to the observed difference in cooling age between the two components of the binary (see Table 5.1). The vertical dotted lines show this observed cooling-age difference with an uncertainty of 50%.

Figure 5.14 shows that of the six systems presented, only two have a mass ratio within the observed range, although values for the other systems may be close. We see that the mass ratios of the solutions for most of the systems are divided in two groups and the difference in mass ratio can amount to a factor of 2 between them. The division arises because in most

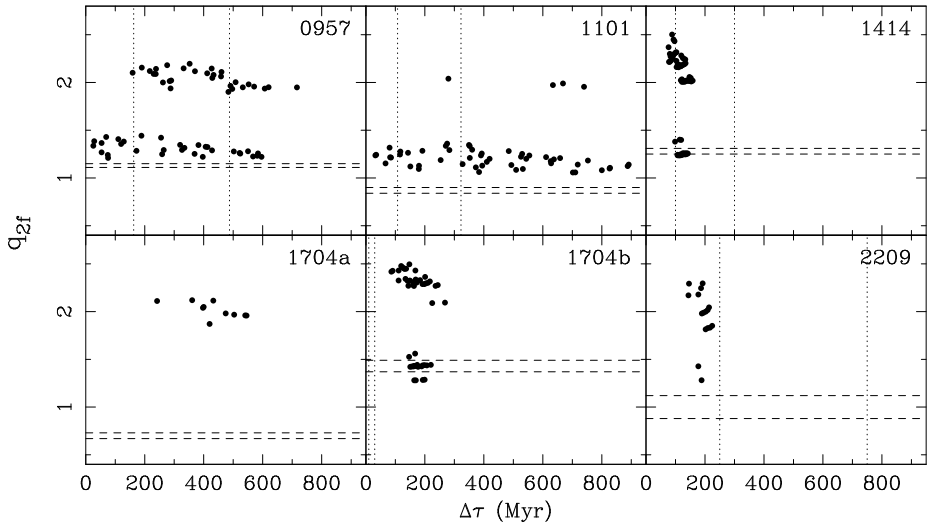

Figure 5.14: The mass ratio of model double white dwarfs formed by a conservative first mass transfer and a common envelope with spiral-in, against the age difference between the two components. The dashed horizontal lines show the observed range of possible mass ratios as shown in Table 5.1. The dotted vertical lines are the estimated cooling-age differences $\pm 50\%$ (see Table 5.1).

models the common envelope is supposed to occur on the short giant branch of stars that are more massive than $2\,M_\odot$. If the secondary is slightly smaller and the orbital period slightly longer than it should be, the star can ignite helium in its core and start shrinking before it has expanded sufficiently to fill its Roche lobe. When this star expands again after core helium exhaustion, it has a much more massive helium core and produces a much more massive white dwarf than desired (see Fig. 5.1). Thus, a small offset in the parameters of the model after the first mass-transfer phase can result in large differences after the spiral-in. Of the 270 stable models shown in Fig. 5.14, 126 (47%) are in the group with lower mass ratios ($q_{2f} \lesssim 1.7$).

The modelled mass ratios for the systems WD 0957–666 and WD 1101+364 are close to the observed values, and we find that this is especially true for the models on the low-mass end of the range in observed white-dwarf masses we used. This can be understood, because the maximum mass of a white dwarf that can be created with conservative mass transfer is set by the total mass in the system. The system mass is determined by the spiral-in calculations in Sect. 5.5.2, where we find that the total mass that is available to create these two systems lies between about 2 and $3.5\,M_\odot$. This system mass is simply insufficient to create white dwarfs with the observed masses. If we would extend the uncertainty in the observed masses to allow lower white-dwarf masses, it seems likely that we could explain these two double white dwarfs with a conservative mass-transfer phase followed by a common en-

velope with spiral-in. The same could possibly be achieved with stable, non-conservative mass transfer. Losing mass from the system stabilises the mass transfer, so that it can still be stable for slightly longer initial periods, and allows higher initial primary masses. Both effects result in higher white-dwarf masses.

All 126 stable solutions in the lower group of mass ratios ($q_{2\rm f} \lesssim 1.7$) have $\alpha_{\rm ce} > 1$ and 83 (66%) have $\alpha_{\rm ce} < 5$. If we become more demanding and insist that $\alpha_{\rm ce}$ should be less than 2, we are left with 14 solutions, all for WD 0957–666. These solutions all have $\alpha_{\rm ce} > 1.6$. If we additionally demand that the age difference of these models be less than 50% from the observed cooling-age difference, only 6 solutions are left with age differences roughly between 190 and 410 Myr, $\alpha_{\rm ce} > 1.8$ and $1.32 \leq q_{2\rm f} \leq 1.44$.

We conclude that although the evolutionary channel of conservative mass transfer followed by a spiral-in can explain some of the observed systems, evolution along this channel cannot produce all observed double white dwarfs. We must therefore reject this formation channel as the single mechanism to create the white-dwarf binaries. The reason that this mechanism fails to explain some of the observed white dwarfs is that the observed masses for the first white dwarfs in these systems are too high to be explained by conservative mass transfer in a binary with the total mass that is set by the spiral-in calculations. Allowing for mass loss from the system during mass transfer could result in better matches for this mechanism. However it is clear from Fig. 5.12 that this will certainly not work for at least 5 of the 10 observed systems because their orbital periods are too large. We will need to consider other mechanisms in addition to stable mass transfer to produce the observed white-dwarf primaries for these systems.

5.6.2 Unstable mass transfer

In this section we try to explain the formation of the first white dwarf in the intermediate systems shown in Fig. 5.10 by unstable mass transfer. Mass transfer occurs on the dynamical timescale if the donor is evolved and has a deep convective envelope. There are two prescriptions that predict the change in orbital period in such an event. The first is a classical common envelope with a spiral-in, based on energy conservation as we have used in Sect. 5.5. The second prescription was introduced by Nelemans et al. (2000) and further explored by Nelemans & Tout (2005) and uses angular-momentum balance to calculate the change in orbital period. Where the first prescription results in a strong orbital shrinkage (spiral-in) for all systems, in the second mechanism this is not necessarily the case so that the orbital period may hardly change while the envelope of the donor star is lost.

In both scenarios we are looking for an initial binary of which the components have masses $M_{1\rm i}$ and $M_{2\rm i}$. The primary will evolve fastest, fill its Roche lobe and eject its envelope due to dynamically unstable mass loss, so that its core becomes exposed and forms a white dwarf with mass $M_{1\rm m}$. We assume that the mass of the secondary star does not change during this process, so that $M_{2\rm i} = M_{2\rm m}$. We use the model stars from Sect. 5.4.1 as the possible progenitors for the first white dwarf. The orbital period before the envelope ejection is again determined by setting the radius of the model star equal to the Roche-lobe

radius and applying Eq. 5.5, where the subscripts 'm' must be replaced by 'i'.

Because we demand that $M_{1\mathrm{i}} > M_{2\mathrm{i}}$, the original secondary can be any but the most massive star from our grid and the total number of possible binaries in our grid is $\sum_{n=1}^{198} n = 19701$ for each system we want to model. The total number of systems that we try to model is 121: the 11 observed systems (the 10 from Table 5.1 plus the system WD 1704+481b) times 11 different assumptions for the masses of the observed stars (between $\pm 0.05\,M_{\odot}$ from the observed value). We have thus tried slightly less than 2.4 million initial binaries to find acceptable progenitors to these systems. All these possible progenitor systems have been filtered by the following criteria, in addition to the ones already mentioned in Sect. 5.5:

1. the radius of the star is larger than the radius at the base of the giant branch $R > R_{\mathrm{BGB}}$, which point is defined by Eq. 5.7,
2. the mass ratio is larger than the critical mass ratio for dynamical mass transfer $q > q_{\mathrm{crit}}$ as defined by Eq. 57 of Hurley et al. (2002). Together with the previous criterium, this ensures that the mass transfer can be considered to proceed on the dynamical timescale,
3. the time since the ZAMS after which the first white dwarf is created τ_1 is less than the same for the second white dwarf (τ_2) and, additionally, $\tau_2 < 13\,\mathrm{Gyr}$.

After we filter the approximately 2.4 million possible progenitor systems with the criteria above, about 204,000 systems are left in the sample (8.5%) for which two subsequent envelope-ejection scenarios could result in the desired masses, provided that we can somehow explain the change in orbital period that is needed to obtain the observed periods. For each of the two prescriptions for dynamical mass loss we will see whether this sample contains physically acceptable solutions in the sections that follow.

Classical common envelope with spiral-in

The treatment of a classical common envelope with spiral-in based on energy conservation has been described in detail in Sect. 5.5 and therefore need not be reiterated here. In the calculations described above, Eq. 5.4 provides us with the parameter α_{ce1} for the first spiral-in. In order to use Eq. 5.4 the subscripts 'm' must be replaced by 'i' and the subscripts 'f' by 'm'. The values of the common-envelope parameter for the first spiral-in must be physically acceptable and we demand that $0.1 \leq \alpha_{\mathrm{ce1}} \leq 10$. When we apply this criterion to the results of our calculations, only 25 possible progenitors out of the 204,000 binaries in our sample survive. All 25 survivors are solutions for WD 0135–052 and have $\alpha_{\mathrm{ce1}} \gtrsim 2.5$.

We find that of the systems that pass the criterion in the second spiral-in and have $0.1 \leq \alpha_{\mathrm{ce2}} \leq 10$, most (99%) need a negative α_{ce1} in order to satisfy Eq. 5.4, so that we reject them. We can clearly conclude that the scenario of two subsequent classical common envelopes with spiral-in can be rejected as the formation mechanism for any of the observed double white dwarfs. This confirms the conclusions of Nelemans et al. (2000) and Nelemans & Tout (2005), based on the value of the product $\alpha_{\mathrm{ce}}\,\lambda_{\mathrm{env}}$, where λ_{env} is the envelope-structure parameter defined in Eq. 5.2.

Envelope ejection with angular-momentum balance

The idea to determine the change in orbital period in a common envelope from balance of angular momentum originates from Paczyński & Ziółkowski (1967). In Nelemans et al. (2000) and Nelemans & Tout (2005) the mechanism was used to model observed double white dwarfs. The principle is similar to that of a classical common envelope, here with an efficiency parameter that we will call γ in the general case. In this section we will use three slightly different prescriptions for mass loss with angular-momentum balance requiring three different definitions of γ. For all three mechanisms the mass loss of the donor is dynamically unstable and its envelope is ejected from the system. Because not all of these mechanisms necessarily involve an envelope that engulfs both stars, we shall refer to them as envelope ejection or dynamical mass loss rather than common-envelope evolution. The first mechanism is that defined by Nelemans et al. (2000), where a common envelope is established first, after which the mass is lost from its surface. The mass thus carries the average angular momentum of the system and we will call the parameter for this mechanism $\gamma_{\rm s}$. In the second mechanism the mass is first transferred and then re-emitted with the specific angular momentum of the accretor. We will designate $\gamma_{\rm a}$ for this mechanism. In the third mechanism the mass is lost directly from the donor in an isotropic wind and the corresponding parameter is $\gamma_{\rm d}$. We will call the companion to the donor star 'accretor', even if no matter is actually accreted.

The prescription for dynamical mass loss with the specific angular momentum of the system as the mechanism for the first mass-transfer phase, using this and earlier subscript conventions, is:

$$\frac{J_{\rm i} - J_{\rm m}}{J_{\rm i}} \;=\; \gamma_{\rm s1}\,\frac{M_{\rm 1i} - M_{\rm 1m}}{M_{\rm 1i} + M_{\rm 2i}}, \tag{5.8}$$

where J is the total orbital angular momentum (Nelemans et al. 2000). Our demands for a physically acceptable solution to explain the observed binaries is now $0.1 \leq \gamma_{\rm s1} \leq 10$ for the first envelope ejection and $0.1 \leq \alpha_{\rm ce2} \leq 10$ for the second. From the set of about 204,000 solutions we found above, almost 150,000 (72%) meet these demands and nearly 134,000 solutions (66%) have values for $\gamma_{\rm s1}$ between 0.5 and 2, in which all observed systems are represented.

We tried to constrain the ranges for $\gamma_{\rm s1}$ and $\alpha_{\rm ce2}$ as much as possible, thereby keeping at least one solution for each observed system. We can write these ranges as $(\gamma_0 - \frac{\Delta\gamma}{2}, \gamma_0 + \frac{\Delta\gamma}{2})$ and $(\alpha_0 - \frac{\Delta\alpha}{2}, \alpha_0 + \frac{\Delta\alpha}{2})$, where γ_0 and α_0 are the central values and $\Delta\gamma$ and $\Delta\alpha$ are the widths of each range. We independently varied γ_0 and α_0 and for each pair we took the smallest values of $\Delta\gamma$ and $\Delta\alpha$ for which there is at least one solution for each observed system that lies within both ranges. The set of smallest ranges thus obtained is considered to be the best range for $\gamma_{\rm s1}$ and $\alpha_{\rm ce2}$ that can explain all systems. Because it is harder to trifle with the angular-momentum budget than with that of energy, we kept the relative width of the range for $\gamma_{\rm s1}$ twice as small as that for $\alpha_{\rm ce2}$ ($2\frac{\Delta\gamma}{\gamma_0} = \frac{\Delta\alpha}{\alpha_0}$). Our calculations show that changing this factor merely redistributes the widths over the two ranges without affecting the central values much and thus precisely which factor we use seems to be unimportant for the result. We find that the set of narrowest ranges that contain a solution for each system is

$1.45 \leq \gamma_{s1} \leq 1.58$ and $0.61 \leq \alpha_{ce2} \leq 0.72$. These results are plotted in Fig. 5.15.

We can alternatively treat the second envelope ejection with the angular-momentum prescription as well, where we need to introduce a factor γ_{s2} by replacing all subscripts 'm' by 'f' and all subscripts 'i' by 'm' in Eq. 5.8. Again we search for the narrowest ranges of γ_{s1} and γ_{s2} that contain at least one solution per observed system. We now force the relative widths of the two ranges to be equal. The best solution is then $1.16 \leq \gamma_{s1} \leq 1.22$ and $1.62 \leq \gamma_{s2} \leq 1.69$.

In both prescriptions above ($\gamma_{s1}\alpha_{ce2}$ and $\gamma_{s1}\gamma_{s2}$) we find that the values for γ lie significantly above unity. This is in accordance with the findings of Nelemans et al. (2000) and Nelemans & Tout (2005), but slightly discomforting because there is no obvious physical mechanism that can transfer this extra angular momentum to the gas of the envelope. We will therefore rewrite Eq. 5.8 for the case where the mass is lost with the specific angular momentum of one of the stars in the binary, so that we can expect that $\gamma \approx 1$. In order to do this we use the equations derived by Soberman et al. (1997) in their Section 2.1. We ignore the finite sizes of the star by putting $A_w = 1$ and assume that no matter is accreted, so that $\alpha_w + \beta_w = 1$ and $\epsilon_w = 0$, where we introduced the subscript 'w' to avoid confusion with α_{ce}. Their Eq. 24 then gives (replacing their notation by ours):

$$\frac{J_m}{J_i} = \left(\frac{q_m}{q_i}\right)^{\alpha_w} \frac{1+q_i}{1+q_m}, \tag{5.9}$$

where we will consider the cases where $\alpha_w = 0$ (hence $\beta_w = 1$), describing isotropic re-emission by the accretor, and $\alpha_w = 1$ for an isotropic wind from the donor. Their q is defined as $m_{donor}/m_{accretor}$. We can now rewrite Eq. 5.8 for these two cases:

$$\frac{J_i - J_m}{J_i} = \gamma_{a1} \frac{M_{1i} - M_{1m}}{M_{1m} + M_{2m}} \quad (\alpha_w = 0), \tag{5.10}$$

$$\frac{J_i - J_m}{J_i} = \gamma_{d1} \frac{M_{1i} - M_{1m}}{M_{1m} + M_{2m}} \frac{M_{2i}}{M_{1i}} \quad (\alpha_w = 1). \tag{5.11}$$

By comparing Eq. 5.8 to Eq. 5.10, we can directly see that for an envelope ejection with given masses and angular momenta, $\gamma_a < \gamma_s$ must hold in order to keep it satisfying the equation. For Eq. 5.11, this is not necessarily true for a first envelope ejection but the effect is even stronger for all second envelope ejections considered in this chapter. The results of the analysis described above, but now for the modified definitions of γ, for the $\gamma\alpha$ and $\gamma\gamma$ scenarios, each with $\alpha_w = 0$ (isotropic re-emission) and $\alpha_w = 1$ (donor wind) are shown in Table 5.2 and compared to the previous results.

We see that the values for γ change drastically, as may be expected. The fact that the values for α_{ce} change slightly has to do with the fact that we now select different solutions to the calculations than before. Numerically, the fifth solution in the table seems the most attractive: $\gamma_{d1} \approx 1.0$ and $\alpha_{ce2} \approx 0.6$. Although the value for α_{ce2} is lower than unity, it may not be unrealistic that 40 % of the freed orbital energy is emitted by radiation. This is the scenario where the mass is lost in an isotropic wind by the donor in the first dynamical

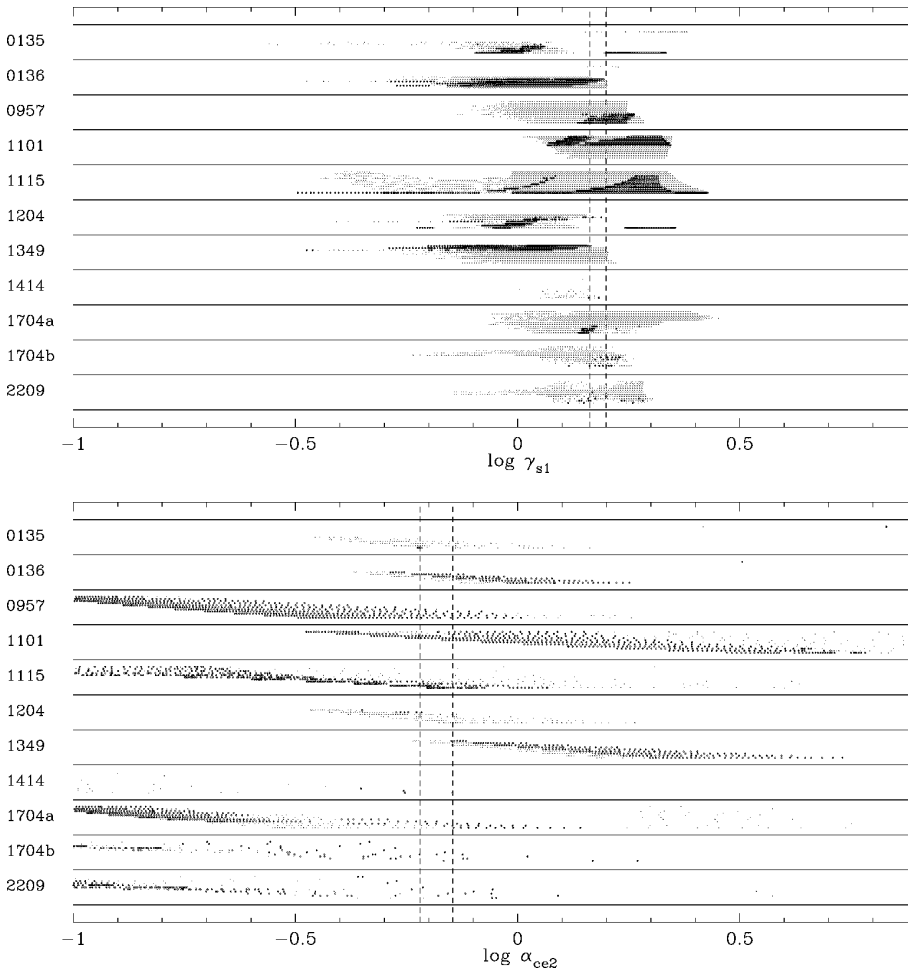

Figure 5.15: Solutions for the double dynamical mass-loss scenario for each system. Each dot represents one system that evolves through an episode of dynamical mass loss with γ_{s1} and then a common envelope with spiral-in with α_{ce2} to form one of the observed white dwarfs. *Upper panel:* (**a**): the value for $\log \gamma_{s1}$ for the first envelope ejection for all solutions with $0.1 \leq \gamma_{s1} \leq 10$ and $0.1 \leq \alpha_{ce2} \leq 10$. Solutions with $0.61 \leq \alpha_{ce2} \leq 0.72$ (the dashed lines in (b)) are plotted as large dots, the rest as small ones. *Lower panel:* (**b**): the value for $\log \alpha_{ce2}$ for the second envelope ejection for the same set of solutions. Here, the large dots have $1.45 \leq \gamma_{s1} \leq 1.58$ (the dashed lines in (a)). The smallest set with at least one solution for each system is the intersection of these two sets (the large dots that lie between the dashed lines). The vertical position of each dot within its line shows the deviation from the observed secondary mass M_2: $M_{2f} = M_2 - 0.05\,M_\odot$ for the lower dots, $M_{2f} = M_2 + 0.05\,M_\odot$ for the upper. The Figure is made after Nelemans & Tout (2005).

Prescription	γ_1	$\gamma_{0,1}$	$\gamma_2/\alpha_{\rm ce2}$	$\gamma_{0,2}/\alpha_{0,2}$
$\gamma_{\rm s1}\alpha_{\rm ce2}$	1.45–1.58	1.52	α: 0.61–0.72	α: 0.66
$\gamma_{\rm s1}\gamma_{\rm s2}$	1.16–1.22	1.19	γ: 1.62–1.69	γ: 1.65
$\gamma_{\rm a1}\alpha_{\rm ce2}$	0.81–0.94	0.88	α: 0.50–0.68	α: 0.59
$\gamma_{\rm a1}\gamma_{\rm a2}$	0.50–0.52	0.51	γ: 0.68–0.70	γ: 0.69
$\gamma_{\rm d1}\alpha_{\rm ce2}$	0.92–1.08	1.00	α: 0.47–0.64	α: 0.56
$\gamma_{\rm d1}\gamma_{\rm d2}$	0.91–1.07	0.99	γ: 2.55–3.02	γ: 2.78

Table 5.2: Narrowest ranges for γ and $\alpha_{\rm ce}$ that contain at least one solution to the envelope-ejection scenario per observed system and their central values. The six different prescriptions are explained in the main text.

mass-loss episode and the second mass loss is a canonical common envelope with spiral-in. We also see that the best solutions with a second envelope ejection based on the angular-momentum prescription obtained with this method has values for γ that lie much farther from unity than the γ-values for the $\gamma\alpha$-scenarios.

5.6.3 Formation by multiple mechanisms

So far, we assumed that all ten observed double white dwarfs were formed by one and the same mechanism. Although some mechanisms are clearly better in explaining the formation of all the observed systems than others, none of them is completely satisfactory, mainly because the parameters γ or $\alpha_{\rm ce}$ are far from the desired values. Furthermore, there is no reason why the ten systems should all have been formed by the same mechanism in nature if there are several options available. We therefore slightly change our strategy here by assuming that different envelope-ejection prescriptions, described in Sect. 5.6.2, can play a role in the formation of the observed systems.

For the dynamical mass loss, we now demand that γ and $\alpha_{\rm ce}$ are close to unity. Because angular momentum should be better conserved than energy, we accept solutions with $0.95 < \gamma < 1.05$ and $0.90 < \alpha_{\rm ce} < 1.10$, except for the mechanism described by Eq. 5.8, for which Nelemans & Tout (2005) show that all systems can be explained with $1.50 < \gamma < 1.75$, which we reduce to $1.54 < \gamma < 1.71$ to give it the same relative width. For each observed system and each mechanism, we look whether there is at least one solution with a envelope-ejection parameter within these ranges. The results are shown as the first symbol in each entry of Table 5.3. The plus signs show which mechanism can explain the mass ratio of an observed double white dwarf. The table shows that although none of the mechanisms can explain all observed systems within the chosen ranges of γ and $\alpha_{\rm ce}$, the second-last column shows that a combination of these mechanisms can. The table also indicates that mechanisms containing only $\gamma_{\rm s}$ and none of the other γ's cannot explain all systems. The same is true for $\gamma_{\rm a}$ and $\gamma_{\rm d}$. If we expand the chosen ranges for γ and $\alpha_{\rm ce}$ with a factor of two, our calculations show that the mechanisms $\gamma_{\rm s}\gamma_{\rm s}$ and $\gamma_{\rm d}\gamma_{\rm a}$ can explain the mass ratios of all systems. Expanding the allowed ranges in this way more than quadruples the total

System	1: $\gamma_s\alpha_{ce}$	2: $\gamma_s\gamma_s$	3: $\gamma_a\alpha_{ce}$	4: $\gamma_a\gamma_a$	5: $\gamma_d\alpha_{ce}$	6: $\gamma_d\gamma_a$	Opt. res.	Best mech.
0135	$-/-$	$+/\sim$	$-/-$	$-/-$	$+/\sim$	$+/-$	$+/\sim$	2,5
0136	$+/+$	$+/+$	$+/\sim$	$-/-$	$+/+$	$-/-$	$+/+$	1,2,5
0957	$+/+$	$+/+$	$+/+$	$+/+$	$+/+$	$+/\sim$	$+/+$	1–5
1101	$+/\sim$	$+/-$	$+/\sim$	$+/-$	$-/-$	$-/-$	$+/\sim$	1,3
1115	$+/\sim$	$+/\sim$	$+/+$	$+/\sim$	$+/+$	$-/-$	$+/+$	3,5
1204	$-/-$	$-/-$	$-/-$	$-/-$	$+/-$	$+/-$	$+/-$	5,6
1349	$+/+$	$+/+$	$+/+$	$-/-$	$+/+$	$-/-$	$+/+$	1,2,3,5
1414	$-/-$	$-/-$	$-/-$	$-/-$	$-/-$	$+/+$	$+/+$	6
1704a	$+/-$	$+/-$	$-/-$	$+/-$	$-/-$	$+/-$	$+/-$	1,2,4,6
1704b	$+/-$	$+/-$	$+/-$	$+/-$	$+/-$	$+/-$	$+/-$	1–6
2209	$-/-$	$+/+$	$-/-$	$+/+$	$-/-$	$+/\sim$	$+/+$	2,4

Table 5.3: Comparison of the different mechanisms used to reconstruct the observed double white dwarfs. The symbols $+$, $\sim$ and $-$ mean that the model solutions are in good, moderate or bad agreement with the observations. The first of the two symbols in each column is based on the mass ratio only and the second includes the age difference. The method for obtaining the first symbol in each entry is described in Sect. 5.6.3, that for the second symbol in Sect. 5.6.4. The symbols in the headers of the columns labelled 1–6 are explained in the main text. The columns for $\gamma_a\gamma_d$ and $\gamma_d\gamma_d$ were left out because they do not contain any solutions. The last two columns show the optimum result and the mechanisms that give this result (1–6).

number of solutions from 7866 to 36 867.

5.6.4 Constraining the age difference

The large number of solutions found in the previous section allows us to increase the number of selection criteria that we use to qualify a solution as physically acceptable. We now include the age difference of the components in our model systems and demand that it is comparable to the observed cooling-age difference for that system. The age difference in our models is the difference in age at which each of the components fills its Roche lobe and causes dynamical mass loss.

Table 5.4 lists the number of model solutions for each mechanism and each system. The columns labelled 1–6 are the same as those in Table 5.3. The first number in each of these columns is the number of solutions that is found within the same ranges for γ and α_{ce} as we used in Table 5.3. This means that a minus sign in that table corresponds to a zero in Table 5.4. Behind the entries with a positive number of solutions the range of age difference that these solutions span is shown. Again, the columns for $\gamma_a\gamma_d$ and $\gamma_d\gamma_d$ are not displayed, because they do not contain any solutions for any system. We have to expand the γ-ranges

System	Obs. $\Delta\tau$ (Myr)	Number of solutions and model age differences (Myr) 1: $\gamma_s\alpha_{ce}$	2: $\gamma_s\gamma_s$	3: $\gamma_a\alpha_{ce}$	4: $\gamma_a\gamma_a$	5: $\gamma_d\alpha_{ce}$	6: $\gamma_d\gamma_a$
0135	175–525	*0*	*1*, 1131	*0*	*0*	*49*, 1302–2610	*56*, 2067–5620
0136	225–675	*35*, 44–281	*32*, 43–237	*2*, 76–94	*0*	*58*, 44–418	*0*
0957	163–488	*36*, 352–818	*1925*, 144–3601	*59*, 163–506	*292*, 308–3387	*30*, 352–851	*1554*, 490–12094
1101	108–323	*318*, 995–10910	*941*, 2202–10917	*242*, 857–9124	*91*, 5897–9577	*0*	*0*
1115	80–240	*159*, 368–1019	*80*, 313–550	*157*, 182–841	*378*, 552–998	*19*, 240–758	*0*
1204	40–120	*0*	*0*	*0*	*0*	*46*, 1329–3780	*75*, 2101–6161
1349	?	*13*, 64–235	*19*, 64–235	*5*, 64–134	*0*	*101*, 64–905	*0*
1414	100–300	*0*	*0*	*0*	*0*	*0*	*34*, 36–385
1704a	-30– -10	*3*, 858-1020	*98*, 216-1381	*0*	*218*, 1565-3313	*0*	*17*, 2735-5386
1704b	10–30	*3*, 519–553	*17*, 217–364	*1*, 465	*43*, 199–781	*2*, 536–553	*237*, 181–1771
2209	250–750	*0*	*188*, 87–781	*0*	*206*, 456–1115	*0*	*26*, 1012–2041

Table 5.4: Results for the various evolution scenarios for double white dwarfs with two unstable mass-transfer episodes. The range of observed $\Delta\tau$ is the observed cooling-age difference $\pm 50\%$. Columns labelled 1 through 6 give the number of model solutions for each scenario followed by the range in age difference of these solutions in Megayears. The columns with $\gamma_a\gamma_d$ and $\gamma_d\gamma_d$ were left out, because they do not contain any solutions. For the different mechanisms we demanded that $1.54 < \gamma_s < 1.71$, $0.95 < \gamma_a < 1.05$, $0.95 < \gamma_d < 1.05$ and $0.90 < \alpha_{ce} < 1.10$.

to 0.25–1.75 in order to get the first solution for just a single system with one of these two mechanisms. All mechanisms that are listed in Table 5.4 provide a solution for more than one observed system, and each observed system has at least one mechanism that provides it with a solution. The number of solutions per combination of mechanism and observed system ranges from zero to several hundreds and the age differences of the accepted models lie between 36 Myr and more than 12 Gyr.

We will use Table 5.4 to compare the age differences of the models to the observed values and use this comparison to judge the 'quality' of the model solutions. We will assume that if the age difference in the model lies within 50% of the measured cooling-age difference (the range in the second column of Table 5.4) that this is a good agreement which we will assign the symbol '+'. If the difference is larger than that, but smaller than a factor of five we will call it 'close' and assign a '$\sim$'. Cases where the nearest solution has an age difference that is more than a factor of five from the observed value is considered 'bad' and assigned the symbol '$-$'. If we do this for all cases, we obtain the second symbol for each entry in Table 5.3, which we can use to directly compare the quality of the solutions for each mechanism and each observed system.

We find that these results are robust, in the sense that if we expand the ranges for γ and $\alpha_{\rm ce}$ with a factor of two, the optimum result does not change, although there are more mechanisms contributing to this result, *i.e.* the column 'opt. result' remains unchanged, while the number of labels in the last column increases. The same is even true if we expand the ranges for $\alpha_{\rm ce}$ with a factor of ten instead of two. If we use a factor of 2 in stead of 5 for the upper limit of a 'close solution', we need to expand the ranges for γ and $\alpha_{\rm ce}$ with a factor of 2.6 to get tildes at the same places in the column 'optimum result' as shown in Table 5.3.

We conclude that our models can form double white dwarfs with the observed masses and orbital periods if we invoke multiple formation mechanisms. Our calculations show that if we double the allowed ranges for γ and $\alpha_{\rm ce}$ with respect to those used in Tables 5.3 and 5.4, it is even possible to form all observed systems with mechanisms $\gamma_{\rm s}\gamma_{\rm s}$ only or $\gamma_{\rm d}\gamma_{\rm a}$ only. If we demand in addition that the age differences of the model systems lie within 50% of the observed value, we can still explain the formation of most observed systems, while for some double white dwarfs this becomes difficult. This is the case with WD 0135–052, WD 1204+450, WD 1704+481b and to a lesser extent WD 1101+364. These four systems can usually either be explained with an acceptable age difference but a value for γ that is off, or an acceptable γ and an age difference that lies (sometimes much) more that 50% from the observed value.

5.6.5 Description of the individual solutions

The goal of this research is, of course, to find out whether we can somehow explain the formation of the observed double white dwarfs. If this is the case, we hope to learn firstly which mechanisms govern this formation and secondly what the progenitor systems are that evolve to the observed white-dwarf binaries. Although we do not find one mechanism that

can explain all observed systems in a satisfying way, we present here the evolution of some of the best solutions among our calculations. We list the five main parameters that describe the evolutionary scenario of a solution (two initial masses, the initial period and the two envelope-ejection parameters) and two minor ones (the actual final masses that the models give) in a table. Because we present solutions for six different formation mechanisms and eleven observed systems that may have more than one 'best' solution this table is quite large. This is particularly the case because we want to remove the arbitrarily chosen boundaries that we have used so far to qualify a solution. We therefore list at least one solution per mechanism per system, independent of how far its parameters lie from the preferred values. We chose to present the complete table as Table 5.6 in Sect. 5.9 and give an excerpt of it in Table 5.5. In this way, the reader may verify how particular models do or do not work.

We manually picked the 'best' solutions for a given combination of formation mechanism and observed system, in the sense that the solution has a γ close to unity (or, in case of $\gamma_{\rm s}$, close to 1.63), an $\alpha_{\rm ce}$ close to the range of 0.5–1.0 and an age difference that is close to the observed value. In the cases where there are different solutions that each excel in a different one of these three properties, we may present more than one solution. If there are several solutions that are similar on these grounds, we prefer those with lower initial masses. We then leave it to the reader to judge whether these solutions are acceptable. The values for $q_{\rm 2f}$ and $P_{\rm f}$ are identical to the value listed in Table 5.1 and therefore not shown in Table 5.5. The intermediate masses are also left out of the table, because no matter is accreted during the dynamical mass loss and thus $M_{\rm 1m} = M_{\rm 1f}$ and $M_{\rm 2m} = M_{\rm 2i}$ in our models. The numbering of the solutions in the excerpted table is the same as in the complete version.

We tabulate 120 solutions in total. The initial binaries have primary masses between $1.09\,M_\odot$ and $5.42\,M_\odot$, though there are only two solutions with $M_{\rm 1i} > 4\,M_\odot$. Of the 120 solutions, 50% have an initial primary mass less than $2\,M_\odot$ and 87% of the primaries are less massive than $3\,M_\odot$. Thus, the models suggest that the double white dwarfs are formed by low-mass stars, as may be required to explain the observed numbers of these binaries. Of the initial systems, 90% have orbital periods between 10 and 1000 days. All proposed solutions undergo a first envelope ejection described by angular-momentum balance of some sort, which allows the orbital period to increase during such a mass-transfer phase. In 61% of the selected solutions this is the case, and for 45% of the solutions the intermediate orbital period is twice or more as long as the initial period. Of the 120 solutions listed, 51% have initial mass ratios $q_{\rm 1i} > 1.07$ while only 17% have $q_{\rm 1i} > 1.2$. A bit worrying may be that for 24% of the solutions, $q_{\rm 1i} < 1.03$. It could be that these initial systems evolve into a double common envelope, where the two white dwarfs are formed simultaneously and the second white dwarf is undermassive. On the other hand, because the orbital period increases in most of the first envelope ejections, the outcome of such a common envelope is uncertain. One should treat these solutions with some scepticism.

We now briefly discuss the solutions for each observed system that are listed in the excerpted Table 5.5. For WD 0135–052 it is difficult to get both γ's close to the preferred values. In solution 5, $\gamma_{\rm a1}$ is off while $\alpha_{\rm ce2}$ is acceptable, solution 8 has a $\gamma_{\rm a1}$ not too far from unity but $\gamma_{\rm a2}$ is off and for solution 9 the reverse is the case. The three solutions have

Nr.	WD	Meth.	γ_1	γ_2, $\alpha_{\rm ce2}$	$\Delta\tau$ Myr	$\Delta(\Delta\tau)$ %	τ_2 Gyr	$M_{1\rm i}$ $M_\odot$	$M_{2\rm i}$ $M_\odot$	$q_{1\rm i}$	$P_{\rm i}$ d	$q_{2\rm m}$	$P_{\rm m}$ d	$M_{1\rm f}$ $M_\odot$	$M_{2\rm f}$ $M_\odot$
5	0135	$\gamma_{\rm a}\alpha_{\rm ce}$	1.31	0.87	377	7.7	3.14	1.51	1.46	1.04	504.5	3.12	264.7	0.47	0.42
8	0135	$\gamma_{\rm a}\gamma_{\rm a}$	1.15	0.66	524	50.	1.36	2.46	2.06	1.20	429.8	3.56	110.9	0.58	0.52
9	0135	$\gamma_{\rm a}\gamma_{\rm a}$	1.40	0.99	454	30.	5.37	1.28	1.25	1.03	596.6	2.68	313.7	0.47	0.42
17	0136	$\gamma_{\rm s}\gamma_{\rm s}$	1.51	1.61	450	0.0	2.39	1.70	1.59	1.07	106.1	4.36	371.4	0.37	0.46
22	0136	$\gamma_{\rm d}\alpha_{\rm ce}$	0.95	1.00	299	34.	2.68	1.59	1.53	1.04	75.88	4.50	269.5	0.34	0.43
28	0957	$\gamma_{\rm a}\alpha_{\rm ce}$	1.02	0.97	321	1.2	1.65	1.90	1.79	1.07	20.15	6.31	27.07	0.28	0.32
30	0957	$\gamma_{\rm d}\alpha_{\rm ce}$	1.00	1.00	427	31.	1.16	2.34	2.00	1.17	8.110	6.66	28.52	0.30	0.34
38	1101	$\gamma_{\rm a}\alpha_{\rm ce}$	1.17	0.96	308	43.	1.57	1.95	1.81	1.08	127.1	4.63	45.28	0.39	0.34
50	1115	$\gamma_{\rm a}\alpha_{\rm ce}$	1.01	1.00	239	49.	0.50	3.70	2.94	1.26	1693.	3.58	980.4	0.82	0.69
54	1115	$\gamma_{\rm d}\alpha_{\rm ce}$	0.97	0.93	240	50.	0.32	5.42	3.42	1.58	201.2	3.84	1012.	0.89	0.75
55	1115	$\gamma_{\rm d}\gamma_{\rm a}$	1.45	1.00	214	34.	1.11	2.40	2.22	1.08	3567.	2.49	2032.	0.89	0.75
58	1204	$\gamma_{\rm s}\gamma_{\rm s}$	1.83	1.30	71	11.	0.25	3.94	3.47	1.14	69.23	5.92	56.81	0.59	0.51
65	1204	$\gamma_{\rm d}\gamma_{\rm a}$	1.10	0.34	74	7.8	0.26	3.89	3.42	1.14	38.82	5.96	51.85	0.57	0.50
68	1349	$\gamma_{\rm s}\gamma_{\rm s}$	1.51	1.63	426	0.0	2.68	1.61	1.53	1.05	115.0	4.20	385.7	0.37	0.46
74	1349	$\gamma_{\rm d}\alpha_{\rm ce}$	0.97	0.98	64	0.0	2.45	1.59	1.57	1.01	120.4	4.31	373.4	0.37	0.46
84	1414	$\gamma_{\rm d}\alpha_{\rm ce}$	0.95	0.71	188	5.9	0.43	3.51	3.09	1.14	70.81	5.99	358.3	0.52	0.66
92	1704a	$\gamma_{\rm a}\alpha_{\rm ce}$	1.01	0.60	52	360.	1.41	2.06	1.88	1.09	40.37	3.66	65.66	0.51	0.36
98	1704a	$\gamma_{\rm d}\gamma_{\rm a}$	1.37	0.63	2	110.	1.48	1.93	1.86	1.04	294.5	3.33	120.2	0.56	0.39
103	1704b	$\gamma_{\rm a}\gamma_{\rm a}$	0.98	0.99	199	895.	2.59	1.59	1.57	1.01	256.0	3.81	664.0	0.41	0.59
114	2209	$\gamma_{\rm a}\alpha_{\rm ce}$	0.98	0.54	517	3.3	1.45	2.37	1.95	1.21	148.5	3.55	168.2	0.55	0.55
115	2209	$\gamma_{\rm a}\gamma_{\rm a}$	1.00	1.00	612	22.	1.65	2.28	1.86	1.23	968.0	2.95	1061.	0.63	0.63

Table 5.5: Selected model solutions for the double envelope-ejection scenario. This table is a excerpt of the total list of 120 entries. The first eight columns show the number of the entry, the double white dwarf that the model is a solution to, the mechanism used, the two envelope-ejection parameters, the age difference of the two components in the model ($\Delta\tau$) in Myr, the relative difference between the observed and model age difference, defined as $\Delta(\Delta\tau) \equiv \left|\frac{\Delta\tau_{\rm mod}-\Delta\tau_{\rm obs}}{\Delta\tau_{\rm obs}}\right|$ in %, the time of the formation of the double white dwarf since the ZAMS (τ_2) in Gyr. The last eight columns list binary parameters: the initial (ZAMS) masses, mass ratio and orbital period, the intermediate mass ratio and period and the final masses.

acceptable age differences. The solutions 17 and 22 for WD 0136+768 and 28 and 30 for WD 0957–666 have values close to desired for both envelope-ejection parameters and the $\Delta\tau$. Solution 38 is by far the best solution for WD 1101+364, though $\gamma_{\rm a1}$ is not very close to unity. Solutions 50 and 54 for PG 1115+116 have envelope-ejection parameters close to the desired values and acceptable $\Delta\tau$'s, though the initial masses are high. This is in accordance with the fact that these stars are required to form white dwarfs with masses as high as $0.7\,M_{\odot}$. Solution 55 shows that one has to accept a large value for $\gamma_{\rm d1}$ in order to find a solution with significantly smaller initial masses.

Solutions 58 and 65 are the only two for WD 1204+450 from the complete table that have age differences within 50% of the observed value, and still the envelope-ejection parameters are far from the desired values. There seems to be no convincing solution for this system in our models. For WD 1349+144 the cooling ages are not known, although the similar Balmer spectra of the two components (Karl et al. 2003a) seem to suggest that $\Delta\tau$ is small. Solution 74 (which is the same as solutions 66, 69 and 70 in the complete table but with a different definition of γ) has a small age difference of 64 Myr but also a disturbingly small initial mass ratio of 1.01. Since the orbital period is supposed to increase with more than 200% during the first dynamical mass-loss episode, it is uncertain how this initial system would evolve. Solution 68 has a larger initial mass ratio, but also a larger age difference. The complete table shows solutions for WD 1349+144 with values for $\Delta\tau$ of about 64, 140, 230, 370 and 450 Myr, so that they span a large range within which the actual age difference is likely to lie. For HE 1414–0848 we find an acceptable solution for almost all mechanisms and 4 out of the 8 solutions listed in the complete table refer to the same solution with different values for the envelope-ejection parameters for the different mechanisms. Since the observed age difference of WD 1704+481a is -20 Myr, we have introduced a system with the reversed mass ratio (WD 1704+481b) and hence an age difference of $+20$ Myr. Interestingly enough, the solutions with closest age difference for WD 1704+481b have $\Delta\tau \gtrsim 180$ Myr, a factor of nine or more than observed, as is the case for solution 103. However, for WD 1704+481a we find solutions with good envelope-ejection parameters and an age difference of around 50 Myr, like solution 92, and with parameters that are more off, but with an age difference of only 2 Myr as in solution 98. The system WD 1704+481a seems therefore better explained by our models than the system with the reverse mass ratio. Because the observed cooling-age difference is only in the order of a few per cent of the total age of the system (see Table 5.1), a change of 10% in the determined cooling age of one of the two components is sufficient to alter the age difference from -20 Myr to $+50$ Myr. For HE 2209–1444, we present solutions 114 and 115, that have envelope-ejection parameters close to the desired values and an age difference that agrees very well with the observed cooling-age difference.

Summarising, we find that for the ten observed systems, two can only be explained with values for γ that differ appreciably from the desired values (WD 0135–052 (31%) and WD 1204+450 (20%)). For two systems the values of the envelope-ejection parameters and age difference may not be too convincing, partially due to uncertainties in the observations (WD 1101+364 ($\gamma = 1.17$) and WD 1704+481(a) ($\Delta\tau = 52$ Myr)) and the other six

systems (WD 0136+768, WD 0957–666, PG 1115+116, WD 1349+144, HE 1414–0848 and HE 2209–1444) can be well explained ($\Delta\gamma \leq 5\%$, $\Delta(\Delta\tau) \leq 50\%$) by one or more of the described mechanisms, although several of these mechanisms are needed to account for all six observed systems.

5.7 Discussion

5.7.1 Comparison to other work

In this chapter we investigate the formation scenarios for double white dwarfs first put forward by Nelemans et al. (2000). Their paper is based on three double white dwarfs and we expanded this to the set of ten that has been observed so far. Rather than using analytical approximations, we used a stellar evolution code to do most of the calculations. One of the advantages of this is that we calculate the binding energy of the donor star at the onset of a common envelope, so that we can directly calculate the common-envelope parameter $\alpha_{\rm ce}$ without the need of the envelope-structure parameter $\lambda_{\rm env}$, that turns out to be far from constant during the evolution of a star (see Fig. 5.4). This allows us to demand physically acceptable values for $\alpha_{\rm ce}$.

The use of an evolution code instead of analytical expressions obviously gives more accurate values for instance for the core-mass–radius relation. Our main conclusions are nevertheless the same as that of Nelemans et al. (2000), even though they are based on a larger sample of observed binaries: stable, conservative mass transfer followed by a common envelope with spiral-in based on energy balance cannot explain the formation of the observed systems, and neither can the $\alpha_{\rm ce}\alpha_{\rm ce}$ scenario of two such spiral-ins. We therefore arrive at the same conclusion, that a third mass-transfer mechanism is needed to explain the first mass-transfer phase of these systems and we use their envelope-ejection prescription, based on angular-momentum conservation (Eq. 5.8).

Nelemans & Tout (2005) use more advanced fits to stellar models, but still need the envelope-structure parameter $\lambda_{\rm env}$ so that it is difficult to interpret the values they find for the product $\alpha_{\rm ce}\,\lambda_{\rm env}$. They use the same ten observed double-lined white dwarfs as we do, next to a number of single-lined systems. They also conclude that a γ-envelope ejection is needed for the first mass transfer and find, like Nelemans et al. (2000), that all observed systems can be explained by $1.50 < \gamma_{\rm s} < 1.75$, for both mass-transfer phases. Alternatively the second mass-transfer episode can be reconstructed with $0 < \alpha_{\rm ce}\,\lambda_{\rm env} < 4$. However, Nelemans & Tout (2005) do not discuss the coupling of the two solution sets for the two phases, *e.g.* it is not described how many of the solutions with $1.50 < \gamma_{\rm s1} < 1.75$ have $\gamma_{\rm s2}$ in the same range. We introduced slightly different definitions for the γ-algorithm in Eqs. 5.10 and 5.11, so that we can demand that γ is in the order of unity. We find indeed that we can explain the observed masses and periods with $\gamma_{\rm a}, \gamma_{\rm d} \sim 1.0$.

We add to the treatment by Nelemans et al. (2000) and Nelemans & Tout (2005) in demanding that, in addition to the masses and orbital period, the age difference of our models must be comparable to the observed value. It turns out that this puts a strong constraint on

the selection of model solutions for all three definitions of γ. However, we can still explain most systems, although we need mass loss described by both $\gamma_{\rm a}$ and $\gamma_{\rm d}$ to do so.

The description for dynamical mass loss with the specific angular momentum of the donor star (Eq.5.11) is similar to the scenario of a tidally-enhanced stellar wind (Tout & Eggleton 1988b,a). In this scenario the mass loss from a (sub)giant due to stellar wind increases up to a factor of 150 with respect to Reimers' empirical law (Reimers 1975) when the star is close to filling its Roche lobe. Tout & Eggleton (1988b) postulate the enhanced wind to explain for instance observed pre-Algol systems such as Z Her. In this binary the more evolved star is less massive than its main-sequence companion by 10%, while only filling about half of its Roche lobe.

Han (1998) uses this tidally-enhanced stellar wind in his research on the formation of double degenerates and concludes, among others, that his models that include this enhanced stellar wind give a better explanation of the observed double-degenerate binaries than models that do not include it. The enhanced mass loss makes subsequent mass transfer due to Roche-lobe overflow dynamically more stable. Envelope ejection due to dynamical mass loss is then more often prevented and binaries evolve to longer orbital periods before the second mass transfer, which is then more likely to produce a CO white dwarf. Thus, the enhanced-wind scenario increases the ratio of CO-helium double white dwarfs to helium-helium binaries.

Envelope ejection described by Eq.5.11 is essentially the same as the limiting case in which most or all of the envelope is lost due to an enhanced wind. Tout & Eggleton (1988b) show that the tidally-enhanced wind can indeed prevent Roche-lobe overflow altogether because the envelope is completely lost by the wind and the core becomes exposed. Without an enhanced wind, this happens for binaries with an initial mass ratio of 2 or less only if they have initial periods of more than 1000 days. When the tidally-enhanced wind is included, core exposure without Roche-lobe overflow occurs for these binaries with initial periods as short as 10–30 days.

5.7.2 Alternative formation scenario for massive white dwarfs

In the present research we have assumed that after envelope ejection occurs, the core of the Roche-lobe filling giant becomes a helium or CO white dwarf with no further evolution other than cooling. However, helium cores that are more massive than $0.33\,M_\odot$ are not degenerate and those more massive than about $0.5\,M_\odot$ will burn most of the helium in their cores and produce a CO core. If exposed, they are in effect helium stars. For helium stars less massive than about $0.75\,M_\odot$ the radius hardly changes during the helium (shell) burning, but stars more massive than that experience a giant phase. This is shown in Fig. 5.16a, where the radius of a selection of helium-star models is plotted as a function of the CO-core mass. For the more massive models in the Figure, the stars expand from the order of a few tenths of a solar radius to a few hundred solar radii. Thus, helium stars with a core mass $M_{\rm CO} \gtrsim 0.7\,M_\odot$ may and those with $M_{\rm CO} \gtrsim 0.8\,M_\odot$ must become giants and could fill their Roche lobes as a consequence. The black dots in Fig. 5.16a indicate the maximum

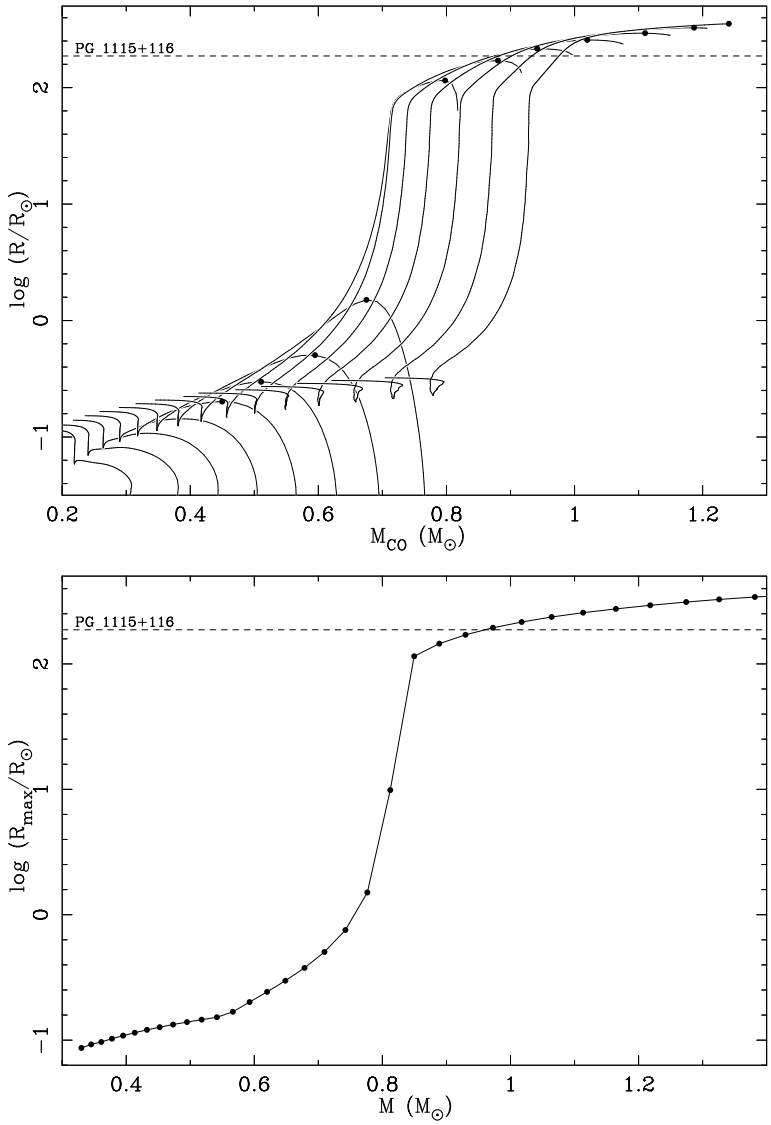

Figure 5.16: *Upper panel* (**a**): The radius of a helium star as a function of its CO-core mass, for a selection of 15 models with total masses between 0.41 and $1.43\,M_{\odot}$. The dots show where the maximum radii are obtained and are used for the lower panel. The dashed line is the Roche-lobe radius for the intermediate primary of PG 1115+116 according to our solution 54. *Lower panel* (**b**): The maximum radius of a low-mass helium star as a function of its total mass, for a selection of 33 models with masses between 0.33 and $1.4\,M_{\odot}$. The dots are the data points, the solid line connects them to guide the eye.

radius for a certain helium-star model and if we plot the maximum radii of these and other models as a function of the total mass of the star, we obtain Fig. 5.16b. This Figure shows that a helium star more massive than about $0.83\,M_\odot$ must evolve through a giant phase (see *e.g.* Paczyński 1971; Habets 1986).

There are two double white dwarfs in the observed sample that have $M_2 > 0.6\,M_\odot$, PG 1115+116 (both components) and HE 1414–0848 (the secondary). The evolutionary scenarios in Table 5.5 suggest that all these stars emerge from the envelope ejection with a CO core, except solution 54 for PG 1115+116, where the $5.42\,M_\odot$ primary progenitor produces a $0.89\,M_\odot$ helium core before helium ignites. The Roche-lobe radius of the $0.89\,M_\odot$ helium star in the intermediate binary is $187\,R_\odot$ according to this solution and shown as the dashed line in Fig. 5.16.

The Figure shows that the mass and Roche-lobe radius of this star are in the proper range to fit the helium-giant scenario. We show a small numerical example to illustrate this scenario. The dot in Fig. 5.16a at $M_{\rm CO}$=$0.88\,M_\odot$ and $R = 171\,R_\odot$, just below the dashed line, is the point where the model of $0.93\,M_\odot$ from our grid of helium-star models reaches its largest radius. The star thus has an envelope mass of only $0.05\,M_\odot$ and with a mass ratio of almost 4, mass transfer would be stable (Eq. 57 of Hurley et al. (2002)). If we assume that this star would be the primary of solution 54 in Table 5.5 and that $0.04\,M_\odot$ would be transferred conservatively, the orbital period after the mass transfer would be 1115 d, so that the period would not change drastically and the ensuing second envelope ejection would be similar to the one found in solution 54. If the mass were lost in a wind, which could be triggered by the fact that the star expands, but for which the Roche lobe need not be filled, the orbital period would change less than 2% to 1031 d. It seems that a complete, detailed model could be found to explain this system along these lines.

Both components in HE 1414–0848 are DA white dwarfs (Napiwotzki et al. 2002), as is the secondary of PG 1115+116. The hydrogen in the spectra of these stars suggests that the surface layer that formed after the envelope was ejected is still present. However, the primary in PG 1115+116 is a DB white dwarf. As Maxted et al. (2002a) point out, the giant phase of a helium star could be the explanation for this and the scenario sketched above might indeed describe the formation of this system.

5.8 Conclusions

We investigated several formation scenarios for the observed ten double white dwarfs listed in Table 5.1 and present the best models in Table 5.5. We draw four main conclusions:

- The scenario where the first mass-transfer phase is stable and conservative, followed by a common envelope with spiral-in based on energy conservation (see Eq. 5.4) cannot explain the observed masses and periods of all double white dwarfs.
- The scenario with envelope ejection based on angular-momentum conservation followed by ejection of the second envelope with either energy or angular-momentum balance can explain the observed masses and orbital periods very well.

- Including the age difference as a quality criterion for model solutions produces strong restrictions to the selection of solutions and makes it much more difficult to find acceptable solutions.
- By taking into account the possibilities that mass is lost either from the donor or from the accretor, we show that the formation of the close double white dwarfs can be explained if the mass carries the specific angular momentum of one of the two binary members.

Acknowledgements We thank P.P. Eggleton for making his binary evolution code available to us.

5.9 Appendix: Table of model solutions

Nr.	Meth.	γ_1	γ_2, $\alpha_{\rm ce2}$	$\Delta\tau$ Myr	$\Delta\Delta\tau$ %	τ_2 Gyr	$M_{1\rm i}$ $M_\odot$	$M_{2\rm i}$ $M_\odot$	$q_{1\rm i}$	$P_{\rm i}$ d	$q_{2\rm m}$	$P_{\rm m}$ d	$M_{1\rm f}$ $M_\odot$	$M_{2\rm f}$ $M_\odot$
WD 0135–052														
1	$\gamma_{\rm s}\alpha_{\rm ce}$	2.02	0.87	377	7.7	3.14	1.51	1.46	1.04	504.5	3.12	264.7	0.47	0.42
2	$\gamma_{\rm s}\alpha_{\rm ce}$	0.81	0.61	899	157.	2.17	2.11	1.63	1.29	33.22	3.20	372.5	0.51	0.46
3	$\gamma_{\rm s}\gamma_{\rm s}$	1.88	1.62	610	74.	1.36	2.55	2.06	1.24	300.5	3.56	110.9	0.58	0.52
4	$\gamma_{\rm s}\gamma_{\rm s}$	2.00	1.74	523	49.	3.29	1.51	1.44	1.05	503.9	3.08	268.9	0.47	0.42
5	$\gamma_{\rm a}\alpha_{\rm ce}$	1.31	0.87	377	7.7	3.14	1.51	1.46	1.04	504.5	3.12	264.7	0.47	0.42
6	$\gamma_{\rm a}\alpha_{\rm ce}$	1.29	0.86	523	49.	3.29	1.51	1.44	1.05	503.9	3.08	268.9	0.47	0.42
7	$\gamma_{\rm a}\alpha_{\rm ce}$	1.28	0.85	667	91.	3.43	1.51	1.42	1.07	503.3	3.04	272.3	0.47	0.42
8	$\gamma_{\rm a}\gamma_{\rm a}$	1.15	0.66	524	50.	1.36	2.46	2.06	1.20	429.8	3.56	110.9	0.58	0.52
9	$\gamma_{\rm a}\gamma_{\rm a}$	1.40	0.99	454	30.	5.37	1.28	1.25	1.03	596.6	2.68	313.7	0.47	0.42
10	$\gamma_{\rm a}\gamma_{\rm a}$	1.29	0.81	523	49.	3.29	1.51	1.44	1.05	503.9	3.08	268.9	0.47	0.42
11	$\gamma_{\rm a}\gamma_{\rm a}$	1.31	0.80	377	7.7	3.14	1.51	1.46	1.04	504.5	3.12	264.7	0.47	0.42
12	$\gamma_{\rm d}\alpha_{\rm ce}$	1.36	0.89	261	25.	3.02	1.51	1.48	1.03	505.1	3.16	260.8	0.47	0.42
13	$\gamma_{\rm d}\gamma_{\rm a}$	1.40	0.89	341	2.6	4.07	1.38	1.35	1.03	553.8	2.89	288.6	0.47	0.42
14	$\gamma_{\rm d}\gamma_{\rm a}$	1.00	0.98	2067	491.	3.43	2.06	1.42	1.45	155.3	2.72	490.6	0.52	0.47

Table 5.6: Selected model solutions for the double envelope-ejection scenario. This is the full table with 120 entries of which Table 5.5 is an excerpt. The first eight columns show the number of the entry, the double white dwarf that the model is a solution to, the mechanism used, the two envelope-ejection parameters, the age difference of the two components in the model ($\Delta\tau$) in Myr, the relative difference between the observed and model age difference, defined as $\Delta\Delta\tau \equiv \left|\frac{\Delta\tau_{\rm mod}-\Delta\tau_{\rm obs}}{\Delta\tau_{\rm obs}}\right|$ in %, the time of the formation of the double white dwarf since the ZAMS (τ_2) in Gyr. The last eight columns list binary parameters: the initial (ZAMS) masses, mass ratio and orbital period, the intermediate mass ratio and period and the final masses. See Sect. 5.6.5 for more details. *(continued on the next pages)*

Nr.	Meth.	γ_1	γ_2, $\alpha_{\rm ce2}$	$\Delta\tau$ Myr	$\Delta\Delta\tau$ %	τ_2 Gyr	$M_{\rm 1i}$ $M_\odot$	$M_{\rm 2i}$ $M_\odot$	$q_{\rm 1i}$	$P_{\rm i}$ d	$q_{\rm 2m}$	$P_{\rm m}$ d	$M_{\rm 1f}$ $M_\odot$	$M_{\rm 2f}$ $M_\odot$
WD 0136+768														
15	$\gamma_{\rm s}\alpha_{\rm ce}$	1.48	1.01	449	0.2	3.73	1.44	1.38	1.04	72.27	4.16	265.9	0.33	0.42
16	$\gamma_{\rm s}\gamma_{\rm s}$	1.53	1.53	300	33.	2.68	1.59	1.53	1.04	64.22	4.60	235.6	0.33	0.42
17	$\gamma_{\rm s}\gamma_{\rm s}$	1.51	1.61	450	0.0	2.39	1.70	1.59	1.07	106.1	4.36	371.4	0.37	0.46
18	$\gamma_{\rm a}\alpha_{\rm ce}$	0.91	0.99	317	30.	3.90	1.40	1.37	1.03	74.07	4.11	269.8	0.33	0.42
19	$\gamma_{\rm a}\gamma_{\rm a}$	0.92	0.99	321	29.	5.24	1.28	1.27	1.01	171.1	3.39	532.9	0.37	0.47
20	$\gamma_{\rm a}\gamma_{\rm a}$	0.90	1.01	460	2.2	5.37	1.28	1.25	1.03	170.9	3.35	540.8	0.37	0.47
21	$\gamma_{\rm d}\alpha_{\rm ce}$	0.93	0.99	317	30.	3.90	1.40	1.37	1.03	74.07	4.11	269.8	0.33	0.42
22	$\gamma_{\rm d}\alpha_{\rm ce}$	0.95	1.00	299	34.	2.68	1.59	1.53	1.04	75.88	4.50	269.5	0.34	0.43
23	$\gamma_{\rm d}\gamma_{\rm a}$	0.94	0.95	599	33.	4.67	1.35	1.30	1.04	162.5	3.48	517.9	0.37	0.47
24	$\gamma_{\rm d}\gamma_{\rm a}$	0.93	0.99	574	28.	5.24	1.30	1.27	1.03	168.8	3.39	532.9	0.37	0.47
WD 0957–666														
25	$\gamma_{\rm s}\alpha_{\rm ce}$	1.74	1.00	341	4.8	1.16	2.25	2.00	1.12	15.22	6.66	28.52	0.30	0.34
26	$\gamma_{\rm s}\alpha_{\rm ce}$	1.62	1.00	427	31.	1.16	2.34	2.00	1.17	8.110	6.66	28.52	0.30	0.34
27	$\gamma_{\rm s}\gamma_{\rm s}$	1.67	1.62	328	0.9	7.77	1.14	1.13	1.01	27.78	3.99	56.90	0.28	0.32
28	$\gamma_{\rm a}\alpha_{\rm ce}$	1.02	0.97	321	1.2	1.65	1.90	1.79	1.07	20.15	6.31	27.07	0.28	0.32
29	$\gamma_{\rm a}\gamma_{\rm a}$	1.04	1.00	309	4.9	9.19	1.09	1.07	1.01	100.2	3.19	195.1	0.34	0.38
30	$\gamma_{\rm d}\alpha_{\rm ce}$	1.00	1.00	427	31.	1.16	2.34	2.00	1.17	8.110	6.66	28.52	0.30	0.34
31	$\gamma_{\rm d}\alpha_{\rm ce}$	1.06	1.00	341	4.8	1.16	2.25	2.00	1.12	15.22	6.66	28.52	0.30	0.34
32	$\gamma_{\rm d}\alpha_{\rm ce}$	1.02	0.71	334	2.8	2.25	1.70	1.61	1.05	13.89	5.70	35.74	0.28	0.32
33	$\gamma_{\rm d}\gamma_{\rm a}$	1.05	1.00	309	4.9	9.19	1.09	1.07	1.01	100.2	3.19	195.1	0.34	0.38
WD 1101+364														
34	$\gamma_{\rm s}\alpha_{\rm ce}$	1.95	0.89	487	126.	1.71	1.98	1.76	1.12	122.8	4.51	48.24	0.39	0.34
35	$\gamma_{\rm s}\alpha_{\rm ce}$	2.08	1.00	208	3.3	2.38	1.63	1.59	1.03	118.7	4.33	39.18	0.37	0.32
36	$\gamma_{\rm s}\gamma_{\rm s}$	1.81	1.30	312	45.	0.80	2.72	2.28	1.20	44.86	5.82	30.61	0.39	0.34
37	$\gamma_{\rm s}\gamma_{\rm s}$	2.13	1.61	216	0.5	4.51	1.33	1.32	1.01	183.1	3.47	62.90	0.38	0.33
38	$\gamma_{\rm a}\alpha_{\rm ce}$	1.17	0.96	308	43.	1.57	1.95	1.81	1.08	127.1	4.63	45.28	0.39	0.34
39	$\gamma_{\rm a}\gamma_{\rm a}$	1.40	0.74	208	3.3	6.12	1.22	1.20	1.01	164.1	3.27	55.68	0.37	0.32
40	$\gamma_{\rm d}\alpha_{\rm ce}$	1.33	1.00	137	36.	3.27	1.46	1.44	1.01	112.2	4.04	35.90	0.36	0.31
41	$\gamma_{\rm d}\alpha_{\rm ce}$	1.26	1.01	256	19.	1.52	1.95	1.83	1.07	127.2	4.69	43.20	0.39	0.34
42	$\gamma_{\rm d}\alpha_{\rm ce}$	1.41	1.00	317	47.	8.09	1.13	1.12	1.01	91.07	3.35	28.96	0.33	0.29
43	$\gamma_{\rm d}\gamma_{\rm a}$	1.51	0.95	299	39.	9.18	1.09	1.07	1.01	265.0	2.74	96.55	0.39	0.34
44	$\gamma_{\rm d}\gamma_{\rm a}$	1.39	0.71	227	5.6	4.29	1.35	1.33	1.01	217.1	3.41	76.52	0.39	0.34
PG 1115+116														
45	$\gamma_{\rm s}\alpha_{\rm ce}$	1.79	1.00	239	49.	0.50	3.70	2.94	1.26	1693.	3.58	980.4	0.82	0.69
46	$\gamma_{\rm s}\alpha_{\rm ce}$	1.95	1.00	203	27.	0.73	2.90	2.59	1.12	2088.	3.24	1017.	0.80	0.67
47	$\gamma_{\rm s}\alpha_{\rm ce}$	1.90	1.00	165	2.9	0.50	3.38	2.94	1.15	1960.	3.58	980.4	0.82	0.69
48	$\gamma_{\rm s}\gamma_{\rm s}$	1.79	1.62	198	24.	0.42	3.94	3.13	1.26	2127.	3.56	1240.	0.88	0.74
49	$\gamma_{\rm s}\gamma_{\rm s}$	1.93	1.62	156	2.4	0.54	3.21	2.87	1.12	2075.	3.49	1020.	0.82	0.69
50	$\gamma_{\rm a}\alpha_{\rm ce}$	1.01	1.00	239	49.	0.50	3.70	2.94	1.26	1693.	3.58	980.4	0.82	0.69
51	$\gamma_{\rm a}\alpha_{\rm ce}$	1.18	1.00	228	42.	0.73	2.94	2.59	1.14	2057.	3.24	1017.	0.80	0.67
52	$\gamma_{\rm a}\gamma_{\rm a}$	1.39	1.00	150	6.2	1.16	2.31	2.19	1.05	3581.	2.49	1952.	0.88	0.74
53	$\gamma_{\rm a}\gamma_{\rm a}$	1.00	0.62	230	44.	0.47	3.84	3.02	1.27	1945.	3.52	1162.	0.86	0.72
54	$\gamma_{\rm d}\alpha_{\rm ce}$	0.97	0.93	240	50.	0.32	5.42	3.42	1.58	201.2	3.84	1012.	0.89	0.75
55	$\gamma_{\rm d}\gamma_{\rm a}$	1.45	1.00	214	34.	1.11	2.40	2.22	1.08	3567.	2.49	2032.	0.89	0.75
56	$\gamma_{\rm d}\gamma_{\rm a}$	1.00	0.54	235	47.	0.32	5.28	3.42	1.54	190.8	3.89	758.6	0.88	0.74

Table 5.6: Selected model solutions for the double envelope-ejection scenario *(continued)*

Nr.	Meth.	γ_1	γ_2, $\alpha_{\rm ce2}$	$\Delta\tau$ Myr	$\Delta\Delta\tau$ %	τ_2 Gyr	$M_{1\rm i}$ $M_\odot$	$M_{2\rm i}$ $M_\odot$	$q_{1\rm i}$	$P_{\rm i}$ d	$q_{2\rm m}$	$P_{\rm m}$ d	$M_{1\rm f}$ $M_\odot$	$M_{2\rm f}$ $M_\odot$
WD 1204+450														
57	$\gamma_{\rm s}\alpha_{\rm ce}$	2.15	0.83	136	70.	5.37	1.27	1.25	1.01	630.3	2.65	274.3	0.47	0.41
58	$\gamma_{\rm s}\gamma_{\rm s}$	1.83	1.30	71	11.	0.25	3.94	3.47	1.14	69.23	5.92	56.81	0.59	0.51
59	$\gamma_{\rm a}\alpha_{\rm ce}$	1.45	0.87	138	72.	4.66	1.32	1.30	1.01	606.6	2.76	263.4	0.47	0.41
60	$\gamma_{\rm a}\gamma_{\rm a}$	0.63	0.65	225	181.	1.58	2.06	1.81	1.14	32.89	3.58	256.2	0.51	0.44
61	$\gamma_{\rm a}\gamma_{\rm a}$	0.78	0.72	491	514.	1.85	2.06	1.72	1.20	86.06	3.33	312.4	0.52	0.45
62	$\gamma_{\rm d}\alpha_{\rm ce}$	0.72	0.96	225	181.	1.58	2.06	1.81	1.14	32.89	3.58	256.2	0.51	0.44
63	$\gamma_{\rm d}\alpha_{\rm ce}$	1.47	0.87	138	72.	4.66	1.32	1.30	1.01	606.6	2.76	263.4	0.47	0.41
64	$\gamma_{\rm d}\gamma_{\rm a}$	1.49	0.97	136	70.	5.37	1.27	1.25	1.01	630.3	2.65	274.3	0.47	0.41
65	$\gamma_{\rm d}\gamma_{\rm a}$	1.10	0.34	74	7.8	0.26	3.89	3.42	1.14	38.82	5.96	51.85	0.57	0.50
WD 1349+144														
66	$\gamma_{\rm s}\alpha_{\rm ce}$	1.56	0.98	64	0.0	2.45	1.59	1.57	1.01	120.4	4.31	373.4	0.37	0.46
67	$\gamma_{\rm s}\alpha_{\rm ce}$	1.45	1.01	461	0.0	4.52	1.35	1.32	1.03	105.9	3.77	364.5	0.35	0.44
68	$\gamma_{\rm s}\gamma_{\rm s}$	1.51	1.63	426	0.0	2.68	1.61	1.53	1.05	115.0	4.20	385.7	0.37	0.46
69	$\gamma_{\rm s}\gamma_{\rm s}$	1.56	1.60	64	0.0	2.45	1.59	1.57	1.01	120.4	4.31	373.4	0.37	0.46
70	$\gamma_{\rm a}\alpha_{\rm ce}$	0.96	0.98	64	0.0	2.45	1.59	1.57	1.01	120.4	4.31	373.4	0.37	0.46
71	$\gamma_{\rm a}\alpha_{\rm ce}$	0.91	1.01	229	0.0	4.52	1.33	1.32	1.01	107.4	3.77	364.5	0.35	0.44
72	$\gamma_{\rm a}\gamma_{\rm a}$	0.91	1.00	143	0.0	5.37	1.27	1.25	1.01	173.1	3.35	540.8	0.37	0.47
73	$\gamma_{\rm a}\gamma_{\rm a}$	0.90	1.00	460	0.0	5.37	1.28	1.25	1.03	170.9	3.35	540.8	0.37	0.47
74	$\gamma_{\rm d}\alpha_{\rm ce}$	0.97	0.98	64	0.0	2.45	1.59	1.57	1.01	120.4	4.31	373.4	0.37	0.46
75	$\gamma_{\rm d}\alpha_{\rm ce}$	0.92	0.99	147	0.0	4.67	1.32	1.30	1.01	108.7	3.72	369.7	0.35	0.44
76	$\gamma_{\rm d}\gamma_{\rm a}$	0.93	0.94	368	0.0	4.67	1.33	1.30	1.03	164.7	3.48	517.9	0.37	0.47
77	$\gamma_{\rm d}\gamma_{\rm a}$	0.92	1.00	460	0.0	5.37	1.28	1.25	1.03	170.9	3.35	540.8	0.37	0.47
78	$\gamma_{\rm d}\gamma_{\rm a}$	0.92	1.00	143	0.0	5.37	1.27	1.25	1.01	173.1	3.35	540.8	0.37	0.47
HE 1414–0848														
79	$\gamma_{\rm s}\alpha_{\rm ce}$	1.52	0.71	188	5.9	0.43	3.51	3.09	1.14	70.81	5.99	358.3	0.52	0.66
80	$\gamma_{\rm s}\gamma_{\rm s}$	1.46	1.79	119	40.	0.90	2.52	2.40	1.05	467.4	4.09	1720.	0.59	0.75
81	$\gamma_{\rm s}\gamma_{\rm s}$	1.52	1.45	188	5.9	0.43	3.51	3.09	1.14	70.81	5.99	358.3	0.52	0.66
82	$\gamma_{\rm a}\alpha_{\rm ce}$	0.83	0.71	188	5.9	0.43	3.51	3.09	1.14	70.81	5.99	358.3	0.52	0.66
83	$\gamma_{\rm a}\gamma_{\rm a}$	0.91	0.99	177	12.	1.33	2.19	2.08	1.05	712.2	3.51	2170.	0.59	0.76
84	$\gamma_{\rm d}\alpha_{\rm ce}$	0.95	0.71	188	5.9	0.43	3.51	3.09	1.14	70.81	5.99	358.3	0.52	0.66
85	$\gamma_{\rm d}\gamma_{\rm a}$	0.95	0.99	219	9.5	1.33	2.22	2.08	1.07	701.3	3.51	2170.	0.59	0.76
86	$\gamma_{\rm d}\gamma_{\rm a}$	0.96	0.98	170	15.	1.28	2.22	2.11	1.05	702.1	3.55	2134.	0.59	0.76
WD 1704+481a														
87	$\gamma_{\rm s}\alpha_{\rm ce}$	1.67	0.60	52	360.	1.41	2.06	1.88	1.09	40.37	3.66	65.66	0.51	0.36
88	$\gamma_{\rm s}\alpha_{\rm ce}$	1.88	0.62	15	175.	1.17	2.19	2.00	1.09	93.52	3.79	66.89	0.53	0.37
89	$\gamma_{\rm s}\alpha_{\rm ce}$	2.05	0.43	7	135.	1.36	2.03	1.90	1.07	252.8	3.51	96.02	0.54	0.38
90	$\gamma_{\rm s}\gamma_{\rm s}$	1.67	1.52	52	360.	1.41	2.06	1.88	1.09	40.37	3.66	65.66	0.51	0.36
91	$\gamma_{\rm s}\gamma_{\rm s}$	1.88	1.50	15	175.	1.17	2.19	2.00	1.09	93.52	3.79	66.89	0.53	0.37
92	$\gamma_{\rm a}\alpha_{\rm ce}$	1.01	0.60	52	360.	1.41	2.06	1.88	1.09	40.37	3.66	65.66	0.51	0.36
93	$\gamma_{\rm a}\alpha_{\rm ce}$	1.13	0.62	15	175.	1.17	2.19	2.00	1.09	93.52	3.79	66.89	0.53	0.37
94	$\gamma_{\rm a}\gamma_{\rm a}$	1.01	0.55	52	360.	1.41	2.06	1.88	1.09	40.37	3.66	65.66	0.51	0.36
95	$\gamma_{\rm d}\alpha_{\rm ce}$	1.11	0.60	52	360.	1.41	2.06	1.88	1.09	40.37	3.66	65.66	0.51	0.36
96	$\gamma_{\rm d}\alpha_{\rm ce}$	1.24	0.62	15	175.	1.17	2.19	2.00	1.09	93.52	3.79	66.89	0.53	0.37
97	$\gamma_{\rm d}\alpha_{\rm ce}$	1.37	0.34	2	110.	1.48	1.93	1.86	1.04	294.5	3.33	120.2	0.56	0.39
98	$\gamma_{\rm d}\gamma_{\rm a}$	1.37	0.63	2	110.	1.48	1.93	1.86	1.04	294.5	3.33	120.2	0.56	0.39

Table 5.6: Selected model solutions for the double envelope-ejection scenario *(continued)*

Nr.	Meth.	γ_1	γ_2, $\alpha_{\rm ce2}$	$\Delta\tau$ Myr	$\Delta\Delta\tau$ %	τ_2 Gyr	$M_{\rm 1i}$ $M_\odot$	$M_{\rm 2i}$ $M_\odot$	$q_{\rm 1i}$	$P_{\rm i}$ d	$q_{\rm 2m}$	$P_{\rm m}$ d	$M_{\rm 1f}$ $M_\odot$	$M_{\rm 2f}$ $M_\odot$
WD 1704+481b														
99	$\gamma_{\rm s}\alpha_{\rm ce}$	1.65	0.53	292	1360.	0.73	2.83	2.59	1.09	47.21	6.37	161.8	0.41	0.58
100	$\gamma_{\rm s}\alpha_{\rm ce}$	1.74	0.76	285	1326.	0.75	2.76	2.55	1.08	49.12	6.40	107.3	0.40	0.57
101	$\gamma_{\rm s}\gamma_{\rm s}$	1.64	1.87	182	810.	2.23	1.68	1.65	1.01	212.1	4.08	478.6	0.41	0.58
102	$\gamma_{\rm a}\alpha_{\rm ce}$	0.96	1.05	465	2223.	1.00	2.62	2.31	1.14	44.02	6.10	63.28	0.38	0.54
103	$\gamma_{\rm a}\gamma_{\rm a}$	0.98	0.99	199	895.	2.59	1.59	1.57	1.01	256.0	3.81	664.0	0.41	0.59
104	$\gamma_{\rm a}\gamma_{\rm a}$	0.94	0.97	181	805.	2.23	1.68	1.65	1.01	284.0	3.88	892.6	0.43	0.61
105	$\gamma_{\rm d}\alpha_{\rm ce}$	1.03	0.15	182	810.	2.23	1.68	1.65	1.01	212.1	4.08	478.6	0.41	0.58
106	$\gamma_{\rm d}\alpha_{\rm ce}$	1.00	0.76	332	1562.	0.75	2.87	2.55	1.12	33.29	6.40	107.3	0.40	0.57
107	$\gamma_{\rm d}\gamma_{\rm a}$	0.95	0.97	181	805.	2.23	1.68	1.65	1.01	284.0	3.88	892.6	0.43	0.61
108	$\gamma_{\rm d}\gamma_{\rm a}$	1.00	0.99	199	895.	2.59	1.59	1.57	1.01	256.0	3.81	664.0	0.41	0.59
HE 2209–1444														
109	$\gamma_{\rm s}\alpha_{\rm ce}$	1.69	0.54	517	3.3	1.45	2.37	1.95	1.21	148.5	3.55	168.2	0.55	0.55
110	$\gamma_{\rm s}\alpha_{\rm ce}$	1.56	0.88	552	10.	0.75	3.79	2.55	1.49	87.01	4.48	113.8	0.57	0.57
111	$\gamma_{\rm s}\gamma_{\rm s}$	1.62	1.64	262	48.	1.20	2.37	2.16	1.09	150.0	3.93	304.6	0.55	0.55
112	$\gamma_{\rm s}\gamma_{\rm s}$	1.63	1.73	510	2.1	1.24	2.59	2.14	1.21	403.6	3.62	596.1	0.59	0.59
113	$\gamma_{\rm a}\alpha_{\rm ce}$	1.19	0.90	42	92.	1.20	2.19	2.16	1.01	121.7	4.08	97.10	0.53	0.53
114	$\gamma_{\rm a}\alpha_{\rm ce}$	0.98	0.54	517	3.3	1.45	2.37	1.95	1.21	148.5	3.55	168.2	0.55	0.55
115	$\gamma_{\rm a}\gamma_{\rm a}$	1.00	1.00	612	22.	1.65	2.28	1.86	1.23	968.0	2.95	1061.	0.63	0.63
116	$\gamma_{\rm a}\gamma_{\rm a}$	1.08	1.00	499	0.2	1.87	2.06	1.76	1.17	809.5	2.94	777.6	0.60	0.60
117	$\gamma_{\rm d}\alpha_{\rm ce}$	1.06	0.53	347	31.	1.35	2.31	2.03	1.14	80.61	3.76	169.5	0.54	0.54
118	$\gamma_{\rm d}\alpha_{\rm ce}$	1.12	0.88	559	12.	0.75	3.84	2.55	1.50	71.51	4.48	113.8	0.57	0.57
119	$\gamma_{\rm d}\gamma_{\rm a}$	1.15	0.86	744	49.	1.35	2.76	2.03	1.36	556.8	3.27	881.7	0.62	0.62
120	$\gamma_{\rm d}\gamma_{\rm a}$	1.00	0.81	731	46.	1.48	2.55	1.93	1.32	135.6	3.38	437.5	0.57	0.57

Table 5.6: Selected model solutions for the double envelope-ejection scenario *(continued)*

Hoofdstuk 6

Vorming en evolutie van compacte dubbelsterren

In dit proefschrift wordt onderzoek naar een bepaald type dubbelsterren beschreven. In hoofdstuk 6.1 geef ik een korte inleiding over het ontstaan en de evolutie van sterren in het algemeen en in hoofdstuk 6.2 beschrijf ik wat er verandert wanneer twee van deze sterren samen een dubbelster vormen. Ik zeg kort iets over de zogenaamde *bolvormige sterhopen*, in de centra waarvan sommige van de dubbelsterren die we hebben onderzocht voorkomen. We hebben dan voldoende kennis van zaken om in hoofdstuk 6.3 in wat meer detail in te gaan op de wetenschappelijke inhoud van dit proefschrift.

6.1 Ontstaan en evolutie van enkele sterren

Sterren worden gevormd uit gaswolken die zich voornamelijk in de spiraalarmen van sterrenstelsels bevinden. Een bekend voorbeeld is de Orionnevel, waarin sterren met leeftijden tussen de 500 000 en 2 miljoen jaar (0.01–0.04% van de leeftijd van de Zon[1]) worden gevonden en waar de stervorming nog steeds aan de gang is. Als zo'n gaswolk samentrekt ontstaan lokale verdichtingen. In zo'n verdichting stijgt de temperatuur, totdat de temperatuur en druk in het centrum voldoende hoog zijn om kernfusie te laten plaatsvinden. Waterstofkernen worden gefuseerd tot heliumkernen en hierbij komt genoeg energie vrij om de het gas te laten stralen. De verdichting is nu in evenwicht en trekt niet langer samen: er is een ster gevormd. Sterren waarin de energieproductie wordt verzorgd door waterstoffusie in de kern worden *hoofdreekssterren* genoemd.

De Zon is een voorbeeld van een hoofdreeksster en heeft na 4,5 miljard jaar waterstoffusie ongeveer de helft van haar totale voorraad waterstof verbruikt. De Zon heeft een massa die ruim 330 000 keer zo groot is als die van de Aarde, een diameter van bijna 110 aarddiameters, een lichtkracht van bijna 4×10^{26} Watt[2] en een oppervlaktetemperatuur van zo'n 5500 °C. Als we deze grootheden voor andere sterren beschrijven, maken we meestal gebruik van deze zonne-eenheden: een zonsmassa ($M_\odot$), een zonsstraal ($R_\odot$) en een zons-

[1] De leeftijd van het zonnestelsel is aan de hand van meteorieten bepaald op ongeveer 4,5 miljard jaar.
[2] 4×10^{26} = 400 000 000 000 000 000 000 000 000, een 4 gevolgd door 26 nullen.

M ($M_\odot$)	t (Mjr)	R ($R_\odot$)	L ($L_\odot$)	T_o (°C)	T_c (miljn °C)	ρ_c (g cm^{-3})	Aantal (t.o.v. 1 $M_\odot$)
0,5	52 600	0,50	0,05	4138	9,8	141	7,07
0,8	11 600	0,79	0,38	5380	13,4	156	2,34
1,0	4900	1,01	1,05	6080	15,9	157	1,00
1,5	1660	1,95	6,75	6930	20,9	102	0,131
2,0	582	2,23	20,4	8500	22,5	69,8	0,0232
2,5	405	2,80	57,8	9800	24,1	48,7	0,009 59
3,0	246	3,09	120	11 100	25,2	37,8	0,003 80
5,0	70,6	4,19	895	15 700	28,6	18,7	0,000 327
10,0	12,7	5,74	8590	23 500	32,8	8,53	0,000 011 6
20,0	5,18	8,78	67 900	31 700	37,0	4,40	0,000 000 93
50,0	2,41	15,9	527 000	39 300	41,4	2,34	0,000 000 05

Tabel 6.1: Enkele eigenschappen van stermodellen met de samenstelling van de Zon, halverwege de hoofdreeks: de massa M, de leeftijd t in miljoenen jaren, de straal R, de lichtkracht L, de temperatuur aan het oppervlak en in het centrum (T_o in °C en T_c in miljoenen °C), de centrale dichtheid ρ_c en het aantal sterren met deze massa voor iedere ster met 1 $M_\odot$. De leeftijd van de 0,5 $M_\odot$-ster is bijna 4 keer de leeftijd van het heelal.

lichtkracht ($L_\odot$). Andere hoofdreekssterren lijken vaak op de Zon, maar hun eigenschappen schalen met de massa van die ster (zie Tabel 6.1). Zo zijn lichtere hoofdreekssterren iets kleiner, een stuk koeler en veel lichtzwakker dan de Zon, terwijl zwaardere sterren op de hoofdreeks juist iets groter, een stuk heter en veel lichtkrachtiger zijn. Zo heeft een ster van 10 zonsmassa's (10 $M_\odot$) op de hoofdreeks een straal van 6 $R_\odot$, een lichtkracht van circa 10 000 $L_\odot$ en een oppervlaktetemperatuur van zo'n 23 000 °C. Doordat zo'n zware ster een ongeveer 10 keer grotere waterstofvoorraad heeft, maar een 10 000 keer hoger verbruik, duurt de hoofdreeksfase dus slechts een duizendste van die van de Zon. Hoofdreekssterren van $0,8\,M_\odot$ of minder hebben meer dan de leeftijd van het heelal nodig om te evolueren en deze zien we dus altijd 'jong'. Zware sterren zijn zeldzaam (voor iedere 10 $M_\odot$-ster zijn er bijna 100 000 'zonnen'), lichte sterren komen zeer veel voor (zie Tabel 6.1).

De hoofdreeks is de langstdurende fase uit het actieve leven van een ster (ongeveer 80%), zodat de meeste sterren die we waarnemen hoofdreekssterren zijn. Zolang waterstoffusie plaatsvindt in de kern is de ster in evenwicht en veranderen zijn lichtkracht en oppervlaktetemperatuur maar weinig. Als het waterstof opraakt verandert de ster echter drastisch. De kern bestaat nu helemaal uit helium en doordat er geen fusie meer plaatsvindt gaat deze heliumkern samentrekken. Hierdoor nemen druk en temperatuur in de kern toe, zodat net buiten de kern een schil ontstaat waarin de druk en temperatuur hoog genoeg worden voor de zogenaamde *schilverbranding*[3] van waterstof. In dit proces wordt waterstof uit de mantel van de ster omgezet in helium en toegevoegd aan de kern. Hierbij wordt de kern

[3]Het begrip *verbranding* wordt vaak gebruikt voor *kernfusie*.

steeds zwaarder, compacter en heter. Door de hoge temperatuur in het centrum van zo'n ster dijt de ster uit. De mantel koelt hierdoor af en wordt convectief, dat wil zeggen dat het energietransport plaatsvindt door middel van opstijgende hete gasbellen. Als de mantel helemaal convectief is, zwelt de ster nog verder op. Het oppervlak van de reuzenster ligt zo ver van het hete centrum dat het koeler is dan voorheen en daardoor rood van kleur. Dit type ster wordt een *rode reus* genoemd. Sterren die lichter zijn dan ongeveer 2,4 $M_\odot$ kunnen een straal tot 150 $R_\odot$ hebben op de rode-reuzentak, zwaardere sterren zwellen minder op (zie bijvoorbeeld Figuur 5.1 op pagina 86). Als de Zon een rode reus wordt kan zij een lichtkracht bereiken die 1000 keer haar huidige lichtkracht bedraagt. Er wordt aangenomen dat deze reuzensterren door de hoge lichtkracht en de lage zwaartekracht aan het oppervlak veel materie verliezen in een zogenaamde *sterrenwind*, al is het moeilijk om uit de waarnemingen of theorie te bepalen hoeveel dit precies is.

Voor alle sterren die zwaarder zijn dan 0,8 $M_\odot$ worden aan het einde van de rode-reuzenfase de centrale druk en temperatuur hoog genoeg om heliumfusie mogelijk te maken. Hierbij wordt helium gefuseerd tot koolstof en zuurstof. Bij sterren met lage massa (minder dan 2,4 $M_\odot$) is de druk in de kern onafhankelijk van de temperatuur. Wanneer heliumfusie begint neemt de temperatuur toe, maar de kern expandeert in eerste instantie nog niet doordat de druk gelijk blijft. Hierdoor versnelt de heliumfusie totdat de ontkoppeling tussen temperatuur en druk opgeheven wordt, de kern alsnog expandeert en de fusiesnelheid omlaag gaat. Deze explosieve heliumverbranding wordt de *heliumflits* genoemd. Bij sterren met een massa groter dan 2,4 $M_\odot$ komt de heliumfusie geleidelijk op gang.

De ster is nu aanbeland op de *horizontale tak*. In de kern vindt heliumfusie plaats, om de kern bevindt zich nog steeds de waterstoffusieschil. Als het helium in de kern opraakt, gaat de koolstof-zuurstofkern op zijn beurt krimpen en de buitenlagen van de ster gaan weer uitzetten, net als aan het einde van de hoofdreeks. Sterren zwaarder dan ongeveer 10 $M_\odot$ kunnen vele van deze kernfusiestadia doorlopen. Bij ieder volgend stadium worden zwaardere elementen geproduceerd en ieder volgend stadium verloopt sneller. Zo heeft een ster van 10 $M_\odot$ een hoofdreeksfase van ongeveer 20 miljoen jaar, de heliumfusie duurt ongeveer 2 miljoen jaar, koolstoffusie zo'n 1000 jaar, zuurstoffusie 2 jaar en siliciumfusie 3 dagen. Uit silicium worden uiteindelijk ijzer en nikkel aangemaakt en door middel van kernfusie kan uit deze elementen geen energie meer worden gehaald. Dit leidt tenslotte tot het instorten van de ijzer-nikkelkern van de ster tot een *neutronenster* of misschien een zwart gat. Een neutronenster is een bal met een massa van ongeveer 1.4 $M_\odot$ en een diameter van slechts 20 km, een zwart gat is iets zwaarder en kleiner. Bij de implosie van de kern komt voldoende energie vrij om de buitenlagen van de ster de ruimte in te blazen. Zo'n explosie van een zware ster staat bekend als een *supernova* (zie Figuur 6.1a).

In dit proefschrift bekijken we de evolutie van sterren die te licht zijn om een supernova-explosie te ondergaan, al komen er ook neutronensterren voor, waarvan we dus weten dat ze in het verleden door een supernova moeten zijn gevormd. Als een ster lichter dan ongeveer 10 $M_\odot$ het helium in zijn kern verbrand heeft, trekt de koolstof-zuurstofkern samen en wordt heter. Om deze kern ontstaat nu een nieuwe schil, waar heliumfusie plaatsvindt. Daarbuiten bevindt zich nog steeds de waterstoffusieschil (zie Figuur 6.2). Zo'n ster bevindt

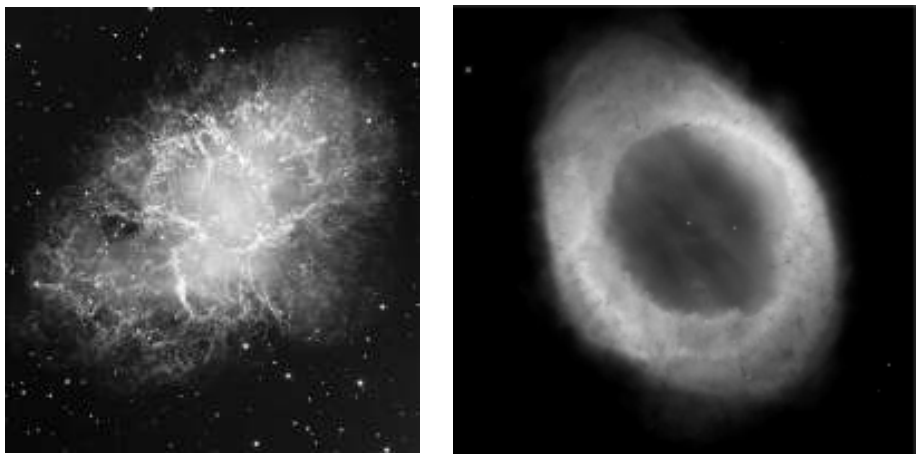

Figuur 6.1: De overblijfselen van sterren. *Links* (**a**): De Krabnevel is het restant van een supernova, de explosie van een zware ster (Foto: European Southern Observatory). *Rechts* (**b**): De Ringnevel is een planetaire nevel, het eindstadium van een lichte ster. In het centrum is de centrale ster nog zichtbaar (Foto: The Hubble Heritage Team (AURA/STScI/NASA)).

zich op de *asymptotische reuzentak* (asymptotic giant branch, AGB) en wordt een AGB-ster genoemd. Doordat de twee verbrandingsschillen hun brandstof van de buitenkant halen en het fusieproduct aan de binnenkant aan de kern toevoegen, 'eten' de schillen zich als het ware een weg naar buiten. Intussen ontwikkelt de ster zogenaamde 'Mira-pulsaties', waarbij de ster uitzet en samentrekt met een periode van ongeveer een jaar. Als de ster expandeert koelt het oppervlak sterk af. Hierdoor kan zich stof vormen, wat ervoor zorgt dat de ster zijn buitenste laag snel verliest. Dit gaat zo door totdat de kern van de ster overblijft, omgeven door de ijle nevel die gevormd is uit de vroegere buitenlagen van de ster.

De sterkern bestaat uit koolstof en zuurstof, of — voor de zwaardere sterren — uit zuurstof en neon. De vroegere buitenlagen van zo'n ster worden nog een tijd aangestraald door het energierijke licht van de centrale ster en zijn zichtbaar als een *planetaire nevel* (Figuur 6.1b) om de kern van de ster. In de voormalige sterkern vindt nu geen fusie meer plaats. De 'ster' straalt nog door zijn hoge temperatuur, maar koelt hierdoor af en wordt dus steeds zwakker. Zo'n overblijfsel van een ster wordt een *witte dwerg* genoemd. Het overblijfsel van de Zon zal vermoedelijk een koolstof-zuurstof witte dwerg zijn met een massa van ongeveer 0,6 $M_\odot$, al is dit getal onzeker door de onzekerheid in het massaverlies door de sterrenwind tijdens de reuzenfase en de AGB-fase. Een witte dwerg van 0,6 $M_\odot$ heeft een diameter van ongeveer 0,015 $R_\odot$, zo'n 10 000 km. Zwaardere witte dwergen hebben een sterkere zwaartekracht en zijn door de grotere compressie kleiner.

Figuur 7.1 op pagina 143 toont een kleur-magnitude-diagram waarin de 'kleur' $B-V$ en visuele magnitude V van 20 546 nabije sterren is uitgezet. Van rechtsonder naar links-

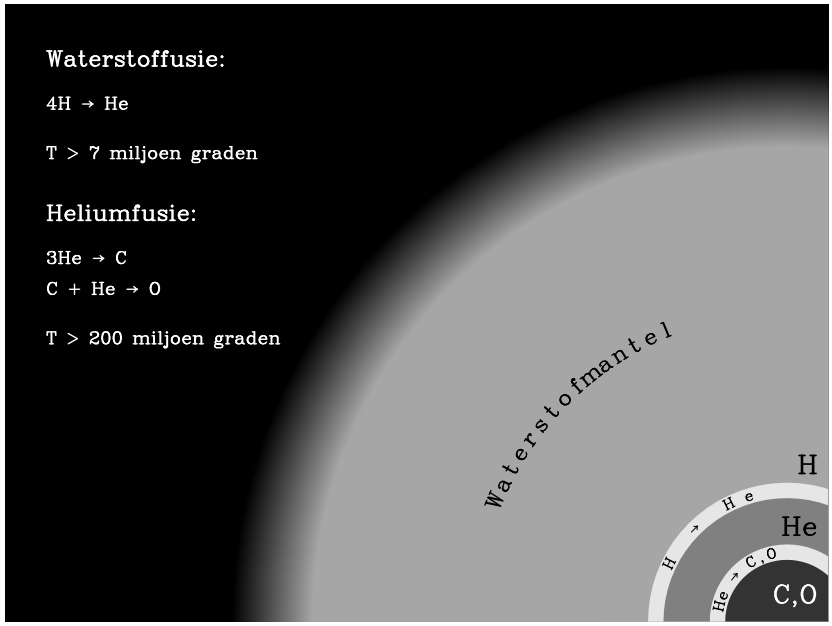

Figuur 6.2: Schematische doorsnede van de kern van een AGB-ster, van binnen naar buiten: de inerte koolstof-zuurstofkern (C,O), de heliumfusieschil, de inerte heliumlaag (He), de waterstoffusieschil en de waterstofmantel (H).

boven is de hoofdreeks (MS). GB is de reuzentak, HB de horizontale tak en WDs zijn witte dwergen. De lijnen zijn evolutiesporen van stermodellen voor 0,5, 1,0, 2,5, 5 en 10 $M_{\odot}$. De gestreepte lijn toont het einde van de evolutie van de 1 $M_{\odot}$-ster, die uiteindelijk een witte dwerg wordt. De lichtkracht L en temperatuur $T_{\rm eff}$ geven een indicatie, maar gelden strikt genomen voor de hoofdreeks.

6.2 Evolutie van dubbelsterren

Van de circa 5000 sterren die men met het blote oog kan waarnemen blijken zo'n 2000 eigenlijk dubbelsterren of meervoudige sterren te zijn. Men denkt dat globaal geldt dat ongeveer 60% van alle sterren zich in een dubbelster bevindt. De ster die het dichtst bij de Zon staat, Proxima Centauri, maakt deel uit van een 'driedubbelster', als begeleider van het veel nauwere paar α Centauri, dat met het blote oog kan worden waargenomen. Sterren in een dubbelster zijn gebonden door elkaars zwaartekracht en draaien in banen om elkaar heen. Wanneer de sterren ver van elkaar staan, zoals in het geval van Proxima Centauri, merken zij weinig van hun begeleiders en zo'n ster zal zijn evolutie effectief als enkele ster doorlopen. Zulke dubbelsterren hebben baanperiodes van 10 jaar of meer. Voor

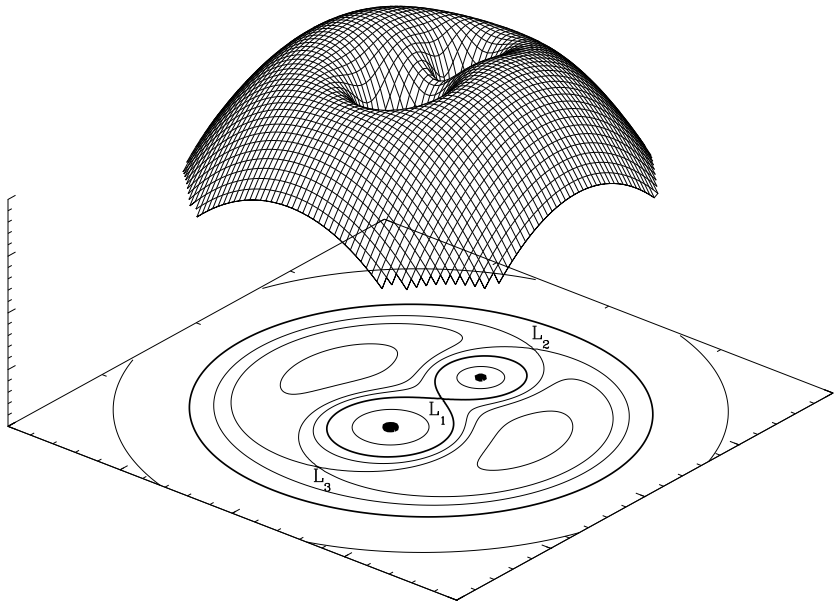

Figuur 6.3: Driedimensionale weergave van het potentiaalveld van een dubbelster met een massaverhouding van 2, in een stelsel dat coroteert met de dubbelster. De druppelvormige gebieden in de equipotentiaalplot op de bodem van de figuur zijn de Roche-lobben van de twee sterren (dikke lijnen). De punten L_1, L_2 en L_3 zijn de punten van Lagrange waar de krachten elkaar opheffen. Via het zadelpunt L_1 kan gas van de ene ster naar de andere vloeien als deze zijn Roche-lob vult.

dubbelsterren met een baanperiode van minder dan 10 jaar geldt dat de sterren tijdens de reuzenfase of op de AGB ongeveer zo groot kunnen worden als de afstand tussen de twee sterren. Het duidelijk dat de twee sterren elkaar dan sterk zullen beïnvloeden en dat de situatie in zo'n geval totaal anders is dan het geval van een enkele ster.

Om te bedenken wat er in een nauwe dubbelster zoal kan gebeuren, stellen we ons een deeltje voor dat zich in de buurt van een van de twee sterren bevindt. Het deeltje wordt dan aangetrokken door de zwaartekracht van de ster en zal naar de ster toe vallen. Als het deeltje zich van de eerste ster af beweegt, in de richting van de tweede ster, dan wordt de zwaartekracht van de eerste ster steeds zwakker en die van de tweede ster steeds sterker. Vanaf een bepaald punt zal het deeltje dus eerder naar de tweede ster vallen dan naar de eerste ster. In werkelijkheid speelt hierbij niet alleen de zwaartekracht van de twee sterren een rol, maar ook de centrifugaalkracht die wordt geïntroduceerd door de baanbeweging in de dubbelster. Het deeltje beweegt dus in het potentiaalveld van deze drie krachten en dit is weergegeven in Figuur 6.3.

De *Roche-lobben* die in de Figuur worden getoond vormen het gebied waar een ster bin-

nen moet blijven om zijn gas aan zich gebonden te houden. In Tabel 6.1 zagen we dat een zwaardere ster sneller evolueert. Van de twee sterren in een dubbelster zal de zwaarste ster dus als eerste van de hoofdreeks afkomen en gaan opzwellen tot een rode reus. Wanneer de ster groter wordt dan zijn Roche-lob, kan het gas van deze ster, via het eerste punt van Lagrange (L_1 in Figuur 6.3), naar de tweede ster vloeien. Er vindt dus materie-overdracht plaats van de zwaardere ster naar zijn begeleider. Aangezien de massa de belangrijkste factor is die de eigenschappen van een ster bepaalt, kan de evolutie van zo'n ster drastisch veranderen. Wanneer de donorster zijn waterstofmantel al voor de AGB verliest door materie-overdracht naar zijn begeleider, ontstaat een witte dwerg die veel lichter is dan de witte dwerg die zou zijn gevormd wanneer de ster zich niet in een dubbelster zou bevinden. Als de materie-overdracht voor of op de rode-reuzentak gebeurt, ontstaat bovendien een helium witte dwerg, in plaats van een koolstof-zuurstof witte dwerg. Daarnaast verandert de baanperiode van een dubbelster aanzienlijk bij materie-overdracht, doordat met de materie impulsmoment[4] wordt overgedragen.

Wanneer de begeleider van de donorster voldoende groot is en de materie-overdrachtsnelheid niet te hoog, dan zal de begeleider het overgedragen gas kunnen invangen. Als deze ster een hoofdreeksster is, dan kan hij behoorlijk aan massa winnen en zich gaan gedragen als een zwaardere ster. Materie-overdracht kan vervolgens in de omgekeerde richting plaatsvinden, nadat de begeleider zelf ook van de hoofdreeks af geëvolueerd is. Echter, in het geval dat de begeleider een compacte ster is, zoals een neutronenster, dan draagt de materie te veel impulsmoment om de ster direct te raken en er vormt zich een *accretieschijf* om het compacte object (zie afbeeldingen *a* en *b* op de voorplaat). Het gas in de accretieschijf wordt versneld door de sterke zwaartekracht van het compacte object, wordt verhit en zendt grote hoeveelheden röntgenstraling uit. We zien deze dubbelsterren als *röntgendubbelsterren* (X-ray binaries). Als de materie-overdrachtsnelheid hoog genoeg is kan een deel van de materie zelfs de dubbelster verlaten.

Wanneer een reuzenster zijn Roche-lob vult is de materie-overdrachtsnelheid vaak erg hoog. De ster heeft dan een diepe convectieve mantel en wanneer zo'n ster een beetje gas verliest doordat hij zijn Roche-lob overvult, dan zet de ster uit en overvult zijn Roche-lob nog meer. Hierdoor neemt de materie-overdrachtsnelheid toe, de ster zet verder uit, enzovoorts. De materie-overdracht is in dat geval instabiel en de begeleider van zo'n ster is in het algemeen niet in staat zoveel gas in zo korte tijd in te vangen. Men denkt dat de mantel van de donor zo snel uitzet, dat deze de begeleider ook omhult en er sprake is van een *gemeenschappelijke mantel* (common envelope). De kern van de donor en de begeleider draaien nu rond binnen deze mantel. Door de wrijving van het gas spiraliseren de twee sterren naar elkaar toe (*spiral-in*) en de baanperiode neemt dus (sterk) af (zie Figuur 6.4).

Een andere methode waarmee dubbelsterren kunnen worden herkend is door de snel-

[4]Met het begrip *impulsmoment* wordt in de natuurkunde de hoeveelheid draaiing aangegeven. Impulsmoment kan net als energie niet verloren gaan, maar wel worden overgedragen. Een voorwerp heeft meer impulsmoment wanneer het sneller draait, zwaarder is of een grotere draairadius heeft. Een bekend voorbeeld van impulsmomentbehoud is de ijsdanser die al draaiende zijn armen intrekt; de draairadius wordt kleiner en dus moet de draaisnelheid groter worden. Als de draaisnelheid niet groter zou worden, zou er impulsmoment verloren zijn gegaan. Als de ijsdanser spontaan sneller zou gaan draaien, zou er impulsmoment worden geproduceerd.

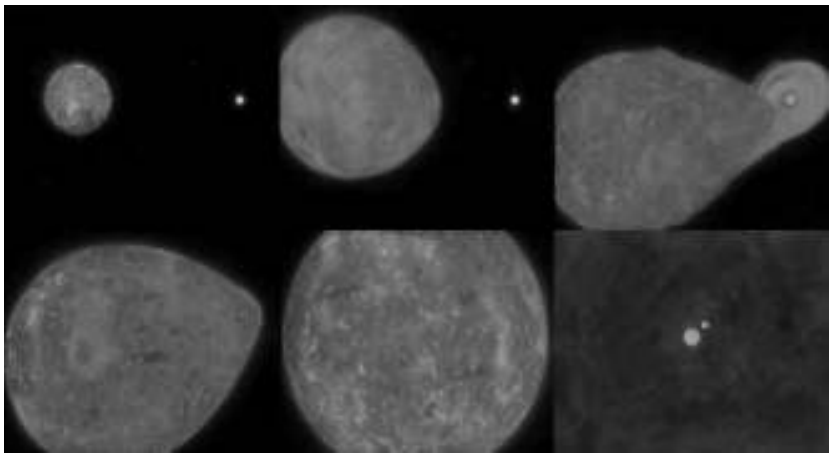

Figuur 6.4: Wanneer een reuzenster zijn Roche-lob vult kan de materie-overdracht instabiel zijn. Er ontwikkelt zich dan een gemeenschappelijke mantel waarbinnen de twee sterren naar elkaar spiraliseren, zodat een zeer nauwe dubbelster kan ontstaan (zie de hoofdtekst en afbeeldingen *c* en *d* op de voorplaat).

heid van sterren te meten. Wanneer twee sterren om elkaar heen draaien, beweegt over het algemeen immers de ene ster naar ons toe terwijl de andere van ons af beweegt en omgekeerd. Dit gedrag herhaalt zich met een periode die gelijk is aan de baanperiode van de dubbelster. Door middel van het Doppler-effect[5] kan deze periodieke verandering worden gevonden en de verhouding in radiële snelheden van de twee sterren is een maat voor hun massaverhouding. Een voorbeeld van zo'n waarneming en de radiële snelheden die hieruit gemeten worden is te vinden in Figuur 1.3 op pagina 11.

In de buurt van de Zon is de gemiddelde afstand tussen sterren vrij groot; in de orde van een *parsec*[6]. De kans dat een (dubbel)ster door een andere ster wordt beïnvloed is daardoor zeer gering en het is aannemelijk dat (dubbel)sterren een geïsoleerd bestaan leiden. Dit is echter anders in gebieden met een hoge sterdichtheid, zoals in het centrum van een sterrenstelsel of in een *bolvormige sterhoop* (zie Figuur 6.5). In het centrum van een bolvormige sterhoop, of bolhoop, kan de sterdichtheid een miljoen keer hoger zijn dan in de buurt van de Zon en hierdoor is de kans op 'botsingen' tussen sterren een biljoen keer groter. Zo'n botsing kan een fysieke botsing zijn tussen twee sterren, maar bijvoorbeeld ook een 'ontmoeting' tussen een ster en een dubbelster of twee dubbelsterren. Bij zo'n ontmoeting kan uitwisseling plaatsvinden tussen de sterren van de dubbelster en de ontmoetende sterren, zodat een totaal andere dubbelster kan ontstaan. Het blijkt dat het aantal heldere röntgendubbelsterren in bolhopen naar verhouding veel groter is dan elders in ons

[5]Het Doppler-effect is ook verantwoordelijk voor de verschuiving in toon van de sirene van een ambulance bij naderen of verwijderen.

[6]Een parsec is 3,26 lichtjaar, ongeveer 30 biljoen kilometer (30 000 000 000 000 km).

Figuur 6.5: De bolvormige sterhoop M15 in het sterrenbeeld Pegasus is net niet zichtbaar met het blote oog. De bolhoop herbergt twee heldere röntgenbronnen. In 2005 werd ontdekt dat een van deze twee bronnen een ultracompacte röntgendubbelster is met een baanperiode van slechts 23 minuten. (Foto: NOAO/AURA/NSF).

Melkwegstelsel en men vermoedt dan ook dat dit te maken heeft met de hoge sterdichtheid in de bolhopen, bijvoorbeeld doordat deze dubbelsterren zijn ontstaan uit botsingen tussen (sub)reuzensterren en neutronensterren.

6.3 Dit proefschrift

In dit proefschrift worden twee typen compacte dubbelsterren onderzocht. In hoofdstuk 2 en 3 onderzoeken we het ontstaan van de heldere röntgendubbelsterren in bolvormige sterhopen. We laten zien dat een van de drie scenario's die zijn bedacht om het ontstaan van deze dubbelsterren te verklaren te weinig of zelfs helemaal geen heldere röntgendubbelsterren oplevert binnen de leeftijd van het heelal. In hoofdstuk 4 wordt een heldere röntgendubbelster in ons Melkwegstelsel onderzocht. Aan de hand van waargenomen uitbarstingen op de neutronenster en een hoog gehalte van neon ten opzichte van zuurstof tonen we aan dat de donorster waarschijnlijk het overblijfsel is van een helium witte dwerg die mogelijk door een inspiralisering in een nauwe baan om de neutronenster is gekomen. In hoofdstuk 5 onderzoeken we de vorming van dubbele witte dwergen, die twee fases van materie-overdracht moeten hebben doorlopen. We concluderen dat onze modellen de waargenomen massa's en

baanperiodes goed verklaren, maar dat het moeilijk is om het leeftijdsverschil tussen de componenten ook te verklaren.

6.3.1 Ontstaan en evolutie van compacte röntgendubbelsterren

In de bolvormige sterhopen die bij ons Melkwegstelsel horen worden 13 heldere röntgenbronnen waargenomen. Dit zijn röntgendubbelsterren en van deze 13 dubbelsterren hebben er zeker 3, waarschijnlijk 5 en mogelijk 6 – 8 een ultrakorte baanperiode van minder dan ongeveer 40 minuten (zie Tabel 1.1 op pagina 5). Dit zijn er in verhouding veel meer dan in ons Melkwegstelsel en de verklaring wordt gezocht in het feit dat de sterdichtheid veel hoger is in de bolhopen dan in het vlak van de Melkweg. In (de centra van) bolhopen vinden veel meer botsingen tussen sterren plaats dan in het galactisch vlak, en een van de theorieën luidt dan ook dat de ultracompacte dubbelsterren ontstaan uit de botsing van een (sub)reuzenster met een neutronenster. In zo'n geval ontstaat een witte dwerg die materie kan overdragen naar de neutronenster en tijdens de materie-overdracht wordt de baanperiode altijd groter.

Een andere theorie zegt dat een ster van ongeveer 1 $M_{\odot}$, die zijn Roche-lob vult aan het einde van de hoofdreeks en zijn materie overdraagt naar een neutronenster, ook kan leiden tot een ultracompacte röntgendubbelster. Normaal gesproken wordt de baanperiode in zo'n geval langer, maar wanneer de ster een ster magnetisch veld heeft en een sterke sterrenwind, dan kan dit leiden tot een kortere periode. Het gas dat de ster in de wind verlaat wordt in dit geval namelijk meegesleurd door de magnetische veldlijnen, die ervoor zorgen dat de wind tot op grote afstand nog coroteert met de ster. Het effect is dan vergelijkbaar met een ijsdanser die zijn armen langzaam uitstrekt; hij gaat langzamer roteren, in dit geval doordat er impulsmoment van de ster wordt afgevoerd door de wind. Dit is slechts een zwak effect, maar het kan miljarden jaren aanhouden. De ster gaat hierdoor langzamer om zijn as draaien en dit proces wordt *magnetische remming* (magnetic braking) genoemd.

De rotatie van een ster die materie overdraagt in een dubbelster is door getijdenkrachten gekoppeld aan de baanbeweging van de dubbelster (net als in het geval van de Maan die altijd met dezelfde zijde naar de Aarde gekeerd is). Het impulsmoment dat wordt verloren door magnetische remming wordt hierdoor effectief uit de baan onttrokken, waardoor de dubbelster nauwer wordt en de baanperiode dus korter! De periode bereikt bij een bepaalde waarde een minimum en neemt vervolgens weer toe. Andere onderzoekers hebben aangetoond dat op deze manier ultracompacte dubbelsterren kunnen worden gevormd waarvan de minimumperiode rond de 5 minuten ligt. Dit scenario wordt ook wel *magnetische vangst* genoemd. Het voordeel van deze theorie is dat het een waargenomen dubbelster in een bolhoop zou kunnen verklaren, waarvan de baanperiode 11 minuten is en lijkt af te nemen. Ons onderzoek toont echter aan dat om een baanperiode van 5 minuten te bereiken meer tijd nodig is dan het heelal oud is. Een periode van 11 minuten lukt net, maar wij vinden dat er zeer specifieke beginomstandigheden vereist zijn om zo'n periode te kunnen bereiken. Dit betekent dat de kans zeer gering is dat deze sterren in de natuur daadwerkelijk gevormd worden, en dat we dit ontstaansscenario dus waarschijnlijk kunnen verwerpen (hoofdstuk 2).

In hoofdstuk 3 zetten we het onderzoek naar het scenario van de magnetische vangst

voort. We gebruiken nu een modernere wet om de magnetische remming te beschrijven, die empirisch is bepaald uit waarnemingen van roterende sterren in de sterhopen Pleiaden en Hyaden. Dit resulteert in een zwakkere afremming, waardoor de kortste minimumperioden verschuiven van ongeveer 11 minuten naar 70 minuten. Hiermee is het scenario van de magnetische vangst definitief van de baan. Dit betekent dat het afnemen van de baanperiode van de 11-minuten dubbelster op een andere manier verklaard moet worden. Het is inderdaad mogelijk dat de dubbelster versneld wordt in het zwaartekrachtsveld van de bolhoop waarin hij zich bevindt en dat hierdoor een schijnbare periode-afname veroorzaakt wordt. Daarnaast werd enkele maanden na het uitbrengen van dit artikel een artikel van een andere onderzoeksgroep gepubliceerd, waarin de onderzoekers laten zien dat ze met behulp van de eerder genoemde botsingen alle waargenomen röntgenbronnen in bolhopen kunnen verklaren.

De heldere röntgendubbelsterren in bolhopen kunnen dus worden verklaard door botsingen. Zo'n botsing is het meest waarschijnlijk wanneer een ster een (sub)reus is en in dat geval zal de begeleider van de neutronenster zeer waarschijnlijk een helium witte dwerg zijn. In het galactisch vlak is de sterdichtheid te gering voor zulke botsingen. Men vermoedt dat de heldere röntgendubbelsterren die daar worden waargenomen ontstaan zijn uit een inspiralisering van een ster met een neutronenster. In zo'n geval kan een helium witte dwerg, een koolstof-zuurstof witte dwerg of zelfs een zuurstof-neon witte dwerg ontstaan. Na de inspiralisering wordt impulsmoment verloren door gravitatiestraling, totdat de baanperiode zo kort is dat de witte dwerg zijn Roche-lob vult en materie gaat overdragen. Vanaf dat moment gaat de dubbelster röntgenstraling uitzenden en wordt de baanperiode weer langer.

Zo'n röntgendubbelster in het galactisch vlak is 2S 0918–549. Doordat dit systeem in optisch licht relatief zwak is en in röntgenstraling erg helder, bestaat het vermoeden dat het hier om een ultracompacte dubbelster gaat. Uit het röntgenspectrum van de dubbelster volgt dat de verhouding neon/zuurstof hoger is dan in bijvoorbeeld de Zon. Hieruit trokken onderzoekers de conclusie dat het hier om een zuurstof-neon witte dwerg zou gaan. In hoofdstuk 4 wordt echter de waarneming van een lange uitbarsting op de neutronenster van 2S 0918–549 besproken. Zulke lange röntgenuitbarstingen kunnen alleen worden verklaard wanneer helium en eventueel waterstof op het oppervlak van de neutronenster aanwezig is en dit kan weer alleen het geval zijn wanneer de begeleider helium (en eventueel waterstof) overdraagt naar de neutronenster. In een witte dwerg komt geen waterstof voor en helium is (nog) niet waargenomen. De vraag die we proberen te beantwoorden in hoofdstuk 4 is dus: wat is de donorster van 2S 0918–549?

Een zuurstof-neon witte dwerg lijkt uitgesloten, ten eerste omdat deze erg zeldzaam zijn (en er nog drie van deze dubbelsterren zijn waargenomen) en ten tweede omdat deze witte dwergen zwaarder zijn dan 1 $M_\odot$ en om die reden waarschijnlijk uit elkaar worden gescheurd wanneer ze materie zouden overdragen naar een neutronenster. Dan blijven dus een helium witte dwerg en een koolstof-zuurstof (CO) witte dwerg over. We hebben modellen berekend voor sterren van verschillende massa's die eerst een heliumkern en later een CO-kern ontwikkelen. Hierin tonen we aan dat tijdens de waterstoffusie, die moet leiden tot de vorming van de heliumkern, zuurstof wordt afgebroken, terwijl er met neon niets gebeurt.

Om die reden is de neon/zuurstof-verhouding in een heliumkern of een helium witte dwerg dus hoog. Tijdens heliumfusie wordt juist veel zuurstof aangemaakt. In een CO-kern is de verhouding neon/zuurstof dus juist erg laag (zie Tabel 4.4 op pagina 76). We concluderen dat de donorster in 2S 0918–549 dus waarschijnlijk een helium witte dwerg is, gebaseerd op de lange röntgenuitbarsting en de hoge neon/zuurstof-verhouding. We stellen daarom in hoofdstuk 4 voor dat wanneer de materie-overdrachtsnelheid in 2S 0918–549 niet al te hoog is, er een grote hoeveelheid helium kan worden opgespaard voordat deze ontbrandt. Als de heliumlaag dan ontbrandt gebeurt dit in een lange uitbarsting, zoals is waargenomen. Wat we niet kunnen verklaren is dat er geen helium wordt waargenomen in het spectrum. Er is echter ook niet onomstotelijk bewezen dat er geen helium aanwezig is en dus zou een toekomstige waarneming van helium in 2S 0918–549 het bestaan van een heliumdonor kunnen bevestigen.

6.3.2 De vorming van dubbele witte dwergen

Wanneer een reuzenster zijn Roche-lob vult is de materie-overdracht vaak instabiel en kan een gemeenschappelijke mantel ontstaan, gevolgd door een inspiralisering van de twee sterren binnen de mantel (zie Figuur 6.4). Bij de inspiralisering komt baanenergie vrij uit de dubbelster. Om te schatten hoeveel de baanperiode korter wordt tijdens dit proces neemt men vaak aan dat er voldoende baanenergie vrij moet komen om de mantel te ontbinden en de ruimte in te sturen. De bindingsenergie van de stermantel, die we kunnen uitrekenen met behulp van een sterevolutiecode, geeft dus een idee van de hoeveelheid energie die moet worden vrijgemaakt uit de baan van de dubbelster en hieruit kunnen we de verandering in baanperiode tijdens de inspiralisering berekenen. Dit is de methode van ‘energiebalans’.

In hoofdstuk 5 gebruiken we deze methode om te evolutie van dubbele witte dwergen te reconstrueren. Aangezien deze witte dwergen vrijwel allemaal te licht zijn om niet in een dubbelster te zijn gevormd, en aangezien de dubbelsterbanen slechts enkele zonsstralen groot zijn (zie Tabel 5.1 op pagina 83), veel minder groot dus dan de reuzenster die zo’n witte dwerg produceert, weten we dat al deze witte dwergen gevormd moeten zijn na materie-overdracht in de dubbelster en dat de baanperiode tijdens de laatste materie-overdrachtsfase behoorlijk moet zijn geslonken. We proberen een aantal scenario’s, zoals stabiele materie-overdracht waarbij de begeleider al het gas invangt en we laten zien dat dit proces niet alle waargenomen dubbelsterren kan verklaren. Ook de inspiralisering met energiebalans blijkt niet voldoende te zijn om alle dubbelsterren te produceren. We gebruiken daarom de veronderstelling van andere onderzoekers dat in een inspiralisering niet de energie, maar het impulsmoment behouden is. Het blijkt dat een variant op deze methode inderdaad de waargenomen massa’s en baanperiodes van de dubbele witte dwergen kan verklaren, zonder dat er impulsmoment verloren gaat of geproduceerd wordt. We vinden ook dat het reproduceren van het gemeten leeftijdsverschil van de twee componenten in de dubbelster een stuk lastiger is. Een voorbeeld van een scenario waarin een dubbele hoofdreeksster via twee fases van een inspiralisering evolueert tot een dubbele witte dwerg is te vinden in Figuur 1.4 op pagina 13.

Kapitel 7

Formation und Evolution von kompakten Doppelsternen

In dieser Dissertation werden Untersuchungen einer bestimmten Klasse von Doppelsternen beschrieben. In Kapitel 7.1 gebe ich eine kurze Einführung über das Entstehen und die Evolution von Sternen im Allgemeinen und in Kapitel 7.2 beschreibe ich die Veränderungen, die sich ergeben, wenn zwei solche Sterne einen Doppelstern bilden. Ich beschreibe kurz die *Kugelsternhaufen*, in deren Zentren manche der untersuchten Doppelsterne vorkommen. Wir haben dann genügend Hintergrundwissen um uns in Kapitel 7.3 den wissenschaftlichen Inhalt der Dissertation im Detail anzuschauen.

7.1 Entstehung und Evolution von einzelnen Sternen

Sterne entstehen aus Gaswolken, die sich hauptsächlich in den Spiralarmen von Galaxien befinden. Ein bekanntes Beispiel ist der Orionnebel, in dem Sterne im Alter zwischen 500 000 und 2 Millionen Jahren (0.01–0.04% des Alters der Sonne[1]) gefunden werden und wo Sternentwicklung immer noch stattfindet. Wenn sich eine solche Wolke zusammenzieht entstehen Verdichtungen. Die Temperatur in einer solchen Verdichtung steigt, bis die Temperatur und der Druck hoch genug sind um Kernfusion zu ermöglichen. Wasserstoffkerne verschmelzen zu Heliumkernen und bei diesem Prozess kommt genügend Energie frei um das Gas leuchten zu lassen. Die Verdichtung ist jetzt im Gleichgewichtszustand und zieht sich nicht länger zusammen: Ein Stern ist entstanden. Sterne, die ihre Energie durch Wasserstofffusion im Zentrum produzieren, werden *Hauptreihensterne* genannt.

Die Sonne ist ein Hauptreihenstern und hat nach 4,5 Milliarden Jahren von Wasserstofffusion etwa die Hälfte ihres Vorrates aufgebraucht. Ihre Masse ist mehr als 330 000 mal so gross wie die der Erde, ihr Durchmesser misst fast 110 Erddurchmesser, ihre Leuchtkraft ist fast 4×10^{26} Watt[2] und ihre Oberflächentemperatur beträgt circa 5500 °C. Andere Sterne beschreiben wir meistens mit Sonneneinheiten: der Sonnenmasse ($M_\odot$), dem Sonnenradius ($R_\odot$) und der Sonnenleuchtkraft ($L_\odot$). Hauptreihensterne sind der Sonne oft ähnlich, aber

[1] Das Alter des Sonnensystems ist durch Meteoritendatierung auf circa 4,5 Milliarden Jahre bestimmt.
[2] 4×10^{26} = 400 000 000 000 000 000 000 000 000, eine 4 gefolgt von 26 Nullen.

die genauen Eigenschaften hängen von der Sternmasse ab. Leichtere Sterne sind ein bisschen kleiner, etwas kühler und viel leuchtkraftschwächer als die Sonne, während schwerere Sterne ein bisschen grösser, etwas heisser und viel heller sind. Ein Stern von 10 Sonnenmassen ($10\,M_\odot$) auf der Hauptreihe hat einen Radius von $6\,R_\odot$, eine Leuchtkraft von $10\,000\,L_\odot$ und eine Oberflächentemperatur von 23 500 °C. Weil ein solcher Stern einen etwa 10 mal grösseren Wasserstoffvorrat hat, aber auch einen 10 000 mal höheren Verbrauch, dauert seine Hauptreihenphase nur ein Tausendstel von der der Sonne. Sterne von $0,8\,M_\odot$ oder weniger brauchen mehr Zeit für die Hauptreihenphase, als das Universum alt ist und wir sehen sie deswegen immer jung. Schwere Sterne sind selten (auf jeden $10\,M_\odot$-Stern gibt es fast 100 000 'Sonnen'), leichte Sterne kommen sehr häufig vor. Tabelle 6.1 auf Seite 128 zeigt von einigen Sternmodellen mit der Zusammenstellung der Sonne die Masse M in $M_\odot$, das Alter t in Millionen Jahren, den Radius R in $R_\odot$, die Leuchtkraft L in $L_\odot$, die Oberflächentemperatur T_o in °C, die Zentraltemperatur T_c in Millionen °C, die zentrale Dichte ρ_c in g cm^{-3} und die Anzahl von Sternen mit dieser Masse für jeden Stern mit $1\,M_\odot$.

Die Hauptreihe ist die längste Phase im aktiven Leben eines Sterns (etwa 80%) und deswegen sind die meisten Sterne, die wir beobachten können, Hauptreihensterne. Solange Wasserstofffusion im Kern stattfindet, ist der Stern im Gleichgewicht und die Leuchtkraft und Oberflächentemperatur ändern sich nur wenig. Wenn der Wasserstoff im Kern aufgebraucht ist, ändert sich der Stern dagegen drastisch. Der Kern besteht jetzt völlig aus Helium, und da keine Fusion mehr stattfindet, zieht sich der Heliumkern zusammen. Dabei steigen Druck und Temperatur im Zentrum und demzufolge entwickelt sich um den Kern eine Schale, in der Temperatur und Druck hoch genug sind für das *Schalenbrennen*[3] von Wasserstoff. Beim Wasserstoffschalenbrennen wird Wasserstoff aus dem Mantel zu Helium fusioniert und zum Kern zugefügt. Dabei wird der Kern immer schwerer, dichter und heisser. Wegen der hohen Temperatur des Sternzentrums dehnt der Stern sich aus. Der Mantel wird dadurch konvektiv, das heisst, dass der Energietransport durch heisse aufsteigende Gasklumpen stattfindet. Wenn der Mantel ganz konvektiv ist, dehnt der Stern sich noch weiter aus. Die Oberfläche des Sterns befindet sich jetzt so weit weg vom heissen Kern, dass sie kühler ist als vorher und deswegen rot erscheint. Diese Sterne werden *Rote Riesen* genannt. Sterne leichter als circa $2{,}4\,M_\odot$ können Radien bis $150\,R_\odot$ am Rote-Riesen-Ast haben, schwerere Sterne dehnen sich weniger aus (siehe Abbildung 5.1 auf Seite 86). Wenn die Sonne ein Roter Riese wird, kann ihre Leuchtkraft das hundertfache ihrer heutigen Leuchtkraft betragen. Wahrscheinlich verlieren diese Riesensterne durch ihre grosse Leuchtkraft und geringe Oberflächengravitation viel Materie durch einen *Sternwind*, obwohl schwer festzustellen ist, wie gross dieser Verlust genau ist.

Für alle Sterne schwerer als $0{,}8\,M_\odot$ werden am Ende der Rote-Riesen-Phase der zentrale Druck und die Temperatur hoch genug um Heliumfusion zu ermöglichen. Dabei wird Helium zu Kohlenstoff und Sauerstoff fusioniert. Für Sterne mit geringer Masse (weniger als $2{,}4\,M_\odot$) ist der Druck im Zentrum unabhängig von der Temperatur. Wenn die Heliumfusion beginnt, steigt die Temperatur, aber der Kern expandiert anfänglich noch nicht, da der Druck gleich bleibt. Demzufolge beschleunigt die Heliumfusion, bis die Entkoppelung

[3] Der Begriff *Brennen* wird oft für *Kernfusion* verwendet.

zwischen Temperatur und Druck aufgehoben wird. Der Kern expandiert nachträglich und die Fusionsgeschwindigkeit sinkt. Dieses explosive Heliumbrennen wird *Heliumblitz* genannt. Für Sterne mit einer Masse höher als 2,4 $M_\odot$ findet die Heliumfusion von Anfang an gemächlich statt.

Der Stern ist jetzt auf dem *horizontalen Ast* angelangt. Im Kern findet Heliumfusion statt, um den Kern herum befindet sich immer noch die Wasserstofffusionsschale. Wenn das Helium im Kern aufgebraucht ist, zieht sich der Kohlenstoff-Sauerstoff-Kern zusammen und der äussere Mantel expandiert wieder, so wie am Ende der Hauptreihenphase. Sterne schwerer als ungefähr 10 $M_\odot$ können viele von diesen Kernfusionsstadien durchlaufen. Bei jeder folgenden Phase werden schwerere Elemente produziert und jede nächste Phase verläuft schneller. Für einen Stern von 10 $M_\odot$ dauert die Heliumfusion im Kern etwa 20 Millionen Jahre, die Heliumfusion 2 Millionen Jahre, die Kohlenstofffusion etwa 1000 Jahre, die Sauerstofffusion 2 Jahre und die Siliziumfusion 3 Tage. Aus Silizium werden schliesslich Eisen und Nickel produziert und aus diesen Elementen kann durch Kernfusion keine weitere Energie gewonnen werden. Dadurch kollabiert der Eisen-Nickelkern des Sterns zu einem *Neutronenstern* oder einem schwarzen Loch. Ein Neutronenstern ist ein Kugel mit einer Masse von circa 1.4 $M_\odot$ und einem Durchmesser von etwa 20 km, ein schwarzes Loch ist etwas schwerer und kleiner. Bei der Implosion des Sternkerns wird genügend Energie frei um den äusseren Mantel ins Weltall wegzuschleudern. Eine solche Explosion eines schweren Sterns wird eine *Supernova* genannt. Abbildung 6.1a auf Seite 130 zeigt den Krebsnebel, den Rest einer Supernova, die im Jahre 1054 sichtbar war.

In dieser Dissertation untersuchen wir die Entwicklung von Sternen, die zu leicht sind um eine Supernova-Explosion zu verursachen. Es kommen allerdings auch Neutronensterne vor, von denen wir wissen, dass sie aus Supernova-Explosionen entstanden sein müssen. Wenn ein Stern, der leichter als etwa 10 $M_\odot$ ist, sein Helium im Kern aufgebraucht hat, zieht sich der Kohlenstoff-Sauerstoff-Kern zusammen und wird heisser. Um diesen Kern herum entsteht eine neue Schicht, in der Helium fusioniert, ausserhalb gibt es immer noch die Wasserstofffusionsschale. Ein solcher Stern liegt auf dem *asymptotischen Riesenast* (asymptotic giant branch, AGB) und wird AGB-Stern genannt. Abbildung 6.2 auf Seite 131 zeigt schematisch den Aufbau eines AGB-Sterns, von innen nach aussen: den Kohlenstoff-Sauerstoff-Kern (C,O), die Heliumfusionsschale, die inerte Heliumschicht (He), die Wasserstofffusionsschale und den Wasserstoffmantel (H). Weil beide Fusionsschalen ihren Brennstoff von ausserhalb der Schale entnehmen und das Fusionsprodukt auf der Innenseite deponieren, 'essen' die Schalen sich einen Weg hinaus durch den Mantel. Währenddessen entwickelt der Stern 'Mira-Pulse', wobei er sich mit einer Periode von etwa einem Jahr ausdehnt und zusammenzieht. Bei jedem Puls kühlt die Oberfläche stark ab, es bildet sich Staub und dadurch verliert der Stern schnell seine äussere Schicht. Schliesslich bleibt nur der Kern übrig, umgeben von einem dünnen Nebel, der aus dem Sternmantel gebildet wurde.

Der Sternkern ist aus Kohlenstoff und Sauerstoff aufgebaut, oder — bei schwereren Sternen — aus Sauerstoff und Neon. Der frühere Sternmantel wird noch von dem energetischen Licht des Zentralsterns angestrahlt und ist als ein *Planetarischer Nebel* sichtbar. Abbildung 6.1b auf Seite 130 zeigt den Ringnebel, einen Planetarischen Nebel, dessen Zen-

tralstern noch sichtbar ist. In dem ehemaligen Sternkern findet jetzt keine Kernfusion mehr statt. Der 'Stern' strahlt noch wegen seiner hohen Temperatur, aber kühlt dabei ab und wird immer schwächer. Ein solcher Rest von einem leichten Stern wird ein *Weisser Zwerg* genannt. Von der Sonne wird vermutlich ein Kohlenstoff-Sauerstoff Weisser Zwerg mit einer Masse von 0,6 $M_\odot$ übrig bleiben. Diese Zahl ist allerdings wegen der Unsicherheit im Massenverlust durch den Sternwind während der Rote-Riesen-Phase und der AGB-Phase nicht genau bekannt. Ein Weisser Zwerg von 0,6 $M_\odot$ hat einen Durchmesser von etwa 0,015 $R_\odot$, circa 10 000 km. Schwerere Weisse Zwerge haben eine grössere Gravitation und sind durch die stärkere Kompression kleiner. Abbildung 7.1 zeigt die verschiedenen Evolutionsstadien in einem Farben-Helligkeits-Diagramm.

7.2 Evolution von Doppelsternen

Von den circa 5000 Sternen, die man mit dem blossen Auge sehen kann, sind etwa 2000 eigentlich Doppelsterne oder Sterne in einem Mehrfachsystem. Man nimmt an, dass sich etwa 60% von allen Sternen in einem Doppelsternsystem befinden. Der nächste Stern nach der Sonne, Proxima Centauri, ist Mitglied von einem 'Drei-Doppelsternsystem' und ist der Begleiter von dem viel engeren Paar α Centauri, das mit dem blossen Auge sichtbar ist. Sterne in einem Doppelsternsystem sind durch die Schwerkraft gebunden und umkreisen einander. Wenn die zwei Sterne weit entfernt von einander stehen, so wie bei Proxima Centauri, merken sie wenig von ihrem Begleiter und evoluieren praktisch wie einzelne Sterne. Solche Doppelsterne haben Bahnperioden von 10 Jahren oder mehr. Für Doppelsterne mit Perioden von weniger als etwa 10 Jahren gilt, dass die Sterne auf dem Rote-Riesen-Ast oder AGB ungefähr so gross werden wie der Abstand zwischen den zwei Sternen. In diesem Fall können beide Sterne einander natürlich stark beeinflussen und die Situation ist ganz anders als im Fall eines einzelnen Sterns.

Um zu überlegen was in einem engen Doppelsternsystem geschehen kann, stellen wir uns ein Teilchen vor, das sich in der Nähe von einem der zwei Sterne befindet. Das Teilchen wird von der Gravitation dieses Sterns angezogen und beginnt auf ihn zu stürzen. Wenn sich das Teilchen vom ersten Stern entfernt und sich dem zweiten Stern nähert, wird die Schwerkraft vom ersten Stern immer schwächer und die vom zweiten Stern immer stärker. Ab einem bestimmten Punkt wird das Teilchen stärker vom zweiten Stern angezogen als vom ersten. In Wirklichkeit spielt nicht nur die Gravitation, sondern auch die Zentrifugalkraft durch die Rotation des Doppelsternsystems eine Rolle. Das Teilchen bewegt sich im Potentialfeld von diesen drei Kräften. Eine dreidimensionale Wiedergabe eines solchen Potentialfelds für einen Doppelstern mit Massenverhältnis 1:2 wird in Abbildung 6.3 auf Seite 132 dargestellt. Die tropfenförmigen Gebiete in der Äquipotentialfigur am Boden der Abbildung (fette Linien) sind die *Roche-Lobes* der Sterne. Die Punkte L_1, L_2 und L_3 sind die Punkte von Lagrange, in denen die Kräfte einander aufheben. Wenn ein Stern sein Roche-Lobe füllt, kann Gas durch den Sattelpunkt L_1 vom einen zum anderen Stern strömen.

Das Roche-Lobe des Sterns ist das Gebiet, innerhalb dessen der Stern beschränkt bleiben soll um sein Gas an sich gebunden zu lassen. Wir haben aber vorher schon gesehen,

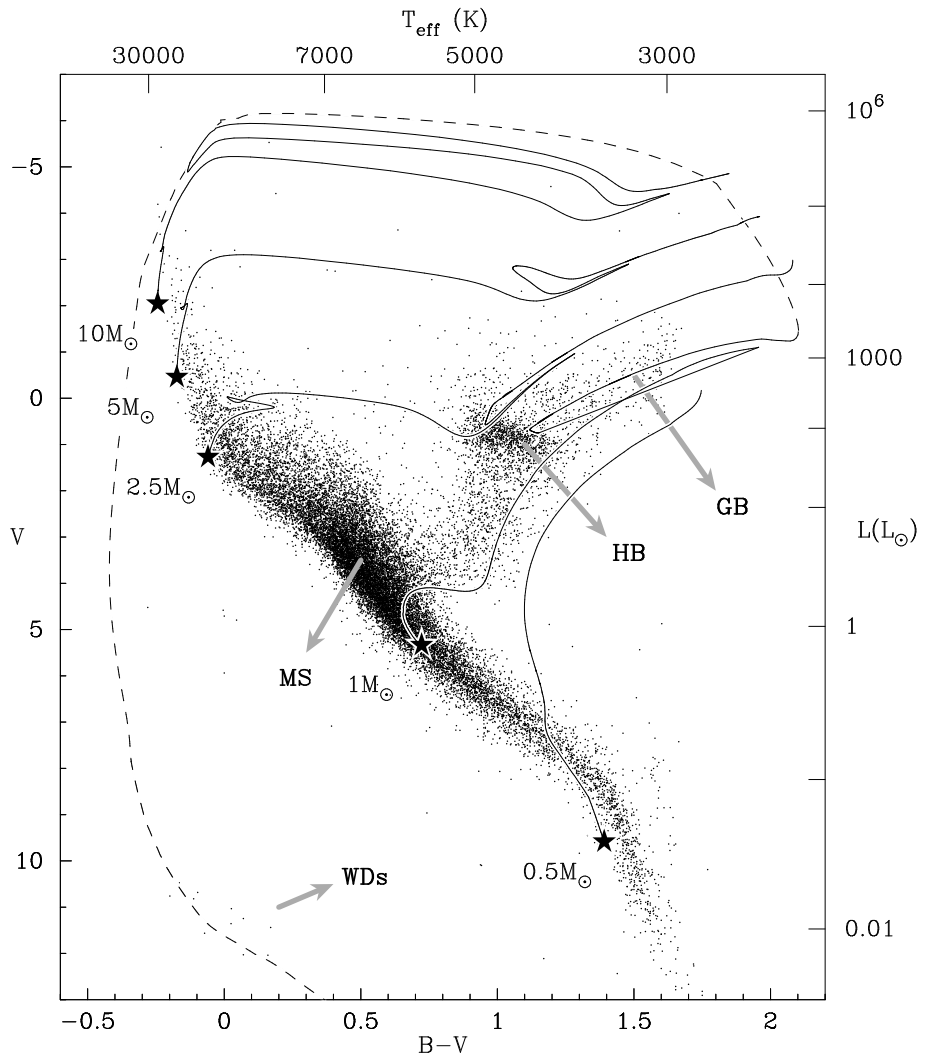

Abbildung 7.1: Ein Farben-Helligkeits-Diagramm zeigt die 'Farbe' $B-V$ und visuelle Magnitude V von 20 546 nahen Sternen. Von rechts unten bis links oben verläuft die Hauptreihe (MS). GB ist der Riesenast, HB der horizontale Ast und WDs sind Weisse Zwerge. Die Linien sind Evolutionsspuren von Sternmodellen von 0,5, 1,0, 2,5, 5 und 10 $M_\odot$. Die gestrichelte Linie zeigt das Ende des 1 $M_\odot$-Modelles, wo der Stern schliesslich ein Weisser Zwerg wird. Es wird ein Hinweis auf die Leuchtkraft L und Temperatur $T_{\rm eff}$ gegeben, die Zahlenwerte gelten aber genau genommen für die Hauptreihe.

dass evoluierende Sterne aufschwellen und dass sich schwerere Sterne schneller entwickeln. Von den zwei Sternen in einem Doppelsternsystem wird also der schwerere als erster von der Hauptreihe evoluieren und zu einem Roten Riesen werden. Wenn der Stern grösser wird als sein Roche-Lobe, kann das Gas von diesem Stern über den Sattelpunkt L_1 zum zweiten Stern strömen. Es findet dann Massenübertragung vom schwereren Stern zu seinem Begleiter statt. Da hauptsächlich die Masse des Sterns seine Evolution bestimmt, ändert sich die Evolution von einem solchen Stern drastisch. Wenn der Donorstern seinen Wasserstoffmantel schon vor dem AGB durch Massenübertragung verliert, entsteht ein Weisser Zwerg, der viel leichter ist als ein resultierender Weisser Zwerg eines Einzelsterns mit der selben ursprünglichen Masse. Wenn Massenübertragung vor oder während der Rote-Riesen-Phase stattfindet, entsteht ausserdem ein Weisser Zwerg aus Helium statt aus Kohlenstoff und Sauerstoff. Zusätzlich ändert sich die Bahnperiode während der Massenübertragung, da mit der Materie auch Drehimpuls[4] übertragen wird.

Falls der Begleiter des Donorsterns gross genug ist und die Geschwindigkeit der Massenübertragung nicht zu hoch, dann kann der Begleiter das übertragene Gas einfangen. Ist dieser Stern ein Hauptreihenstern, dann nimmt seine Masse signifikant zu und der Stern wird sich wie ein schwererer Stern verhalten. Massenübertragung kann daraufhin in die andere Richtung stattfinden, wenn der Begleiter selbst auch von der Hauptreihe evoluiert. Falls der Begleiter aber ein kompakter Stern ist, wie etwa ein Neutronenstern, dann hat die Materie zu viel Drehimpuls um den Begleiter direkt zu treffen. Um das kompakte Objekt herum entsteht in dem Fall eine *Akkretionsscheibe* (siehe vorderer Buchumschlag, Abbildungen *a* und *b*). Das Gas in der Akkretionsscheibe wird durch die starke Gravitation des kompakten Objekts beschleunigt, wird erhitzt und sendet viel Röntgenstrahlung aus. Wir sehen solche Doppelsterne als *Röntgendoppelsterne* (X-ray binaries). Wenn die Massenübertragungsgeschwindigkeit hoch genug ist, kann ein Teil der Materie den Doppelstern verlassen.

Füllt ein Riesenstern sein Roche-Lobe, dann ist die Massenübertragungsgeschwindigkeit oft sehr gross. Der Stern hat dann einen tiefen konvektiven Mantel. Verliert ein solcher Stern etwas Gas, weil er sein Roche-Lobe überfüllt, dann dehnt sich der Stern aus und überfüllt sein Roche-Lobe noch mehr. Dadurch steigt die Massenübertragungsgeschwindigkeit, der Stern dehnt weiter aus, und so weiter. Die Massenübertragung ist in diesem Fall instabil und der Begleiter eines solchen Sterns kann im Allgemeinen nicht soviel Gas in so kurzer Zeit einfangen. Der Mantel des Donorsterns dehnt so schnell aus, dass er auch den Begleiter umhüllt und so entsteht ein *gemeinsamer Mantel* (common envelope). Der Kern des Donors und der Begleiter umkreisen einander jetzt innerhalb dieses Mantels. Durch den Widerstand vom Gas spiralisieren beide Sterne aufeinander zu (spiral-in) und wird die Bahnperiode (viel) kürzer. Abbildung 6.4 auf Seite 134 zeigt eine Skizze dieses Prozesses der Einspiralisierung, siehe auch Abbildungen *c* und *d* auf dem vorderen Buchumschlag.

[4]Mit dem Begriff *Drehimpuls* wird in der Physik die Quantität der Rotation ausgedrückt. Drehimpuls geht wie Energie nicht verloren, kann aber übertragen werden. Ein Körper hat mehr Drehimpuls, wenn er schneller rotiert, schwerer ist oder einen grösseren Drehradius hat. Ein bekanntes Beispiel von Drehimpulserhaltung ist der Eistänzer, der seine Arme einzieht; der Drehradius wird kleiner und deswegen muss er schneller rotieren. Wenn die Rotationsgeschwindigkeit nicht grösser würde, ginge Drehimpuls verloren. Wenn der Eistänzer spontan schneller rotierte, würde Drehimpuls produziert.

Die Messung der Geschwindigkeit von Sternen ist eine andere Methode um Doppelsterne zu erkennen. Wenn zwei Sterne einander umkreisen, bewegt nämlich ein Stern auf uns zu, während der andere von uns weg bewegt, und umgekehrt. Dies wiederholt sich mit einer Periode, die gleich der Bahnperiode des Doppelsterns ist. Durch den Doppler-Effekt[5] kann diese periodische Änderung gefunden werden und das Verhältnis der Radialgeschwindigkeiten der beiden Sterne ist ein Mass für das Massenverhältnis. Ein Beispiel für eine solche Beobachtung und die Radialgeschwindigkeiten, die daraus abgeleitet wurden, wird in Abbildung 1.3 auf Seite 11 gezeigt.

In der Nähe der Sonne ist die Durchschnittdistanz zwischen den Sternen mit ungefähr einem *Parsec*[6] relativ gross. Die Chance, dass ein Doppelstern von einem anderen Stern beeinflusst wird, ist dadurch sehr gering und man kann annehmen, dass Doppelsterne isoliert evoluieren. Das ist aber anders in Gebieten mit viel höheren Sterndichten, so wie im Zentrum einer Galaxie oder in einem *Kugelsternhaufen* (siehe Abbildung 6.5 auf Seite 135). Im Zentrum eines Kugelsternhaufens kann die Sterndichte eine Million mal dichter sein als in der Nähe der Sonne und dadurch ist die Chance auf 'Kollisionen' zwischen Sternen eine Billion mal grösser. Eine sogenannte Kollision kann eine direkte Kollision zwischen zwei Sternen sein, aber auch eine 'Begegnung' von einem Stern mit einem Doppelstern oder zwischen zwei Doppelsternen. Bei einer solchen Begegnung können Sterne des Doppelsternsystems mit den begegnenden Sternen ausgetauscht werden und es kann ein ganz anderer Doppelstern entstehen. Man beobachtet, dass die Zahl von hellen Röntgendoppelsternen in Kugelsternhaufen im Verhältnis grösser ist als sonstwo in unserer Milchstrasse. Dies ist vermutlich die Folge der höheren Sterndichte in Kugelsternhaufen, da ein solcher Doppelstern beispielsweise durch eine direkte Kollision zwischen einem Riesenstern und einem Neutronenstern gebildet wird.

7.3 Diese Dissertation

In dieser Dissertation werden zwei Typen von kompakten Doppelsternen erforscht. In den Kapiteln 2 und 3 untersuchen wir das Entstehen von hellen Röntgendoppelsternen in Kugelsternhaufen. Wir zeigen, dass eines der drei Szenarios, die erstellt wurden um das Entstehen dieser Doppelsterne zu erklären, zu wenig oder gar keine Röntgendoppelsterne innerhalb des Alters des Weltalls produziert. In Kapitel 4 wird ein heller Röntgendoppelstern in unserer Milchstrasse untersucht. Aufgrund von beobachteten Röntgenausbrüchen auf dem Neutronenstern und einem hohen Neon/Sauerstoff-Verhältnis zeigen wir, dass der Donorstern wahrscheinlich der Rest eines Helium Weissen Zwerges ist, der möglicherweise durch eine Einspiralisierung in eine enge Bahn um den Neutronenstern gekommen ist. In Kapitel 5 untersuchen wir die Formation von doppelten Weissen Zwergen, die zwei Phasen von Massenübertragung durchlaufen haben. Wir konkludieren, dass unsere Modelle die beobachteten Massen und Bahnperioden gut erklären, aber dass es schwieriger ist auch den

[5] Der Doppler-Effekt ist auch die Ursache, dass sich der Ton der Sirene verschiebt, wenn sich eine Ambulanz nähert oder entfernt.

[6] Ein Parsec sind 3,26 Lichtjahre, etwa 30 Billionen Kilometer (30 000 000 000 000 km).

Altersunterschied zwischen den Sternen zu erklären.

7.3.1 Formation und Evolution von kompakten Röntgendoppelsternen

In den Kugelsternhaufen unserer Galaxie sind 13 helle Röntgenquellen beobachtet worden. Diese sind Röntgendoppelsterne und von den 13 Doppelsternen haben sicher 3, wahrscheinlich 5 und möglicherweise 6 bis 8 eine ultrakurze Bahnperiode von weniger als circa 40 Minuten (siehe Tabelle 1.1 auf Seite 5). Das ist im Verhältnis mehr als in unserer Galaxie und die Erklärung liegt vermutlich in der viel höheren Sterndichte in Kugelsternhaufen. In einem Kugelsternhaufen finden mehr Kollisionen zwischen Sternen statt als in der galaktischen Ebene und eine der Theorien sagt, dass ein solcher ultrakompakter Doppelstern durch die Kollision von einem (Unter-)Riesenstern mit einem Neutronenstern entsteht. In diesem Fall entsteht ein Weisser Zwerg, der sein Gas zum Neutronenstern übertragen kann. Während einer solchen Massenübertragung nimmt die Bahnperiode immer zu.

Laut einer anderen Theorie kann ein Stern von ungefähr 1 $M_{\odot}$, der sein Roche-Lobe am Ende der Hauptreihe füllt und sein Gas zu einem Neutronenstern überträgt, auch zu einem ultrakompakten Röntgendoppelstern werden. Normalerweise wird die Bahnperiode in so einem Fall länger, aber falls der Stern ein starkes Magnetfeld und einen starken Sternwind hat, kann das zu kürzeren Perioden führen. Das Gas, das den Stern im Sternwind verlässt, wird von den magnetischen Feldlinien mitgeführt und bis auf grosse Distanz zu Korotation mit dem Stern gezwungen. Dieser Effekt ist ähnlich wie bei einem Eistänzer, der seine Arme ausstreckt; er wird langsamer rotieren. Im Fall des Sterns ist der Grund, dass Drehimpuls durch den Wind vom Stern abtransportiert wird. Dieser Effekt ist nur schwach, er kann aber Milliarden Jahre lang anhalten. Der Stern wird dadurch langsamer rotieren und dieser Prozess wird *magnetisches Bremsen* (magnetic braking) genannt.

Die Rotation eines Sterns, der Masse in einem Doppelsternsystem überträgt, ist durch Gezeitenkräfte an die Bahnbewegung vom Doppelstern gekoppelt (wie der Mond, der immer die gleiche Seite zur Erde gekehrt hat). Der Drehimpuls, der durch das magnetische Bremsen verloren geht, wird dadurch effektiv aus der Bahn entnommen, wodurch die Bahn enger wird und die Periode kürzer. Die Bahnperiode erreicht bei einem bestimmten Wert ein Minimum und nimmt daraufhin wieder zu. Andere Forscher haben gezeigt, dass auf diese Weise Doppelsterne mit Minimumperioden von 5 Minuten gebildet werden können. Dieses Szenario wird *magnetischer Fang* genannt. Der Vorteil dieser Theorie ist, dass sie ein beobachtetes Doppelsternsystem erklären könnte, von dem die Bahnperiode 11 Minuten beträgt und abzunehmen scheint. Unsere Untersuchungen dagegen zeigen, dass ein Doppelstern länger braucht, als das Weltall alt ist, um eine Bahnperiode von 5 Minuten zu erreichen. Eine Minimumperiode von 11 Minuten ist gerade noch möglich, aber eine sehr spezifische Anfangssituation ist für eine so kurze Periode notwendig. Folglich ist die Chance sehr gering, dass diese Sterne in der Natur tatsächlich gebildet werden und daher können wir dieses Entstehungsszenario wahrscheinlich ausschliessen (Kapitel 2).

In Kapitel 3 führen wir die Untersuchungen des Szenarios des magnetischen Fangs fort. Wir verwenden jetzt ein neueres Gesetz um das magnetische Bremsen zu beschreiben,

das aus Beobachtungen von rotierenden Sternen empirisch bestimmt wurde. Die Folge ist ein schwächeres magnetisches Bremsen und eine Verschiebung der kürzesten Minimumperioden von circa 11 Minuten bis zu 70 Minuten. Damit ist das Szenario vom magnetischen Bremsen nicht mehr zutreffend. Das heisst aber, dass das Abnehmen der 11 Minuten-Periode auf eine andere Weise erklärt werden soll. Es ist tatsächlich möglich, dass der Doppelstern im Gravitationsfeld des Kugelsternhaufens, in dem er sich befindet, beschleunigt wird. Ausserdem wurde vor einigen Monaten ein Artikel von anderen Forschern publiziert, in dem gezeigt wird, dass man mit Sternkollisionen alle beobachteten Röntgenquellen in Kugelsternhaufen erklären kann.

Die hellen Röntgendoppelsterne in Kugelsternhaufen können also durch Kollisionen erklärt werden. Eine solche Kollision ist mit einem (Unter-)Riesen am wahrscheinlichsten und in diesem Fall wird der Begleiter des Neutronensterns ein Weisser Zwerg sein. In der galaktischen Ebene ist die Sterndichte zu gering für Sternkollisionen. Man vermutet, dass die hellen Röntgendoppelsterne hier durch eine Einspiralisierung in einem Doppelsternsystem mit einem Neutronenstern entstehen. So kann ein Weisser Zwerg aus Helium, Kohlenstoff und Sauerstoff, oder sogar Sauerstoff und Neon entstehen. Nach der Einspiralisierung verliert der Doppelstern durch Gravitationsstrahlung Drehimpuls, bis die Bahnperiode so kurz ist, dass der Weisse Zwerg sein Roche-Lobe füllt und Materie zum Neutronenstern überträgt. Ab diesem Moment sendet der Doppelstern Röntgenstrahlung aus und die Bahnperiode wird wieder länger.

Ein solcher Röntgendoppelstern in der galaktischen Ebene ist 2S 0918–549. Weil dieses System im optischen relativ schwach ist und im Röntgenbereich sehr hell, vermutet man, dass es sich um einen ultrakompakten Doppelstern handelt. Aus dem Röntgenspektrum des Doppelsterns schliesst man auf ein Verhältnis Neon/Sauerstoff, das höher ist als zum Beispiel in der Sonne. Daraus wird gefolgert, dass es sich um einen Weissen Zwerg aus Sauerstoff und Neon handelt. In Kapitel 4 wird die Beobachtung eines langen Ausbruchs auf dem Neutronenstern von 2S 0918–549 beschrieben. Solche lange Röntgenausbrüche können nur erklärt werden, wenn sich Wasserstoff und Helium auf dem Neutronenstern befinden. Das kann nur der Fall sein, wenn sein Begleiter Wasserstoff und Helium zum Neutronenstern überträgt. In einem Weissen Zwerg kommt kein Wasserstoff vor und Helium wurde (noch) nicht beobachtet. Die Frage, die wir in Kapitel 4 beantworten wollen, ist also: Was ist der Donorstern von 2S 0918–549?

Ein Sauerstoff-Neon Weisser Zwerg scheint ausgeschlossen, erstens weil diese Art sehr selten ist (und es wurden insgesamt vier dieser Doppelsterne gefunden) und zweitens weil diese Weissen Zwerge schwerer sind als 1 $M_{\odot}$ und deswegen wahrscheinlich auseinander gerissen werden, wenn sie Masse zu einem Neutronenstern übertragen. Damit bleiben also ein Helium Weisser Zwerg und ein Kohlenstoff-Sauerstoff (CO) Weisser Zwerg übrig. Wir berechneten Modelle für Sterne mit verschiedenen Massen, die zuerst einen Heliumkern und später einen CO-Kern produzieren. Wir zeigen, dass während der Wasserstofffusion, die zu der Formation eines Heliumkernes führen soll, Sauerstoff zerstört wird und mit Neon nichts passiert. Deswegen ist das Neon/Sauerstoff-Verhältnis in einem Heliumkern oder Helium Weissen Zwerg hoch. Während der Heliumfusion wird viel Sauerstoff produziert,

wodurch das Neon/Sauerstoff-Verhältnis in CO Weissen Zwergen sehr gering ist (siehe Tabelle 4.4 auf Seite 76). Wir folgern, dass der Donorstern in 2S 0918–549 wahrscheinlich ein Helium Weisser Zwerg ist, basierend auf dem langen Röntgenausbruch und dem hohen Neon/Sauerstoff-Verhältnis. Daher schlagen wir in Kapitel 4 vor, dass ein grosser Heliumvorrat aufgebaut werden kann, wenn die Massenübertragungsgeschwindigkeit nicht allzu hoch ist. Wenn die Heliumschicht dann schliesslich entzündet, gibt es einen langen Ausbruch, wie auch beobachtet wurde. Was wir nicht erklären können ist, dass kein Helium im Spektrum beobachtet wird. Es ist aber auch nicht eindeutig bewiesen, dass sich kein Helium im Doppelstern befindet und eine zukünftige Beobachtung von Helium könnte die Existenz vom Heliumdonor in 2S 0918–549 bestätigen.

7.3.2 Die Formation von doppelten Weissen Zwergen

Wenn ein Riesenstern sein Roche-Lobe füllt, ist die Massenübertragung oft instabil und ein gemeinsamer Mantel kann entstehen, gefolgt von einer Einspiralisierung der zwei Sterne innerhalb des Mantels (siehe Abbildung 6.4 auf Seite 134). Beim Einspiralisieren wird Bahnenergie aus dem Doppelsternsystem frei. Um abzuschätzen um wieviel die Bahnperiode bei einer Einspiralisierung kürzer wird, wird oft angenommen, dass genügend Bahnenergie freigemacht werden soll um den Mantel loszulösen und ins Weltall zu schicken. Die Bindungsenergie des Sternmantels, die wir mit dem Evolutionscode ausrechnen können, gibt also einen Hinweis auf die Quantität der Energie, die aus der Bahn des Doppelsterns freigemacht werden soll. Daraus können wir die Änderung der Bahnperiode während der Einspiralisierung berechnen. Dies nennt man die Methode der Energiebilanz.

In Kapitel 5 verwenden wir diese Methode um die Evolution von doppelten Weissen Zwergen zu rekonstruieren. Fast alle dieser Weissen Zwerge sind zu leicht um nicht in einem Doppelstern formiert zu sein. Die Bahnen der Doppelsterne sind nur einige Sonnenradien gross (siehe Tabelle 5.1 auf Seite 83) — viel kleiner also als der Riesenstern, der einen solchen Weissen Zwerg produziert. Daher wissen wir, dass alle dieser Weissen Zwerge nach der Massenübertragung im Doppelstern gebildet sind und dass die Bahnperiode während der letzten Massenübertragungsphase bedeutend kleiner geworden ist.Wir probieren verschiedene Szenarios aus, so wie stabile Massenübertragung, wobei der Begleiter das ganze Gas einfängt und wir zeigen, dass der Prozess nicht alle beobachteten Doppelsterne erklären kann. Auch die Einspiralisierung mit Energiebilanz reicht nicht aus um alle Doppelsterne zu produzieren. Wir verwenden darum die Annahme von anderen Forschern, dass während einer Einspiralisierung nicht die Energie, sondern der Drehimpuls erhalten wird. Wir finden, dass eine Variante dieser Methode die beobachteten Massen und Bahnperioden der doppelten Weissen Zwerge tatsächlich erklären kann, ohne dass Drehimpuls verloren geht oder produziert wird. Wir finden auch, dass es viel schwieriger ist die beobachtete Altersdifferenz der beiden Komponenten zu reproduzieren. Ein Beispiel eines Evolutionsszenarios, wobei ein doppelter Hauptreihenstern über zwei Phasen von Einspiralisierung zu einem doppelten Weissen Zwerg evoluiert, wird in Abbildung 1.4 auf Seite 13 gezeigt.

Acknowledgements

First of all I would like to thank my supervisors Frank Verbunt and Onno Pols for sharing with me their broad knowledge of astrophysics. I found it very useful to have two supervisors with different backgrounds, which has allowed me to convert your advice into well-considered work (or so I hope). Not only was working with you interesting in terms of science, it was also a very pleasant experience. Thank you Frank for being patient when I needed some time and for letting me work in Innsbruck whenever I felt like it.

I am also grateful to the members of the reading committee, Johan Bleeker, John Heise, Christoph Keller, Henny Lamers and GertJan Savonije. Thank you for reading the manuscript of this thesis and for your recommendations to improve it.

Thank you Peter Eggleton for allowing me to use your stellar evolution code that has been used for all of the chapters in this thesis. Because it is so fast, your code was especially useful for Chapters 2, 3 and 5, where we calculated large grids of models. Thank you Jean in 't Zand for our cooperation that led to Chapter 4 and for improving my knowledge of X-ray bursts. Thanks Gijs Nelemans for the scientific discussions we had and for your comments on Chapter 5. Thank you Sung-Chul Yoon for providing me with the LaTeX template of your thesis, which has made it much easier to convert the articles into this book.

Many thanks to Marion Wijburg for helping with the administrative part that comes with research and for being the solution to sometimes seemingly hopeless problems. Thanks Ed van der Zalm and Sake Hogeveen for the computer support that makes our lives so much easier. Thanks to many other people at the Astronomical Institute in Utrecht for the pleasant working atmosphere.

'Klop!' to the true Massive Nate Bastian and 'tot sinas' to Guillaume-Jean LeBlanc and his Magellanic Clouds for willing to be my paranymphomaniacs, a.k.a. 'paranichten'. I am very grateful and I hope I'll be all right after the defense. Nate, thanks for being around when needed.

I am grateful to a number of people in Austria. For (the arrangement of) housing, thanks Judith, Stefanie, Paul, Arntraud, Giovanna, Kathi and Harald. For arranging room to work at the University of Innsbruck, thank you Mr. Hartl, Stefan Kimeswenger, Sabine Schindler and Mr. Weinberger. You all helped Birgit and me to spend lots of time together in Innsbruck.

Thank you very much Daphny for supporting me in starting my PhD research. I had hoped that the promise of taking care of each other for life would have turned out to be more of a challenge. I am very grateful for the years we have spent together and I will cherish the memories for the rest of my life.

Many thanks to my parents, Frank and Susanne and the rest of my family for your presence and support when I needed them. Thank you for inviting me for dinner so often that I didn't have to cook for several weeks in a row and for all your patient listening.

Thank you very much Birgit for your understanding and patience with me. You made the sun[1] shine again after a difficult period. Thank you also for supporting me in my work, which would have been a lot less fun without you. I am very happy that we can continue to share our lives.

Thank you Pink Floyd for your great music, and for providing us with the meaning of life:

All that you touch, all that you see,
all that you taste, all you feel.

All that you love, all that you hate,
all you distrust, all you save.

All that you give, all that you deal,
all that you buy, beg, borrow or steal.

All you create, all you destroy,
all that you do, all that you say.

All that you eat, and everyone you meet,
all that you slight, and everyone you fight.

All that is now, all that is gone,
all that's to come,
and everything under the sun is in tune,
but the sun is eclipsed by the moon.

[1] See the bottom of page 139

References

Alexander, D. R. & Ferguson, J. W. 1994, ApJ, 437, 879 18, 44, 82

Andronov, N., Pinsonneault, M., & Sills, A. 2003, ApJ, 582, 358 46

Arnaud, K. A. 1996, in ASP Conf. Ser. 101: Astronomical Data Analysis Software and Systems V, 17–+ 66

Böhm-Vitense, E. 1958, Zeitschrift für Astrophysik, 46, 108 46

Belczynski, K. & Taam, R. E. 2004, ApJ, 603, 690 76

Bergeron, P. & Liebert, J. 2002, ApJ, 566, 1091 83

Bergeron, P., Wesemael, F., Fontaine, G., & Liebert, J. 1989, ApJ, 345, L91 83

Bildsten, L., Chang, P., & Paerels, F. 2003, ApJ, 591, L29 59

Bildsten, L., Salpeter, E. E., & Wasserman, I. 1992, ApJ, 384, 143 59

Boella, G., Butler, R. C., Perola, G. C., et al. 1997a, A&AS, 122, 299 59, 66

Boella, G., Chiappetti, L., Conti, G., et al. 1997b, A&AS, 122, 327 66

Bondi, H. & Hoyle, F. 1944, MNRAS, 104, 273 96

Bragaglia, A., Greggio, L., Renzini, A., & D'Odorico, S. 1990, ApJ, 365, L13 83

Brandt, S., Castro-Tirado, A. J., Lund, N., et al. 1992, A&A, 262, L15+ 58

Brown, E. F. 2000, ApJ, 531, 988 69

Brown, E. F., Bildsten, L., & Chang, P. 2002, ApJ, 574, 920 72

Chevalier, C. & Ilovaisky, S. A. 1987, A&A, 172, 167 9, 61

Chou, Y. & Grindlay, J. E. 2001, ApJ, 563, 934 7, 17, 55

Cominsky, L., Forman, W., Jones, C., & Tananbaum, H. 1977, ApJ, 211, L9 58

Cominsky, L. R. 1981, Ph.D. Thesis 58

Cornelisse, R. 2004, in RMxAC Conf. Ser., 10–11 72

Cornelisse, R., in 't Zand, J. J. M., Verbunt, F., et al. 2003, A&A, 405, 1033 72

Cornelisse, R., Verbunt, F., in 't Zand, J. J. M., et al. 2002, A&A, 392, 885 58, 59, 61

Cumming, A. & Bildsten, L. 2000, ApJ, 544, 453 69

Cumming, A. & Bildsten, L. 2001, ApJ, 559, L127 71

Cumming, A. & Macbeth, J. 2004, ApJ, 603, L37 70, 71

Davies, M. B. & Hansen, B. M. S. 1998, MNRAS, 301, 15 16

De Kool, M., van den Heuvel, E. P. J., & Pylyser, E. 1987, A&A, 183, 47 87

Deloye, C. J. & Bildsten, L. 2003, ApJ, 598, 1217 68, 76

Deutsch, E. W., Anderson, S. F., Margon, B., & Downes, R. A. 1996, ApJ, 472, L97+ 6, 16

Dewi, J. D. M. & Tauris, T. M. 2000, A&A, 360, 1043 87

Dieball, A., Knigge, C., Zurek, D. R., et al. 2005, ApJ, 634, L105 5

Eggleton, P. P. 1971, MNRAS, 151, 351 18, 44, 73, 82

Eggleton, P. P. 1972, MNRAS, 156, 361 18, 44, 73, 82

Eggleton, P. P. 1983, ApJ, 268, 368 96

Eggleton, P. P. & Kiseleva-Eggleton, L. 2002, ApJ, 575, 461 18, 45, 84

Evans, C. R., Iben, I. J., & Smarr, L. 1987, ApJ, 323, 129 11

Fabian, A. C., Pringle, J. E., & Rees, M. J. 1975, MNRAS, 172, 15P 37

Frontera, F., Costa, E., dal Fiume, D., et al. 1997, A&AS, 122, 357 66

Fujimoto, M. Y., Hanawa, T., & Miyaji, S. 1981, ApJ, 247, 267 59

Galloway, D., Muno, M. P., Chakrabarty, D., et al. 2006, in preparation 58, 59, 61

Galloway, D. K., Cumming, A., Kuulkers, E., et al. 2004, ApJ, 601, 466 59, 68

Habets, G. M. H. J. 1986, A&A, 167, 61 122

Han, Z. 1998, MNRAS, 296, 1019 120

Harmon, B. A., Wilson, C. A., Fishman, G. J., et al. 2004, ApJS, 154, 585 67

Heinke, C. O., Edmonds, P. D., & Grindlay, J. E. 2001, ApJ, 562, 363 16

Hils, D., Bender, P. L., & Webbink, R. F. 1990, ApJ, 360, 75 11

Hoffman, J. A., Cominsky, L., & Lewin, W. H. G. 1980, ApJ, 240, L27 58

Homer, L., Charles, P. A., Naylor, T., et al. 1996, MNRAS, 282, L37 5, 9, 16, 40, 58

Hua, X.-M. & Titarchuk, L. 1995, ApJ, 449, 188 66

Hurley, J. R., Pols, O. R., & Tout, C. A. 2000, MNRAS, 315, 543 102

Hurley, J. R., Tout, C. A., & Pols, O. R. 2002, MNRAS, 329, 897 108, 122

Hut, P. 1981, A&A, 99, 126 18

Iben, I. & Tutukov, A. V. 1984, ApJS, 54, 335 11, 80

Iben, I. J. 1967, ApJ, 147, 624 74

Iglesias, C. A., Rogers, F. J., & Wilson, B. G. 1992, ApJ, 397, 717 18, 44, 82

In 't Zand, J., Verbunt, F., Heise, J., et al. 2004a, NuPhS, 132, 486 62

In 't Zand, J. J. M., Cornelisse, R., & Cumming, A. 2004b, A&A, 426, 257 65

In 't Zand, J. J. M., Verbunt, F., Kuulkers, E., et al. 2002, A&A, 389, L43 62, 65

In 't Zand, J. J. M., Verbunt, F., Strohmayer, T. E., et al. 1999, A&A, 345, 100 66

Isern, J., Hernanz, M., Mochkovitch, R., & Garcia-Berro, E. 1991, A&A, 241, L29 74

Ivanova, N., Rasio, F. A., Lombardi, J. C., Dooley, K., & Proulx, Z. 2005, ApJ, 621, L109 6

Ivanova, N. & Taam, R. E. 2003, ApJ, 599, 516 45

Jager, R., Mels, W. A., Brinkman, A. C., et al. 1997, A&AS, 125, 557 59

Jonker, P. G., van der Klis, M., Homan, J., et al. 2001, ApJ, 553, 335 10, 58, 59, 61, 62

Juett, A. M. & Chakrabarty, D. 2003, ApJ, 599, 498 9, 58, 65, 67, 74

Juett, A. M. & Chakrabarty, D. 2005, ApJ, 627, 926 58

Juett, A. M., Psaltis, D., & Chakrabarty, D. 2001, ApJ, 560, L59 9, 57, 58, 61, 66

Karl, C., Napiwotzki, R., Heber, U., et al. 2003a, in NATO ASIB Proc. 105: White Dwarfs, 43–+ 83, 118

Karl, C. A., Napiwotzki, R., Nelemans, G., et al. 2003b, A&A, 410, 663 83

Kawaler, S. D. 1988, ApJ, 333, 236 45

King, I. R., Stanford, S. A., Albrecht, R., et al. 1993, ApJ, 413, L117 7, 8, 55

Krishnamurthi, A., Pinsonneault, M. H., Barnes, S., & Sofia, S. 1997, ApJ, 480, 303 46

Kuulkers, E. 2004, NuPhS, 132, 466 62, 65

Kuulkers, E., den Hartog, P. R., in 't Zand, J. J. M., et al. 2003, A&A, 399, 663 6, 16

Levine, A. M., Bradt, H., Cui, W., et al. 1996, ApJ, 469, L33+ 66

Marsh, T. R. 1995, MNRAS, 275, L1 83

Maxted, P. F. L., Burleigh, M. R., Marsh, T. R., & Bannister, N. 2002a, MNRAS, 334, 833 12, 79, 83, 122

Maxted, P. F. L., Marsh, T. R., & Moran, C. K. J. 2002b, MNRAS, 332, 745 11, 82, 83

Maxted, P. F. L., Marsh, T. R., Moran, C. K. J., & Han, Z. 2000, MNRAS, 314, 334 83

Mochnacki, S. W. 1981, ApJ, 245, 650 45

Moran, C., Marsh, T. R., & Bragaglia, A. 1997, MNRAS, 288, 538 83

Moran, C., Marsh, T. R., & Maxted, P. F. L. 1999, in ASP Conf. Ser. 169: 11th European Workshop on White Dwarfs, 275–+ 83

Morrison, R. & McCammon, D. 1983, ApJ, 270, 119 66

Nakagawa, Y. E., Yamazaki, T., Suzuki, M., et al. 2004, in AIP Conf. Proc. 727: Gamma-Ray Bursts: 30 Years of Discovery, 566–569 58

Napiwotzki, R., Edelmann, H., Heber, U., et al. 2001, A&A, 378, L17 10, 80

Napiwotzki, R., Koester, D., Nelemans, G., et al. 2002, A&A, 386, 957 80, 83, 122

Narayan, R. & Heyl, J. S. 2003, ApJ, 599, 419 72

Nelemans, G., Jonker, P. G., Marsh, T. R., & van der Klis, M. 2004, MNRAS, 348, L7 9, 58, 74, 77

Nelemans, G. & Tout, C. A. 2005, MNRAS, 356, 753 12, 107, 108, 109, 110, 111, 112, 119

Nelemans, G., Verbunt, F., Yungelson, L. R., & Portegies Zwart, S. 2000, A&A, 360, 1011 11, 12, 79, 80, 81, 98, 99, 100, 102, 107, 108, 109, 110, 119

Nelson, L. A., Rappaport, S. A., & Joss, P. C. 1986, ApJ, 304, 231 58

Paczyński, B. 1971, Acta Astronomica, 21, 1 122

Paczynski, B. & Sienkiewicz, R. 1981, ApJ, 248, L27 7, 16

Paczyński, B. & Ziółkowski, J. 1967, Acta Astronomica, 17, 7 100, 109

Parmar, A. N., Martin, D. D. E., Bavdaz, M., et al. 1997, A&AS, 122, 309 66

Peters, P. 1984, Phys. Rev., 136, 1224 19, 44

Podsiadlowski, P., Rappaport, S., & Pfahl, E. D. 2002, ApJ, 565, 1107 7, 17, 19, 20, 39, 40, 44, 46

Pols, O. R., Tout, C. A., Eggleton, P. P., & Han, Z. 1995, MNRAS, 274, 964 18, 44, 73, 74, 82

Pols, O. R., Tout, C. A., Schröder, K., Eggleton, P. P., & Manners, J. 1997, MNRAS, 289, 869 18, 84

Pylyser, E. & Savonije, G. J. 1988, A&A, 191, 57 7, 17, 38

Pylyser, E. H. P. & Savonije, G. J. 1989, A&A, 208, 52 38

Rappaport, S., Verbunt, F., & Joss, P. C. 1983, ApJ, 275, 713 19, 45

Rasio, F. A., Pfahl, E. D., & Rappaport, S. 2000, ApJ, 532, L47 16

Rasio, F. A. & Shapiro, S. L. 1991, ApJ, 377, 559 16

Ray, A., Kembhavi, A. K., & Antia, H. M. 1987, A&A, 184, 164 37

Refsdal, S. & Weigert, A. 1970, A&A, 6, 426 80

Reimers, D. 1975, Memoires of the Societe Royale des Sciences de Liege, 8, 369 90, 120

Saffer, R. A., Liebert, J., & Olszewski, E. W. 1988, ApJ, 334, 947 83

Savonije, G. J., de Kool, M., & van den Heuvel, E. P. J. 1986, A&A, 155, 51 16, 36, 41

Schröder, K., Pols, O. R., & Eggleton, P. P. 1997, MNRAS, 285, 696 18, 84

Sidoli, L., Parmar, A. N., Oosterbroek, T., et al. 2001, A&A, 368, 451 6, 16

Sigurdsson, S. & Phinney, E. S. 1993, ApJ, 415, 631 36

Sills, A., Pinsonneault, M. H., & Terndrup, D. M. 2000, ApJ, 534, 335 8, 46

Skumanich, A. 1972, ApJ, 171, 565 45

Soberman, G. E., Phinney, E. S., & van den Heuvel, E. P. J. 1997, A&A, 327, 620 110

Stella, L., Priedhorsky, W., & White, N. E. 1987, ApJ, 312, L17 5, 16

Stepien, K. 1995, MNRAS, 274, 1019 45

Strohmayer, T. E. 2004, ApJ, 608, L53 76

Strohmayer, T. E. & Brown, E. F. 2002, ApJ, 566, 1045 66

Swank, J. H., Becker, R. H., Pravdo, S. H., Saba, J. R., & Serlemitsos, P. J. 1976, IAU Circ., 3010, 1 58

Swank, J. H., Boldt, E. A., Holt, S. S., Serlemitsos, P. J., & Becker, R. H. 1978, MNRAS, 182, 349 58

Terndrup, D. M., Stauffer, J. R., Pinsonneault, M. H., et al. 2000, AJ, 119, 1303 45

Titarchuk, L. 1994, ApJ, 434, 570 66

Titarchuk, L. & Lyubarskij, Y. 1995, ApJ, 450, 876 66

Tout, C. A. & Eggleton, P. P. 1988a, ApJ, 334, 357 120

Tout, C. A. & Eggleton, P. P. 1988b, MNRAS, 231, 823 120

Tutukov, A. V., Fedorova, A. V., Ergma, E. V., & Yungelson, L. R. 1985, SAL, 11, 52 7, 17, 72

Tutukov, A. V., Fedorova, A. V., Ergma, E. V., & Yungelson, L. R. 1987, SAL, 13, 328 35

Ubertini, P., Bazzano, A., Cocchi, M., et al. 1999, ApJ, 514, L27 59

Van der Klis, M., Hasinger, G., Dotani, T., et al. 1993a, MNRAS, 260, 686 7, 8, 55

Van der Klis, M., Hasinger, G., Verbunt, F., et al. 1993b, A&A, 279, L21 7, 17, 55

Van Paradijs, J. 1996, ApJ, 464, L139+ 68

Van Paradijs, J. & McClintock, J. E. 1994, A&A, 290, 133 6, 9, 16, 58

Verbunt, F. 1984, MNRAS, 209, 227 45

Verbunt, F. 1987, ApJ, 312, L23 6, 40, 41, 73

Verbunt, F. 2005, in AIP Conf. Proc. 797: Interacting Binaries: Accretion, Evolution, and Outcomes, 30–39 5, 6

Verbunt, F. & Lewin, W. 2004, in Compact stellar X-ray sources, ed. W. Lewin & M. van der Klis (Cambridge: Cambridge U.P.) 5, 6, 16

Verbunt, F. & Zwaan, C. 1981, A&A, 100, L7 7, 44, 45, 52, 55

Vilhu, O. 1982, A&A, 109, 17 45

Vilhu, O. & Rucinski, S. M. 1983, A&A, 127, 5 45

Wallace, R. K. & Woosley, S. E. 1981, ApJS, 45, 389 68

Wang, Z. & Chakrabarty, D. 2004, ApJ, 616, L139 9, 16, 58

Webbink, R. F. 1984, ApJ, 277, 355 11, 80, 95

Webbink, R. F., Rappaport, S., & Savonije, G. J. 1983, ApJ, 270, 678 7, 17, 73

Werner, K., Nagel, T., Dreizler, S., & Rauch, T. 2004, in RMxAC Conf. Ser., 146–147 77

White, N. E., Kaluzienski, J. L., & Swank, J. H. 1984, in AIP Conf. Ser., 31–+ 67

Yungelson, L. R., Nelemans, G., & van den Heuvel, E. P. J. 2002, A&A, 388, 546 16, 73, 74